High-Pressure Studies on Molecular Systems at Ambient and Low Temperatures

Christopher A. Cameron

A Thesis submitted in fulfilment of the requirements for the
degree of Doctor of Philosophy to the School of Chemistry,
University of Edinburgh

August 2014

Declaration

I declare that this Thesis has been written by me and that the work detailed within is my own, or otherwise I have made a substantial contribution towards it except where specific reference is made to another. This work has not been submitted for another degree or professional qualification.

Christopher A. Cameron

Abstract

Pressure and temperature are two environmental variables that are increasingly being exploited by solid-state researchers probing structure-property relationships in the crystalline state. Modern high-pressure apparatus is capable of generating many billions of Pascals in the laboratory, and therefore can produce significantly greater alterations to crystalline materials than changes in temperature, which can typically be varied by only a few thousand Kelvin. Many systems such as single-molecule magnets exhibit interesting properties under low-temperature regimes that can be substantially altered with pressure. The desire by investigators to perform analogous single-crystal X-ray diffraction studies has driven the development of new high-pressure apparatus and techniques designed to accommodate low-temperature environments.

$[Ni(en)_3][NO_3]_2$ undergoes a displacive phase transition from $P6_322$ at ambient pressure to a lower symmetry $P6_122/P6_522$ structure between 0.82 and 0.87 GPa, which is characterized by a tripling of the unit cell *c* axis and the number of molecules per unit cell. The same transition has been previously observed at 108 K. The application of pressure leads to a general shortening of O···H hydrogen bonding interactions in the structure, with the greatest contraction (24%) occurring diagonally between stacks of Ni cation moieties and nitrate anions.

A novel Turnbuckle Diamond Anvil Cell designed for high-pressure low-temperature single-crystal X-ray experiments on an open-flow cryostat has been calibrated using the previously reported phase transitions of five compounds: $NH_4H_2PO_4$ (148 K), ferrocene (164 K), barbituric acid dihydrate (216 K), ammonium bromide (235 K), and potassium nitrite (264 K). From the observed thermal differentials between the reported and observed transition temperatures a linear calibration curve has been constructed that is applicable between ambient-temperature and 148 K. Low-temperature measurements using a thermocouple have been shown to vary significantly depending on the experimental setup for the insertion wire, whilst also adding undesirable thermal energy into the sample chamber which was largely independent of attachment configuration.

High-pressure low-temperature single-crystal X-ray diffraction data of $[Mn_{12}O_{12}(O_2CMe)_{16}(H_2O)_4]$ (known as $Mn_{12}OAc$) reveals a pressure-induced expulsion of the crystallized acetic acid from the crystal structure and resolution of the Jahn-Teller axes disorder between ambient pressure and 0.87 GPa. These structural changes have been correlated with high-pressure magnetic data indicating the elimination of a slow-relaxing isomer over this pressure range. Further application of pressure to 2.02 GPa leads to the expansion of these Jahn-Teller axes, resulting in an enhancement of the slow-relaxing magnetic anisotropy as observed in the literature. Relaxation of pressure leads to a resolvation of the crystal structure and re-disordering of the Jahn-Teller axes, demonstrating that this structural-magnetic phenomenon is fully reversible with respect to pressure.

The space group of the Prussian blue analogue $Mn_3[Cr(CN)_6].15H_2O$ has been re-evaluated as *R*-3*m* between ambient pressure and 2.07 GPa using high-pressure single-crystal X-ray and high-pressure neutron powder data. Reductions in metal-metal distances and gradual distortions of the Mn octahedral geometry have been correlated with previously reported increases in T_c and declines in ferrimagnetic moment in the same pressure range. Increasing the applied pressure to 2.97 GPa leads to partial amorphization and results in a loss of long-range magnetic order as shown by the literature.

The application of pressure (1.8 GPa) to the structure of $K_2[Pt(CN)_4]Br_{0.24}.3.24H_2O$ (KCP(Br)) causes a reduction in the Pt intra-chain and inter-chain distances, and results in an enhancement of the overall conductivity under these conditions as demonstrated in the literature. Almost no changes occur to the high-pressure crystal structure upon cooling to 4 K, except in the Pt-Pt intra-chain distances which converge and suppress the Peierls distortion known to occur at 4 K, resulting in a comparatively greater electrical conductivity under these conditions.

Acknowledgements

I would like to begin by thanking my supervisor Professor Simon Parsons for giving me the opportunity to become his PhD student and benefit from his wisdom (and wit) over these past four years. Not only have you improved my scientific skills and crystallographic knowledge tremendously, but your many humorous anecdotes and funny impersonations have helped make the experience truly memorable.

My thanks also go to my second supervisor Dr Stephen Moggach for all invaluable assistance he has given me throughout my PhD. You have helped me understand crystallography, driven me home on several occasions, and gifted me with your many funny stories, all of which has been genuinely appreciated.

Similarly I wish to extend my thanks to the many former and current members of the Parsons (Pete, Nick, Andy, Jack, and Giles) and Moggach (Scott, Alex G, Jorje, and Claire) groups, as well as Gary, Fraser, and Alex P. All of you have supported me in ways beyond counting and for that I am extremely grateful.

Thanks go to the beamline scientists at Diamond Light Source (Dr David Allan, Dr Harriott Nowell, Dr Sarah Barnett, Drs Anna and Mark Warren) and Dr Mike Probert at the University of Newcastle for their invaluable contributions to my research, as well as the various members of the Arnold and Pulham groups for kindly letting me use their laboratory and office space respectively.

I would also like to acknowledge the special contribution made by my friends and flatmates in providing me with many happy memories during my studies, and in particular Lorcan Cook, Alexander Delf, Adrian Bennett, and Chris McLellan for also helping maintain my sanity during the dark thesis-writing period.

My special thanks go to my family who have supported me from the beginning, especially my Mum who has always taken an active interest in my education and driven me to fulfil my potential, even though I may not have been as appreciative as I should have been at the time.

Lastly I would like to give heartfelt appreciation to my secondary school chemistry teachers Mr Kirkhope and Mrs Lindsay, for helping kindle my fascination with chemistry using exploding custard tins and pretty colours in test tubes.

Abbreviations

AC	Alternating-Current
CN	Cyanide Ligand
CSD	Cambridge Structural Database
DAC	Diamond Anvil Cell
DSC	Differential Scanning Calorimetry
En	Ethylenediamine
EOS	Equation of State
FR1	First $Mn_{12}OAc$ Fast Relaxing Isomer
INS	Inelastic Neutron Scattering
KCP(X)	$K_2[Pt(CN)_4]X_{0.3}.3.2H_2O$ (X = Br, Cl)
MnCrPBA	$Mn_3[Cr(CN)_6]_2.15H_2O$
$Mn_{12}OAc$	$[Mn_{12}O_{12}(O_2CCH_3)_{16}(H_2O)_4].2CH_3COOH.4H_2O$
$Mn_{12}OAc^tBu$	$[Mn_{12}O_{12}(O_2CCH_2{}^tBu)_{16}(H_2O)_4].CH_2Cl_2.MeNO_2$
$Mn_{12}OAcPh$	$[Mn_{12}O_{12}(C_6H_5CO_2)_{16}(H_2O)_4].2C_6H_5CO_2H$
PBA	Prussian blue Analogue
POTPs	Partially-Oxidized Tetracyanoplatinates
Pyz	Pyrazine
SMM	Single Molecule Magnet
SR1	First $Mn_{12}OAc$ Slow Relaxing Isomer
SR2	Second $Mn_{12}OAc$ Slow Relaxing Isomer
Sm:SBO	$Sm_x:Sr_{1-x}B_4O_7$
Sm:YAG	$Sm:Y_3Al_5O_{12}$
TBA	Tetrabutylammonium
TMTSF	Tetramethyltetraselenafulvalene
TSeT	Tetraselenotetracene
XIPHOS	X-ray Interface for Photo-Induced High-Pressure Low-Temperature Structural Studies

Contents

Chapter 1 – Introduction

Chapter 2 - A Pressure-Induced Displacive Phase Transition in Tris(ethyelenediamine) Nickel(II) Nitrate

Chapter 3 - Low-Temperature Calibration of a Novel Diamond Anvil Cell

Chapter 4 - A High-Pressure Low-Temperature Single-Crystal X-ray Study of $Mn_{12}OAc$

Chapter 5 - The Effect of Pressure on the Prussian Blue Analogue $Mn_3[Cr(CN)_6]_2.15H_2O$

Chapter 6 – A High-Pressure Low-Temperature Single-Crystal X-ray Study of KCP(Br)

Chapter 7 – Conclusions

Chapter 1

Introduction

1.1 Background

One of the challenges facing structural chemists lies in understanding and controlling the relationship between structure and physicochemical properties in the crystalline state (Moggach, Parsons, & Wood, 2008). Probing this relationship requires detailed knowledge of the crystal atomic composition and arrangement, and in this respect X-ray crystallography is one of the primary tools utilized in structure-property analysis (Goeta & Howard, 2004). Although many crystallographic investigations have been conducted under ambient conditions there is increasing interest among researchers in utilizing temperature and pressure to analyse the crystalline state (Katrusiak, 2008). The effect of pressure and temperature on crystal systems can be understood in terms of the Gibbs free energy equation (Equation 1.1) where application of pressure or temperature will result in the system changing as it attempts to minimize free energy (Kurpiewska & Lewinski, 2010), which can be achieved through reduction in volume, destabilization of interatomic contacts, or an increase in entropy (Johnstone *et al.*, 2010). Molecular crystalline materials are very susceptible to changes in temperature and pressure due to the relatively weak nature of intermolecular interactions compared with intramolecular bonding energies. Analysing the changes in crystal interactions in relation to temperature and pressure thus provides an insight into how the structures of materials give rise to their properties (Boldyreva *et al.*, 2004).

$$\Delta G = U + P\Delta V - T\Delta S \qquad (1.1)$$

A major avenue of current interest in this regard is polymorphism – the ability of a compound to exhibit multiple crystal structures under different temperature and pressure regimes. Polymorphism poses particular challenges to the pharmaceutical industry, as properties such as solubility will have huge impacts on synthetic production techniques and bioavailability, and are entirely defined by the nature of the solid state (Moggach, Parsons, & Wood, 2008). The polymorphs produced by pressure may be very different to those caused by temperature, (McGregor *et al.*, 2005), generating additional interest into how these variables affect the intermolecular interactions of the solid state (Boldyreva, 2008). The ultimate goal of crystal structure analysis lies in the prediction and engineering of structure such that a polymorph can be designed with a particular property, based on knowledge and understanding of the structure-property relationship, and requiring intensive theoretical modelling of the potential energies of the solid state coupled with experimental research (Boldyreva *et al.*, 2004).

1.2 High-Pressure Ambient-Temperature Crystallography

Pressure is a highly efficient mechanism for probing the structure of materials: unlike temperature which can typically only be varied by several thousand Kelvin in the laboratory, modern apparatus is capable of generating many billions of Pascals, resulting in far greater changes in crystalline thermodynamics (Moggach, Parsons, & Wood, 2008). High-pressure conditions have historically been employed much less by structural chemists compared to low temperatures (Moggach & Parsons, 2009), principally because of the greater difficulty in performing experiments using the former compared to the latter. A survey of the Cambridge Structural Database demonstrates that by 2012 there had been 277497 crystal structures determined below 283 K but only 667 were collected at non-ambient pressure (Allen, 2002). This comparative lack of research into high-pressure crystallography can be attributed to the expense and bulk of the early pressure devices. The invention (Merrill & Bassett, 1974) and refinement (Allan *et al.*, 1996) of the Diamond Anvil Cell (DAC) has made achieving high-pressure conditions much cheaper and less technically challenging, and created the possibility for simultaneous studies probing the electromagnetic, optical, and spectroscopic properties of crystalline materials under pressure (Moggach, Parsons, & Wood, 2008).

There have been a number of DAC designs over the years intended to complement the unique requirements of different diffractometers, samples, and environmental conditions desired (Katrusiak, 2008). One of the most common designs found in crystallography laboratories is the Merrill-Bassett cell (Figure 1.1) having achieved this status through its small size, ease of use, and compatibility with most modern diffractometers (Jamieson, 1981). The Merrill-Bassett cell is capable of reaching pressures in excess of 30 GPa, with PV terms in the Gibbs Free Energy equation equalling or exceeding the energies of organic covalent bonds (Hemley, 2000). Further advances relating to larger opening angles of the cell, improved detectors, more intense X-rays and the possibility of synchrotron radiation have succeeded in making high pressure crystallography even more attractive to structural chemists (Allan *et al.*, 1996).

As a result a wide variety of materials have now been studied under pressure ranging from simple molecules such as alcohols (Allan *et al.*, 1998, Allan *et al.*, 2002, McGregor *et al.*, 2005, Moggach *et al.*, 2005) and amino acids (Boldyreva *et al.*, 2005, Dawson *et al.*, 2005, Moggach *et al.*, 2006, Minkov *et al.*, 2010), to more complicated structures such as single molecule magnets (Prescimone *et al.*, 2008, Parois *et al.*, 2010), pharmaceuticals (Fabbiani *et al.*, 2003, Fabbiani *et al.*, 2007, Oswald *et al.*, 2010), energetic materials (Fabbiani & Pulham, 2006, Davidson *et al.*, 2008, Millar *et al.*, 2010), metal-organic frameworks (Chapman *et al.*, 2008, Moggach *et al.*, 2009, Bennett *et al.*, 2010, Graham *et al.*, 2011, Graham *et al.*, 2012, Gagnon *et al.*, 2013, Gould *et al.*, 2014), Prussian-blue analogues (Moritomo *et al.*, 2003, Bleuzen *et al.*, 2008, Giriat, 2011), and zeolites (Rutter *et al.*, 2001, Lee *et al.*, 2002, Colligan *et al.*, 2004, Gatta & Lee, 2007, Lee *et al.*, 2010, Readman *et al.*, 2014). High pressure crystallography has also formed an increasingly active area of research in polymorphism (Fabbiani *et al.*, 2004, Fabbiani *et al.*, 2005, Oswald *et al.*, 2009, Johnstone *et al.*, 2010), co-crystallization (Oswald & Pulham, 2008, Boldyreva, 2014), and the crystallization of liquids and gases at pressure (Merrill & Bassett, 1974, Allan *et al.*, 1998, Ridout & Probert, 2013).

1.2.1 Diamond Anvil Cell

The pressure in a DAC is applied via two opposed diamond anvils with polished flat faces (culets), and is a function of the applied force F and the anvil face area A. Diamond possesses several advantages that make it ideal for use in pressure cells: hardness (10 on the Mohs scale), low linear absorption coefficient for molybdenum X-ray radiation (0.202 mm^{-1}), and transparency to UV, IR, and visible radiation.

Figure 1.1: Schematic of the Merrill-Bassett cell and internal view of the gasket hole under a microscope

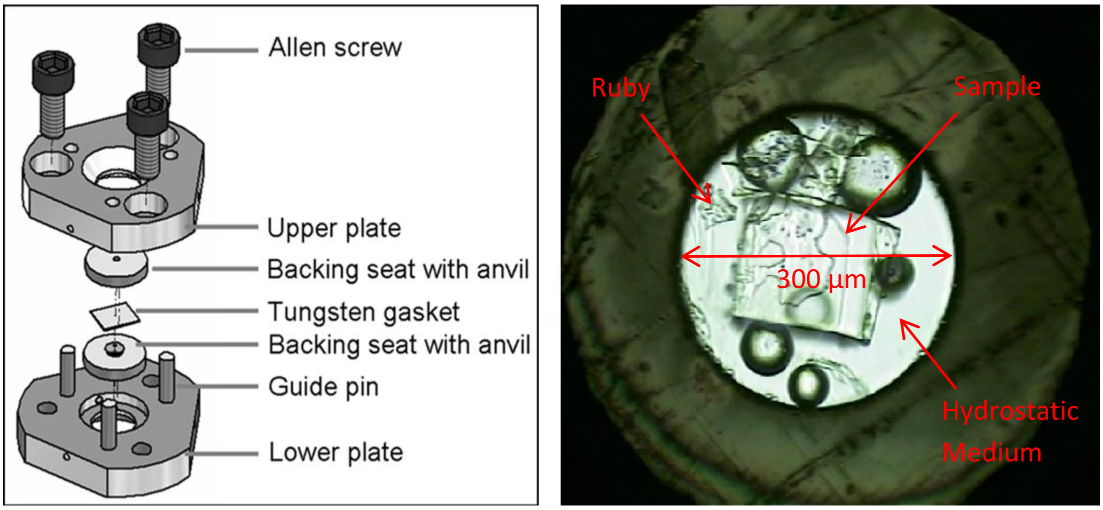

A deformable metal gasket 0.25 mm thick is placed between the anvils, and a central hole 0.3 – 0.4 mm in diameter comprises the walls of the samples chamber, with the anvil faces acting as the floor and ceiling (Katrusiak, 2008). Metal platens constructed from steel (or another suitably strong alloy) provide support to the anvils and form the bulk of the cell. Conical-shaped holes on the exterior surface of the platen define the path through which X-rays can enter and leave the sample chamber (Moggach, Parsons, & Wood, 2008). To provide further support the anvils are mounted in adjustable backing seats on the interior platen surface. Beryllium is the most common material utilized for the construction of backing discs due to its small linear absorption coefficient for molybdenum X-rays (Moggach & Parsons, 2009). Significant problems do occur however with beryllium in the pressure cell: the background signal is substantially increased by X-rays travelling through the backing disc, and since the beryllium is polycrystalline, intense powder rings appear in the diffraction pattern (see Figure 1.2). Conically ground tungsten-carbide overcomes many of these issues, although since it is opaque to the X-rays larger conical holes are required to maintain the opening angle of the cell (Moggach, Allan, *et al.*, 2008).

Figure 1.2: Detector images of crystal diffraction when using beryllium backing discs (left) and tungsten-carbide backing discs (right)

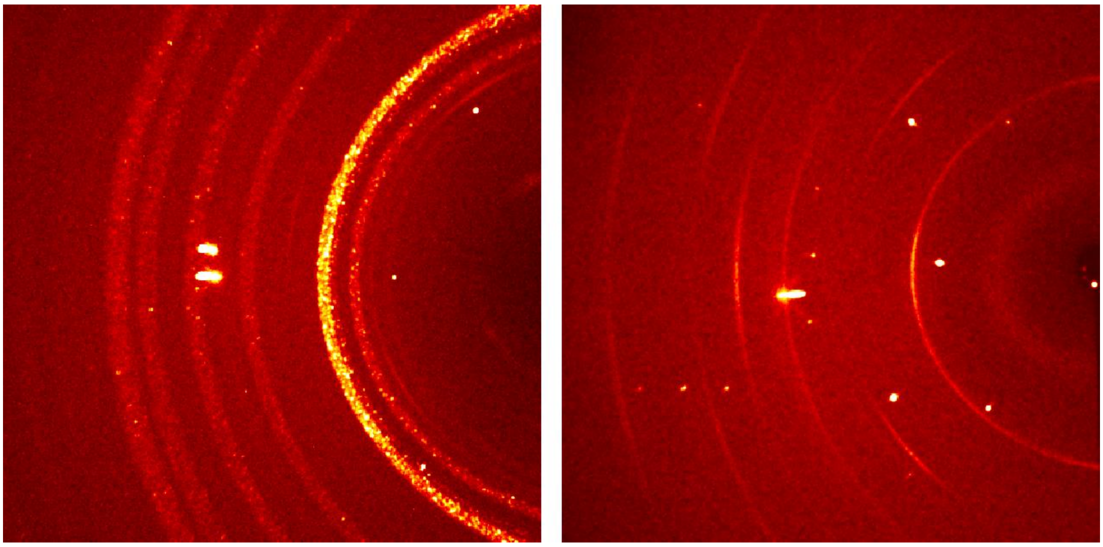

1.2.2 Pressure Measurement

Measuring the sample chamber pressure is inherently difficult due to the uneven distribution of plastic and elastic deformations throughout the DAC under applied loads, prompting the development of several different techniques to overcome this problem (Ridley & Kamenev, 2014). Pressure dependant liquid-solid phase transitions such as those in chloroform (0.54 GPa), *n*-hexane (1.04 GPa), and ethanol (2.22 GPa) have been used to produce single-point pressure calibration curves, although the reliance on single data points makes these curves less reliable (Moggach, Parsons, & Wood, 2008).

More accurate pressure measurements can be achieved using internal diffraction standards for which the equation of state (EOS) has been well-defined over an appropriately wide pressure range (Ridley & Kamenev, 2014). Suitable candidate materials typically possess small-volume high-symmetry unit cells with low mosaic spreads to minimize contamination of the diffraction pattern and improve intensity statistics (Hazen & Finger, 1981). The pressure marker should also possess a relatively low bulk modulus for enhanced pressure sensitivity, whilst remaining chemically inert in the presence of the hydrostatic medium (McMahon, 2012). A large number of strongly-diffracting EOS materials have been reported in the literature ranging from single-crystal compounds (e.g. NaCl, CaF_2, and SiO_2) (Birch, 1978, Hazen & Finger, 1981, Angel, 1993, Angel *et al.*, 1997, Brown, 1999) to powdered transition metals (e.g. Ag, Al, Au, Cu, Mo, Pd, Pt, Ta, and W) (Heinz & Jeanloz, 1984, Cynn & Yoo, 1999, Hanfland *et al.*, 2002, Shimizu, 2007). Consequently the choice of pressure probe is principally influenced by the method of X-ray diffraction (single-crystal or powder) as well as the calibration limit of the EOS compound, with both NaCl and CaF_2 undergoing known phase transitions at 30.0 GPa and 9.2 GPa respectively (Angel *et al.*, 1997).

Both single-point phase transition materials and internal diffraction standards involve time consuming data processing, requiring tedious separation of reflections in the diffraction pattern, and (Katrusiak, 2008). Alternatively pressure measurements can be more readily and easily obtained by exploiting the pressure-dependence of single-crystal fluorescence using a Raman or Fluorescence spectrometer (Jayaraman, 1984). Ruby (~0.5% Cr doped α-Al_2O_3) is the most common fluorescent probe utilized in this manner (Spain & Dunstan, 1989, Syassen, 2008), and is characterized by an intense sharp fluorescence doublet (Figure 1.3) arising from splitting of the E_{2g} excited state, with R1 and R2 peak wavelengths of approximately 694.2 and 692.7 nm respectively under ambient conditions (Adams *et al.*, 1976, Jayaraman, 1983). The pressure-fluorescence wavelength relationship for the R1 line under hydrostatic conditions has been calibrated up to 100 GPa (Piermarini *et al.*, 1975, Piermarini & Block, 1975, Mao *et al.*, 1978) and is described by Equation 1.2, where λ_0 and $\Delta\lambda$ are the ambient-pressure fluorescence wavelength and change in fluorescence wavelength at pressure *P* respectively.

$$P(Mb) = 3.81\left[\left(1+\frac{\Delta\lambda}{\lambda_0}\right)^5 - 1\right] \qquad (1.2)$$

Conversely the fluorescence wavelength shift of the lower intensity R2 peak is rarely utilized in routine high-pressure studies (Jayaraman, 1986), although it is a much more reliable pressure determinant than R1 under non-hydrostatic regimes (Gupta & Shen, 1991). Both the R1-R2 wavelength separation and R1 peak width are highly sensitive to the absence of hydrostatic conditions (Adams *et al.*, 1976), and the latter has been extensively exploited for the determination of hydrostatic limits in numerous pressure media (Tateiwa & Haga, 2010, McMahon, 2012). Above 200 GPa the ruby fluorescence method is unsuitable as the R1 peak becomes too broad (Jamieson, 1981).

Ruby diffraction is weak and thus does not typically affect unit cell indexing procedures unless the sample is also weakly diffracting or high intensity X-ray sources are being used. Additional advantages of the ruby method include the inertness of the compound and the requirement of only a very small crystal (less than 1% of sample chamber volume) for measurable fluorescence (Angel *et al.*, 1997, Piermarini, 2001). Improvements in experimental precision can be obtained through recording fluorescence measurements from multiple ruby crystals spread evenly throughout the sample chamber. Standard deviations associated with these average pressures are more sensitive to the presence of non-hydrostatic forces than individual R1 line widths or R1-R2 peak separations, and as such these have been utilized for the determination of pressure limits for numerous hydrostatic media (Klotz *et al.*, 2009).

Alternative pressure probes such as $Sm:Y_3Al_5O_{12}$ (Sm:YAG – yttrium aluminium garnate) and $Sm_x:Sr_{1-x}B_4O_7$ (Sm:SBO) have received significant interest because of the significantly lower temperature-dependence of their fluorescence wavelengths compared to ruby, and these will be discussed in greater detail in the high-pressure low-temperature section further below. Meanwhile the presence of optically transparent windows to the sample chamber also facilitates the employment of several other spectroscopic pressure measurement techniques. Visible light absorption in nickel dimethylglyoxime displays a linear relationship between pressure and absorption wavelength up to 3.0 GPa (Zahner & Drickamer, 1960, Guionneau *et al.*, 2004), whilst luminescence in thin-film semiconductors such as InP are significantly more sensitive to pressure than ruby fluorescence up to 10 GPa (Spain & Dunstan, 1989). Pressure-dependent phonon mode wavelengths of diamond theoretically offer the largest pressure range of all the aforementioned measurement techniques, but with the added disadvantage of reduced accuracy compared to the ruby fluorescence method (Jayaraman, 1986).

Figure 1.3: Fluorescence doublet for ruby at standard temperature and pressure

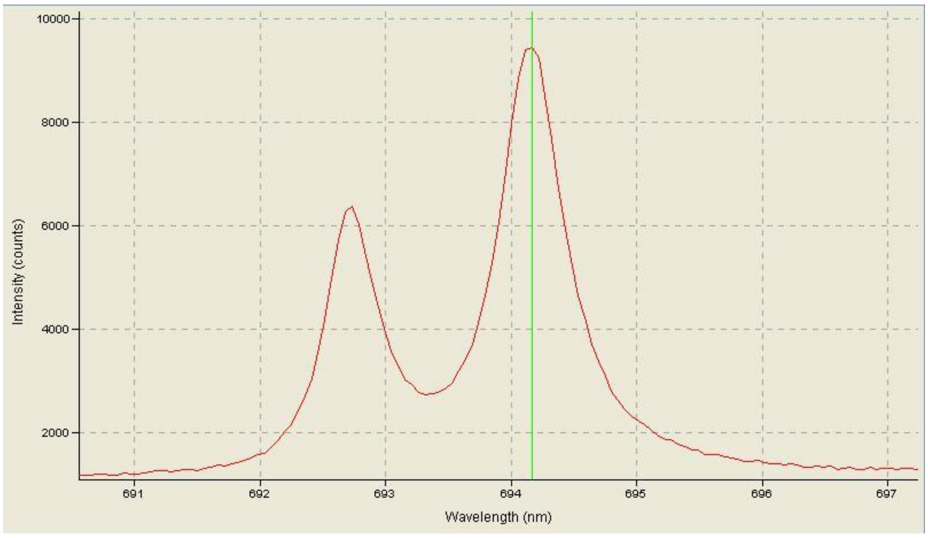

1.2.3 Hydrostatic Media

Non-hydrostatic conditions inside the sample chamber are undesirable since they result in inhomogeneous shear strain and differential shear stress in the crystal. Broadening of the diffraction peaks can be expected under this regime, leading to decreased signal to noise ratio (Klotz *et al.*, 2009). Phase transitions become much more difficult to observe, and pressure measurements cease to be reliable when utilizing either the ruby or internal standard methods. Hydrostatic conditions are created by filling the sample chamber with a pressure transmitting medium that possesses no shear strength, and thus no ability to produce anisotropic shear stress (Angel *et al.*, 2007). The maximum pressure at which these properties are observed is known as the hydrostatic limit, and is known for a wide variety of common liquids and gases (Table 1.1) (Miletich *et al.*, 2001). Solids are seldom chosen as the hydrostatic medium for high-pressure molecular studies below 10 GPa because of their highly anisotropic mechanical properties which result in non-hydrostatic effects. Pb and NaCl are prominent examples of this type of pressure media as they possess a reduced resistance to deformation and therefore lower shear stress compared to many other solids (Ridley & Kamenev, 2014).

Suitable media are chosen based principally on the pressure range desired for the study and the ability of the crystal to remain inert throughout the experiment (Katrusiak, 2008). Other important considerations for pressure media include X-ray transparency, low coherent scattering cross-section, availability, and loading complexity (Ridley & Kamenev, 2014). 4:1 methanol:ethanol is routinely utilized for pressure studies up to 10 GPa due to simple preparation and handling of the medium (Spain & Dunstan, 1989), while 16:3:1 methanol:ethanol:water is another easy to use medium that remains hydrostatic up to 14.4 GPa (Piermarini, 2001). Notably more recent literature studies suggest that the water fraction in 16:3:1 methanol:ethanol:water provides no overall improvement in the hydrostatic range compared with 4:1 methanol:ethanol (Klotz *et al.*, 2009). In cases where 4:1 methanol:ethanol reacts with or dissolves the sample 1:1 pentane:isopentane is often sufficient to a lower hydrostatic limit of 7.4 GPa (Jamieson, 1981). Extremely high pressures can be achieved using gases such as Ar and He although the technical difficulty associated with gas loading makes this approach much less common than liquid loading (Piermarini *et al.*, 1973, Jayaraman, 1986). The most popular gas medium is He as it possesses the largest hydrostatic range of any pressure medium.

Table 1.1: List of hydrostatic media found in the literature (Miletich *et al.*, 2001)

Medium	Hydrostatic Limit (GPa)
Silicon oil	0.9
Glycerol	1.4
Paraffin	2.0
Anhydrous 2-propanol	4.2
Isopropyl alcohol	4.3
Petroleum Ether	6.0
1:1 Pentane:Isopentane	7.4
Methanol	8.6
4:1 Methanol:Ethanol	10.4
16:3:1 Methanol:Ethanol:Water	14.4
Argon	**1.9***
Nitrogen	**3.0***
Helium	**11.8***

*Although the hydrostatic limit has effectively been reached for these media, low shear strengths ensure pseudo-hydrostatic conditions continue until much higher pressures

1.2.4 Data Collection and Processing

The various components of the DAC limit optical access to the sample which makes the centring process on the diffractometer more difficult compared to routine single-crystal experiments. Optical centring of the sample can be approximated by focussing the sample through the diamond axis using an in-built video camera or telescope. Further improvements in sample position can be achieved through implementing the gasket shading method, which determines the centre position by obtaining two X-ray images at ω angles of equal magnitude but opposite signs. Once the cell has been centred a subtraction of the pixels in both images leads to zero intensity at the gasket hole, although it should be noted that this procedure centres the gasket chamber rather than the sample. The bulky DAC also places substantial restrictions on potential diffracting positions and useable data collection strategies, and a typical high-pressure strategy used for a DAC with 40° opening angle is presented in Table 1.2 (Dawson *et al.*, 2004).

Processing data from a study involving the DAC also poses several challenges to analysts. The platens forming the bulk of the cell block access to most of the reciprocal space, leading to a reduction in data completeness and therefore the accuracy and precision of structural information. In some cases the completeness of data can be as low as 30 %, and this is especially problematic for low-symmetry crystal structures (Katrusiak, 2008). This problem can be circumvented by using multiple differently orientated crystals grown in-situ in the sample chamber for which the diffraction data can be merged (Johnstone *et al.*, 2010). Low wavelength synchrotron radiation can be used to mitigate low completeness which is achieved through an increase in the volume of the reflecting sphere. Alternatively a cell with a higher opening angle can be utilized when these are available, but otherwise incomplete data is associated with most DAC pressure studies (Moggach & Parsons, 2009, Kurpiewska & Lewinski, 2010).

Manual manipulation of harvested reflections in a graphical lattice viewer is often required as automatic indexing programs can inadvertently index the diamond or the pressure probe rather than the crystal of interest. Masks generated by a computer program using information about the cell geometry are applied to exclude regions shaded on the detector so that these regions are not integrated by the software. Powder rings from the backing discs and gasket can also be removed in this manner and this is especially useful when beryllium backing discs are used, although loss of data will result for shaded reflections that overlap with the powder rings (Figure 1.4).

Absorption of X-rays by the cell is a significant systematic error that is corrected by applying an experimental absorption profile or through determining the beam paths through the cells various components. Gasket shading is another important systematic error which can be accounted for using equations that model the dimensions of the gasket chamber and crystal and their respective positions. Multi-scan programs such as SADABS and SORTAV can account for additional sources of error such as crystal decay, incident beam inhomogeneity, and crystal volume variations. The high redundancy available from modern CCD detectors is especially advantageous in this regard, and persistent outliers can be removed through application of a suitable weighting scheme or manually during merging or refinement (Moggach, Parsons, & Wood, 2008).

Figure 1.4: Shading of the detector by the platens (left) and masking of the shaded region plus powder rings using a computer program (right)

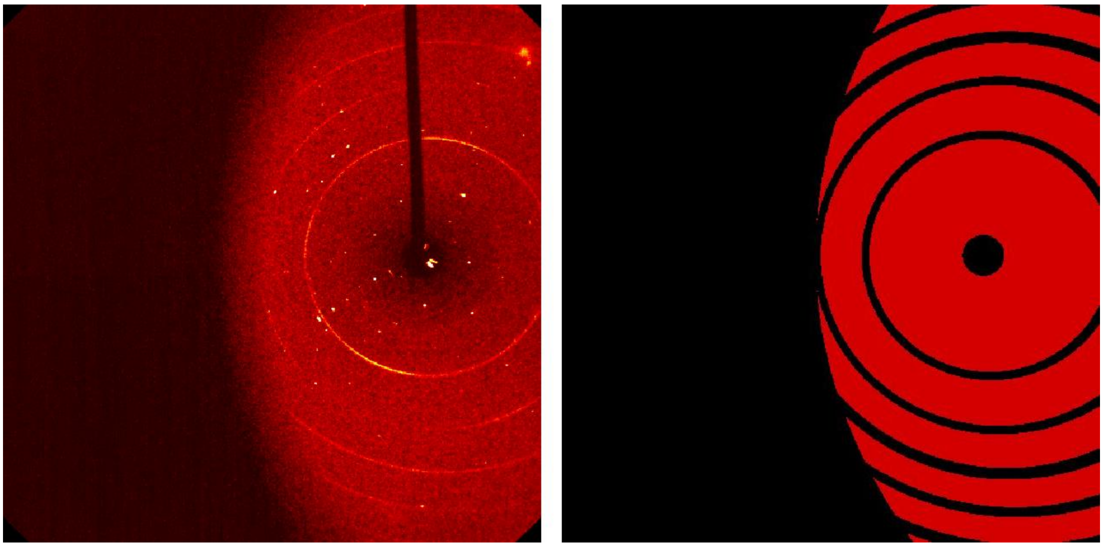

Table 1.2: Typical data collection strategy for high-pressure diffraction experiments

#	Type	Start ω	End ω	2θ	κ	φ
1	ω	-10	-40	-28	74	90
2	ω	40	-25	28	74	90
3	ω	-155	-220	-28	74	90
4	ω	-140	-170	28	74	90
5	ω	-155	-220	-28	74	270
6	ω	-140	-170	28	74	270
7	ω	-10	-40	-28	74	270
8	ω	40	-25	28	74	270

1.3 Low Temperature Crystallography

Structural investigations have been conducted under non-ambient temperature conditions for a significant period of time and are becoming increasingly popular (Goeta & Howard, 2004). A search of the Cambridge Structural Database v 5.35 (Allen, 2002) demonstrates that between 1978 and 2012 the percentage of publications using temperatures below 283 K in single crystal X-ray diffraction rose from 6 % to 62 %. Technological advances have made open-flow nitrogen cryostats capable of reaching temperatures as low as 80 K commonplace (Macchi, 2012). The Oxford Cryosystems Cryostream (Cosier & Glazer, 1986) is the most popular example of this type of temperature device, which immerses the sample in a continuous nozzle-directed nitrogen gas flow supplied by an external liquid nitrogen Dewar. Flow rate and temperature of the cryogen are controlled using a pump system and heating filament respectively, and icing of the crystal through contact with the atmosphere is prevented by sheathing the cryflow in dry air. Alternatively by using an analogous Helium open-flow cryostat the lowest accessible temperature can be reduced to approximately 10 K, although the greater operational expenses, technical challenges, and specialized applications of these instruments make this approach less ubiquitous (Copley *et al.*, 1997, Hardie *et al.*, 1998, Ribaud *et al.*, 2001).

Further reductions in temperature typically require a closed-cycle refrigerator system which instead utilizes the cooling capacity of compressed Helium upon expansion (Ridley & Kamenev, 2014). A cold stage on the refrigerator acts as a heat exchanger between the sample and expanding gas, allowing the mounted sample to be cooled prior to the gas being recovered and recycled. Both the cold stage and sample are fully enclosed in an evacuated shroud to improve thermal stability and prevent icing. Since the most frequently used shroud material is polycrystalline Beryllium the X-ray diffraction data suffers from enhanced absorption effects and contamination of frames by powder rings (Samson *et al.*, 1980). The bulk and expense of these devices make them generally unsuitable for the standard X-ray laboratory, and consequently they are often restricted to large central facilities more capable of accommodating their disadvantages. A notable exception is the XIPHOS facility at the University of Durham where researchers have succeeded in developing a modified Helium cryogenic refrigerator that makes temperatures down to 2 K within reach in the laboratory (Probert *et al.*, 2010). The combination of increased access to low temperature equipment, and the benefits and applications of these experimental conditions (discussed below), has resulted in greater exploitation of low temperature crystallography by structural chemists.

1.3.1 Thermal Vibration

The main reason for the increasing use of low temperatures is to reduce the impact of lattice vibrations on the scattering power of the atoms (Copley *et al.*, 1997). If all the atoms were stationary point scatterers then the atomic scattering factor would be equal to the number of electrons. However given that the electrons are distributed about a series of orbitals with finite volume a path difference for diffraction exists between these electrons causing a loss of intensity (Massa, 2004). Thermally induced atomic vibrations also displace the atoms from their equilibrium positions, reducing the intensity of scattered X-rays as the atoms spend more time away from their mean positions. The degree of destructive interference depends on the difference in path length between the scattered waves, with larger values of 2θ producing waves increasingly out of phase (Reilly, Morrison & Rankin, 2011). This has the consequence of decreasing the scattering intensity (Figure 1.5) and makes collection of data at high resolution problematic. Low temperature conditions are desirable if thermal lattice motion is to be mitigated allowing for the collection of high resolution data at meaningful intensity (Macchi, 2012).

Figure 1.5: The convoluted scattering factor *f* and temperature factor *T* for oxygen at different mean square amplitudes of vibration $<u^2>$ as a function of θ (Goeta & Howard, 2004)

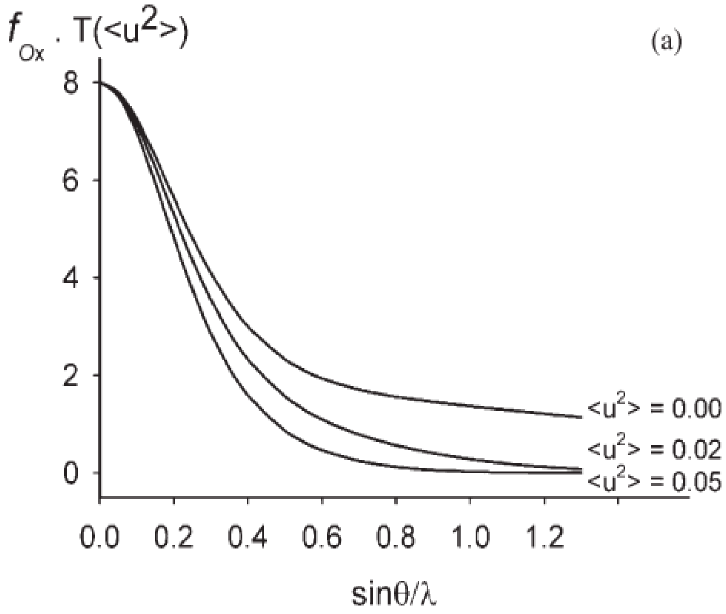

1.3.2 Anharmonicity

Modelling of the atomic temperature factor most commonly invokes a trivariate Gaussian approximation which models the atomic motion as harmonic along three unique orthogonal axes. Under this system any displacement of the atom from its equilibrium position causes a force to be exerted on the atom proportional to its relative displacement. The atomic temperature factor for the harmonic approximation involves six anisotropic displacement parameters that define the atoms position on the three orthogonal axes alongside three covariance terms (Reilly, Morrison & Rankin, 2011). These six parameters define an object that is ellipsoidal in shape and within which the atom has a certain probability of being located. Often however the harmonic approximation is an inadequate description of the atomic vibrations as the atoms lie in asymmetric potential wells (Kuhs, 1988). Higher-order terms are needed to describe the forces acting upon the atoms and this has historically necessitated the inclusion of many more atomic displacement parameters in the atomic temperature factor for proper modelling of the electron density (Figgis *et al.*, 1992). Implementing low temperature conditions reduces the vibrational amplitude of the atoms thus making them behave more like harmonic oscillators and decreasing the number of parameters required for refinement (Figure 1.6) (Coppens & Vos, 1971, Larsen, 1995). This method can also be supplemented be using more recently developed anharmonic temperature factors that require substantially less parameters compared to historical methods (Reilly, Morrison, Rankin, *et al.*, 2011).

Figure 1.6: The potential wells for a harmonic (dashed) and anharmonic (solid) oscillator (Sleight, 2003). The trapped and expansion terms refer to the overall change in bond lengths upon vibrational excitation.

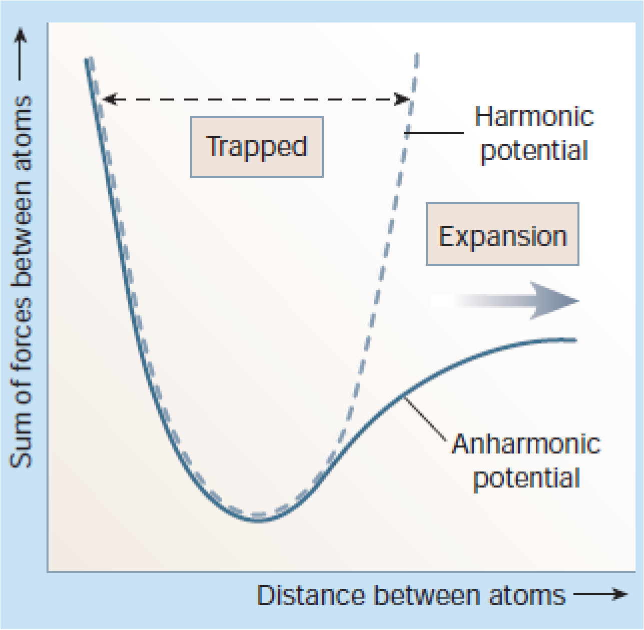

1.3.3 Thermal Diffuse Scattering

Inelastic scattering of the X-rays through interaction with crystal lattice phonons gives rise to thermal diffuse scattering (Hudspeth *et al.*, 2014), the greatest contributor to which is single-phonon scattering by low frequency acoustic modes. Since the vibration of atoms in a lattice is coupled the diffraction peaks produced by this scattering overlap the Bragg intensities from elastic scattering (Dam *et al.*, 1983). The X-rays can also interact with the high-frequency optical modes in a multi-phonon scattering process, leading to an increase in the background intensity of the diffraction pattern (Muller *et al.*, 2001). Removal of the single-phonon scattering contributions can be performed using knowledge about the X-ray wavelength, experimental temperature, Bragg angle and peak width for each reflection, and the elastic constants of the crystal, although information on the last of these is not always available (Lucas, 1969). Alternatively the impact of phonon modes this can be mitigated by lowering the temperature of the experiment as this will reduce the vibrational frequency of the phonon modes (Macchi, 2012). Conducting the experiment at liquid nitrogen temperatures minimizes the impact of phonon modes above 100 cm^{-1} due to reduced lattice vibration, while temperatures as low as 10 K would be necessary to effectively eliminate phonon modes below this wavenumber (Larsen, 1995).

1.3.4 Radiation Damage

Damage to the crystal occurs whenever it is subject to ionizing radiation such as X-rays, causing a steady decline in the intensity of reflections and loss of crystalline order (Seiler & Dunitz, 1985). The mechanism for this radiation damage consists of two stages: the primary radiation damage phase where interaction of the X-rays with the crystal produces electrons and positively charged atoms, and the secondary radiation damage phase involving movement of these radiation products through the crystal structure resulting in chemical bond breaking, redox reactions, and free radical generation (Gonzalez & Nave, 1994, Kmetko *et al.*, 2006). While the former is purely a function of the scattering angle, intensity of the beam, and exposure time, the latter has been shown to be temperature dependant and continues even after the incident beam has been switched off. This is because the radiation products continue to react and interact even once the most of the X-ray photon energy is also absorbed by the crystal and is transformed into heat which further enhances the movement of radiation products (Garman & Nave, 2009). Biological macromolecules are particularly susceptible to the effects of radiation damage, such that multiple crystals are typically required to collect a full data set (Hope, 1988, Garman & Weik, 2013). Diffusion of the radiation products throughout the lattice and their subsequent reaction are vastly reduced at temperatures below 100 K, although some radiation damage still occurs at temperatures as low as 9 K (Gonzalez *et al.*, 1992, Nave, 1995, Teng & Moffat, 2000, Meents *et al.*, 2009).

1.3.5 Disorder

Dynamic disorder in the crystal structure is another significant problem for crystallographic analysis as spherical groups such as PF_6^- and ClO_4^- are often rotationally disordered at room temperature. All orientations of the molecule are energetically equivalent, requiring little energy for the group to rotate freely in the crystal structure. Lowering the temperature reduces the ability of groups to overcome the kinetic barriers to rotation and allows for better modelling of the electron density. Static disorder such as impurities and defects are impossible to remove by lowering the temperature although they can be better resolved as the components of the disorder become easier to model. Librational disorder results in artificial shortening of bond lengths due to inaccurate thermal ellipsoid fitting; however the reduced size of the thermal ellipsoids at low temperatures provides a more accurate calculation of the bond lengths (Figure 1.7) (Goeta & Howard, 2004, Macchi, 2012).

Figure 1.7: a) Electron distribution of atom B b) Shortening of bond length due to ellipsoidal fit c) Reduction in temperature allowing for better modelling of bond length (Goeta & Howard, 2004)

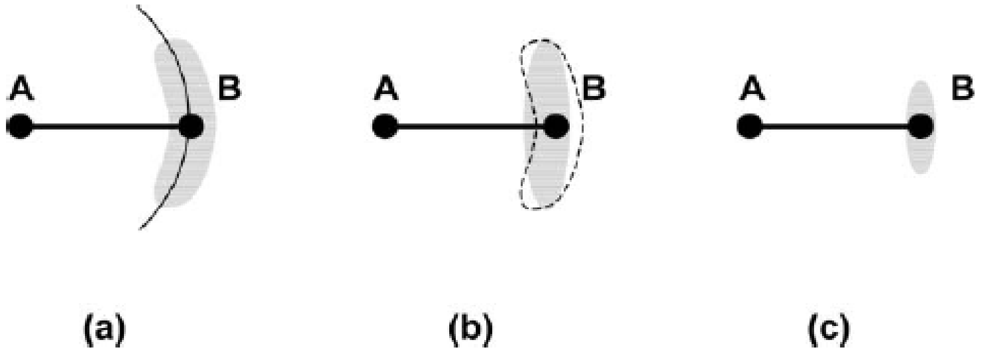

1.3.6 Applications

Exploitation of low temperature conditions thus provides significant benefits to crystallographic analysis, although these will not necessarily outweigh potentially inherent defects present in the crystal. The location and modelling of the electron density in a Fourier map becomes much easier due to reduced thermal motion and anharmonicity. Analysis of weakly diffracting crystals is more viable than at room temperature, and high resolution enables better modelling of the atomic thermal parameters, leading to better characterization of electron density features such as hydrogen atoms and lone pairs. Inhibition of radiation damage ensures crystals last much longer before losing crystallinity, which is necessary particularly for biological studies due to the susceptibility of proteins to radiation damage.

Many studies also utilize low temperature conditions for purposes other than improved data. A wide variety compounds exhibit phenomena such as spin-crossover (Money *et al.*, 2003), single-molecule magnetism (Sessoli *et al.*, 1993), and Peierls distortions (Comes *et al.*, 1973) under low-temperature regimes, and by collecting crystallographic data under the same conditions researchers can improve their understanding of the structure-property relationship in these systems (Farrell *et al.*, 2013). The relative binding strengths of gas adsorption sites in metal-organic frameworks can be probed using variations in temperature, and this information employed for tailoring the gas-uptake properties of subsequent gas-storage materials (Rowsell *et al.*, 2005). Investigations of polymorphism invariably involve consideration of low temperature conditions as one of the key variables used to induce phase transitions (Herbert & Campbell, 1977, Larsen, 1995). Low temperatures are also useful for the crystallization of compounds that are liquid or gaseous under ambient temperatures conditions (Copley *et al.*, 1997). Samples produced in this manner are often polycrystalline and so produce cluttered diffraction patterns, however this problem can be overcome through the application of an infrared laser for localized heating of the sample, melting the crystallites until only one remains which can form the nucleus of a larger crystal (Maloney *et al.*, 2014).

Compounds that are air-sensitive or susceptible to solvent loss require low temperatures in order to preserve the crystal structure long enough to obtain a structure, and this is achieved by immersing the crystal in an oil that undergoes a glass transition when cooled. The oil holds the crystal in place while contributing only a small level of scattering to the background of the diffraction pattern. Additionally the inert oil allows for easier manipulation and cutting of the crystals with minimal stress and damage and as such is now the major technique used for handling crystals in small molecule structural analysis (Hope, 1988, Kottke & Stalke, 1993).

1.4 High-Pressure Low-Temperature Crystallography

Since a large number of interesting phenomena are known to occur under low temperatures, researchers have become increasingly interested in conducting high-pressure X-ray diffraction experiments under these conditions. A significant obstacle to performing these structural investigations has been the lack of suitable high-pressure low-temperature instrumentation and methodology. Merrill-Bassett cells in particular are not suitable for low-temperature experiments where their relatively large size and composition makes cooling to low-temperatures extremely difficult. As a result researchers studying the structure-property relationship in materials with interesting properties under low-temperatures using high-pressure have to compare ambient-temperature high-pressure data with high-pressure low-temperature property measurements. This is an undesirable situation because the application of low-temperature conditions can produce significant changes in structure compared to ambient-temperatures (Cornia *et al.*, 2002) (Farrell *et al.*, 2013), and potentially invalidates any conclusions drawn from these investigations. However over the past several decades technological advances in cryogenic instruments and pressure cell apparatus have made these investigations increasingly feasible. Subsequently a wide array of specialized high-pressure low-temperature apparatus has been reported in the literature optimized for varying pressures, temperatures, and measurements (Gerard & Pernolet, 1973, Jones *et al.*, 1975, Schuele & Schmidt, 1982, Sinha & Srinivasan, 1983, Trokiner *et al.*, 1984, Silvera & Wijngaarden, 1985, Sterer *et al.*, 1990, Simmons *et al.*, 1993, Tang *et al.*, 1998, Takemura *et al.*, 2002, Rondinone *et al.*, 2003, Suzuki & Endo, 2003, Petrova *et al.*, 2005, Kamenev *et al.*, 2006, Mittal *et al.*, 2011).

1.4.1 Low-Temperature Diamond Anvil Cells

The thermal and mechanical properties of the various components in a high-pressure cell are highly influential in determining the maximum pressure and temperature ranges attainable for experiments (Walker, 2005, Ridley & Kamenev, 2014). Properties such as heat capacity, thermal expansion, thermal conductivity, yield strength and toughness are particularly affected by the application of low-temperature conditions, and this leads to limitations regarding the potential materials utilized in the pressure device as well complications in successful implementation under these regimes. Accurately determining the applied pressure under low-temperatures is a major source of error in this regard, as the sample chamber may contract or expand depending upon the thermal expansion coefficients of the surrounding components, rendering some ambient-temperature pressure measurement techniques unreliable (Feng *et al.*, 2010). Yield strength generally increases for all metals upon cooling leading to an enhancement of the maximum possible pressure that can be applied to the sample. Conversely the toughness and ductility of metallic species varies considerably under these regimes, with body-centred cubic structures generally experiencing reductions in toughness and increased brittleness, while face-centred cubic analogues frequently undergo relatively minor changes in toughness (± 30 %) and retain comparatively greater ductility. Hexagonal-close-packed crystal structures typically exhibit a range of mechanical properties somewhere between the aforementioned metallic substances (Walker, 2005).

One of the most commonly employed cryogenic substances is BeCu (~ 2.0 % Be) which possesses several advantageous characteristics including relatively high strength for a non-magnetic metal (Jones *et al.*, 1975), good thermal diffusivity, minimal thermal contraction down to 1.1 K (Silvera & Wijngaarden, 1985), ease of construction, and commercial availability (Walker, 2005). The potential risk of berylliosis during handling (Be content > 2.2 %) and machining, as well as paramagnetism arising from impurities at very low-temperatures (Dunstan & Spain, 1989), represent notable disadvantages of this material. Co-Ni alloys have similarly been incorporated into many low-temperature pressure devices since they exhibit greater yield strength than BeCu, have no known problems surrounding toxicity, and are also commercially available (Walker, 2005). These alloys have their own drawbacks as they are much harder to machine and several orders of magnitude more magnetic than BeCu. Another material noted for its utility in high-pressure research is Inconel (nickel-chromium alloy) which possesses many of the same advantageous properties as the BeCu and Co-Ni alloys, although this also comes at the expense of being much more difficult to manufacture (Dunstan & Spain, 1989). Other alloys such as Ti and Al have been recognized for their small neutron scattering crosssections, relatively low yield strengths, and potential for superconductivity at low temperatures (Walker, 2005).

1.4.2 Pressure Measurement

Measurement of the applied pressure in cryogenic diffraction experiments utilizes many of the same techniques that are frequently employed for ambient-temperature studies. However accurate pressure determination using the ruby fluorescence method is complicated by the significant temperature-dependence of the R1 and R2 wavelength shifts. Furthermore the intensity of both these fluorescence peaks declines as the ruby is cooled making measurements more difficult, and the R2 line disappears entirely at liquid He temperatures. Ambient-temperature ruby pressure equations are therefore completely unreliable for cryogenic experiments, necessitating the development of several different methods for obtaining reliable pressure measurements.

Several high-pressure low-temperature R1 calibration curves have been devised using different temperature and pressure ranges (Yamaoka *et al.*, 2012), although the limitation in utility of these calibrations to specific temperatures represents a significant disadvantage of this approach. The lowest-temperature pressure equation for ruby currently available is given by Equation 1.3 which describes the R1 wavelength-pressure relationship between ambient-pressure and 15.8 GPa at 4.5 K. (Feng *et al.*, 2010). Alternatively the temperature-induced fluorescence shift can be recorded independently at ambient pressure and subtracted from the total wavelength change of a ruby inside the sample chamber (Ragan *et al.*, 1992). The wavelength of ruby R1 fluorescence in the temperature range 15 K – 600 K is represented by Equation 1.4.

$$P(GPa) = 1762\left[\ln\left(\frac{\lambda}{\lambda_0}\right)\right] \qquad (1.3)$$

$$R1\left(cm^{-1}\right) = 14423 + 4.49x10^{-2}T - 4.81x10^{-4}T^2 + 3.71x10^{-7}T^3 \qquad (1.4)$$

Attempts to circumvent the known disadvantages of the ruby fluorescence technique have driven investigations into the suitability of alternative pressure probes, ideally featuring reduced temperature sensitivity and enhanced intensity under low-temperature conditions. Notable examples of such materials that have been reported in the literature for implementation in high-pressure variable-temperature experiments are the rare-earth doped compounds Sm:$Y_3Al_5O_{12}$ (Sm:YAG – yttrium aluminium garnate) and Sm_x:$Sr_{1-x}B_4O_7$ (Sm:SBO). Sm:YAG displays a fluorescence doublet at 615.9 nm and 617.7 nm and possesses both similar pressure dependence and negligible temperature dependence compared to ruby. The high-pressure fluorescence relationship for this compound has been calibrated up to 26 GPa and is presented in Equation 1.5. A wider pressure range has been achieved using Sm:SBO with a fluorescence singlet at 685 nm which is approximately 70 times less sensitive to temperature than ruby R1, and has been calibrated to 108 GPa using Equation 1.6.

$$P(GPa) = -10280\left(\frac{\lambda}{\lambda_0 - 1}\right)^2 + 2085\left(\frac{\lambda}{\lambda_0 - 1}\right) \qquad (1.5)$$

$$P(GPa) = 4.032\Delta\lambda\left(\frac{1 + 9.29x10^{-3}\Delta\lambda}{1 + 2.32x10^{-2}\Delta\lambda}\right) \qquad (1.6)$$

1.4.3 Hydrostatic Media

The behaviour of the hydrostatic medium in cryogenic pressure studies can deviate substantially compared to ambient temperature experiments (Tateiwa & Haga, 2010). Reductions in applied temperature produces non-linear and sometimes complex changes in mechanical properties of the pressure medium (Paureau, 1977). Additionally the onset of solidification at the pressure-dependent freezing point gives rise to undesirable non-hydrostatic forces inside the gasket chamber. Consequently the range of potential pressure media for low-temperature experiments is severely impacted by the unavoidable decline in hydrostatic limits and diffraction data quality. Noble gases such as He, Ar, and Xe demonstrate the widest known pseudo-hydrostatic pressure range and thus are often considered the best pressure media for cryogenic studies (Spain & Dunstan, 1989, Burnett *et al.*, 1990). However the loading and handling procedures for these gaseous media are notably difficult compared to liquid alternatives and require specialist equipment not available in every laboratory (Ridley & Kamenev, 2014). Meanwhile the commonly utilized high-pressure media 4:1 methanol:ethanol, 1:1 *n*-pentane:isopentane, and petroleum ether have all been deemed adequately hydrostatic up to approximately 10 GPa. Comparatively greater increases in pressure inhomogeneity for many other known liquid media at low-temperatures such as isopropyl alcohol, glycerol, and silicon oil limit their effectiveness to much lower pressure regimes (Feng *et al.*, 2010, Tateiwa & Haga, 2010).

1.4.4 Previous High-Pressure Low-Temperature Single-Crystal Diffraction Studies

Only a handful of single-crystal X-ray diffraction studies under conditions of high-pressure and low-temperature have been reported. The earliest such experiment involved analyzing the symmetry of several $[(CH_3)_4N][MnCl_3]$ phases by comparing precession photographs collected under different temperatures and pressures (Morosin & Schirber, 1974). High-pressure conditions utilized a polycrystalline cylindrical beryllium cell with niobium ring base which was attached to a thermally-isolating pressure line mounted on the goniometer. Cooling of the cell was achieved through a directed flow of cooled N_2 gas or continual dripping of liquid N_2 upon the cell. A polyethylene bag surrounding the apparatus was intended to prevent the formation of ice during the experiment. These measurements indicated that the phase III diffraction pattern was similar to that found in a low-temperature Cd analogue, and furthermore suggested that diffraction patterns of phases II and IV were identical.

Much later the first high-pressure low-temperature single-crystal X-ray crystal structures were determined for the low-temperature metallic conductors tetraselenotetracene chloride ($(TSeT)_2Cl$) (Le Pevelen, Gaultier, *et al.*, 1999) and tetramethyltetraselenafulvalene perchlorate $(TMTSF)_2ClO_4$ (Le Pevelen, Barrans, *et al.*, 1999, Le Pevelen *et al.*, 2001). For these experiments a modified Ahsbahs cell with beryllium gasket was operated in transverse mode, and mounted on a closed-cycle He refrigerator enclosed by a double-walled beryllium container to allow cooling under pressure (Guionneau *et al.*, 2004). A varied response to high-pressure low-temperature environments was demonstrated by these materials, as the $(TSeT)_2Cl$ structure underwent negligible changes compared to high-pressure ambient-temperatures, whilst $(TMTSF)_2ClO_4$ reverted back from its low-temperature phase to the structure exhibited under ambient conditions.

Another later single-crystal study using a He gas-driven DAC mounted on a He refrigerator was conducted on the magnetic material NaV_2O_5 (Ohwada *et al.*, 2001), in order to discern the nature of structural distortions responsible for stabilizing a quadrupled *c*-axis resulting from charge-ordering of $V^{4.5+}$ oxidation states at low-temperatures. More recent experiments on the lanthanide compounds $La_{2-x}Ba_xCuO_4$ (Zimmermann *et al.*, 2008) and RVO_3 (R = Tb or Y) (Bizen *et al.*, 2008) have also been reported, involving a clamp-cell comprised mostly of MP35N alloy mounted on a Displex and a He gas-driven DAC mounted on a He refrigerator respectively. The appearance of a low-temperature orthorhombic phase in $La_{2-x}Ba_xCuO_4$ under ambient-pressure was suppressed at 2.7 GPa, and the application of pressure at low-temperatures stabilized a particular orientation of d-orbitals in both $TbVO_3$ and YVO_3.

1.5 Synchrotron Radiation

Synchrotron radiation has provided many benefits to crystallographers investigating a wide variety of structures from small organic molecules to macromolecular structures. The focussed intense radiation from synchrotrons drastically increases the intensity of reflections collected on the diffractometer, allowing for the observation of ultra – weak reflections that may reveal the presence of a previously unknown weakly diffracting phase. Alternatively the high intensity of the beam can be used to shorten collection times and thus conduct many experiments over a short time period. Another useful property of synchrotron radiation is the ability to reach ultra-low wavelengths for higher resolution experiments. High pressure crystallographers are particularly interested in exploiting short wavelength X-rays as they help counteract the reduced completeness afforded by DAC’s through enlargement of the Ewald Sphere. Further advances in synchrotron technology offer the potential for many new avenues of investigation including time-resolved crystallography for the study of reaction mechanisms, high resolution studies locating ultra-fine features of the electron density, and high-throughput crystallography.

Diamond Light Source (Figure 1.8), a facility built in the United Kingdom in 2003, is typical of the latest and most advanced design of synchrotron facilities, offering X-ray beams 100 billion times more intense than a standard X-ray source in a laboratory. Production of synchrotron radiation begins in the electron gun where heating of a thermionic material such as $Ba(AlO_2)_2$ generates electrons approximately 90 keV in energy. The electrons are attracted electrostatically towards a positively charged copper screen with a frequency of 500 MHz, causing loose bunching of the electron beam. A doughnut shaped anode then guides the electrons into the buncher where the electrons are accelerated or decelerated by microwave radiation from a Klystron until they are in phase with each other and approaching 60 % of the speed of light. Further acceleration is provided by the linear accelerator, an extension of the buncher which further groups the electrons together and increases their velocity closer to the speed of light. Linear accelerators would need to be prohibitively long in order to achieve full acceleration towards the speed of light, so instead the electrons leave the linear accelerator and enter a booster synchrotron. A radiofrequency cavity increases the velocity of the electrons each time they complete a circuit of the booster synchrotron until they reach approximately 99.999994 % of the speed of light and energy of 1 – 3 GeV. Once this energy has been attained the electrons are injected into the storage ring which forms the main body of the synchrotron and consists of a series of straight and arced sections. Magnetic insertion devices called undulators and wigglers force deviations of the electron beam path in the straight sections, thereby creating focussed and intense monochromatic photon beams of tuneable wavelength and low divergence that are directed into beamlines where the experiments occur (Harding, 1995, Hendrickson, 2000, McClarence, 2008, Synchrotron light, 2011).

Figure 1.8: Schematic of Diamond Light Source (Diamond, 2011): 1 – Electron gun 2 – Booster synchrotron 3 – Storage ring 4/5 – Beamlines 6/7 – Experimental hutches 8 – Office

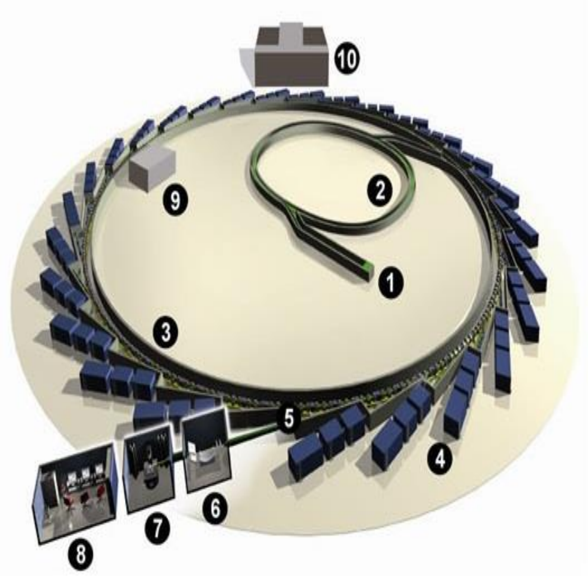

1.5 References

Adams, D. M., Appleby, R. & Sharma, S. K. (1976). *J. Phys. E* **9**, 1140-1144.

Allan, D. R., Clark, S. J., Brugmans, M. J. P., Ackland, G. J. & Vos, W. L. (1998). *Phys. Rev. B: Condens. Matter Mater. Phys.* **58**, R11809-R11812.

Allan, D. R., Clark, S. J., Dawson, A., McGregor, P. A. & Parsons, S. (2002). *Acta Crystallogr., Sect. B: Struct. Sci.* **B58**, 1018-1024.

Allan, D. R., Miletich, R. & Angel, R. J. (1996). *Rev. Sci. Instrum.* **67**, 840-842.

Allen, F. H. (2002). *Acta Crystallogr., Sect. B: Struct. Sci.* **B58**, 380-388.

Angel, R. J. (1993). *J. Phys.: Condens. Matter* **5**, L141-L144.

Angel, R. J., Allan, D. R., Miletich, R. & Finger, L. W. (1997). *J. Appl. Crystallogr.* **30**, 461-466.

Angel, R. J., Bujak, M., Zhao, J., Gatta, G. D. & Jacobsen, S. D. (2007). *J. Appl. Crystallogr.* **40**, 26-32.

Bennett, T. D., Tan, J.-C., Moggach, S. A., Galvelis, R., Mellot-Draznieks, C., Reisner, B. A., Thirumurugan, A., Allan, D. R. & Cheetham, A. K. (2010). *Chem. - Eur. J.* **16**, 10684-10690, S10684/10681-S10684/10610.

Birch, F. (1978). *JGR, J. Geophys. Res.* **83**, 1257-1268.

Bizen, D., Nakatsuka, K., Murata, T., Nakao, H., Murakami, Y., Miyasaka, S. & Tokura, Y. (2008). *Phys. Rev. B: Condens. Matter Mater. Phys.* **78**, 224104/224101-224104/224106.

Bleuzen, A., Cafun, J.-D., Bachschmidt, A., Verdaguer, M., Munsch, P., Baudelet, F. & Itie, J.-P. (2008). *J. Phys. Chem. C* **112**, 17709-17715.

Boldyreva, E. V. (2008). *Acta Crystallogr., Sect. A: Found. Crystallogr.* **64**, 218-231.

Boldyreva, E. V. (2014). *Z. Kristallogr. - Cryst. Mater.* **229**, 236-245.

Boldyreva, E. V., Drebushchak, T. N., Shakhtshneider, T. P., Sowa, H., Ahsbahs, H., Goryainov, S. V., Ivashevskaya, S. N., Kolesnik, E. N., Drebushchak, V. A. & Burgina, E. B. (2004). *Arkivoc*, 128-155.

Boldyreva, E. V., Ivashevskaya, S. N., Sowa, H., Ahsbahs, H. & Weber, H.-P. (2005). *Z. Kristallogr.* **220**, 50-57.

Brown, J. M. (1999). *J. Appl. Phys.* **86**, 5801-5808.

Burnett, J. H., Cheong, H. M. & Paul, W. (1990). *Rev. Sci. Instrum.* **61**, 3904-3905.

Chapman, K. W., Halder, G. J. & Chupas, P. J. (2008). *J. Am. Chem. Soc.* **130**, 10524-10526.

Colligan, M., Forster, P. M., Cheetham, A. K., Lee, Y., Vogt, T. & Hriljac, J. A. (2004). *J. Am. Chem. Soc.* **126**, 12015-12022.

Comes, R., Lambert, M., Launois, H. & Zeller, H. R. (1973). *Phys. Rev. B* **8**, 571-575.

Copley, R. C. B., Goeta, A. E., Lehmann, C. W., Cole, J. C., Yufit, D. S., Howard, J. A. K. & Archer, J. M. (1997). *J. Appl. Crystallogr.* **30**, 413-417.

Coppens, P. & Vos, A. (1971). *Acta Crystallogr., Sect. B* **27**, 146-158.

Cornia, A., Fabretti, A. C., Sessoli, R., Sorace, L., Gatteschi, D., Barra, A. L., Daiguebonne, C. & Roisnel, T. (2002). *Acta Crystallogr., Sect. C: Cryst. Struct. Commun.* **C58**, m371-m373.

Cosier, J. & Glazer, A. M. (1986). *J. Appl. Crystallogr.* **19**, 105-107.

Cynn, H. & Yoo, C.-S. (1999). *Phys. Rev. B: Condens. Matter Mater. Phys.* **59**, 8526-8529.

Dam, J., Harkema, S. & Feil, D. (1983). *Acta Crystallogr., Sect. B: Struct. Sci.* **B39**, 760-768.

Davidson, A. J., Oswald, I. D. H., Francis, D. J., Lennie, A. R., Marshall, W. G., Millar, D. I. A., Pulham, C. R., Warren, J. E. & Cumming, A. S. (2008). *CrystEngComm* **10**, 162-165.

Dawson, A., Allan, D. R., Belmonte, S. A., Clark, S. J., David, W. I. F., McGregor, P. A., Parsons, S., Pulham, C. R. & Sawyer, L. (2005). *Cryst. Growth Des.* **5**, 1415-1427.

Dawson, A., Allan, D. R., Parsons, S. & Ruf, M. (2004). *J. Appl. Crystallogr.* **37**, 410-416.

Diamond (2011). *Technology*.

Dunstan, D. J. & Spain, I. L. (1989). *J. Phys. E: Sci. Instrum.* **22**, 913-923.

Fabbiani, F. P. A., Allan, D. R., David, W. I. F., Davidson, A. J., Lennie, A. R., Parsons, S., Pulham, C. R. & Warren, J. E. (2007). *Cryst. Growth Des.* **7**, 1115-1124.

Fabbiani, F. P. A., Allan, D. R., David, W. I. F., Moggach, S. A., Parsons, S. & Pulham, C. R. (2004). *CrystEngComm* **6**, 504-511.

Fabbiani, F. P. A., Allan, D. R., Dawson, A., David, W. I. F., McGregor, P. A., Oswald, I. D. H., Parsons, S. & Pulham, C. R. (2003). *Chem. Commun. (Cambridge, U. K.)*, 3004-3005.

Fabbiani, F. P. A., Allan, D. R., Parsons, S. & Pulham, C. R. (2005). *CrystEngComm* **7**, 179-186.

Fabbiani, F. P. A. & Pulham, C. R. (2006). *Chem. Soc. Rev.* **35**, 932-942.

Farrell, A. R., Coome, J. A., Probert, M. R., Goeta, A. E., Howard, J. A. K., Lemee-Cailleau, M.-H., Parsons, S. & Murrie, M. (2013). *CrystEngComm* **15**, 3423-3429.

Feng, Y., Jaramillo, R., Wang, J., Ren, Y. & Rosenbaum, T. F. (2010). *Rev. Sci. Instrum.* **81**, 041301/041301-041301/041308.

Figgis, B. N., Khor, L., Kucharski, E. S. & Reynolds, P. A. (1992). *Acta Crystallogr., Sect. B: Struct. Sci.* **B48**, 144-151.

Gagnon, K. J., Beavers, C. M. & Clearfield, A. (2013). *J. Am. Chem. Soc.* **135**, 1252-1255.

Garman, E. F. & Nave, C. (2009). *J. Synchrotron Radiat.* **16**, 129-132.

Garman, E. F. & Weik, M. (2013). *J. Synchrotron Radiat.* **20**, 1-6.

Gatta, G. D. & Lee, Y. (2007). *Micropor. Mesopor. Mater.* **105**, 239-250.

Gerard, N. & Pernolet, R. (1973). *J. Phys. E* **6**, 512.

Giriat, G. (2011). PhD thesis, University of Edinburgh, Edinburgh.

Goeta, A. E. & Howard, J. A. K. (2004). *Chem. Soc. Rev.* **33**, 490-500.

Gonzalez, A. & Nave, C. (1994). *Acta Crystallogr., Sect. D: Biol. Crystallogr.* **D50**, 874-877.

Gonzalez, A., Thompson, A. W. & Nave, C. (1992). *Rev. Sci. Instrum.* **63**, 1177-1180.

Gould, J. A., Rosseinsky, M. J., Warren, J. E. & Moggach, S. (2014). *Z. Kristallogr. - Cryst. Mater.* **229**, 123-128.

Graham, A. J., Allan, D. R., Muszkiewicz, A., Morrison, C. A. & Moggach, S. A. (2011). *Angew. Chem., Int. Ed.* **50**, 11138-11141, S11138/11131-S11138/11137.

Graham, A. J., Tan, J.-C., Allan, D. R. & Moggach, S. A. (2012). *Chem. Commun. (Cambridge, U. K.)* **48**, 1535-1537.

Guionneau, P., Le Pevelen, D., Marchivie, M., Pechev, S., Gaultier, J., Barrans, Y. & Chasseau, D. (2004). *J. Phys.: Condens. Matter* **16**, S1151-S1159.

Gupta, Y. M. & Shen, X. A. (1991). *Appl. Phys. Lett.* **58**, 583-585.

Hanfland, M., Syassen, K. & Kohler, J. (2002). *J. Appl. Phys.* **91**, 4143-4148.

Hardie, M. J., Kirschbaum, K., Martin, A. & Pinkerton, A. A. (1998). *J. Appl. Crystallogr.* **31**, 815-817.

Harding, M. M. (1995). *Acta Crystallogr., Sect. B: Struct. Sci.* **B51**, 432-446.

Hazen, R. M. & Finger, L. W. (1981). *J. Appl. Crystallogr.* **14**, 234-236.

Heinz, D. L. & Jeanloz, R. (1984). *J. Appl. Phys.* **55**, 885-893.

Hemley, R. J. (2000). *Annu. Rev. Phys. Chem.* **51**, 763-800.

Hendrickson, W. A. (2000). *Trends Biochem. Sci.* **25**, 637-643.

Herbert, I. R. & Campbell, S. J. (1977). *J. Appl. Crystallogr.* **10, Pt. 1**, 18-20.

Hope, H. (1988). *Acta Crystallogr., Sect. B: Struct. Sci.* **B44**, 22-26.

Hudspeth, J. M., Goossens, D. J. & Welberry, T. R. (2014). *J. Appl. Crystallogr.* **47**, 544-551.

Jamieson, J. C. (1981). *Annu. Rev. Mater. Sci.* **11**, 233-243.

Jayaraman, A. (1983). *Rev. Mod. Phys.* **55**, 65-108.

Jayaraman, A. (1984). *Sci. Am.* **250**, 54-62, 154.

Jayaraman, A. (1986). *Rev. Sci. Instrum.* **57**, 1013-1031.

Johnstone, R. D. L., Lennie, A. R., Parker, S. F., Parsons, S., Pidcock, E., Richardson, P. R., Warren, J. E. & Wood, P. A. (2010). *CrystEngComm* **12**, 1065-1078.

Jones, R. E., Jr., Anderson, G. C. & Keeler, W. J. (1975). *Rev. Sci. Instrum.* **46**, 1025-1027.

Kamenev, K. V., Tancharakorn, S., Robertson, N. & Harrison, A. (2006). *Rev. Sci. Instrum.* **77**, 073905/073901-073905/073905.

Katrusiak, A. (2008). *Acta Crystallogr., Sect. A: Found. Crystallogr.* **64**, 135-148.

Klotz, S., Chervin, J. C., Munsch, P. & Le Marchand, G. (2009). *J. Phys. D: Appl. Phys.* **42**, 075413/075411-075413/075417.

Kmetko, J., Husseini, N. S., Naides, M., Kalinin, Y. & Thorne, R. E. (2006). *Acta Crystallogr., Sect. D: Biol. Crystallogr.* **D62**, 1030-1038.

Kottke, T. & Stalke, D. (1993). *J. Appl. Crystallogr.* **26**, 615-619.

Kuhs, W. F. (1988). *Aust. J. Phys.* **41**, 369-382.

Kurpiewska, K. & Lewinski, K. (2010). *Cent. Eur. J. Biol.* **5**, 531-542.

Larsen, F. K. (1995). *Acta Crystallogr., Sect. B: Struct. Sci.* **B51**, 468-482.

Le Pevelen, D., Barrans, Y., Gaultier, J. & Chasseau, D. (1999). *Synth. Met.* **102**, 1609-1610.

Le Pevelen, D., Gaultier, J., Barrans, Y. & Chasseau, D. (1999). *Synth. Met.* **103**, 2183-2184.

Le Pevelen, D., Gaultier, J., Barrans, Y., Chasseau, D., Castet, F. & Ducasse, L. (2001). *Eur. Phys. J. B* **19**, 363-373.

Lee, Y., Hriljac, J. A. & Vogt, T. (2010). *J. Phys. Chem. C* **114**, 6922-6927.

Lee, Y., Vogt, T., Hriljac, J. A., Parise, J. B. & Artioli, G. (2002). *J. Am. Chem. Soc.* **124**, 5466-5475.

Lucas, B. W. (1969). *Acta Crystallogr., Sect. A* **25**, 627-631.

Macchi, P. (2012). *Top. Curr. Chem.* **315**, 33-68.

Maloney, A. G. P., Wood, P. A. & Parsons, S. (2014). *CrystEngComm* **16**, 3867-3882.

Mao, H. K., Bell, P. M., Shaner, J. W. & Steinberg, D. J. (1978). *J. Appl. Phys.* **49**, 3276-3283.

Massa, W. (2004). *Crystal Structure Determination*, 2nd ed. Springer.

McClarence, E. (2008). Industrial Diamond Review.

McGregor, P. A., Allan, D. R., Parsons, S. & Pulham, C. R. (2005). *Acta Crystallogr., Sect. B: Struct. Sci.* **B61**, 449-454.

McMahon, M. I. (2012). *Top. Curr. Chem.* **315**, 69-110.

Meents, A., Gutmann, S., Wagner, A. & Schulze-Briese, C. (2009). *Proc. Natl. Acad. Sci. U. S. A., Early Ed.*, 1-6, 6 pp.

Merrill, L. & Bassett, W. A. (1974). *Rev. Sci. Instrum.* **45**, 290-294.

Miletich, R., Allan, D. R. & Kuhs, W. F. (2001). *Rev. Mineral. Geochem.* **41**, 445-519.

Millar, D. I. A., Marshall, W. G., Oswald, I. D. H. & Pulham, C. R. (2010). *Crystallogr. Rev.* **16**, 115-132.

Minkov, V. S., Tumanov, N. A., Cabrera, R. Q. & Boldyreva, E. V. (2010). *CrystEngComm* **12**, 2551-2560.

Mittal, R., Mishra, S. K., Chaplot, S. L., Ovsyannikov, S. V., Greenberg, E., Trots, D. M., Dubrovinsky, L., Su, Y., Brueckel, T., Matsuishi, S., Hosono, H. & Garbarino, G. (2011). *Phys. Rev. B: Condens. Matter Mater. Phys.* **83**, 054503/054501-054503/054511.

Moggach, S. A., Allan, D. R., Clark, S. J., Gutmann, M. J., Parsons, S., Pulham, C. R. & Sawyer, L. (2006). *Acta Crystallogr., Sect. B: Struct. Sci.* **B62**, 296-309.

Moggach, S. A., Allan, D. R., Lozano-Casal, P. & Parsons, S. (2005). *J. Synchrotron Radiat.* **12**, 590-597.

Moggach, S. A., Allan, D. R., Parsons, S. & Warren, J. E. (2008). *J. Appl. Crystallogr.* **41**, 249-251.

Moggach, S. A., Bennett, T. D. & Cheetham, A. K. (2009). *Angew. Chem., Int. Ed.* **48**, 7087-7089, S7087/7081-S7087/7085.

Moggach, S. A. & Parsons, S. (2009). *Spectrosc. Prop. Inorg. Organomet. Compd.* **40**, 324-354.

Moggach, S. A., Parsons, S. & Wood, P. A. (2008). *Crystallogr. Rev.* **14**, 143-184.

Money, V. A., Radosavljevic Evans, I., Halcrow, M. A., Goeta, A. E. & Howard, J. A. K. (2003). *Chem. Commun. (Cambridge, U. K.)*, 158-159.

Moritomo, Y., Hanawa, M., Ohishi, Y., Kato, K., Takata, M., Kuriki, A., Nishibori, E., Sakata, M., Ohkoshi, S., Tokoro, H. & Hashimoto, K. (2003). *Phys. Rev. B: Condens. Matter Mater. Phys.* **68**, 144106/144101-144106/144107.

Morosin, B. & Schirber, J. E. (1974). *J. Appl. Crystallogr.* **7**, 295-296.

Muller, D. A., Edwards, B., Kirkland, E. J. & Silcox, J. (2001). *Ultramicroscopy* **86**, 371-380.

Nave, C. (1995). *Radiat. Phys. Chem.* **45**, 483-490.

Ohwada, K., Fujii, Y., Takesue, N., Isobe, M., Ueda, Y., Nakao, H., Wakabayashi, Y., Murakami, Y., Ito, K., Amemiya, Y., Fujihisa, H., Aoki, K., Shobu, T., Noda, Y. & Ikeda, N. (2001). *Phys. Rev. Lett.* **87**, 086402/086401-086402/086404.

Oswald, I. D. H., Chataigner, I., Elphick, S., Fabbiani, F. P. A., Lennie, A. R., Maddaluno, J., Marshall, W. G., Prior, T. J., Pulham, C. R. & Smith, R. I. (2009). *CrystEngComm* **11**, 359-366.

Oswald, I. D. H., Lennie, A. R., Pulham, C. R. & Shankland, K. (2010). *CrystEngComm* **12**, 2533-2540.

Oswald, I. D. H. & Pulham, C. R. (2008). *CrystEngComm* **10**, 1114-1116.

Parois, P., Moggach, S. A., Sanchez-Benitez, J., Kamenev, K. V., Lennie, A. R., Warren, J. E., Brechin, E. K., Parsons, S. & Murrie, M. (2010). *Chem. Commun. (Cambridge, U. K.)* **46**, 1881-1883.

Paureau, J. (1977). *J. Phys. E* **10**, 1093-1103.

Petrova, A. E., Sidorov, V. A. & Stishov, S. M. (2005). *Physica B (Amsterdam, Neth.)* **359-361**, 1463-1465.

Piermarini, G. J. (2001). *J. Res. Natl. Inst. Stand. Technol.* **106**, 889-920.

Piermarini, G. J. & Block, S. (1975). *Rev. Sci. Instrum.* **46**, 973-979.

Piermarini, G. J., Block, S. & Barnett, J. D. (1973). *J. Appl. Phys.* **44**, 5377-5382.

Piermarini, G. J., Block, S., Barnett, J. D. & Forman, R. A. (1975). *J. Appl. Phys.* **46**, 2774-2780.

Prescimone, A., Milios, C. J., Moggach, S., Warren, J. E., Lennie, A. R., Sanchez-Benitez, J., Kamenev, K., Bircher, R., Murrie, M., Parsons, S. & Brechin, E. K. (2008). *Angew. Chem., Int. Ed.* **47**, 2828-2831.

Probert, M. R., Robertson, C. M., Coome, J. A., Howard, J. A. K., Michell, B. C. & Goeta, A. E. (2010). *J. Appl. Crystallogr.* **43**, 1415-1418.

Ragan, D. D., Gustavsen, R. & Schiferl, D. (1992). *J. Appl. Phys.* **72**, 5539-5544.

Readman, J. E., Lennie, A. & Hriljac, J. A. (2014). *Acta Crystallogr., Sect. B: Struct. Sci., Cryst. Eng. Mater.* **70**, 510-516.

Reilly, A. M., Morrison, C. A. & Rankin, D. W. H. (2011). *Acta Crystallogr., Sect. A: Found. Crystallogr.* **67**, 336-345.

Reilly, A. M., Morrison, C. A., Rankin, D. W. H. & McLean, K. R. (2011). *Acta Crystallogr., Sect. A: Found. Crystallogr.* **67**, 346-356.

Ribaud, L., Wu, G., Zhang, Y. & Coppens, P. (2001). *J. Appl. Crystallogr.* **34**, 76-79.

Ridley, C. J. & Kamenev, K. (2014). *Z. Kristallogr.* **229**, 171-199.

Ridout, J. & Probert, M. R. (2013). *Cryst. Growth Des.* **13**, 1943-1948.

Rondinone, A. J., Jones, C. Y., Marshall, S. L., Chakoumakos, B. C., Rawn, C. J. & Lara-Curzio, E. (2003). *Can. J. Phys.* **81**, 381-385.

Rowsell, J. L. C., Spencer, E. C., Eckert, J., Howard, J. A. K. & Yaghi, O. M. (2005). *Science (Washington, DC, U. S.)* **309**, 1350-1354.

Rutter, M. D., Uchida, T., Secco, R. A., Huang, Y. & Wang, Y. (2001). *J. Phys. Chem. Solids* **62**, 599-606.

Samson, S., Goldish, E. & Dick, C. J. (1980). *J. Appl. Crystallogr.* **13**, 425-432.

Schuele, P. J. & Schmidt, V. H. (1982). *Rev. Sci. Instrum.* **53**, 1724-1726.

Seiler, P. & Dunitz, J. D. (1985). *Aust. J. Phys.* **38**, 405-411.

Sessoli, R., Gatteschi, D., Caneschi, A. & Novak, M. A. (1993). *Nature (London)* **365**, 141-143.

Shimizu, K. (2007). *J. Phys.: Condens. Matter* **19**, 125207/125201-125207/125211.

Silvera, I. F. & Wijngaarden, R. J. (1985). *Rev. Sci. Instrum.* **56**, 121-124.

Simmons, C. J., Hitchman, M. A., Stratemeier, H. & Schultz, A. J. (1993). *J. Am. Chem. Soc.* **115**, 11304-11311.

Sinha, S. & Srinivasan, R. (1983). *Rev. Sci. Instrum.* **54**, 1492-1496.

Sleight, A. (2003). *Nature (London, U. K.)* **425**, 674-676.

Spain, I. L. & Dunstan, D. J. (1989). *J. Phys. E: Sci. Instrum.* **22**, 923-933.

Sterer, E., Pasternak, M. P. & Taylor, R. D. (1990). *Rev. Sci. Instrum.* **61**, 1117-1119.

Suzuki, E. & Endo, S. (2003). *Rev. Sci. Instrum.* **74**, 3726-3729.

Syassen, K. (2008). *High Pressure Res.* **28**, 75-126.

Synchrotron light (2011). Institute of Physics.

Takemura, K., Yamawaki, H., Fujihisa, H. & Kikegawa, T. (2002). *J. Phys.: Condens. Matter* **14**, 10563-10568.

Tang, J., Matsumoto, T. & Mori, N. (1998). *Rev. High Pressure Sci. Technol.* **7**, 1496-1498.

Tateiwa, N. & Haga, Y. (2010). *J. Phys.: Conf. Ser.* **215**, No pp. given.

Teng, T.-y. & Moffat, K. (2000). *J. Synchrotron Radiat.* **7**, 313-317.

Trokiner, A., Dahan, N., Theveneau, H. & Papon, P. (1984). *Rev. Sci. Instrum.* **55**, 1616-1619.

Walker, I. R. (2005). *Cryogenics* **45**, 87-108.

Yamaoka, H., Zekko, Y., Jarrige, I., Lin, J.-F., Hiraoka, N., Ishii, H., Tsuei, K.-D. & Mizuki, J.-i. (2012). *J. Appl. Phys. (Melville, NY, U. S.)* **112**, 124503/124501-124503/124505.

Zahner, J. C. & Drickamer, H. G. (1960). *J. Chem. Phys.* **33**, 1625-1628.

Zimmermann, M. v., Nowak, R., Gu, G. D., Mennerich, C., Klauss, H. H. & Hucker, M. (2008). *Rev. Sci. Instrum.* **79**, 033906/033901-033906/033906.

Chapter 2

A Pressure-Induced Displacive Phase Transition in Tris(ethylenediamine) Nickel(II) Nitrate*

*Cameron, C. A., Allan, D. R., Kamenev, K., Moggach, S. A., Murrie, M. & Parsons, S. (2014). *Z. Kristallogr.* **229**, 200-209.

2.1 Introduction

Ethylenediamine is one of the most common bidentate ligands used in coordination chemistry. When coordinated to a metal centre it forms a five-membered ring which offers increased stability over similar monodentate ligands, and analysis of this effect played an important role in the understanding of metal-ligand coordination.

The crystal structure for $[Ni(en)_3][NO_3]_2$ was first obtained by Swink and Atoji (Cambridge Database refcode = TEANIN) (Swink & Atoji, 1960). These studies determined that under ambient conditions the crystal structure consisted of two formula units in a hexagonal unit cell where $a = b = 8.87(1)$ Å and $c = 11.41(2)$ Å. The nickel cation has an approximately octahedral geometry but skewed due to non-90° N–Ni–N angles with the ligands adopting a *gauche* conformation. Extensive bifurcated hydrogen bonding networks were observed involving ethylenediamine hydrogen atoms and nitrate oxygen atoms, which helped stabilize the close proximity of the two staggered nitrate anions. The structure has been most recently determined by Macchi *et al.*, (Macchi *et al.*, 2011) who analysed the effect of microsource Mo X-ray radiation on crystal data quality.

Molecular materials are very susceptible to changes in temperature and pressure due to the relatively weak nature of observed intermolecular interactions (Boldyreva *et al.*, 2004). The accuracy and precision of data collections can also be significantly improved through the application of low temperature conditions (Goeta & Howard, 2004). Consequently there is increasing interest among researchers in utilizing temperature and pressure to analyse the solid state (Katrusiak, 2008). The earliest crystal structure determination of $[Ni(en)_3][NO_3]_2$ at low-temperatures was conducted by Farrugia *et al.*, (Farrugia *et al.*, 2003) with the goal of investigating the electron density distribution. In the process the researchers discovered a phase transition occurring at 109 K from the $P6_322$ ambient phase to a new $P6_522$ phase, where $a = b = 8.82020(10)$ Å, $c = 33.1447(4)$ Å, and $V = 2233.07(4)$ Å^3. The enlargement of the unit cell through tripling of the c axis was observed to coincide with an increase in Z from 2 to 6, caused by a displacement of the nickel cations towards a position of lower symmetry. This transition was discovered to be sharp and reversible, as well as easily observable in precession images, making the compound ideal as a low-temperature calibrant for cryostats.

Pressure is a highly efficient variable for probing the structure of materials: unlike temperature which can typically be varied by up to a few hundred Kelvin for molecular materials, modern apparatus is capable of generating many billions of Pascals, resulting in far greater changes in crystalline thermodynamics (Moggach, Parsons, *et al.*, 2008). Additionally the phase changes induced by pressure may be very different to those caused by temperature, generating interest into the reasons why these two variables induce different responses in the crystalline state (Boldyreva, 2008).

Metal-ligand bonds in transition metal complexes have been found to be more sensitive to pressure than covalent bonds in organic materials, (Moggach & Parsons, 2009) leading to changes in coordination number, (Allan *et al.*, 2006, Moggach, Galloway, *et al.*, 2009, Prescimone *et al.*, 2012) bond angles (Espallargas *et al.*, 2008), and conformation (Casati *et al.*, 2005). This makes high pressure a very valuable tool for exploring the relationship between structure and physical properties in coordination compounds including magnetism (Prescimone *et al.*, 2008, Parois *et al.*, 2010), colour (Galloway *et al.*, 2010, Byrne *et al.*, 2012), spin state (Granier *et al.*, 1993, Guetlich *et al.*, 2007), and absorption characteristics of metal-organic frameworks (Moggach, Bennett, *et al.*, 2009, Graham *et al.*, 2011, Graham *et al.*, 2012).

The pressure-sensitivity of intramolecular geometry in coordination complexes raises the question of how the compressibility of coordination bonds compares to that of intermolecular interactions such as hydrogen bonds. $[Ni(en)_3][NO_3]_2$ is an ideal candidate for this kind of study since it contains both kinds of interaction. No studies have been conducted on $[Ni(en)_3][NO_3]_2$ under high-pressure conditions. The aim of this work is therefore to determine the behaviour of $[Ni(en)_3][NO_3]_2$ under pressure with the aims of (i) comparing the effects of high pressure with those of low temperature and (ii) comparing the compressibility of metal-ligand coordination bonds with those of hydrogen bonds.

2.2 Experimental

2.2.1 Sample Preparation

$[Ni(en)_3][NO_3]_2$ was synthesized and crystallized following the literature method (Farrugia *et al.*, 2003). Different $[Ni(en)_3][NO_3]_2$ crystals were used for pressure experiments for data collections with synchrotron radiation at Diamond Light Source and with a conventional lab-source at the University of Edinburgh.

2.2.2 Apparatus

The high pressure studies utilized a Boehler-Almax Merrill-Bassett DAC (Merrill & Bassett, 1974) with an opening angle of 40°, 600 μm culet brilliant-cut diamonds, tungsten-carbide backing discs and tungsten gasket (Moggach, Allan, *et al.*, 2008). 4:1 methanol-ethanol was used as the hydrostatic medium. High-pressure single crystal X-ray diffraction measurements were carried-out on a three-circle Bruker APEX diffractometer with Mo-K_α radiation monochromated with a TRIUMPH curved-crystal monochromator and with synchrotron radiation at the Diamond Light Source on beamline I19-EH1 using radiation of wavelength 0.48590 Å and a four-circle Crystal Logic diffractometer equipped with a Rigaku Saturn CCD detector. The pressure was measured using the ruby fluorescence method (Piermarini *et al.*, 1975). Data collection strategies were as described by Dawson *et al*. (Dawson *et al.*, 2004).

In Section 3, below, structural analyses are based on the synchrotron data-sets; data collected using the conventional lab source were utilized for determination of lattice parameters and phase identification.

2.2.3 Data Processing

Cell indexing and integration were carried out using the Bruker APEX II(Bruker, 2001) software with dynamic masks generated by ECLIPSE (Dawson *et al.*, 2004). Absorption corrections were carried out using SADABS (Sheldrick, 2008). Structures were solved by charge-flipping (Oszlanyi & Süto, 2004) using SUPERFLIP (Palatinus & Chapuis, 2007). Distance and angle restraints were derived from the ambient-pressure structure determination and applied to the positions of non-metal atoms, but not to distances or angles involving the nickel atom. Merging and refinement of the data was performed using CRYSTALS (Betteridge *et al.*, 2003). All structures were refined against $|F|$ with reflections with $|F| < 4\sigma(|F|)$ omitted. Atomic scattering factors for the synchrotron data were calculated using FPRIME (Kissel & Pratt, 1990). Crystal and refinement of data are recorded in Table 2.1.

Table 2.1: Crystal data

Pressure (GPa)	0.13	0.87	1.93
λ (Å)	0.4859	0.4859	0.4859
Sinθ/λ (Å)	0.7	0.7	0.7
Crystal System	Hexagonal	Hexagonal	Hexagonal
Space Group	$P6_322$	$P6_122$	$P6_122$
a (Å)	8.8403(6)	8.7393(4)	8.6308(4)
c (Å)	11.2668(8)	32.9084(17)	32.2623(16)
V (Å^3)	762.54(9)	2176.66(18)	2081.27(17)
Z	2	6	6
D_{calc} (Mg m^{-3})	1.58	1.66	1.74
Reflections	6809	18938	18407
Unique Reflections	833	2174	2102
R_{int}	0.055	0.061	0.048
R	0.0243	0.0329	0.0250
R_w	0.0302	0.0438	0.0272
GooF	1.0050	1.1424	1.0162
Data:Parameters	702:34	1784:97	1734:97
Flack Parameter	-0.05(7)	-0.02(7)	-0.01(4)
No. Restraints	56	84	84
ρ_{max}/ρ_{min} (e.Å^{-3})	0.21/-0.13	0.39/-0.28	0.32/-0.25

2.2.4 Structural Analysis

Analysis of the bonding interactions was conducted using the program PLATON (Spek, 2003) while MERCURY (Macrae *et al.*, 2006) and DIAMOND (Brandenburg, 1999) were utilized for visualization. Calculation of interstitial voids was carried-out using the contact surface algorithm in MERCURY, a probe radius of

0.5 Å and a grid spacing of 0.1 Å. Searches of the Cambridge Structural Database v5.32 (Allen, 2002) employed the program CONQUEST v1.13. ISODISTORT v 5.4.5 (Campbell *et al.*, 2006) was used for symmetry-mode analysis; the animation of the distortion mode available in the ESI was produced with GIMP v 2.8.2 (Kimball & Mattis, 1995) using frames generated with ISODISTORT.

2.2.5 Differential Scanning Calorimetry

DSC data were collected at the Durham University Chemistry Department using a Perkin Elmer DSC 8500 instrument. The sample was contained in a sealed aluminium pan, with an empty pan as a reference. The scan rate was 10 °C min^{-1}.

2.3 Results

2.3.1 General Comments

The crystal structure of $[Ni(en)_3][NO_3]_2$ has been determined at ambient temperature up to a pressure of 1.93 GPa. Beyond 1.93 GPa data quality deteriorated with substantial broadening of diffraction peaks and loss of high-resolution data, possibly ascribable to the on-set of amorphization.

The crystal system remains hexagonal throughout the pressure range studied. The change in unit cell parameters in response to pressure is presented in Figure 2.1. In order to place the values for phase I and II on a comparable scale, the *c* axis length in Figure 2.1b and cell volume in Figure 2.1c have been divided by *Z* (2 for phase I and 6 for phase II). The data shown in the plot were collected using a lab source, and numerical values of the parameters plotted are available in the supplementary material. The *c*-axis and volume plots show small discontinuities between 0.82 and 1.02 GPa, indicative of the phase transition. Observation of phase II in the synchrotron study at 0.87 GPa enables us to bracket the transition pressure between 0.82 and 0.87 GPa.

The phase transition leads to a tripling of the unit cell *c*-axis and a change in symmetry from $P6_322$ (phase I) to $P6_122$ or $P6_522$ (phase II). The space group obtained for phase-II depends on whether the Ni complex in the starting phase (I) had Δ (giving $P6_522$) or Λ ($P6_122$) chirality (Farrugia *et al.*, 2003).

Figure 2.1: Trends in (*a*) *a* axis length, (*b*) *c* axis length and (*c*) molar volume with pressure.

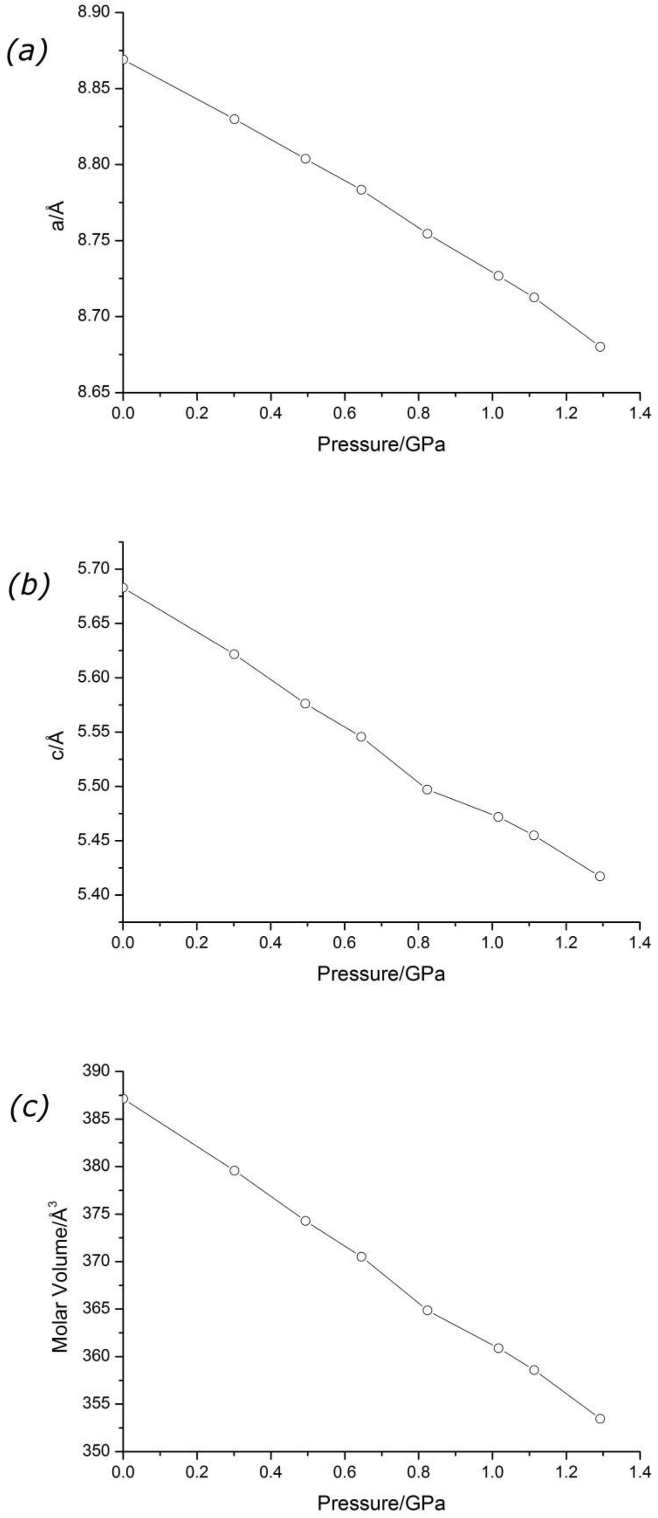

The same transition from phase I to II has been found to occur at ~109 K and ambient pressure by diffraction measurements. As part of this work a differential scanning calorimetry trace was measured, and this showed an endotherm centred at 108 K as temperature was scanned from 99 K to 150 K. The width of the transition is similar to that seen in Figure 2.3 in Farrugia *et al.*'s paper (Farrugia *et al.*, 2003). The enthalpy change for the transition is 142 J mol^{-1}, and the entropy change 1.32 J mol^{-1} K^{-1}. Though small, the non-zero values for these quantities show that the transition is first order. This is in agreement with the conclusion drawn by Farrugia *et al.* on the basis of the shapes of plots of cell dimensions and volume against temperature and the large displacements of molecular centres of gravity which occur at the transition.

2.3.2 Response of the Nickel Coordination Environment to Pressure

The nickel atom in $[Ni(en)_3][NO_3]_2$ is six coordinate with a distorted octahedral NiN_6 coordination environment (Figure 2.2). In phase I (Figure 2.2a) the metal atom occupies a site of 3.2 point symmetry which makes all six Ni-N bonds symmetry equivalent with a distance of 2.1309(17) Å observed at 0.13 GPa (Table 2.2). This compares to 2.1362(4) Å at 123 K (Farrugia *et al.*, 2003). The bond angles vary between 82.04(7)° and 93.41(7)°.

In phase II (Figure 2.2b) there are three unique Ni-N interactions. At 1.93 GPa the Ni-N bonds have a range of 2.1171(18) - 2.1297(15) Å; in phase II at 100 K the range is 2.1345(5)-2.1389(5) Å, indicating that pressure has a modest effect on metal-ligand distances. Though the C-C distances in the ethylenediamine ligands appear to increase in length in phase II (Table 2.2), this is likely a consequence of diminished thermal motion at elevated pressure (U_{eq}(C) = 0.054 Å^2 at 0.13 GPa and 0.036-0.041 Å^2 at 0.87 GPa).

The maximum change in N-Ni-N bond angle and NCCN torsion angle (Table 2.3) are 1.88(9)° (N1-Ni1-N3a) and 1.8(4)° (N2-C21-C31a-N3), respectively.

Figure 2.2: Structures of $[Ni(en)_3]^{2+}$ at (a) 0.13 GPa and (b) 0.87 GPa showing atom numbering. Thermal ellipsoids enclose 50% probability surfaces.

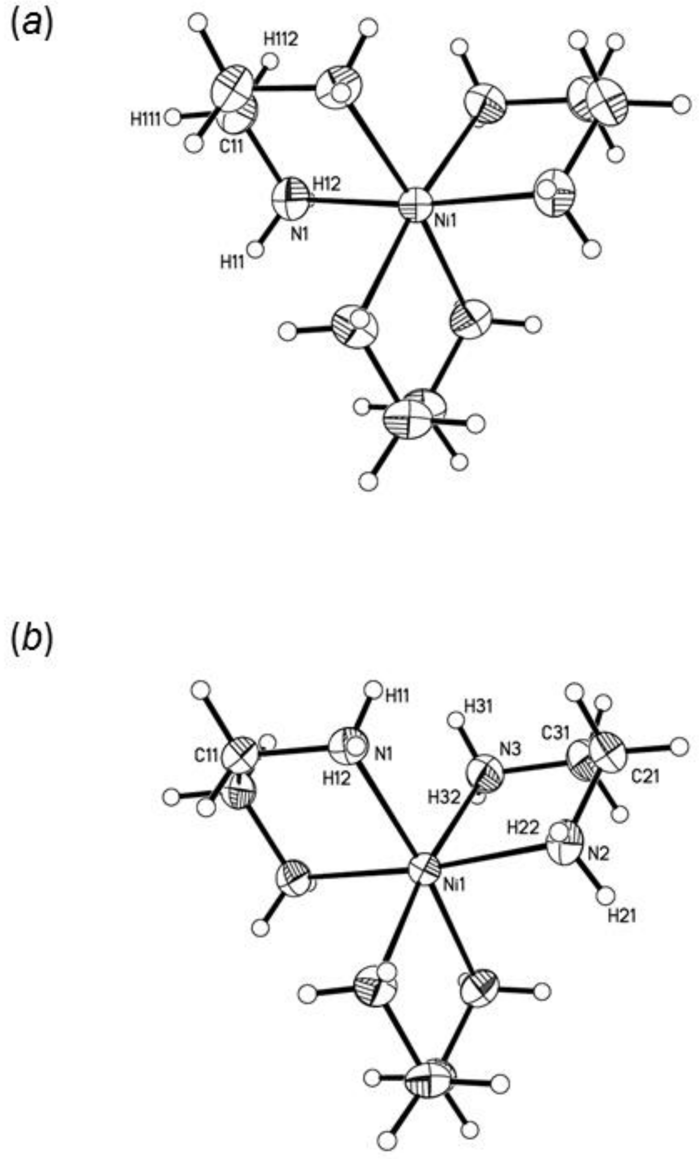

Table 2.2: Intramolecular bond lengths as a function of pressure

Pressure (GPa)	0.13	0.87	1.93
Ni1–N1 (Å)	2.1309(17)	2.129(2)	2.1231(15)
Ni1–N2 (Å)	2.1309(17)	2.127(3)	2.1171(18)
Ni1–N3 (Å)	2.1309(17)	2.134(2)	2.1297(15)
N1–C11 (Å)	1.477(2)	1.474(5)	1.474(3)
N2–C21 (Å)	1.477(2)	1.474(4)	1.481(3)
N3–C31 (Å)	1.477(2)	1.461(5)	1.472(3)
C11–C11a (Å)	1.487(3)	1.503(4)	1.510(2)
C21– C31 (Å)	1.487(3)	1.523(4)	1.514(2)

Table 2.3: Intramolecular bond angles and torsion angles as a function of pressure

Pressure (GPa)	0.13	0.87	1.93
<N1–Ni1–N2 (°)	93.41(7)	92.74(1)	92.54(6)
<N1–Ni1–N3 (°)	91.50(8)	90.50(9)	89.98(6)
<N1–Ni1–N1a (°)	82.04(7)	82.16(9)	81.98(6)
<N1–Ni1–N2a (°)	173.49(9)	174.00(11)	173.78(7)
<N1–Ni1–N3a (°)	93.41(7)	95.06(9)	95.29(6)
τN1–C11–C11a–N1a (°)	53.4(3)	54.8(3)	55.2(2)
τN2–C21–C31a–N3 (°)	53.4(3)	53.7(3)	55.5(2)

2.3.3 Response of Hydrogen Bonds to Pressure

In phase I at 0.13 GPa the Ni1 of the cations and N4 of the anions are distributed along the same three-fold axes running parallel to **c**. Pairs of anions are located above and below the upper and lower faces of the cation octahedra, interacting through bifurcated N1-H12···O41 H-bonds (Figure 2.3a). The bifurcation is unsymmetrical with H12···O41 distances of 2.22 and 2.57 Å (Table 2.4, NH distances normalised to 1.01 Å). These units are stacked along **c** with pairs of anions facing one another. When viewed along **c** these pairs of nitrates are staggered relative to each other, but with N···N distances of 3.130(3) Å (Figure 2.4a). This apparently unfavourable electrostatic interaction is stabilised by inter-stack N1-H11···O41 H-bonds formed in layers parallel to the *ab* face of the unit cell. These contacts are also bifurcated with H11···O41 distances measuring 2.30 and 2.68 Å. The 'diagonal' distance between

H11 and O41 in the nitrate anion directly below that forming the primary H-bonds to the cation is 3.20 Å.

Figure 2.3: (*a*) Phase I at 0.13 GPa and (*b*) phase II at 0.87 GPa viewed perpendicular to (110). Colour scheme: Ni green, O red, N blue, C black and H white. The scale of both figures is the same.

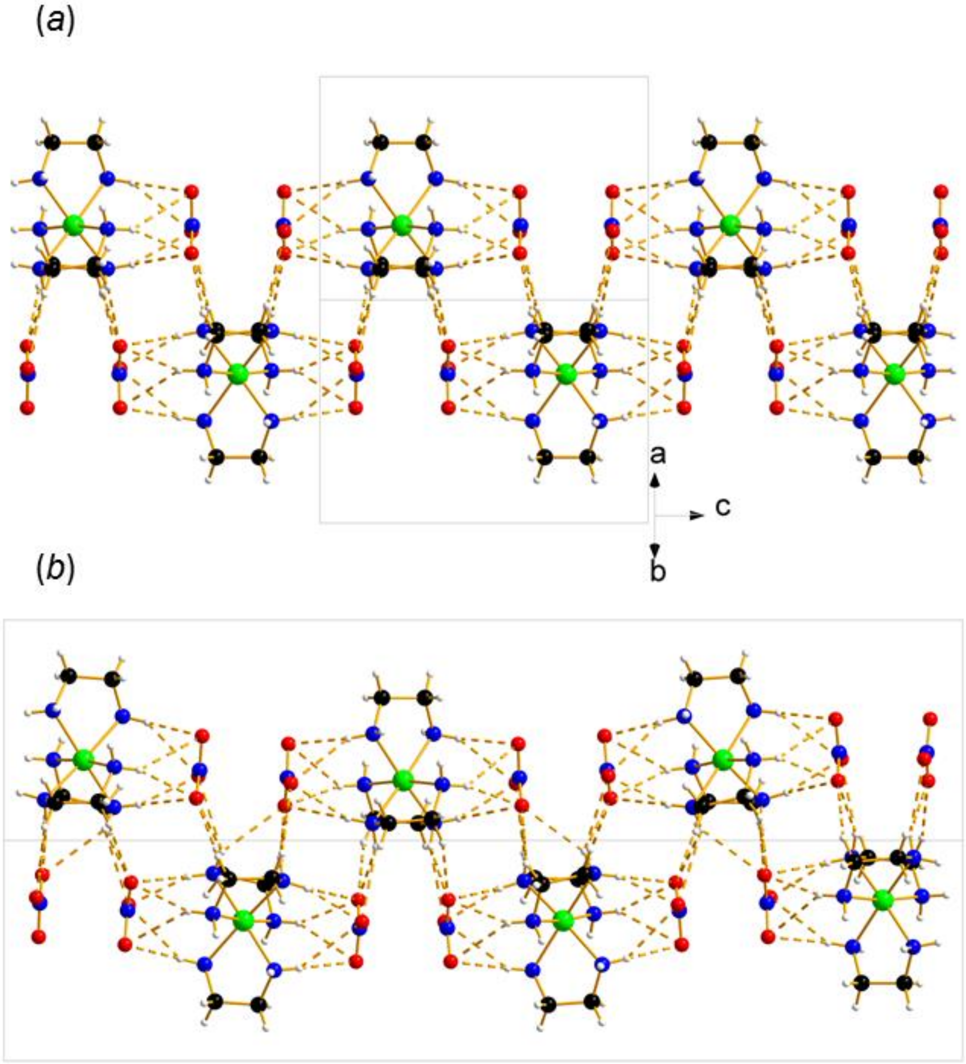

Figure 2.4: Hydrogen bonding network viewed along **c** in (a) phase I at 0.13 GPa and (b) phase II at 0.87 GPa. The colour scheme is the same as Figure 2.3.

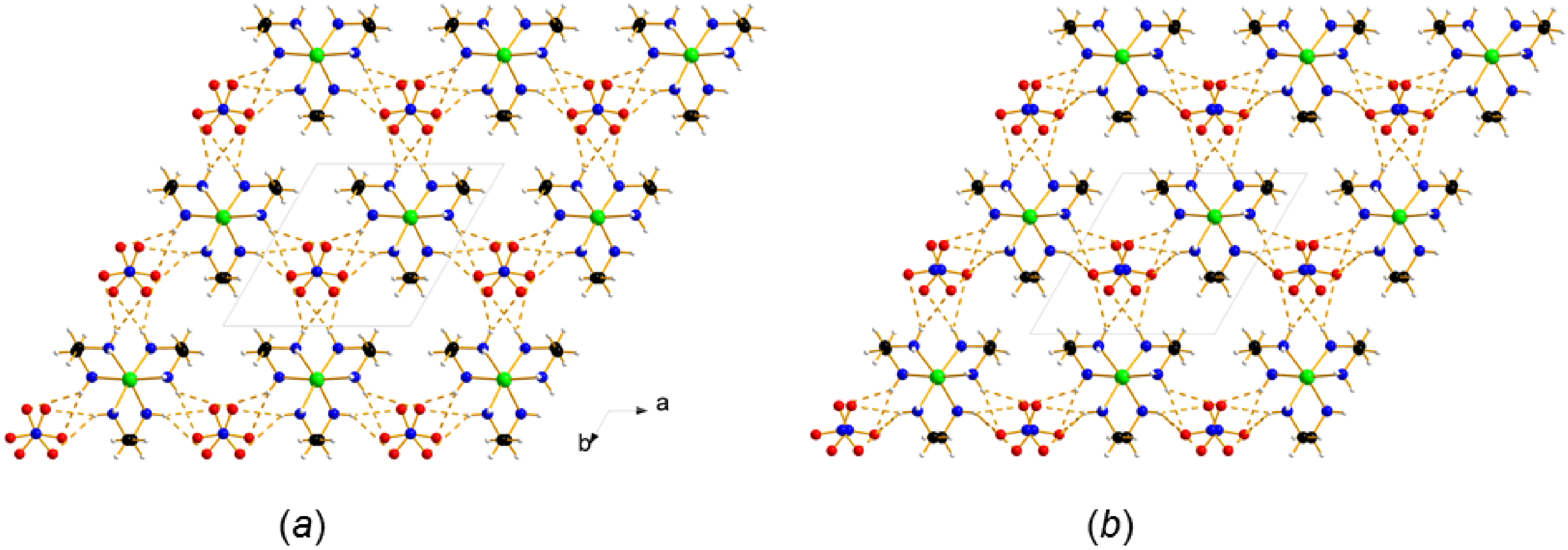

The transition from phase I to II modifies the orientations of the cations and anions. Over the course of the phase transition, the point symmetries of the cations and anions are reduced from 3.2 to ..2 and 3 to 1, respectively, breaking the three-fold degeneracy of the intra and inter-stack interactions. Phase II is thus a distorted version of phase I, consisting of the same intra- and inter-stack interactions described above for phase I, but with the set of four bifurcated NH···O independent interactions of phase I developing into twelve independent interactions in phase II (Figures 2.3b and 2.4b).

Related interactions in phases I and II are correlated in Table 2.4. The O···H distances forming the shorter components of the bifurcated intra-stack H-bonds change by up to 8.56%, whilst the longer interactions in the same stack change by up to 5.45% from 0.13 to 1.93 GPa, so that the bifurcation becomes more unsymmetrical. Similarly the shorter O···H interstack distances change by up to 8.26%, whilst the longer interactions change by up to 7.09% over the same pressure range. The greatest change in O···H distances occurs for the diagonal H11···O41 hydrogen bond, which contracts by 24.06% from 3.20 Å to 2.43 Å at 1.93 GPa. This substantial change is a consequence of the shift in the nitrate positions during the phase transition. This shift, which can be seen by comparing Figures 2.3 a and b, is clearest in an animation of the displacements during the transition which is available in the supplementary material.

The short N···N distance formed between nitrate anions is 3.130(3) Å at 0.13 GPa. After the transition to phase II this decreases to 3.026(3) Å at 0.87 GPa and 2.9704(18) Å at 1.9 GPa.

Table 2.4: Normalized hydrogen bond lengths/angles as a function of pressure. (d(D···A) < r(D) + r(A) + 0.50, d(H···A) < r(H) + r(A) – 0.12 Å, <D-H···A > 100°)

Phase I Pressure (GPa)	0.13^{a}	Phase II Pressure (GPa)	0.87^{b}	1.93	% change
Intrastack					
N1-H12···O41(Å)	3.170(2)^{i}	N1-H12···O43 (Å)	3.106(3)	3.0510(19)	3.74
H12···41 (Å)	2.22	H12···O43 (Å)	2.17	2.14	3.60
<N1-H12···O41 (°)	156	< N1-H12···O43 (°)	153	149	4.49
		N2-H22···O41 (Å)	3.157(3)	3.143(2)	0.83
		H22···O41 (Å)	2.21	2.18	1.80
		< N2-H22···O41 (°)	156	158	-1.28
		N3-H32···O42 (Å)	3.071(3)^{i}	3.0153(19)	4.87
		H32···O42 (Å)	2.10	2.03	8.56
		< N3-H32···O42 (°)	162	164	-5.13
N1-H12···O41 (Å)	3.431(2)^{ii}	N1-H12···O41 (Å)	3.358(3)	3.306(2)	3.64
H12···O41 (Å)	2.57	H12···O41 (Å)	2.47	2.43	5.45
<N1-H12···O41 (°)	143	<N1-H12···O41 (°)	146	148	-3.49
		N3-H32···O43 (Å)	3.341(3)*^{i}	3.305(2)	3.67
		H32···O43 (Å)	2.52	2.53	1.56
		<N3-H32···O43 (°)	137	133	7.00
		N2-H22···O42 (Å)	3.451(3)*	3.439(2)	-0.23
		H22···O42 (Å)	2.60	2.59	-0.78
		<N2-H22···O42 (°)	141	141	1.40

[a] Symmetry operations: (i) y, 1-x+y, -1/2+z; (ii) x-y, x, -1/2+z; (iii) x, x-y, 3/2-z; (iv) x, x-y, 3/2-z; (v) 1–x+y, y, 3/2-z; (vi) 1-x+y, 1-x, z. [b] Symmetry operations: (i) 1-y, 1-x, 5/6-z; (ii) 1+x-y, 2-y, -1-z; (iii) y, 1-x+y, -1/6+z; (iv) 1+x-y, 1-y, 1-z

Table 2.4 continued: Normalized hydrogen bond lengths/angles as a function of pressure. (d(D···A) < r(D) + r(A) + 0.50, d(H···A) < r(H) + r(A) – 0.12 Å, <D-H···A > 100°)

Phase I Pressure (GPa)	0.13[a]	Phase II Pressure (GPa)	0.87[b]	1.93	% change
Interstack					
N1-H11···O41 (Å)	3.229(3)[iii]	N1-H11···O41 (Å)	3.198(4)[ii]	3.171(2)	1.80
H11···O41 (Å)	2.30	H11···O41 (Å)	2.40	2.36	-2.61
<N1-H11···O41 (°)	152	< N1-H11···O41 (°)	135	136	10.53
		N3-H31···O42 (Å)	3.149(4)[iii]	3.098(3)	4.01
		H31···O42 (Å)	2.16	2.11	8.26
		< N3-H31···O42 (°)	165	167	-9.87
		N2-H21···O43 (Å)	3.197(4)[iv]	3.162(2)	2.08
		H21···O43 (Å)	2.27	2.22	3.48
		< N2-H21···O43 (°)	153	156	-2.63
N1-H11···O41 (Å)	3.455(3)[v]	N1-H11···O43	3.397(3)[ii]	3.335(2)	3.47
H11···O41 (Å)	2.68	H11···O43	2.70	2.61	2.61
<N1-H11···O41	137	<N1-H11···O43	126	129	5.84
		N3-H31···O41 (Å)	3.367(4)*[iii]	3.298(3)	4.55
		H31···O41 (Å)	2.55*	2.49	7.09
		< N3-H31···O41 (°)	137*	136	0.73
		N2-H21···O42	3.411(5)[iv]	3.364(3)	2.63
		H21···O42	2.61	2.53	5.60
		<N2-H21···O42	136	139	-1.46
Diagonal					
N1-H11···O41	3.830(3)[vi]	N1-H11···O42 (Å)	3.382(3)*[iii]	3.181(2)	16.96
H11···O41 (Å)	3.20	H11···O42 (Å)	2.59*	2.43	24.06
<N1-H11···O41 (°)	128	< N1-H11···O42 (°)	135*	131	-2.34

[a] Symmetry operations: (i) y, 1-x+y, -1/2+z; (ii) x-y, x, -1/2+z; (iii) x, x-y, 3/2-z; (iv) x, x-y, 3/2-z; (v) 1–x+y, y, 3/2-z; (vi) 1-x+y, 1-x, z. [b] Symmetry operations: (i) 1-y, 1-x, 5/6-z; (ii) 1+x-y, 2-y, -1-z; (iii) y, 1-x+y, -1/6+z; (iv) 1+x-y, 1-y, 1-z

Interstitial voids in the crystal structure are displayed in Figure 2.5. The interstitial void volume per formula unit is 60.56 Å^3 at 0.13 GPa, 40.00 Å^3 at 0.87 GPa, and 26.37 Å^3 at 1.93 GPa, representing 15.9 %, 11.0 %, and 7.6 % of the total unit cell volume respectively. The largest and most persistent of the interstitial voids in phase I have an approximately oblate shape with the long principal axes in the *ab* plane, and the short axis parallel to *c*.

Figure 2.5: Interstitial voids (yellow) at 0.13 (phase I), 0.87 (phase II), and 1.93 GPa (phase II) viewed along **a**.

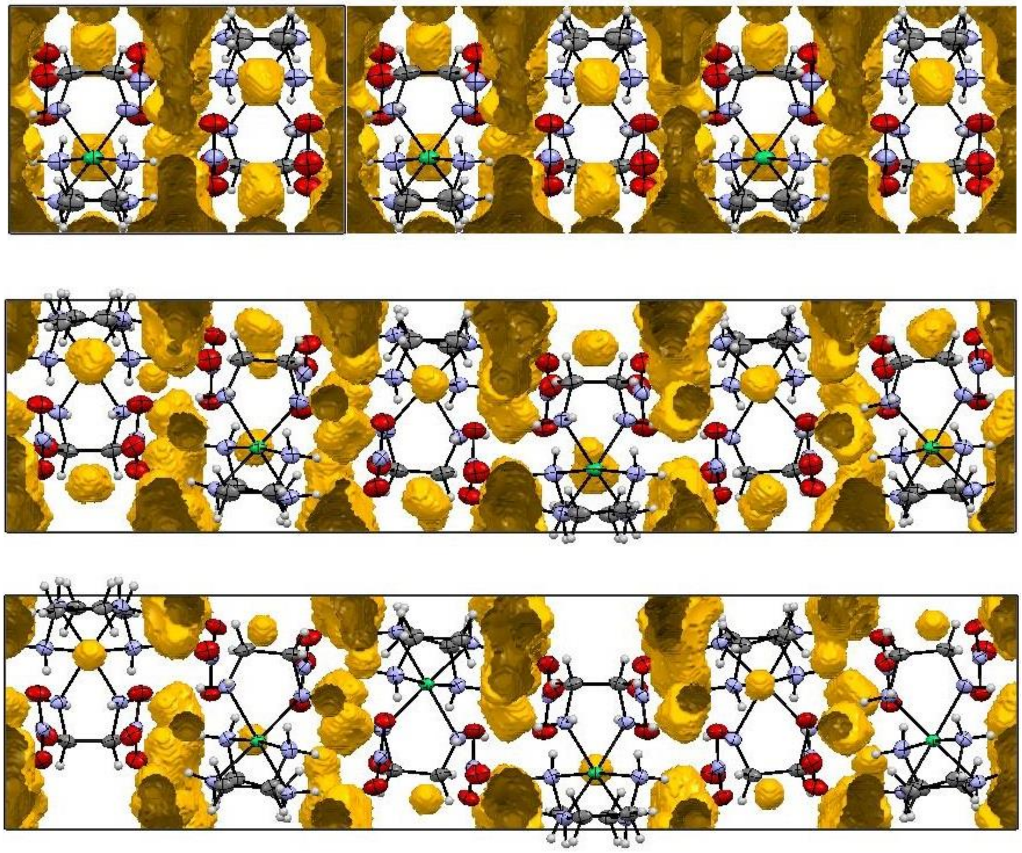

2.4 Discussion

2.4.1 Distortion analysis

The phase transition from phase I to phase II between 0.82 GPa and 0.87 GPa is similar to that observed by Farrugia *et al.* (Farrugia *et al.*, 2003) at 109 K. The discontinuities present in Figures 2.1b and c it seems reasonable to infer that the transition at high pressure is also first order.

Symmetry mode analysis based on the Ni, N and O positions of phase I at ambient pressure and phase II and 0.87 GPa (ISODISTORT) shows that the structure evolves via a displacive mechanism in which two modes (corresponding to irreducible representations Γ_1 and Δ_6) are active. The first of these represents the contraction of the structure with pressure; the second corresponds to rotations of the cations and anions in which the magnitudes of the rotations vary in a wave-like fashion along the *c*-direction of the unit cell. This mode is illustrated in an animation available in the supplementary material.

The displacements revealed by symmetry mode analysis can be interpreted in the context of the distribution of interstitial voids. The largest voids in phase I at ambient pressure are distributed between the layers illustrated in Figure 2.5 at the points where ethylenediamine ligands in neighbouring layers meet. The reduction in symmetry enables the cations and anions to reorient and access these voids. The reorientation of the anions, which sit directly above one another in phase 1, also leads to a small displacement of like-charged atoms away from one another, reducing electrostatic repulsion.

The distribution of voids is also consistent with the anisotropy of the contraction of the unit cell parameters. The greatest contraction occurs for the *c* axis at 7.41 % over the pressure series; the *c* axis also undergoes the largest reduction as a result of the phase transition at 2.71 %, corresponding to flattening of the large oblate voids described above (Figure 2.5). Movement of the structure along the *a* = *b* axes is hindered by the lack of void space between the stacks.

2.4.2 Effect of Pressure on H-bonding

One of the aims of this work was to compare the compressibility of Ni-N and NH···O H-bonds, which are both present in the structure of $[Ni(en)_3][NO_3]_2$. The maximum compression seen for the Ni-N bond distance was 0.014(2) Å, but 0.19 Å for the O···H distances. The compression in the H-bond distances is thus an order of magnitude greater. This effect is unlikely to be a simple effect of bond strength. The Cu-N bond energies in copper(II) ammine complexes have been estimated to be between 90 and 180 kJ mol^{-1}, (Nimmermark *et al.*, 2013) and the values for Ni-N bonds are likely to be similar; the intermolecular interactions mediated by charge-assisted H-bonds in $[Ni(en)_3][NO_3]_2$ likely have similar energies (*cf* similar charge-assisted interactions in amino acids have energies of up to 150 kJ mol^{-1}) (Funnell *et al.*, 2010).

The geometry of the H-bonds in $[Ni(en)_3][NO_3]_2$ can be compared to those found in similar structures. The frequency distribution for the N···O distance in metal-bound NH···nitrate H-bonds in the CSD is shown in Figure 2.6a and has a maximum frequency where the H···O distance is 2.08 Å. The hydrogen bond lengths calculated for phase-I at 0.13 GPa correspond to those structures that reside in the 2.20-2.30 Å region of the histogram, demonstrating a potential for compression. Compression of the hydrogen bonding network can be compared to pressure trends observed in the amino acids. D–A distances in L-cysteine (Moggach *et al.*, 2006) undergo a reduction in length by up to 5.4% from ambient pressure to 1.8 GPa. In L-alanine (Funnell *et al.*, 2010) for example, some of the N–H···O interactions decrease in length by up to 4.3% from ambient pressure to 2.30 GPa while other hydrogen bonds demonstrate very little change over the same pressure range. When the pressure is increased to 13.60 GPa the same interactions undergo a compression of up to 9.74%. In $[Ni(en)_3][NO_3]_2$ the majority of hydrogen bond therefore undergo compression similar to that observed in the amino acids.

A characteristic of the H-bond distributions described above, and exemplified by that in Figure 2.6a, is that they are very broad compared to a histogram on Ni-N distances in octahedral nickel complexes (Figure 2.6b). This points to a much flatter potential energy versus distance surface for H-bonds than for Ni-N bonds, and this explains why H-bonds are the more sensitive to pressure. Coordination bonds with flatter potentials, such as elongated Cu-N or O bonds in Jahn-Teller distorted Cu(II) complexes, show much greater sensitivity to pressure (Prescimone *et al.*, 2008, Galloway *et al.*, 2010, Parois *et al.*, 2010, Prescimone *et al.*, 2012). The response of structures under pressure is also to minimise free energy by packing molecules more efficiently, and reducing interstitial voids. This naturally also affects intermolecular interactions to a greater extent than intramolecular bonds.

Figure 2.6: Histograms of (a) normalised NH···O H-bond distances involving metal-bound amino and nitrate moieties and (b) Ni-N distances in six coordinate nickel complexes. CSD search criteria were: R factor ≤ 5%, 3D coordinates determined, no errors, no disorder. Both plots have the same horizontal scale.

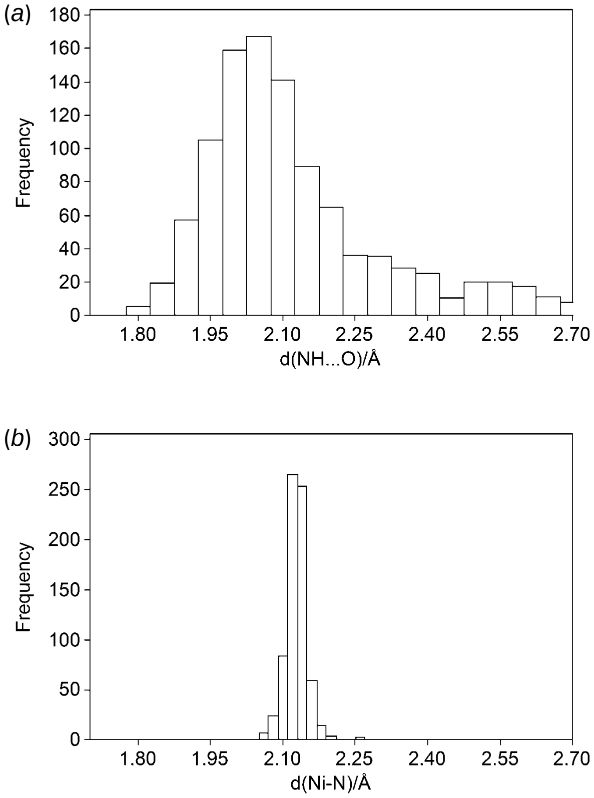

2.5 Conclusion

We have shown that [Ni(en)$_3$][NO$_3$]$_2$ undergoes a phase transition between 0.82 and 0.87 GPa in which the structure undergoes a distortion involving rotations of the cations and anions leading to a tripling of the unit cell volume. The structure remains in this phase up to 1.93 GPa. Previous work had shown that the same transition occurs on cooling the crystal at ambient pressure below 109 K. While most intermolecular H-bonding interactions shorten by around 5% between ambient pressure and 1.93 GPa, the reorientations of the cations and anions during the phase transition shorten one such interaction by almost 0.8 Å, or 24%. The compression in

Ni-N distances is an order of magnitude less than that seen for the H-bonds. CSD searches indicate that this reflects the shape of the H-bonding and Ni-N bonding interatomic potentials.

2.6. Acknowledgements

We thank Diamond Light Source and EPSRC for studentship funding to CAC, and the former also for provision of synchrotron beamtime. We also thank Mr Douglas Carswell of the Durham University Chemistry Department for collection of DSC data.

2.7 References

Allan, D. R., Blake, A. J., Huang, D., Prior, T. J. & Schroeder, M. (2006). *Chem. Commun. (Cambridge, U. K.)*, 4081-4083.

Allen, F. H. (2002). *Acta Crystallogr., Sect. B: Struct. Sci.* **B58**, 380-388.

Betteridge, P. W., Carruthers, J. R., Cooper, R. I., Prout, K. & Watkin, D. J. (2003). *J. Appl. Crystallogr.* **36**, 1487.

Boldyreva, E. V. (2008). *Acta Crystallogr., Sect. A: Found. Crystallogr.* **64**, 218-231.

Boldyreva, E. V., Drebushchak, T. N., Shakhtshneider, T. P., Sowa, H., Ahsbahs, H., Goryainov, S. V., Ivashevskaya, S. N., Kolesnik, E. N., Drebushchak, V. A. & Burgina, E. B. (2004). *Arkivoc*, 128-155.

Brandenburg, K. (1999). *DIAMOND.*

Bruker (2001). *Bruker AXS Inc., Madison, Wisconsin, USA.*

Byrne, P. J., Richardson, P. J., Chang, J., Kusmartseva, A. F., Allan, D. R., Jones, A. C., Kamenev, K. V., Tasker, P. A. & Parsons, S. (2012). *Chem. - Eur. J.* **18**, 7738-7748, S7738/7731.

Campbell, B. J., Stokes, H. T., Tanner, D. E. & Hatch, D. M. (2006). *J. Appl. Crystallogr.* **39**, 607-614.

Casati, N., Macchi, P. & Sironi, A. (2005). *Angew. Chem., Int. Ed.* **44**, 7736-7739.

Dawson, A., Allan, D. R., Parsons, S. & Ruf, M. (2004). *J. Appl. Crystallogr.* **37**, 410-416.

Espallargas, G. M., Brammer, L., Allan, D. R., Pulham, C. R., Robertson, N. & Warren, J. E. (2008). *J. Am. Chem. Soc.* **130**, 9058-9071.

Farrugia, L. J., Macchi, P. & Sironi, A. (2003). *J. Appl. Crystallogr.* **36**, 141-145.

Funnell, N. P., Dawson, A., Francis, D., Lennie, A. R., Marshall, W. G., Moggach, S. A., Warren, J. E. & Parsons, S. (2010). *CrystEngComm* **12**, 2573-2583.

Galloway, K. W., Moggach, S. A., Parois, P., Lennie, A. R., Warren, J. E., Brechin, E. K., Peacock, R. D., Valiente, R., Gonzalez, J., Rodriguez, F., Parsons, S. & Murrie, M. (2010). *CrystEngComm* **12**, 2516-2519.

Goeta, A. E. & Howard, J. A. K. (2004). *Chem. Soc. Rev.* **33**, 490-500.

Graham, A. J., Allan, D. R., Muszkiewicz, A., Morrison, C. A. & Moggach, S. A. (2011). *Angew. Chem., Int. Ed.* **50**, 11138-11141, S11138/11131-S11138/11137.

Graham, A. J., Tan, J.-C., Allan, D. R. & Moggach, S. A. (2012). *Chem. Commun. (Cambridge, U. K.)* **48**, 1535-1537.

Granier, T., Gallois, B., Gaultier, J., Real, J. A. & Zarembowitch, J. (1993). *Inorg. Chem.* **32**, 5305-5312.

Guetlich, P., Gaspar, A. B., Garcia, Y. & Ksenofontov, V. (2007). *C. R. Chim.* **10**, 21-36.

Katrusiak, A. (2008). *Acta Crystallogr., Sect. A: Found. Crystallogr.* **64**, 135-148.

Kimball, S. & Mattis, P. (1995). *GIMP.* Version 2.8.2.

Kissel, L. & Pratt, R. H. (1990). *Acta Crystallogr., Sect. A: Found. Crystallogr.* **A46**, 170-175.

Macchi, P., Bürgi, H. B., Chimpri, A. S., Hauser, J. & Gal, Z. (2011). *J. Appl. Crystallogr.* **44**, 763-771.

Macrae, C. F., Edgington, P. R., McCabe, P., Pidcock, E., Shields, G. P., Taylor, R., Towler, M. & van, d. S. J. (2006). *J. Appl. Crystallogr.* **39**, 453-457.

Merrill, L. & Bassett, W. A. (1974). *Rev. Sci. Instrum.* **45**, 290-294.

Moggach, S. A., Allan, D. R., Clark, S. J., Gutmann, M. J., Parsons, S., Pulham, C. R. & Sawyer, L. (2006). *Acta Crystallogr., Sect. B: Struct. Sci.* **B62**, 296-309.

Moggach, S. A., Allan, D. R., Parsons, S. & Warren, J. E. (2008). *J. Appl. Crystallogr.* **41**, 249-251.

Moggach, S. A., Bennett, T. D. & Cheetham, A. K. (2009). *Angew. Chem., Int. Ed.* **48**, 7087-7089, S7087/7081-S7087/7085.

Moggach, S. A., Galloway, K. W., Lennie, A. R., Parois, P., Rowantree, N., Brechin, E. K., Warren, J. E., Murrie, M. & Parsons, S. (2009). *CrystEngComm* **11**, 2601-2604.

Moggach, S. A. & Parsons, S. (2009). *Spectrosc. Prop. Inorg. Organomet. Compd.* **40**, 324-354.

Moggach, S. A., Parsons, S. & Wood, P. A. (2008). *Crystallogr. Rev.* **14**, 143-184.

Nimmermark, A., Öhrström, L. & Reedijk, J. (2013). *Z. Kristallogr. - Cryst. Mater.* **228**, 311-317.

Oszlanyi, G. & Süto, A. (2004). *Acta Crystallogr., Sect. A: Found. Crystallogr.* **A60**, 134-141.

Palatinus, L. & Chapuis, G. (2007). *J. Appl. Crystallogr.* **40**, 786-790.

Parois, P., Moggach, S. A., Sanchez-Benitez, J., Kamenev, K. V., Lennie, A. R., Warren, J. E., Brechin, E. K., Parsons, S. & Murrie, M. (2010). *Chem. Commun. (Cambridge, U. K.)* **46**, 1881-1883.

Piermarini, G. J., Block, S., Barnett, J. D. & Forman, R. A. (1975). *J. Appl. Phys.* **46**, 2774-2780.

Prescimone, A., Milios, C. J., Moggach, S., Warren, J. E., Lennie, A. R., Sanchez-Benitez, J., Kamenev, K., Bircher, R., Murrie, M., Parsons, S. & Brechin, E. K. (2008). *Angew. Chem., Int. Ed.* **47**, 2828-2831.

Prescimone, A., Morien, C., Allan, D., Schlueter, J. A., Tozer, S. W., Manson, J. L., Parsons, S., Brechin, E. K. & Hill, S. (2012). *Angew. Chem., Int. Ed.* **51**, 7490-7494, S7490/7491-S7490/7498.

Sheldrick, G. M. (2008). *SADABS.* Version 2008-1.

Spek, A. L. (2003). *J. Appl. Crystallogr.* **36**, 7-13.

Swink, L. N. & Atoji, M. (1960). *Acta Crystallographica* **13**, 639-643.

Chapter 3

Low-Temperature Calibration of a Novel Diamond Anvil Cell

3.1 Introduction

Solid-state researchers are interested in understanding the relationship between structure and physicochemical properties (Moggach *et al.*, 2008). Molecular systems are very susceptible to changes in pressure and temperature due to the relatively weak nature of intermolecular interactions and coordination bonds (Boldyreva *et al.*, 2004). Consequently there has been increasing interest in the application of pressure and temperature for probing the structure-property relationships of crystalline materials (Katrusiak, 2008). The application of low-temperature conditions during X-ray experiments has become routine, as the benefits of these environments for improving data accuracy and precision and inducing the crystallization of liquids have become increasingly recognized (Larsen, 1995, Goeta & Howard, 2004). Conversely the utilization of pressure during X-ray experiments has historically been less common (Boldyreva, 2008), although interest in high-pressure crystallography has been greatly facilitated by the invention and refinement of the Diamond Anvil Cell (DAC) (Piermarini, 2001). Furthermore advances in technology and methodology for these devices has made access to high-pressure conditions much less technically challenging and therefore more widespread, as well as allowing for greater changes in crystalline thermodynamics compared to temperature (Moggach *et al.***,** 2008).

Many systems such as single-molecule magnets (Gatteschi *et al.*, 2008), spin-crossover compounds (Guetlich *et al.*, 2007), and electrical conductors (Kobayashi *et al.*, 1980) exhibit interesting properties under low-temperature regimes which can be altered with pressure. However standard high-pressure single-crystal X-ray methodologies are unsuitable for low-temperature experiments, as the typical DAC composition and size causes uneven cooling and prolonged equilibration times. Consequently researchers often have to correlate high-pressure low-temperature property measurements with high-pressure ambient-temperature structural data (Sieber *et al.*, 2005, Prescimone *et al.*, 2008, Parois *et al.*, 2010). This situation is undesirable as the reduction in temperature may result in significant changes in crystal structure, rendering the comparisons between experimental data less meaningful. Additionally the application of low-temperature regimes would also help mitigate the reduced quality of high-pressure data (ref. KCP chapter: 1.8 GPa Pt1

U_{iso} = 0.0188 Å^2 and 0.0164 Å^2 at 300 K and 4 K respectively) and therefore improve our understanding of the structure-property relationships in these systems.

Previous work by Gaetan Giriat (Giriat *et al.*, in preparation) at the University of Edinburgh has led to design of a novel DAC optimized for high-pressure low-temperature single-crystal X-ray studies (Figure 3.1). This cell has been constructed from a beryllium-copper alloy (BERYLCO25) with dimensions of 8 mm x 8 mm x 6 mm, allowing the cell to cool more rapidly than a normal DAC and remain within the laminar flow of an open-flow cryostat during goniometer movement. The application of pressure in the cell is based on the turnbuckle mechanism (Giriat *et al.*, 2010, Graf *et al.*, 2011); by fixing the end screws in a metal clamp and rotating the cell body the internal pressure is altered, with the direction of rotation defining whether the pressure increases or decreases (Figure 3.2). A specially designed stalk constructed of thermally insulating polyether ether ketone can be inserted into one side of the cell allowing it to be mounted on any typical goniometer head. On the three remaining sides of the cell small holes allow the insertion of a thermocouple device for *in-situ* temperature measurement.

Figure 3.1: Schematic of the turnbuckle cell (Giriat *et al.*, in preparation)

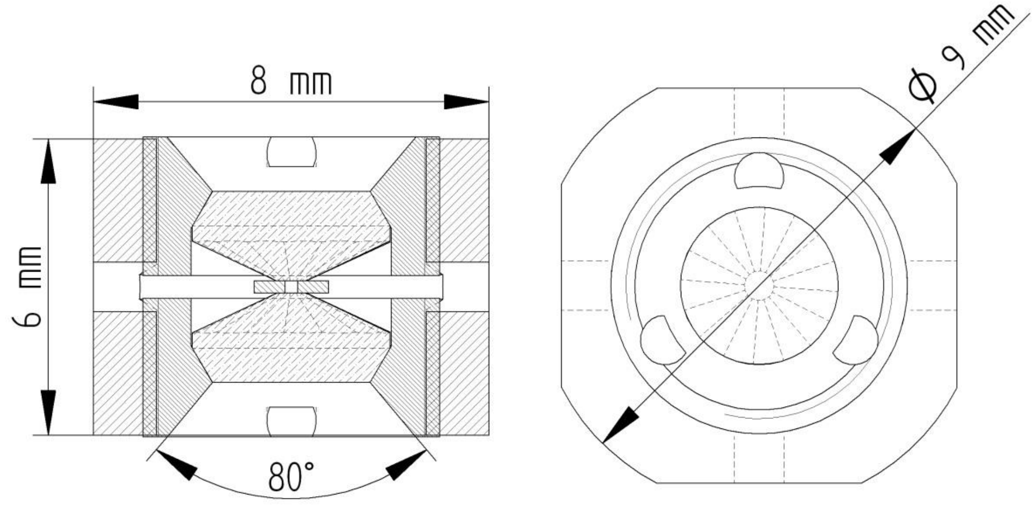

Figure 3.2: Clamps used for applying pressure in the turnbuckle cell

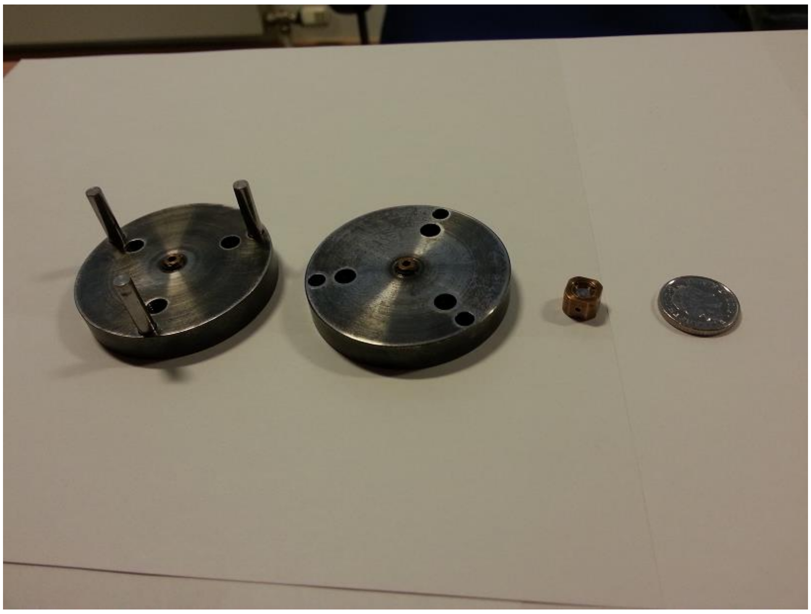

No crystallographic experiments have yet been conducted on the turnbuckle cell to measure its high-pressure low-temperature properties on an open-flow cryostat. A thermal differential between the cryostat and the sample is expected due to the closer proximity of the cell to the ambient-temperature laboratory compared with a crystal on a fibre. The aim of the work described in this chapter is to characterize the magnitude of this thermal differential and to explore how it varies with temperature. Although a thermocouple can be inserted into cell this setup is not ideal since it does not measure the temperature of the gasket chamber but rather that of the cell body. Therefore it would be preferable to record the temperature through observation of temperature-induced crystal changes over a wide range of temperatures.

Thermal differentials have been measured using five compounds (Table 3.1) which undergo phase transitions at a variety of temperatures between room temperature and 100 K. The aim of these transition studies is to construct a calibration curve for the turnbuckle cell, which can then be utilized to calculate the sample temperature given a defined cryostat temperature. Experiments have also been conducted on the most effective configuration for attachment of a thermocouple to the cell for *in-situ* temperature measurements. Thermocouple measurements have also been conducted simultaneously with respect to one of the phase transitions to ascertain the level of thermal transfer to the cell when the thermocouple is attached.

Table 3.1: Reported unit cell parameters (with errors if available) of phase transition materials above (top) and below (bottom) the transition temperature

Compound	$[\mathrm{Ni(en)_3}][\mathrm{NO_3}]_2$[i]	Ferrocene*[ii]	Barbituric acid[iii]
Phase Transition (K)	109	164	216
Crystal System	Hexagonal	Monoclinic	Orthorhombic
Space Group	$P6_3/mmm$	$P2_1/n$	$Pnma$
a (Å)	8.83550(10)	5.929	6.2144(7)
b (Å)	8.83550	7.611	12.7512(14)
c (Å)	11.08960(10)	9.041	8.8841(10)
α (°)	90	90	90
β (°)	90	93.16	90
γ (°)	120	90	90
Crystal System	Hexagonal	Triclinic	Monoclinic
Space Group	$P6_1/mmm$	$P\bar{1}$	$P2_1/n$
a (Å)	8.82020(10)	9.095	6.1313(12)
b (Å)	8.82020	9.392	12.703(2)
c (Å)	33.1447(4)	9.476	8.8456(17)
α (°)	90	105.50	90
β (°)	90	91.53	92.187(4)
γ (°)	120	91.9	90

*The unit cell parameters reported in the literature use alternate settings for the unit cells before and after the transition.

References: (i) - (Farrugia *et al.*, 2003); (ii) - (Dunitz *et al.*, 1956, Edwards *et al.*, 1960, Seiler & Dunitz, 1979); (iii) - (Nichol & Clegg, 2005)

Table 3.1 continued: Reported unit cell parameters (with errors if available) of phase transition materials above (top) and below (bottom) the transition temperature

Compound	NH_4Br[iv]	KNO_2[v]	$NH_4H_2PO_4$†[vi]
Phase Transition (K)	235	264	148
Crystal System	Cubic	Rhombohedral	Tetragonal
Space Group	$Pm\bar{3}m$	$R\bar{3}m$	$I\bar{4}2d$
a (Å)	4.0596	5.011(1)	-
b (Å)	4.0596	5.011	-
c (Å)	4.0596	10.153(5)	-
α (°)	90	90	90
β (°)	90	90	90
γ (°)	90	120	90
Crystal System	Tetragonal	Monoclinic	Orthorhombic
Space Group	$P4/nmm$	$P2_1/c$	$P2_12_12_1$
a (Å)	5.7284	4.401(2)	-
b (Å)	5.7284	9.596(2)	-
c (Å)	4.0628	6.981(2)	-
α (°)	90	90	90
β (°)	90	108.28(4)	90
γ (°)	90	90	90

†The literature paper cited does not disclose the unit cell parameters of this compound in either phase.

References: (iv) – (Bonilla *et al.*, 1970); (v) - (Solbakk & Stroemme, 1969, Onoda-Yamamuro *et al.*, 1998, Duan *et al.*, 2001); (vi) - (Tomaszewski, 1992)

3.2. Experimental

3.2.1 Sample Preparation

$[Ni(en)_3][NO_3]_2$ and barbituric acid dihydrate were synthesized and crystallized following the literature methods (Farrugia *et al.*, 2003, Nichol & Clegg, 2005). The remaining compounds (Table 3.1) were obtained commercially and used without recrystallization.

3.2.2 Apparatus

The low-temperature studies utilized the turnbuckle cell with an opening angle of 40°, 600μm culet BOEHLER-ALMAX cut diamonds, and Inconel gasket. Single crystal X-ray experiments were conducted on a three-circle Bruker Smart APEX diffractometer equipped with an Oxford Cryosystems Cryostream Plus (Cosier & Glazer, 1986) (Figure 3.3). No hydrostatic medium was inserted inside the gasket hole so that no pressure was applied to the sample. An Omega HH66R thermocouple was used for the *in-situ* temperature measurements and attached to the cell using GE Varnish (CMR-Direct).

Figure 3.3: The experimental setup with turnbuckle cell and cryostat

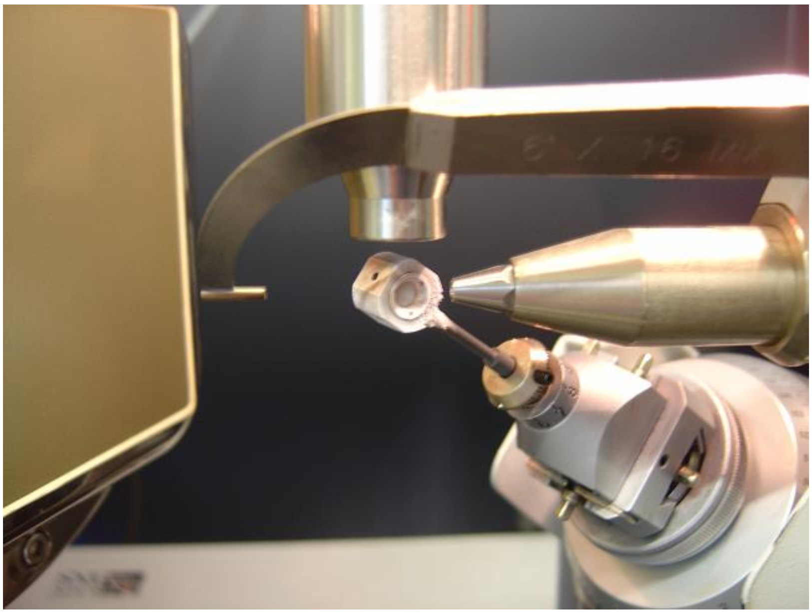

3.2.3 Data Collection Procedure

The transition temperature of each compound was determined by collecting data at a series of temperatures from ambient to low temperature conditions, with smaller temperature change increments around the literature transition temperatures. After every decrease in temperature the cell was allowed to equilibrate for approximately 15 minutes. The similarity of the ambient and low temperature phases in barbituric acid dihydrate and $[Ni(en)_3][NO_3]_2$ necessitated the collection of full high-pressure data sets to define accurately the transition temperatures. Conversely only partial data sets were collected for the remaining phase transition compounds since the different phases were more easily distinguishable. The data collection strategy employed was as described by Dawson *et al.* (Dawson *et al.*, 2004).

3.2.4 Data Processing

Cell indexing and integration were carried out using the Bruker APEX II (Bruker, 2001b) software with dynamic masks generated by ECLIPSE (Dawson *et al.*, 2004). Absorption corrections were carried out using SADABS (Sheldrick, 2008) and TWINABS (Bruker, 2001a) for all single and multi-domain integrations respectively. The ambient-temperature structure of $[Ni(en)_3][NO_3]_2$ was solved using SUPERFLIP (Palatinus & Chapuis, 2007), whilst the two phases of ferrocene were solved at 180 K and 100 K using SIR92 (Altomare *et al.*, 1994). Distance, angle, thermal similarity, and vibrational similarity restraints were applied to the positions of non-metal atoms in both $[Ni(en)_3][NO_3]_2$ and ferrocene. Ambient and low-temperature structures of barbituric acid dihydrate were obtained from the Crystal Structure Database v5.34 (REFCODE = BARBADxx). Distance and angle restraints were derived from the monoclinic and orthorhombic structure determinations at 200 K and 225 K respectively and applied to the positions of non-metal atoms. The IUCr minimum publication resolution limit of 0.84 Å was used as the integration limit, except for barbituric acid dihydrate where 0.9 Å was used due to the lack of higher resolution data. Merging and refinement of the data were performed using CRYSTALS (Betteridge *et al.*, 2003). All structures were refined against $|F|$ with reflections with $|F| < 4\sigma(|F|)$ omitted.

3.3 Results

3.3.1 Calibration using a Thermocouple

Ferrocene undergoes a reported phase transition from a monoclinic $P2_1/n$ phase to a triclinic $P\bar{1}$ phase at 164 K (Seiler & Dunitz, 1979). The response of the unit cell axes of ferrocene to temperature with a thermocouple attached to the cell and simultaneous temperature readings from the thermocouple are reported in Figure 3.4 and 5 respectively. When the thermocouple is inserted into the cell the phase transition is observed at a cryostat temperature of 149 K, however when the thermocouple is wrapped round the cell (Figure 3.6) the phase transition occurs at a cryostat temperature of 150 K. Once the thermocouple is inserted into the cell the temperature reading decreases from 300.2 K to 207 K over the cryostat temperature range of 300 K – 140 K, whilst the thermocouple measurements decline from 254.4 K to 158.6 K over a cryostat range of 250 K – 145 K when the thermocouple is wrapped around the cell.

Figure 3.4: The unit cell parameters of ferrocene *versus* temperature with a thermocouple inserted into the cell (top) and wrapped round the cell (bottom)

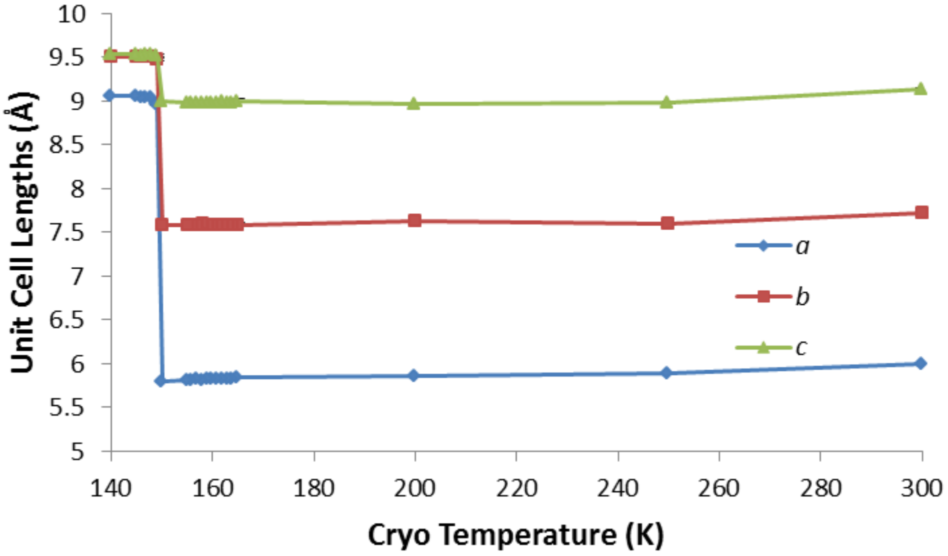

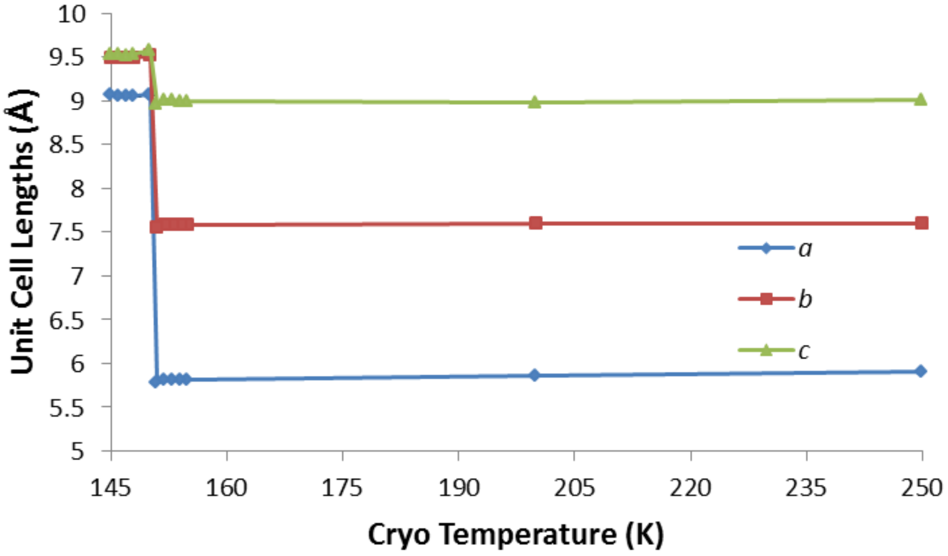

Figure 3.5: Thermocouple temperature readings *versus* cryostat temperature

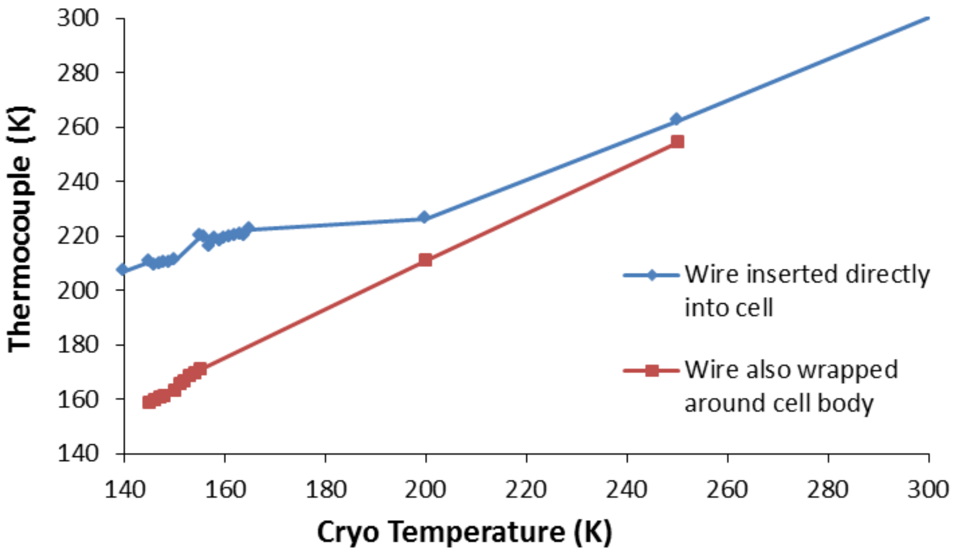

Figure 3.6: Turnbuckle cell with thermocouple inserted directly (left) and also wrapped around cell body (right)

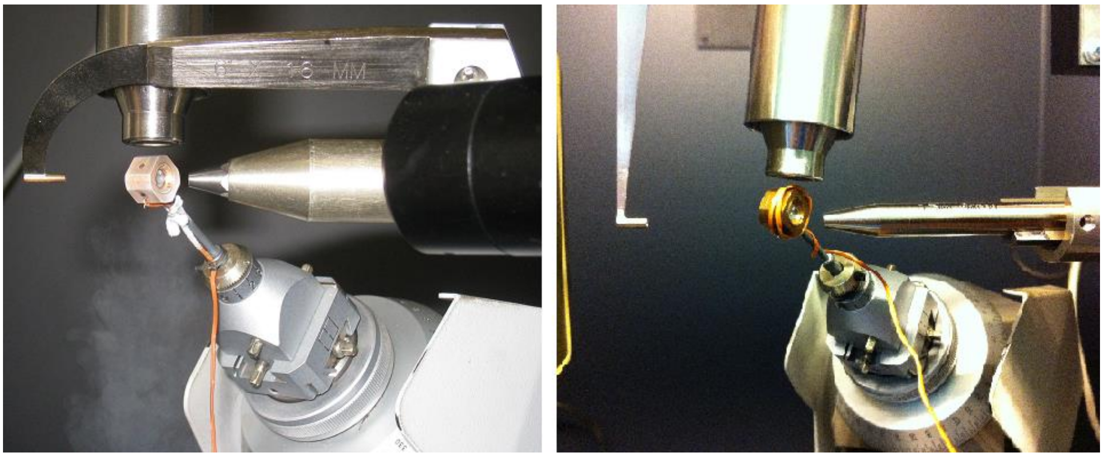

3.3.2 Calibrations using Phase Transitions

3.3.2.1 Ferrocene

The change in unit cell parameters for ferrocene in response to cooling in the turnbuckle cell is presented in Figure 3.7. No thermocouple was attached during these measurements. Between 300 K and 160 K the crystal system is monoclinic P with unit cell parameters remaining approximately constant at 5.5 Å, 7.6 Å, and 9.0 Å for the *a*, *b*, and *c* axes respectively. At 158 K both the monoclinic and triclinic unit cells could be indexed since both phases share almost identical lattices while the additional reflections which suggest the presence of the triclinic phase are less numerous and have relatively low intensity (Table 3.2). However a comparison of the refinement statistics for both crystal structures at 158 K provided in Table 3.3 reveals that the monoclinic structure has the lower *R*1 (6.2 %), and is therefore the correct phase at this temperature. Upon subsequent cooling the crystal system became triclinic with unit cell parameters remaining approximately constant at 8.9 Å, 9.4 Å, and 9.3 Å for the *a*, *b*, and *c* axes respectively, and therefore the phase transition of ferrocene inside the turnbuckle cell occurs at 157 K.

Figure 3.7: Unit cell axes lengths (top) and angles (bottom) of ferrocene *versus* temperature

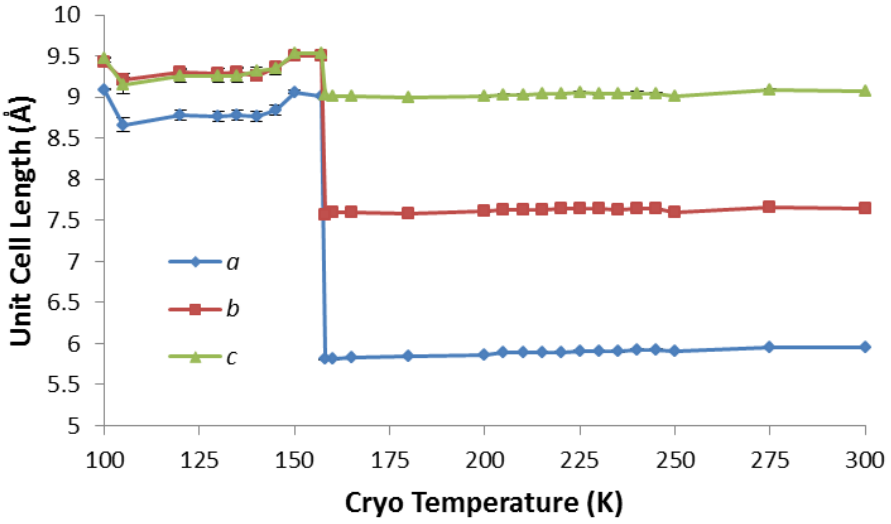

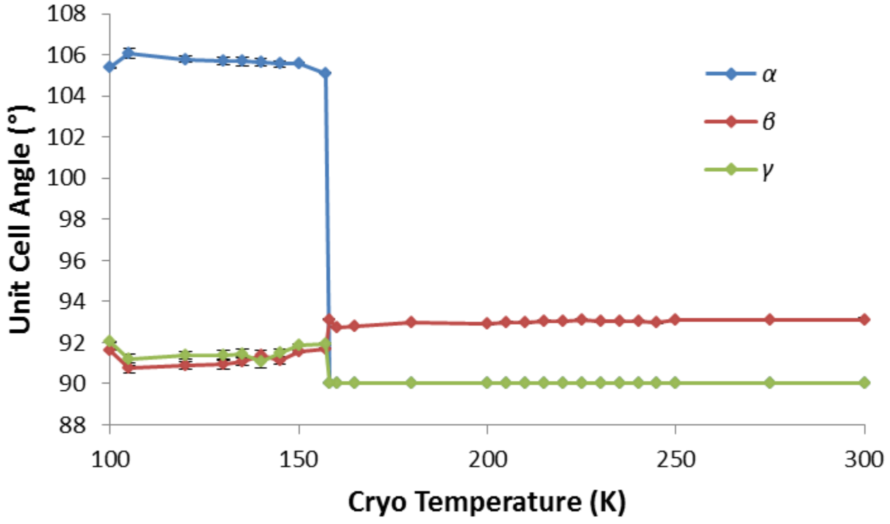

Table 3.2: Reflection harvesting and indexing statistics for the monoclinic and triclinic phases of ferrocene at 158 K

Minimum I/σ	Total harvested	Monoclinic lattice	Triclinic lattice
5	794	257	19
6	628	219	9
7	449	209	6

Table 3.3: Crystal data for ferrocene at 158 K

Crystal System	Monoclinic	Triclinic
Space Group	$P2_1/n$	$P\bar{1}$
a (Å)	5.806(2)	9.027(3)
b (Å)	7.5679(12)	9.538(4)
c (Å)	9.022(2)	9.5413(19)
β (°)	93.10(2)	91.93(2)
V (Å^3)	395.85(18)	792.5(4)
Z	2	4
D_{calc} (Mg m^{-3})	1.561	1.559
Reflections	1395	2498
Unique Reflections	321	796
R_{int}	0.053	0.069
R	0.0620	0.0652
R_w	0.0621	0.0513
GooF	1.2414	1.5841
Data:Parameters	209:52	329:199
No. Restraints	95	363
ρ_{max}/ρ_{min} (e.Å^{-3})	0.95/-0.53	0.16/-0.16

3.3.2.2 Barbituric acid dihydrate

Barbituric acid dihydrate is reported to undergo a phase transition at 216 K from an orthorhombic *Pnma* phase to a non-merohedrally twinned monoclinic $P2_1/n$ phase (Nichol & Clegg, 2005). This phase transition occurs gradually with decreasing temperature with a corresponding increase in the lattice β angle for the two monoclinic twin domains (Figures 3.8 and 3.9). The unit cells are otherwise identical for both phases, with *a*, *b*, and *c* unit cell parameters of approximately 6.15 Å, 12.74 Å, and 8.87 Å respectively, and therefore the two phases can only be distinguished around the transition temperature through refinement of their crystal structures (Nichol & Clegg, 2005).

Figure 3.8: Diffraction image of barbituric acid dihydrate at 225 K (left) and 200 K (right) illustrating the emergence of non-merohedral twinning upon cooling

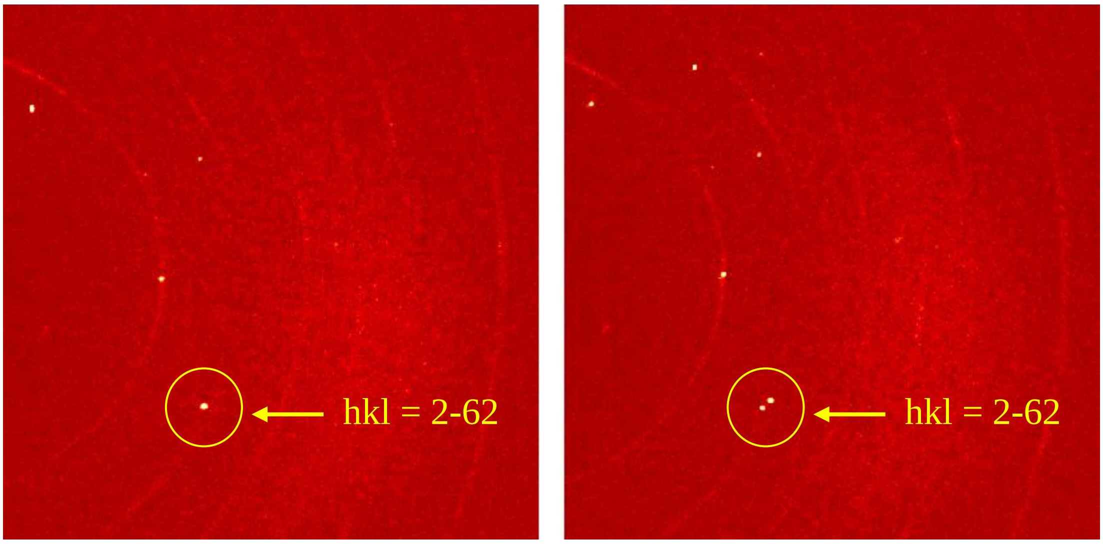

The list of *R*1 factors for each phase at each temperature is given in Table 3.4, demonstrating that between 225 K and 213 K the orthorhombic refinement produced the lower *R*1 factor, whilst the monoclinic phase possessed the lower *R*1 value from 212 K to 200 K. The indexing and refinement data are presented in Table 3.5, and the change in unit cell parameters in response to cooling is given in Figure 3.10. As demonstrated in the previously conducted variable-temperature study (Nichol & Clegg, 2005) the unit cell axes undergo no appreciable change upon cooling between 225 K and 200 K. By contrast the β angle undergoes a significant increase from 91.138(6)° to 91.954(6)° between 212 K and 200 K, and a comparison to the monoclinic β angles reported in the literature (Nichol & Clegg, 2005) (Figure 3.11) indicates that the monoclinic unit cell reported at 216 K (β = 91.180(5)°) is analogous to that observed at 212 K (β = 91.138(6)°) in the turnbuckle cell. The orthorhombic to monoclinic phase transition for barbituric acid dihydrate therefore occurs at 212 K inside the turnbuckle cell.

Figure 3.9: 3D intensity profile of 2-62 reflection splitting *versus* temperature

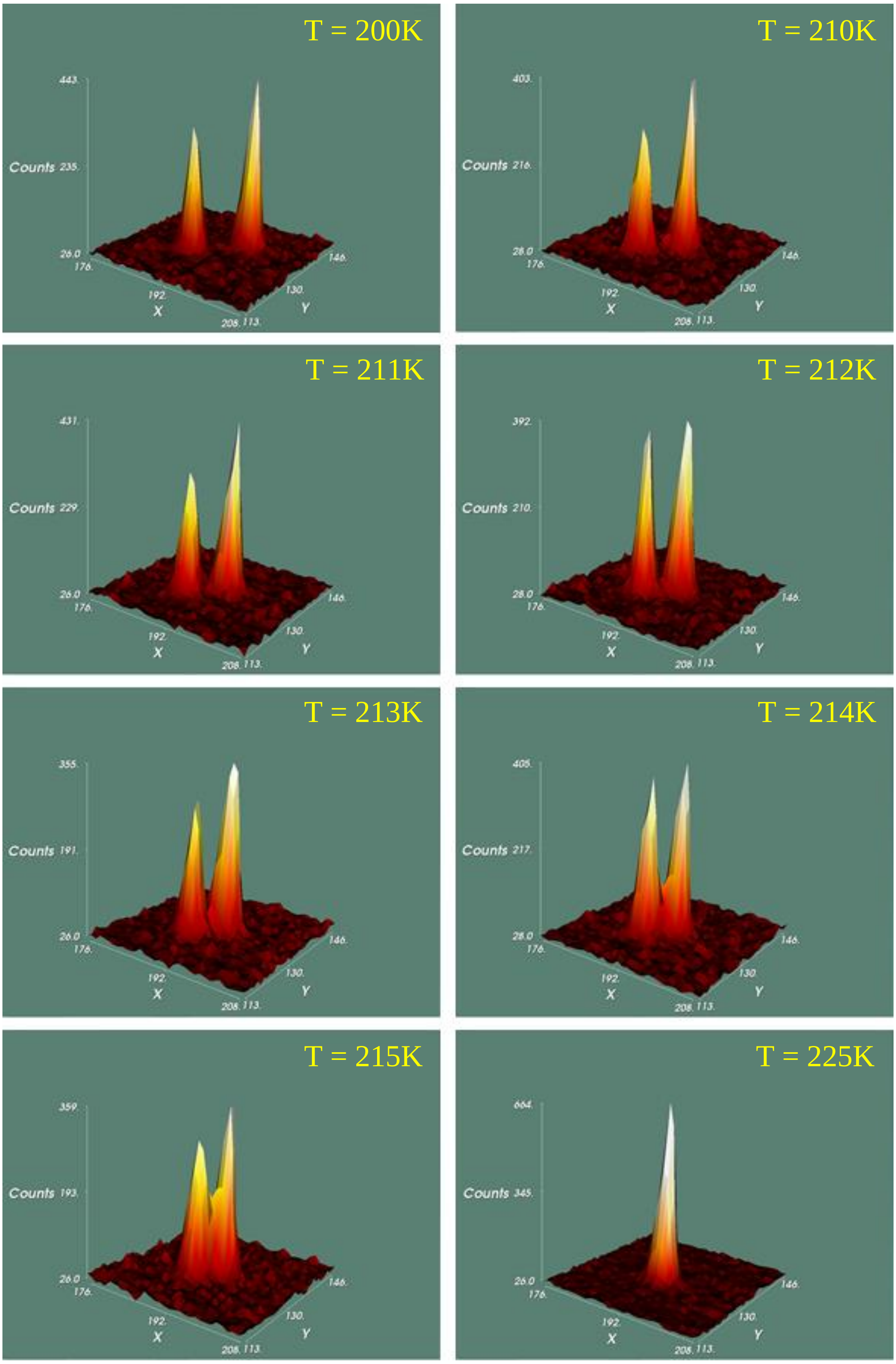

T = 200K

T = 210K

T = 211K

T = 212K

T = 213K

T = 214K

T = 215K

T = 225K

Table 3.4: *R*1 values for crystal structure refinements of barbituric acid dihydrate

Crystal System	Monoclinic	Orthorhombic
200 K	0.0530	0.0845
209 K	0.0451	0.0671
210 K	0.0510	0.0633
211 K	0.0517	0.0577
212 K	0.0545	0.0601
213 K	0.0587	0.0565
214 K	0.0608	0.0536
215 K	0.0671	0.0485
225 K	N/A*	0.0407

*The monoclinic structure could not be refined fully at this temperature

Table 3.5: Crystal data for barbituric acid dihydrate

Temperature (K)	200	209	210	211	212
Crystal System	Monoclinic	Monoclinic	Monoclinic	Monoclinic	Monoclinic
Space Group	$P2_1/n$	$P2_1/n$	$P2_1/n$	$P2_1/n$	$P2_1/n$
a (Å)	6.1491(7)	6.1537(7)	6.1558(7)	6.1549(7)	6.1538(6)
b (Å)	12.7386(8)	12.7401(7)	12.7392(7)	12.7398(8)	12.7416(7)
c (Å)	8.8661(6)	8.8690(5)	8.8695(5)	8.8713(6)	8.8720(5)
β (°)	91.954(6)	91.433(6)	91.402(6)	91.246(6)	91.138(6)
V (Å^3)	694.09(1)	695.10(10)	695.34(10)	695.45(10)	695.51(9)
Z	4	4	4	4	4
D_{calc} (Mg m^{-3})	1.570	1.568	1.568	1.567	1.567
Reflections	1938	1938	1920	1951	2002
Unique Reflections	956	934	921	932	954
R_{int}	0.0682	0.889	0.0682	0.0746	0.0878
R	0.0530	0.0451	0.0510	0.0517	0.0545
R_w	0.0639	0.0523	0.0603	0.0601	0.0616
GooF	1.1735	1.1826	1.0981	1.1574	1.1439
Data:Parameters	577:101	501:101	512:101	488:101	496:101
No. Restraints	21	21	21	21	21
ρ_{max}/ρ_{min} (e.Å^{-3})	0.19/-0.21	0.16/-0.16	0.23/-0.23	0.19/-0.18	0.17/-0.17

Table 3.5 continued: Crystal data for barbituric acid dihydrate

Temperature (K)	213	214	215	225
Crystal System	Orthorhombic	Orthorhombic	Orthorhombic	Orthorhombic
Space Group	*Pnma*	*Pnma*	*Pnma*	*Pnma*
a (Å)	6.1579(9)	8.5410(5)	6.1582(9)	6.1668(8)
b (Å)	8.8713(7)	8.8698(7)	8.8702(6)	8.8704(6)
c (Å)	12.7419(9)	12.7419(9)	12.7429(8)	12.7442(8)
β (°)	90	90	90	90
V (Å^3)	696.07(13)	695.88(13)	696.07(12)	697.13(11)
Z	4	4	4	4
D_{calc} (Mg m^{-3})	1.566	1.566	1.566	1.564
Reflections	2280	2193	2192	2546
Unique Reflections	408	406	407	512
R_{int}	0.067	0.059	0.060	0.062
R	0.0565	0.0536	0.0485	0.0407
R_w	0.0557	0.0575	0.0542	0.0351
GooF	1.2135	1.2052	1.1456	1.2502
Data:Parameters	269:72	281:72	280:72	281:72
No. Restraints	32	32	32	32
ρ_{max}/ρ_{min} (e.Å^{-3})	0.26/-0.21	0.24/-0.24	0.25/-0.22	0.19/-0.19

Figure 3.10: Unit cell axes of barbituric acid dihydrate *versus* temperature

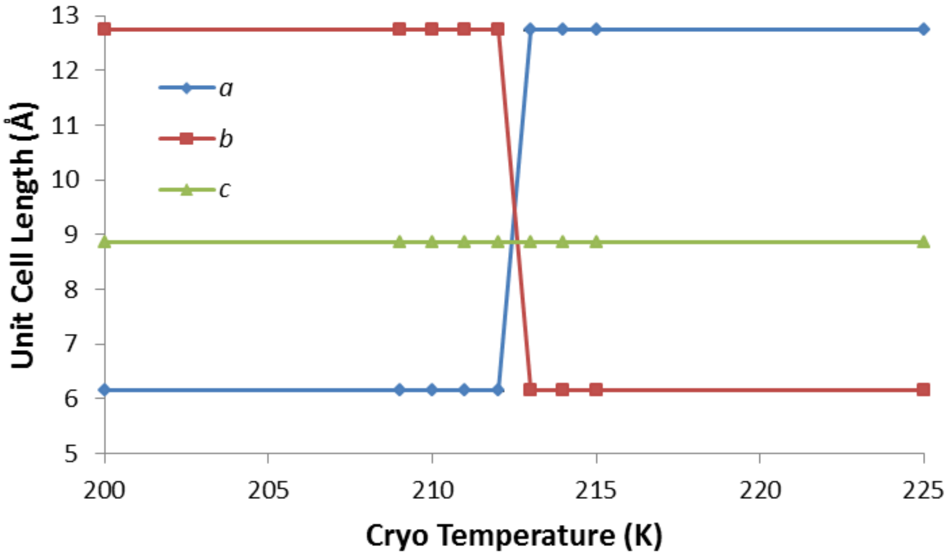

Figure 3.11: Comparison of β angle for turnbuckle variable-temperature study with literature data

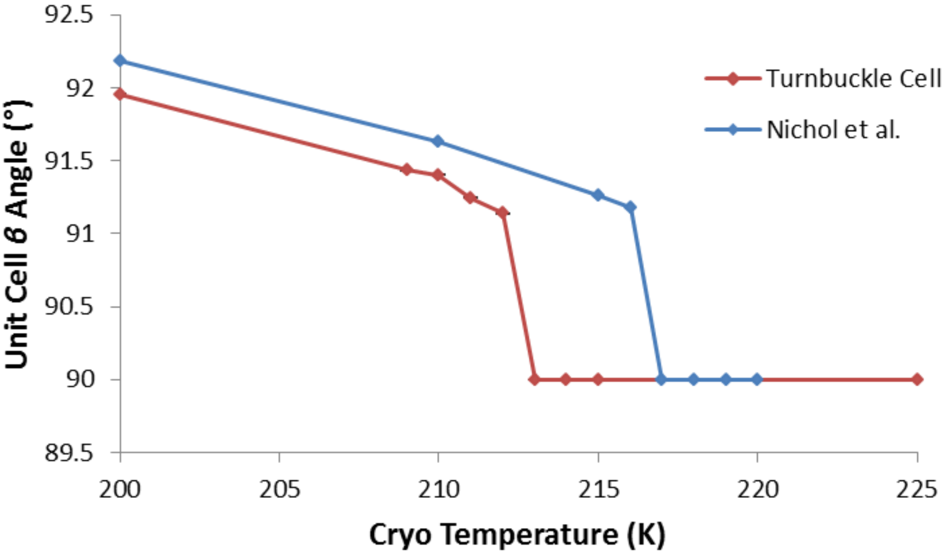

3.3.2.3 Potassium nitrite

KNO_2 is reported to undergo a phase transition at 264 K from a rhombohedral $R\bar{3}m$ phase to a monoclinic $P2_1/c$ phase (Duan *et al.*, 2001). The change in unit cell parameters for both phases in response to temperature in the turnbuckle cell is presented in Figure 3.12. Between 300 K and 260 K the crystal was indexed as rhombohedral with the $a = b$ axes increasing from 4.986(6) to 5.0458(6) Å and c axis decreasing from 10.278(10) Å to 9.9702(16) Å. At 259 K the crystal system changes to monoclinic, with a corresponding doubling of the unit cell volume. The unit cell a, b and c axes remain approximately constant at 4.47 Å, 9.64 Å, and 6.97Å respectively between 259 K and 216 K, whilst the β angle undergoes a continued increase from 106.55(3)° and 106.419(18)° over the same temperature range. The phase transition temperature of KNO_2 inside the turnbuckle cell is therefore 259 K.

3.3.2.4 Nickel Trisethylenediamine dinitrate

$[Ni(en)_3][NO_3]_2$ has been observed to undergo a phase transition at 109 K, or between 0.13 GPa and 0.87 GPa, from a hexagonal $P6_322$ phase to a hexagonal $P6_122/P6_522$ phase, and which is characterised by a tripling of the c axis, easily observed in the diffraction images (Farrugia *et al.*, 2003, Cameron *et al.*, 2014). The impact of decreasing temperature on the unit cell parameters of this compound are presented in Figure 3.13, which reveals that between 300 K and 95 K the unit cell *a* = *b* axes remain approximately constant at 8.8 Å whilst the *c* axis undergoes a significant contraction from 11.3756(4) Å to 11.0858(6) Å. The tripling of the *c* axis associated with the transformation to the $P6_122/P6_522$ phase was not observed at any temperature. A similar variable-temperature study was conducted using the low-temperature setup at EH1-I19 Diamond Light Source, where the phase transition was likewise not observed down to a cryostat temperature of 80 K.

Figure 3.12: Unit cell axes (top) and angles (bottom) of KNO_2 *versus* temperature

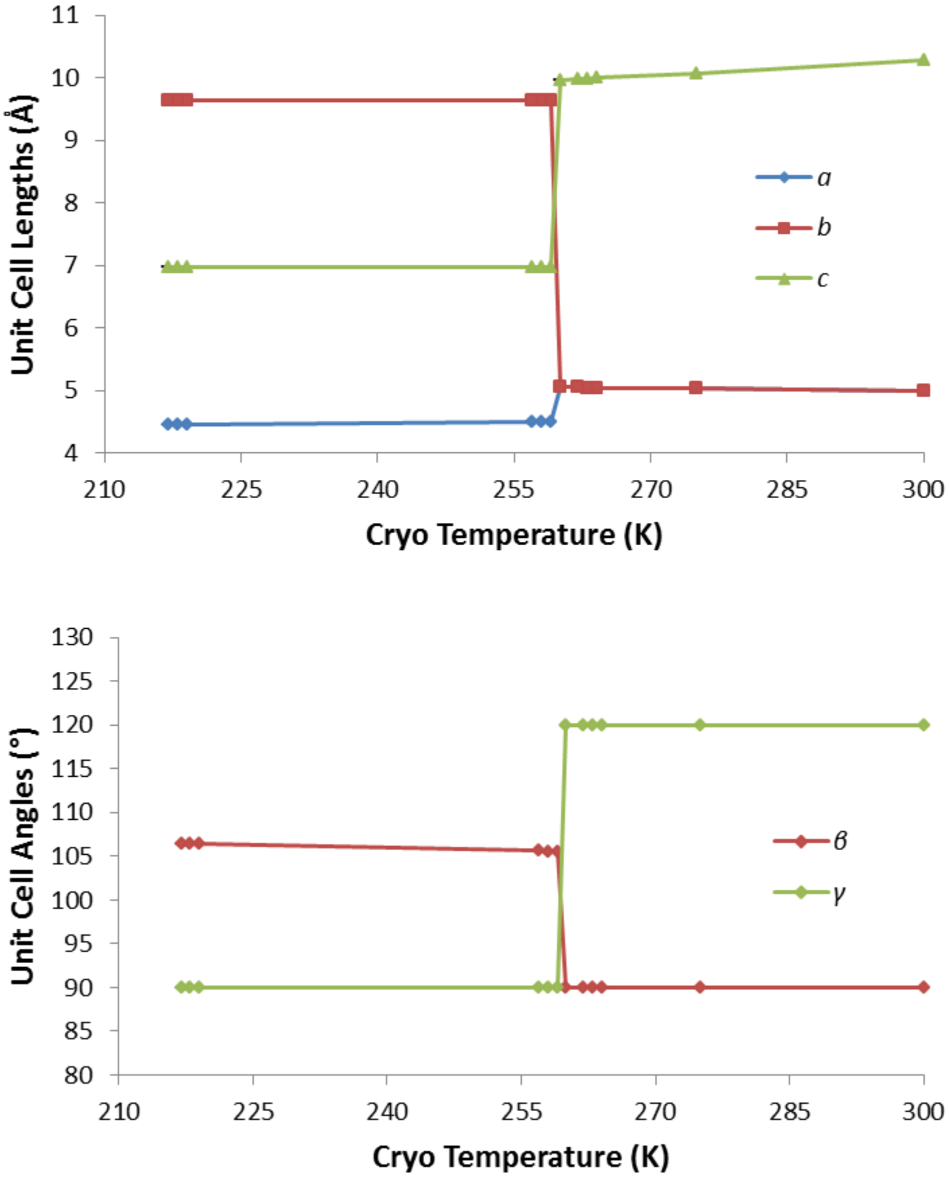

Figure 3.13: Unit cell axes of $[Ni(en)_3][NO_3]_2$ *versus* temperature

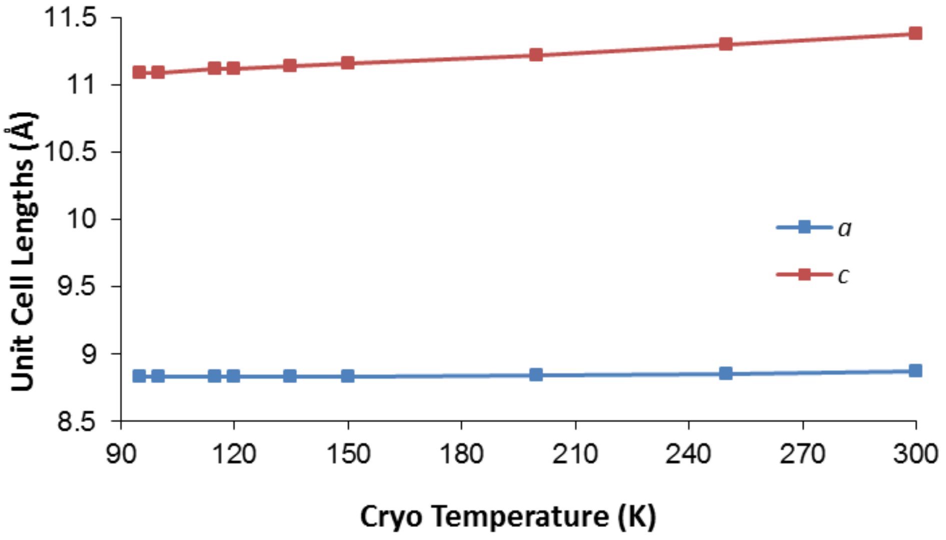

3.3.2.5 Ammonium dihydrogen phosphate

$NH_4H_2PO_4$ is reported to undergo a phase transition from a tetragonal $I\bar{4}2d$ phase to an orthorhombic $P2_12_12_1$ phase at 148 K (Tomaszewski, 1992). Unit cell parameters for both phases are identical with *a*, *b*, and *c* axes of approximately 7.5 Å, and therefore the phase transition is principally distinguished through the presence or absence of I-centring in the crystal lattice (Figure 3.14). Changes in intensity of the reflections which satisfy the systematic absence condition for *I*-centring as a result of cooling are given in Figure 3.15. These reflections were found to have negligible intensity between 300 K and 138 K and significantly increased upon further reductions in temperature, demonstrating a phase transition of 137 K for $NH_4H_2PO_4$.

3.3.2.6 Ammonium bromide

NH_4Br crystallizes in a cubic $Pm\bar{3}m$ phase under ambient temperatures which transforms to a tetragonal *P*4/*nmm* at 235 K (Bonilla *et al.*, 1970). The change in unit cell parameters for NH_4Br in response to cooling in the turnbuckle cell is presented in Figure 3.16. The cubic *P* phase was indexed between 300 K and 233 K with unit axes cell axes remaining approximately constant at 4.05 Å. Upon reaching 232 K the crystal lattice transforms to the tetragonal *P* phase with the *c* axis remaining unchanged whilst the *a* = *b* axes increase from approximately 4.05 Å to 5.72 Å and the unit cell volume doubles from 66 Å^3 to 132 Å^3. Consequently the phase transition temperature of NH_4Br inside the turnbuckle cell is 232 K.

Figure 3.14: Precession images of the 2kl Miller planes of $NH_4H_2PO_4$ at 300 K (top) and 130 K (bottom) with the *I*-centring reflection positions highlighted

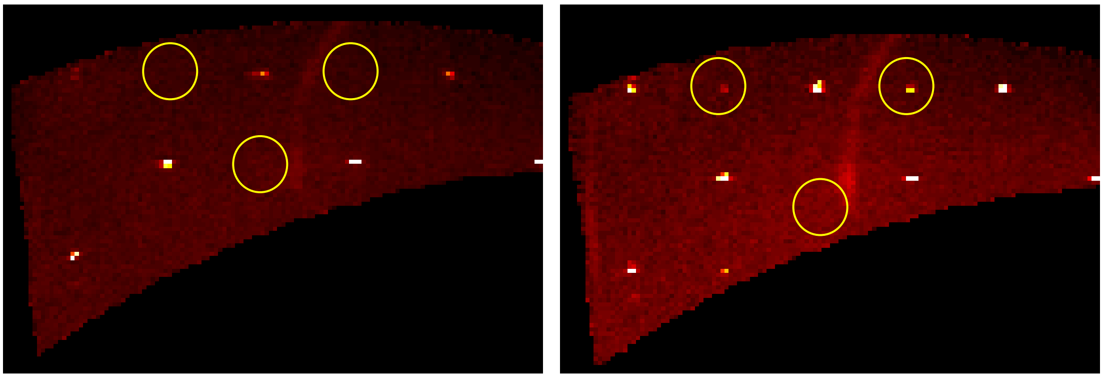

Figure 3.15: Intensity of selected reflections which meet the systematic absence conditions for *I*-centring *versus* temperature

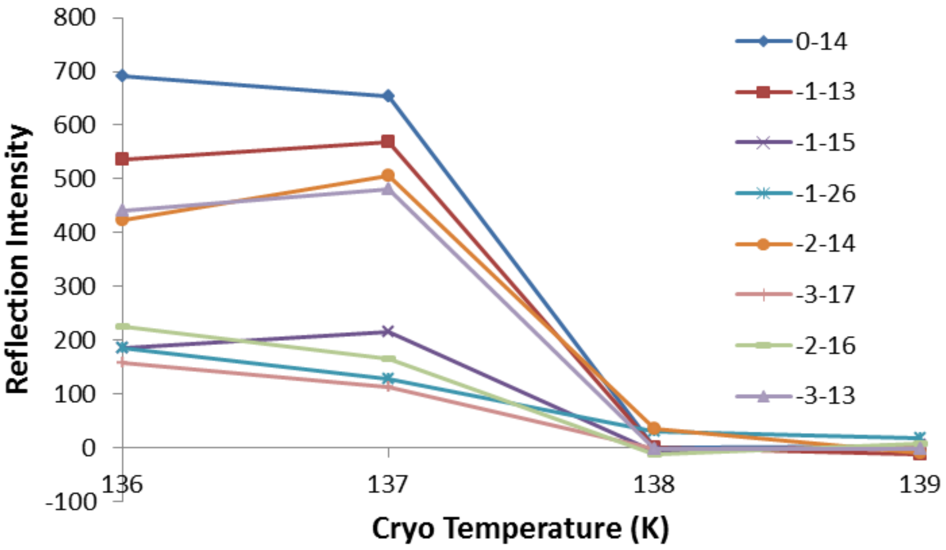

Figure 3.16: Unit cell axes (top) and volume (bottom) of NH_4Br *versus* temperature

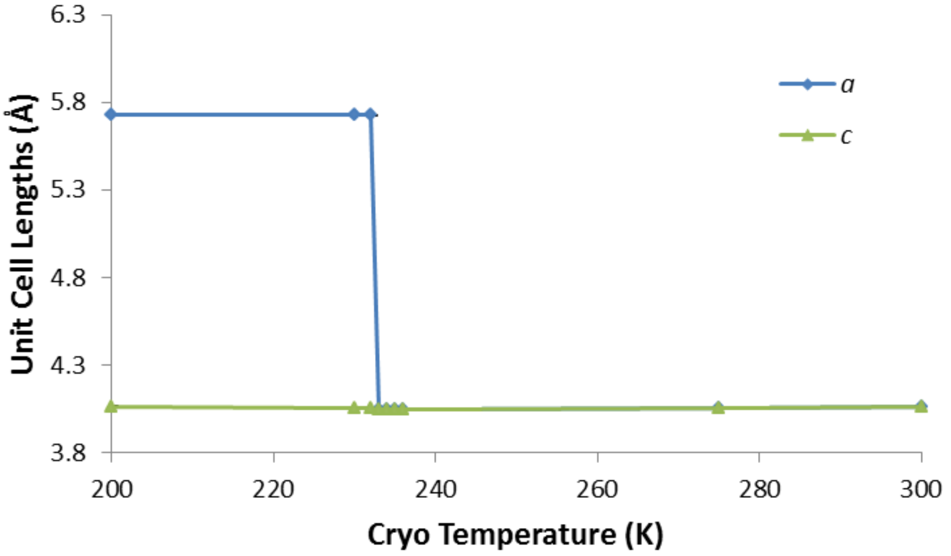

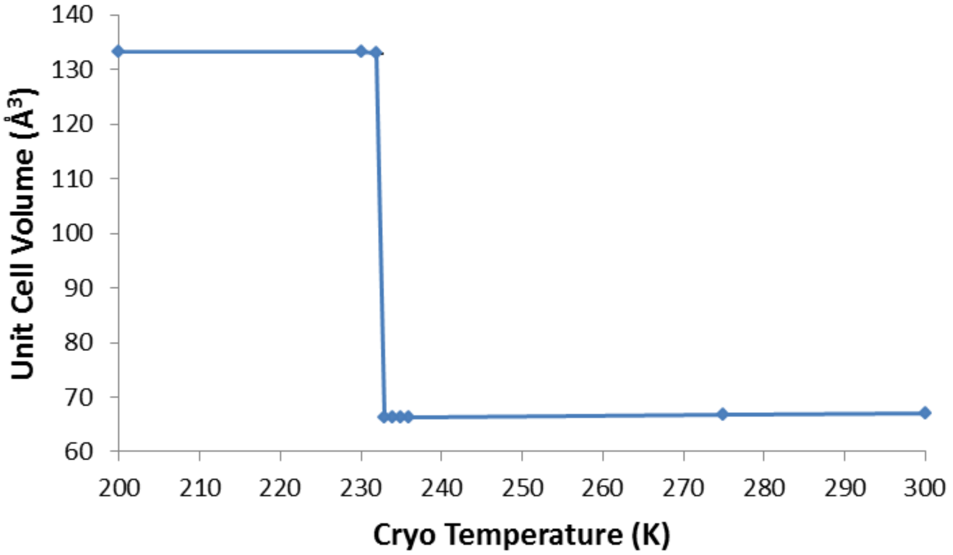

3.3.3 Calibration Curve

Using the the observed and reported phase transition temperatures (Table 3.6) a calibration curve has been constructed for the cell (Figure 3.17), which can be used to determine the relationship between cryostat temperature and internal cell temperature (Equation 3.1).

Table 3.6: Observed phase transition temperatures and associated thermal differentials

Compound	Lit. Transition (K)	Obs. Transition (K)	ΔK
$[Ni(en)_3][NO_3]_2$	109	N/A	N/A
$NH_4H_2PO_4$	148	137	11
Ferrocene	164	157	7
Barbituric acid dihydrate	216	212	3
NH_4Br	235	232	3
KNO_2	264	259	5

Figure 3.17: Calibration curve for turnbuckle cell based on phase transitions

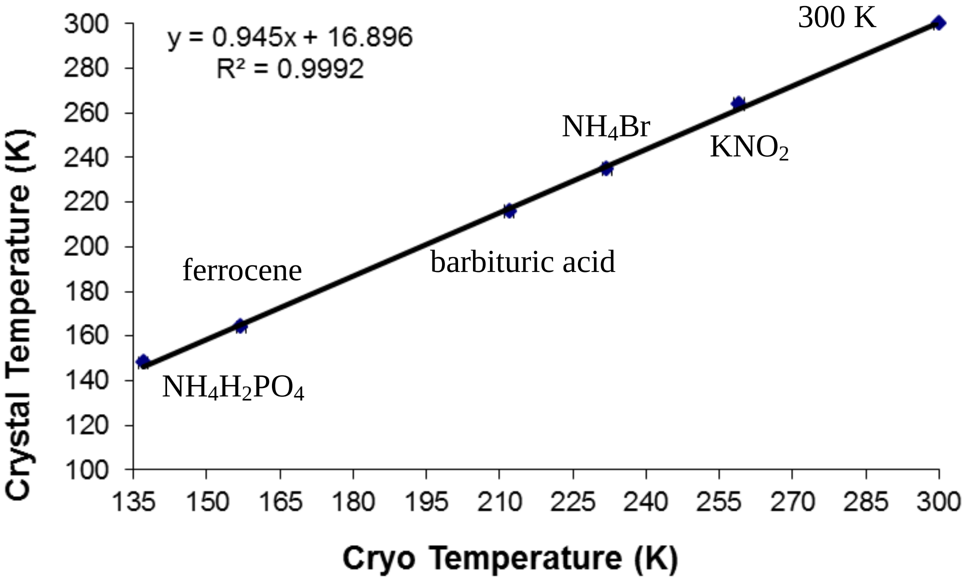

$$T_{crystal}\ (K) = 0.945(13)T_{cryo}\ (K) + 17(3) \qquad (3.1)$$

3.4 Discussion

The observed phase transitions are identical to those expected from the literature however the individual transition temperatures vary significantly from the reported temperatures. This thermal differential increases as the cryostat temperature decreases with the notable exception of KNO_2, which possess the greatest thermal differential (5 K) of all compounds between 300 K and 200 K. Reasons for this unusual behaviour could include an inadequate cooling time, changing flow-rate of the cryostat with temperature, and a broader phase transition than for some other compounds. Transformation of $[Ni(en)_3][NO_3]_2$ from the hexagonal $P6_322$ phase to the $P6_122$ phase was not observed in the variable-temperature study, suggesting that the cryostat temperature had not reached low enough to induce the phase transition. Extrapolation of the phase transition calibration curve indicates that a crystal temperature of 107 K would require a decrease in cryostat temperature to 95.3 K. The absence of the low-temperature phase at this cryostat temperature indicates that either the thermal differential or the flow rate deviates from the calibration curve in this temperature range. Attempts to probe further below this temperature were unsuccessful due to the instability of the cryostat temperature control.

Direct measurement of the cell temperature through the utilization of a thermocouple yielded mixed results. Attachment of the thermocouple imparts thermal energy to the cell as demonstrated through the decreased temperature of the ferrocene phase transition (149 K – 150 K). The source of this additional thermal differential derives from the physical link between the cell and the thermocouple, which acts a bridge between the cold cell and ambient temperature laboratory through which thermal energy flows. Temperature readings from the thermocouple were significantly different from the applied temperature and the calibrated temperature, indicating an inadequate ability of the cryostat to cool the thermocouple effectively. Altering the setup of the thermocouple was found to be crucial to limiting the degree of thermal transfer to the cell, and hence improving the accuracy of these temperature measurements. Wrapping the wire round the cell was correlated with greater temperature stability as well as temperature readings much closer to the cryostat temperature, behaviour which likely arises due to the greater amount of the thermocouple presented to the cryo-flow during data collection and more efficient cooling of the thermocouple. However the reduction in thermal energy transferred to the cell was minimal with the ferrocene transition being observed at 150 K rather than 149 K, suggesting that the primary benefit of this method lies in obtaining more accurate temperature measurements.

3.5 Conclusion

The five phase transition compounds studied have provided a calibration curve for the turnbuckle cell between 300 K and 138 K. Attachment of a thermocouple has been found to alter this calibration curve, therefore necessitating further study into the optimal configuration, operating temperature range, and suitability of these devices with the current experimental setup.

3.6 References

Altomare, A., Cascarano, G., Giacovazzo, C., Guagliardi, A., Burla, M. C., Polidori, G. & Camalli, M. (1994). *J. Appl. Cryst.* **27**, 435.

Betteridge, P. W., Carruthers, J. R., Cooper, R. I., Prout, K. & Watkin, D. J. (2003). *J. Appl. Crystallogr.* **36**, 1487.

Boldyreva, E. V. (2008). *Acta Crystallogr., Sect. A: Found. Crystallogr.* **64**, 218-231.

Boldyreva, E. V., Drebushchak, T. N., Shakhtshneider, T. P., Sowa, H., Ahsbahs, H., Goryainov, S. V., Ivashevskaya, S. N., Kolesnik, E. N., Drebushchak, V. A. & Burgina, E. B. (2004). *Arkivoc*, 128-155.

Bonilla, A., Garland, C. W. & Schumaker, N. E. (1970). *Acta Crystallogr., Sect. A* **26**, 156-158.

Bruker (2001a). *TWINABS.*

Bruker (2001b). *Bruker AXS Inc., Madison, Wisconsin, USA.*

Cameron, C. A., Allan, D. R., Kamenev, K., Moggach, S. A., Murrie, M. & Parsons, S. (2014). *Z. Kristallogr.* **229**, 200-209.

Cosier, J. & Glazer, A. M. (1986). *J. Appl. Crystallogr.* **19**, 105-107.

Dawson, A., Allan, D. R., Parsons, S. & Ruf, M. (2004). *J. Appl. Crystallogr.* **37**, 410-416.

Duan, C.-g., Mei, W. N., Smith, R. W., Liu, J., Ossowski, M. M. & Hardy, J. R. (2001). *Phys. Rev. B: Condens. Matter Mater. Phys.* **63**, 144105/144101-144105/144106.

Dunitz, J. D., Orgel, L. E. & Rich, A. (1956). *Acta Crystallogr.* **9**, 373-375.

Edwards, J. W., Kington, G. L. & Mason, R. (1960). *Trans. Faraday Soc.* **56**, 660-667.

Farrugia, L. J., Macchi, P. & Sironi, A. (2003). *J. Appl. Crystallogr.* **36**, 141-145.

Gatteschi, D., Bogani, L., Cornia, A., Mannini, M., Sorace, L. & Sessoli, R. (2008). *Solid State Sci.* **10**, 1701-1709.

Giriat, G., Kamenev, K., Moggach, S. A. & Parsons, S. (in preparation). Edinburgh: University of Edinburgh.

Giriat, G., Wang, W., Attfield, J. P., Huxley, A. D. & Kamenev, K. V. (2010). *Rev. Sci. Instrum.* **81**, 073905/073901-073905/073905.

Goeta, A. E. & Howard, J. A. K. (2004). *Chem. Soc. Rev.* **33**, 490-500.

Graf, D. E., Stillwell, R. L., Purcell, K. M. & Tozer, S. W. (2011). *High Pressure Res.* **31**, 533-543.

Guetlich, P., Gaspar, A. B., Garcia, Y. & Ksenofontov, V. (2007). *C. R. Chim.* **10**, 21-36.

Katrusiak, A. (2008). *Acta Crystallogr., Sect. A: Found. Crystallogr.* **64**, 135-148.

Kobayashi, H., Kobayashi, A., Asaumi, K. & Minomura, S. (1980). *Solid State Commun.* **35**, 293-296.

Larsen, F. K. (1995). *Acta Crystallogr., Sect. B: Struct. Sci.* **B51**, 468-482.

Moggach, S. A., Parsons, S. & Wood, P. A. (2008). *Crystallogr. Rev.* **14**, 143-184.

Nichol, G. S. & Clegg, W. (2005). *Acta Crystallogr., Sect. B: Struct. Sci.* **B61**, 464-472.

Onoda-Yamamuro, N., Honda, H., Ikeda, R., Yamamuro, O., Matsuo, T., Oikawa, K., Kamiyama, T. & Izumi, F. (1998). *J. Phys.: Condens. Matter* **10**, 3341-3351.

Palatinus, L. & Chapuis, G. (2007). *J. Appl. Crystallogr.* **40**, 786-790.

Parois, P., Moggach, S. A., Sanchez-Benitez, J., Kamenev, K. V., Lennie, A. R., Warren, J. E., Brechin, E. K., Parsons, S. & Murrie, M. (2010). *Chem. Commun. (Cambridge, U. K.)* **46**, 1881-1883.

Piermarini, G. J. (2001). *J. Res. Natl. Inst. Stand. Technol.* **106**, 889-920.

Prescimone, A., Milios, C. J., Moggach, S., Warren, J. E., Lennie, A. R., Sanchez-Benitez, J., Kamenev, K., Bircher, R., Murrie, M., Parsons, S. & Brechin, E. K. (2008). *Angew. Chem., Int. Ed.* **47**, 2828-2831.

Seiler, P. & Dunitz, J. D. (1979). *Acta Crystallogr., Sect. B* **B35**, 2020-2032.

Sheldrick, G. M. (2008). *SADABS.* Version 2008-1.

Sieber, A., Bircher, R., Waldmann, O., Carver, G., Chaboussant, G., Mutka, H. & Guedel, H.-U. (2005). *Angew. Chem., Int. Ed.* **44**, 4239-4242.

Solbakk, J. K. & Stroemme, K. O. (1969). *Acta Chem. Scand.* **23**, 300-313.

Tomaszewski, P. E. (1992). *Phase Transit.* **38**, 127-220.

Chapter 4

A High-Pressure Low-Temperature Single-Crystal X-ray Study of $Mn_{12}OAc$

4.1 Introduction

Compared to traditional bulk magnets where the magnetic properties arise from long-range order in clusters above the nanoscale (100 nm), single-molecule magnets (SMMs) (Bagai & Christou, 2009) are monodisperse (uniform size) crystalline materials exhibiting magnetic phenomena on the molecular level independent of intermolecular interactions (Gatteschi, 2001). Characteristic features of SMMs include a large ground spin state (S) and a large negative magnetic anisotropy (D) due to alignment through intramolecular coupling of individual magnetic moments with the magnetic easy axis. The combination of these structural features creates a large energy barrier (ΔE) to reorientation of magnetic moments below a specific blocking temperature (T_B) (Figure 4.1) (Christou, 2005).

Figure 4.1: Energy barrier to magnetic reorientation of quantum spins in an S = 10 spin system

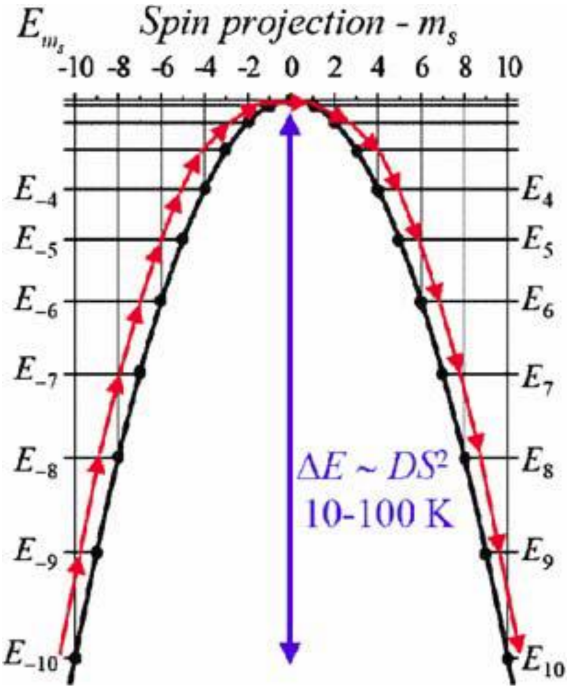

Retention of magnetization in the absence of a magnetic field is observed with a lifetime (τ) potentially extending over many months. SMMs therefore have theoretical applications as qubits in information storage, and there has been much recent work on the incorporation of SMMs in thin films (Kim *et al.*, 2004, Meenakshi *et al.*, 2004, Seo *et al.*, 2006, Cavallini *et al.*, 2008) and other surfaces (Cornia *et al.*, 2003, Cornia *et al.*, 2006). There has also been considerable interest in the observation of magneto-calorific and quantum tunnelling effects, the latter of which provides a lower energy route to magnetic reorientation and thus compromises the magnetic lifetime (Mertes *et al.*, 2002, Evangelisti & Brechin, 2010).

$[Mn_{12}O_{12}(O_2CCH_3)_{16}(H_2O)_4].2CH_3COOH.4H_2O$ ($Mn_{12}OAc$) is the prototypical SMM, having been synthesized and characterized in 1980 (Lis, 1980) and identified as an SMM in 1993 (Sessoli *et al.*, 1993). The structure of $Mn_{12}OAc$ consists of a central $Mn_4^{IV}O_4$ cube situated on a $\overline{4}$ crystallographic axis, surrounded by a ring of eight Jahn-Teller distorted octahedral Mn^{III} ions bridged by oxide and acetate ligands, and alternately coordinated to a single water ligand (Figure 4.2).

Figure 4.2: View of $Mn_{12}OAc$ molecular structure along **c** (solvent excluded for clarity)

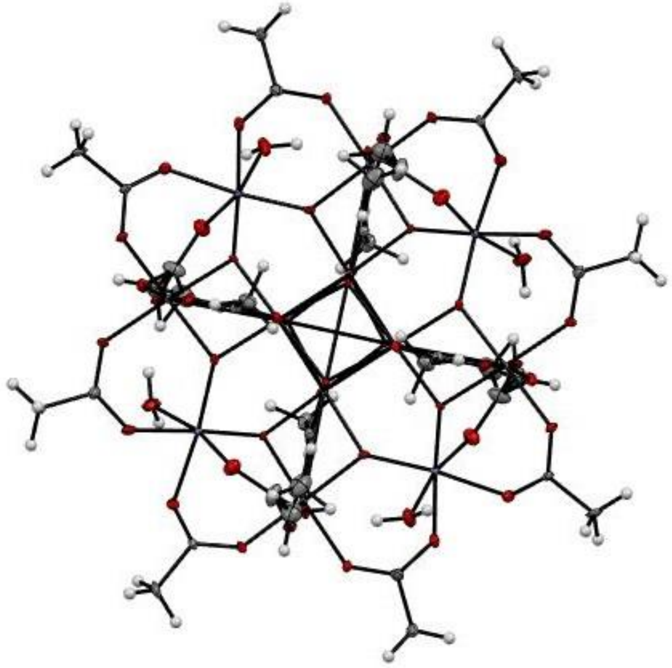

Solvent accessible voids between these moieties in the crystalline state contain water and acetic acid molecules which interact with the Mn_{12} clusters via hydrogen bonding. The acetic acid molecules are disordered about a 2-fold rotation axis with each component possessing 50 % occupancy by symmetry, due to the mutually exclusive and non-preferential availability of potential hydrogen bonding interactions on adjacent Mn_{12} clusters (Figure 4.3). These opposing orientations of the acetic acid induce positional disorder in the hydrogen-bonded acetate ligand, creating two Mn-O bonds and two terminal methyl groups with 50 % occupancy each at low-temperatures (Cornia, Fabretti, *et al.*, 2002, Farrell *et al.*, 2013). Both acetic acid and water molecules are susceptible to expulsion by heat treatment and thereby causing an ordering of the disordered Mn-O bonds (Larionova *et al.*, 2003, Farrell *et al.*, 2013).

Figure 4.3: View of $Mn_{12}OAc$ unit cell along **c** axis. Hydrogen atoms removed for clarity. Colour scheme: solvent accessible voids yellow, Mn_{12} cluster red, crystallized acetic acid blue, and crystallized water purple.

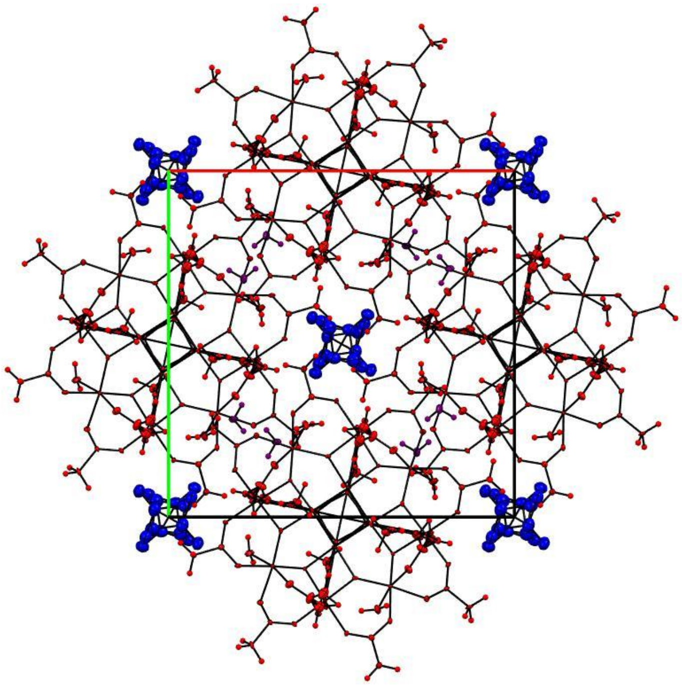

Antiferromagnetic exchange between the $S = 2$ Mn^{III} and $S = 3/2$ Mn^{IV} centres gives rise to a total molecular ground state $S = 10$, and pseudo-alignment of the Mn^{III} distorted Jahn-Teller axes with the crystalline magnetic easy axis produces a large magnetic anisotropy $D = -0.50\ cm^{-1}$. A combination of these two structural features gives $Mn_{12}OAc$ an energy barrier to magnetic spin randomization $\Delta E \approx 70$ K and blocking temperatures $T_B \approx 2$ K (Christou *et al.*, 2000). The retention of magnetization ($\tau \approx 2$ months at 2 K) is complicated by the presence of magnetic spin quantum tunnelling effects, which leads to a characteristic step pattern in the magnetic hysteresis at resonant field frequencies (Langan *et al.*, 2001). The mechanism of quantum tunnelling in $Mn_{12}OAc$ and other SMMs is not fully understood, although a variety of models have been proposed such as anti-symmetric exchange, solvent-induced symmetry lowering, and dipolar coupling (Cornia, Sessoli, *et al.*, 2002).

The relationship between the structure of $Mn_{12}OAc$ and its properties is further complicated by the presence of magnetic isomerism in the crystalline phase. Low-temperature alternating-current (AC) susceptibility and inelastic neutron scattering (INS) studies have demonstrated that bulk $Mn_{12}OAc$ contains a minority fast-relaxing species (FR1), which possesses the same ground spin state but a smaller magnetic anisotropy and lower blocking temperature compared to the majority slow-relaxing species (SR1) (Evangelisti *et al.*, 1999, Sieber *et al.*, 2005). This magneto-structural phenomenon has been identified in other SMMs such as the $Mn_{12}OAc$ derivatives $[Mn_{12}O_{12}(O_2CCH_2{}^tBu)_{16}(H_2O)_4].CH_2Cl_2.MeNO_2$ ($Mn_{12}OAc^tBu$) (Sun *et al.*, 1999) and $[Mn_{12}O_{12}(C_6H_5CO_2)_{16}(H_2O)_4].2C_6H_5CO_2H$ ($Mn_{12}OAcPh$) (Awaga *et al.*, 2006), although in the former all molecules adopt the fast-relaxing structure and in the latter the dominant structure was sample dependent. The source of magnetic isomerism in SMMs originates either in partial alignment of Jahn-Teller axes perpendicular to the magnetic easy-axes (known as Jahn-Teller isomerism) or in partial compression of the Jahn-Teller distortion.

Conventional attempts to alter the magnetic properties of SMMs such as $Mn_{12}OAc$ have focussed on structural modification through synthetic variations of solvent, ligands, oxidation state, and transition metal. A wide array of SMMs has therefore been reported in the literature with different ground spin states, magnetic anisotropies, blocking temperatures, and quantum tunnelling rates (Aromí & Brechin, 2006). Recently however there has been increased interest in the utilization of pressure as a method for probing the structure-property relationship in $Mn_{12}OAc$. These developments have been driven by growing recognition of the efficiency of pressure for inducing structural changes, as well as the advances made in making high-pressure methodologies less technically challenging and consequently more widespread (Boldyreva, 2008, Katrusiak, 2008, Moggach *et al.*, 2008). Transition metal coordination bonds in particular have been demonstrated to be relatively susceptible to pressure (e.g. Jahn-Teller isomerism and polymerization in $CuF_2(H_2O)_2(pyz)$ antiferromagnet) (Allan *et al.*, 2006, Moggach *et al.*, 2009, Moggach & Parsons, 2009, Prescimone *et al.*, 2012), a phenomenon which has been exploited in a wide variety of studies investigating other physical properties such as colour (Galloway *et al.*, 2010, Byrne *et al.*, 2012), porosity (Graham *et al.*, 2011, Graham *et al.*, 2012), and spin state (Granier *et al.*, 1993, Guetlich *et al.*, 2007).

There have been several studies reported in the literature detailing the effect of pressure on the structure or magnetic properties of $Mn_{12}OAc$ and its derivatives. The orientation of Mn^{III} Jahn-Teller axes was found to be pressure dependent in a high-pressure $Mn_{12}OAc^tBu$ structural study (Parois *et al.*, 2010), where the fast-relaxing isomer was reversibly converted to the slow-relaxing isomer through realignment of the misaligned Jahn-Teller axis, a structural transformation that was also verified through high-pressure magnetic data. Conversely a high-pressure magnetic investigation on $Mn_{12}OAcPh$ observed partial conversion from slow-relaxing to fast-relaxing isomers, and was rationalized as a consequence of Jahn-Teller compression of one Mn^{III} centre (Awaga *et al.*, 2006). A similar response to pressure was also observed in a high-pressure inelastic neutron scattering study of $Mn_{12}OAc$ (Sieber *et al.*, 2005), as revealed through similar reductions in magnetic relaxation activation energy (Δ_{rel}) and anisotropy barrier (Δ), and which also calculated that the magnetic anisotropy of both SR1 and FR1 species increased in response to pressure. Quantum tunnelling rates were also found to decrease substantially in another high-pressure magnetic study of $Mn_{12}OAc$, and which coincided with a reduction in magnetic hysteresis width and overall magnetic anisotropy (Levchenko *et al.*, 2004). Previously unpublished high-pressure AC-susceptibility data collected by Pascal Parois (University of Glasgow) also suggests the presence of a second slow-relaxing species (SR2) of $Mn_{12}OAc$ at 1.5 GPa, which is obscured with overlapping SR1 magnetic saturation in the AC field (Figure 4.4). No high-pressure structural studies have been conducted on $Mn_{12}OAc$ to date.

Figure 4.4: Unpublished AC-susceptibility data highlighting the overlapping contributions of two slow-relaxing magnetic species at 1.5 GPa (collected by Pascal Parois)

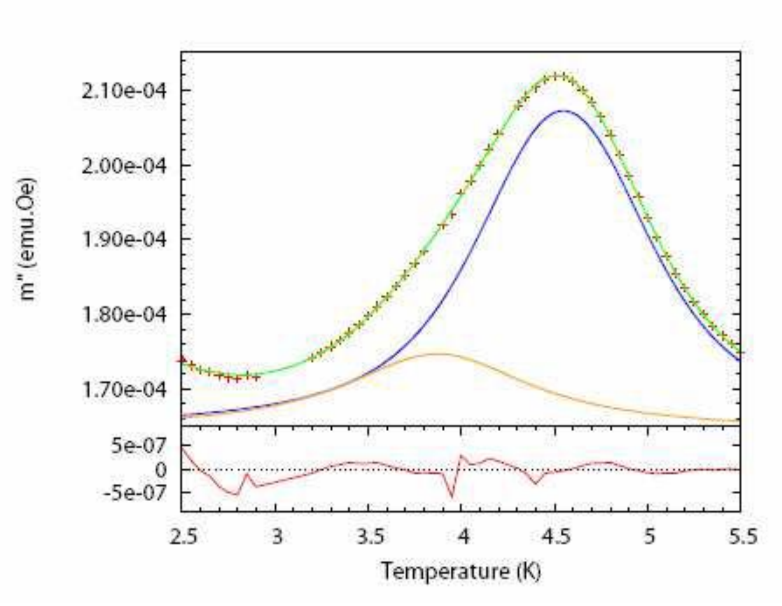

One of the major problems associated with probing the magneto-structural relationship in SMMs is the low-temperature conditions required for magnetic properties to arise. High-pressure single-crystal X-ray techniques are not optimized for low-temperature conditions as the size and composition of typical Diamond Anvil Cells (DACs) produces long and erratic cooling times. A compromise is made whereby high-pressure low-temperature magnetic measurements are compared with high-pressure ambient-temperature structural data. Naturally this is an undesirable situation as the application of low-temperature conditions could induce significant changes in the structure of SMMs (Cornia, Fabretti, *et al.*, 2002) (Farrell *et al.*, 2013), thereby compromising the validity of conclusions drawn in comparisons between experimental data sets. The application of low-temperature conditions would also provide meaningful benefits to the accuracy and quality of data collected at high-pressure conditions (Goeta & Howard, 2004).

We therefore report the first high-pressure low-temperature single-crystal X-ray diffraction study of $Mn_{12}OAc$, with the aim of improving our understanding of the structural and magnetic phenomena previously reported, particularly with regards to the high-pressure AC-susceptibility data collected by Pascal Parois. To facilitate these experiments a novel DAC has been designed by Somchai Tankarakorn at the University of Edinburgh (Figure 4.5). The mode of operation for this cell is analogous to that of a typical Merrill-Bassett DAC, with pressure being generated through the turning of screws which force two diamond culets closer together. The cell is significantly smaller than a conventional DAC and constructed from a beryllium-copper alloy (BERYLCO25), and thus the cell is capable of reaching temperature equilibration much more quickly and in a closed-flow cryostat. A hole was drilled in each side of the cell to allow it to be screwed into the accompanying beryllium-copper table in any desired orientation, and another rectangular slot on one side allows for the insertion of a thermocouple device for measuring temperature *in-situ*. The cell has been named the micro-Merrill-Bassett cell to distinguish it from its larger Merrill-Bassett equivalents.

Figure 4.5: Micro-cell (left) sitting next to a typical Merrill-Bassett cell (right)

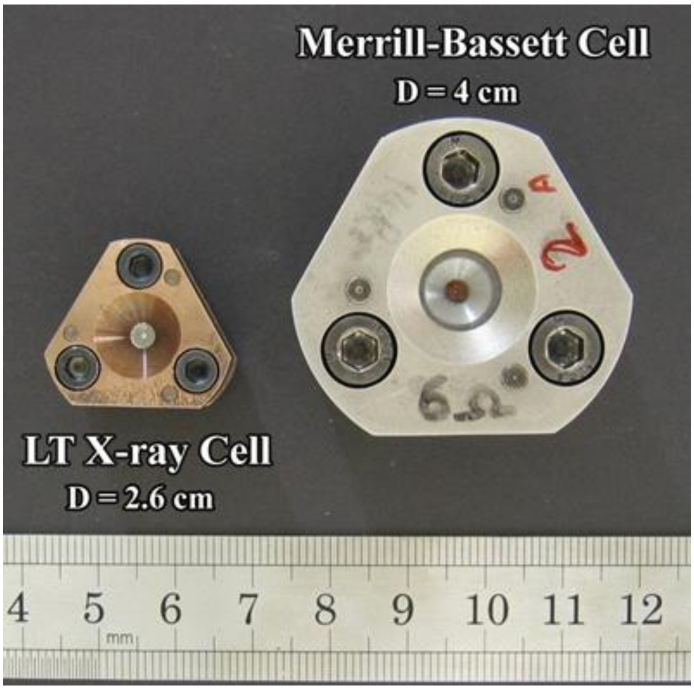

4.2 Experimental

4.2.1 Sample Preparation

$Mn_{12}OAc$ was synthesized by Andrew Farrell at the University of Glasgow and crystallized following the literature method (Lis, 1980).

4.2.2 Apparatus

The high pressure studies utilized the micro-Merrill-Bassett DAC, constructed from a beryllium-copper alloy (BERYLCO25) with an opening angle of 40°, 1000 µm culet BOEHLER-ALMAX diamonds, and tungsten gasket. One diamond was supported by a backing disc while the other diamond was supported directly on one of the platens forming the cell body. A table for mounting the cell on the goniometer head was also constructed from the same beryllium-copper alloy as the cell body. Paraffin was used as the hydrostatic medium.

High-pressure low-temperature single crystal X-ray diffraction measurements were carried-out at Diamond Light Source on beamline I19-EH2 using a wavelength of 0.48590 Å and a four-circle Newport diffractometer equipped with an Agilent Atlas CCD detector. The ultra-low-temperature conditions (6.5 K) were provided by an ARS pneumatic drive closed cycle CSW-202SK cryocooler equipped with an ARS-4HW Helium compressor. The shrouds for the closed-cycle cryostat consisted of a copper radiation shield with a transparent transmission window and a steel vacuum shield with transparent Mylar windows (Figure 4.6). A data collection strategy was designed accounting for the spatial limitations of the cryostat, pressure cell, and goniometer (Table 4.1). The pressure inside the gasket hole was measured using the ruby fluorescence method (Piermarini *et al.*, 1975) at ambient temperature between data sets.

Ambient pressure experiments were conducted at the University of Edinburgh using Mo-Kα radiation with a three-circle Bruker APEX diffractometer equipped with an Oxford Cryosystems Cryostream Plus (Cosier & Glazer, 1986) low-temperature device.

Figure 4.6: Micro cell mounted on goniometer with steel shrouds on I19-EH2

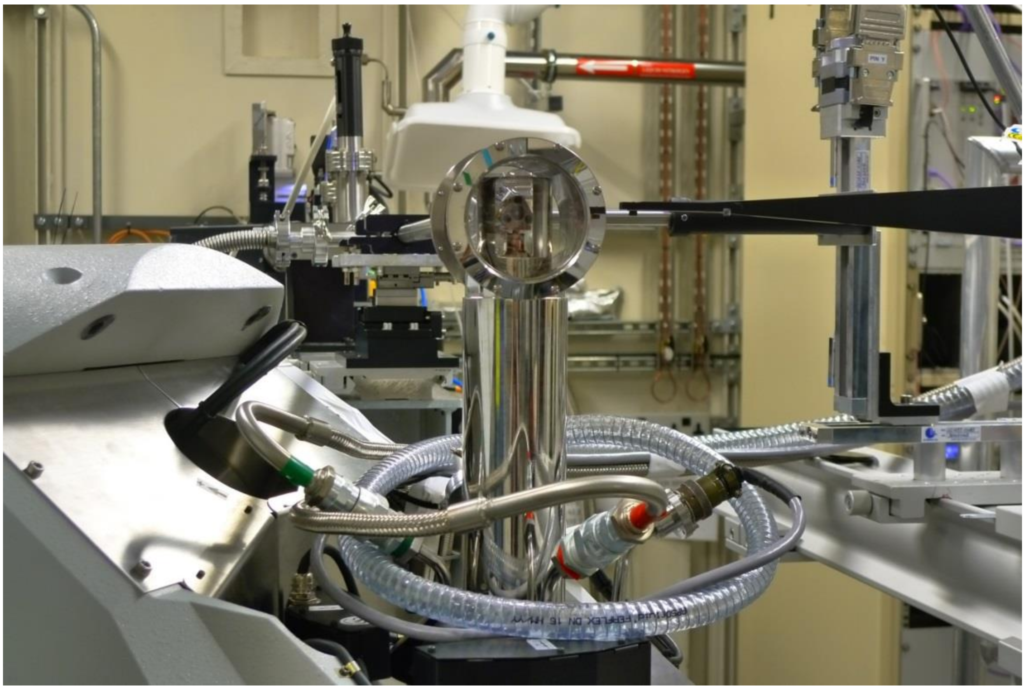

Table 4.1: Data collection strategy for experiment

#	Type	Start ω	End ω	2θ	κ	Start φ	End φ
1	ω	-63	0	20	-135	-32.8	-32.8
2	ω	-63	-32	-10	-135	-32.8	-32.8
3	θ	-33	-33	20	-135	-72.8	12.2
4	θ	-33	-33	-8	-135	-72.8	12.2
5	ω	-96	-35	20	-70	-66	-66
6	ω	-96	-65	-10	-70	-66	-66
7	ω	-145	-90	-20	70	-114	-114
8	ω	-115	-74	10	70	-114	-114
9	ω	-130	-50	20	0	-90	-90
10	ω	-130	-50	-20	0	-90	-90

Detector distance = 110 mm; Width = 0.5°; Attenuators = 3.75 mm Al

4.2.3 Data Processing

Cell indexing, integration, and dynamic mask generation for synchrotron data were carried out using the CrysAlisPro software (Agilent, 2012). The powder rings from the tungsten gasket were masked to remove their contribution to the diffraction data. Frame backgrounds were modelled using the “Smart” algorithm to account for the varying impact of the gasket hole and shrouds on X-ray transmission. Low-resolution sample reflections causing detector overload were integrated with an intensity overload modelling function available in CrysAlisPro. A large number of frames principally at the peripheries of data runs were characterized by high frame R_{int} statistics and therefore found unsuitable for integration. These frames were identified and systematically removed although inter-frame R_{int} correlation necessitated an iterative approach to integration. Overloading diamond reflections were omitted in a similar process. Finally the remaining frames with an R_{int} > than 19 % were removed post-integration to eliminate any remaining poorly modelled reflections. Cell indexing and integration of the ambient-pressure data-sets were carried out using the Bruker APEX II (Bruker, 2001) software, with absorption corrections performed by SADABS (Sheldrick, 2008)

Merging and refinement of the data was performed using CRYSTALS (Betteridge *et al.*, 2003). All structures were refined against $|F|$ with reflections with $|F| < 4\sigma(|F|)$ omitted. Distance, angle, and thermal similarity restraints were derived from previous ambient-pressure least-squares refinements at 150 K and applied to the positions of non-metal atoms. Only Mn and O atoms in the Mn_{12} cluster were refined anisotropically at higher pressures in response to the decline in data available for refinement. The Jahn-Teller disordered O15/O16 atoms were assigned occupancies of 40 %/60 % at 0.15 GPa and 30 %/70 % at 0.00 GPa as these were found to produce the lowest $R1$ factors and approximately equivalent thermal parameters. However both O15 and O16 were refined isotropically at these pressures to minimize potential errors arising from partial occupancy determinations in high-pressure data sets. Since the O15 atoms and acetic acid molecules are co-existent the occupancies for these two moieties were kept equivalent. Atomic scattering factors for the synchrotron data were calculated using FPRIME (Kissel & Pratt, 1990). Crystal data and refinement statistics are recorded in Table 4.3.

Table 4.3: Crystal data (AF = ambient pressure 2 K data collected by Farrell et al. included for reference)

Pressure (GPa)	0.00 (AF)	0.15	0.87
T_{Cryo}	2	6.5	6.5
T_{Thermo}	N/A	44	56
λ (Å)	0.71073	0.4859	0.4859
$\sin\theta/\lambda$ (Å)	0.72	0.71	0.65
Crystal System	Tetragonal	Tetragonal	Tetragonal
Space Group	$I\bar{4}$	$I\bar{4}$	$I\bar{4}$
a (Å)	17.1875(2)	17.1640(3)	16.9284(3)
c (Å)	12.1717(2)	12.2854(3)	12.0001(5)
V (Å^3)	3595.64(8)	3619.31(13)	3438.88(17)
Z	2	2	2
D_{calc} (Mg m^{-3})	1.903	1.883	1.873
Reflections	24483	11586	7448
Unique Reflections	4861	3344	2167
R_{int}	0.0287	0.074	0.072
R	0.0366	0.0491	0.0577
R_w	0.0907	0.0550	0.0670
GooF	1.077	1.0039	1.1321
Data:Parameters	4861:231	2875:262	1759:227
Flack Parameter	0.546(19)	0.19(9)	0.65(10)
No. Restraints	92	360	328
ρ_{max}/ρ_{min} (e.Å^{-3})	0.826/-0.674	0.87/-0.70	0.65/-0.58

Table 4.3 continued: Crystal data (AF = ambient pressure 2 K data collected by Farrell et al. included for reference)

Pressure (GPa)	1.40	2.02	0.00
T_{Cryo}	6.5	6.5	300
T_{Thermo}	48	61	N/A
λ (Å)	0.4859	0.4859	0.7107
$\sin\theta/\lambda$ (Å)	0.57	0.52	0.60
Crystal System	Tetragonal	Tetragonal	Tetragonal
Space Group	$I\bar{4}$	$I\bar{4}$	$I\bar{4}$
a (Å)	16.7570(5)	16.6058(8)	17.126(10)
c (Å)	11.8810(7)	11.7950(14)	12.207(8)
V (Å^3)	3336.1(2)	3252.5(4)	3580(4)
Z	2	2	2
D_{calc} (Mg m^{-3})	1.931	1.981	1.903
Reflections	5804	4142	9163
Unique Reflections	1573	1105	2956
R_{int}	0.073	0.069	0.060
R	0.0650	0.0641	0.0415
R_w	0.0772	0.0742	0.0438
GooF	1.1550	1.1908	1.0474
Data:Parameters	1172:177	806:177	2336:262
Flack Parameter	0.50(16)	0.67(19)	0.26(5)
No. Restraints	208	208	360
ρ_{max}/ρ_{min} (e.Å^{-3})	0.79/-0.48	0.80/-0.49	0.62/-0.68

4.2.4 Data Analysis

Analysis of the bonding interactions was conducted using the program PLATON (Spek, 2003) while MERCURY (Macrae *et al.*, 2006) and DIAMOND (Brandenburg, 1999) were utilized for visualization. Calculation of interstitial and solvent accessible voids (Barbour, 2006) was carried-out with the contact surface and solvent accessible voids algorithms in MERCURY, using a probe radius of 0.5 Å and a grid spacing of 0.1 Å. Interstitial voids and solvent accessible voids are defined as the volume occupied by the spherical probe and solely by the centre of the probe respectively. The alignment of Jahn-Teller axes alignment with the crystallographic **c** axis was similarly determined in MERCURY.

4.3 Results

4.3.1 General comments

The crystal structure of $Mn_{12}OAc$ has been determined at a cryostat temperature of 6.5 K up to 2.02 GPa, by which point the crystal quality had declined substantially. Upon subsequently decreasing the pressure to 0.00 GPa the observed splitting of diffraction peaks suggested that the crystal had separated into two or more crystallites, which was later verified by visual inspection. After leaving the crystal in the cell for a fortnight at ambient conditions the largest crystal remaining was mounted on a fibre and the crystal structure determined at a cryostat temperature of 300 K and 0.00 GPa.

The sample remained in space group $I\bar{4}$ at all temperatures and pressures (Table 4.3). Compression of the crystal produces a linear reduction in the $a = b$ axis of 17.1640(3) Å^3 to 16.6058(8) Å^3 and c axis of 12.2854(3) to 11.7950(14) from 0.15 GPa to 2.02 GPa, corresponding to reductions of 3.25 % and 3.99 % respectively. Relaxation of the applied pressure to 0.00 GPa results in an increase of these parameters, with an $a = b$ axis of 17.126(1) Å^3 and c axis of 12.207(8) Å^3.

4.3.2 Response of the acetic acid and water of crystallization to pressure

Throughout the pressure study the void structure is distributed principally between the crystallized acetic acid, water solvent, and Mn_{12} clusters. Fourier maps showed that between 0.15 GPa and 0.87 GPa the acetic acid molecules are expelled from the crystal structure, leading to an increase in the interstitial and solvent accessible voids (Table 4.4 and Figure 4.7). By contrast the water solvent molecules remain in the crystal structure throughout the pressure study. The interstitial void volume increases from 683.38 Å^3 at 0.15 GPa to 849.86 Å^3 at 0.87 GPa followed by a linear decrease to 687.45 Å^3 at 2.02 GPa, corresponding to 18.9 %, 24.7 %, and 21.1% of the unit cell volume respectively.

Figure 4.7: Solvent accessible voids at 0.15 GPa (top) and 2.02 GPa (bottom) viewed along **c**. Colour scheme: solvent accessible voids yellow, Mn12 cluster red, crystallized acetic acid blue, and crystallized water purple.

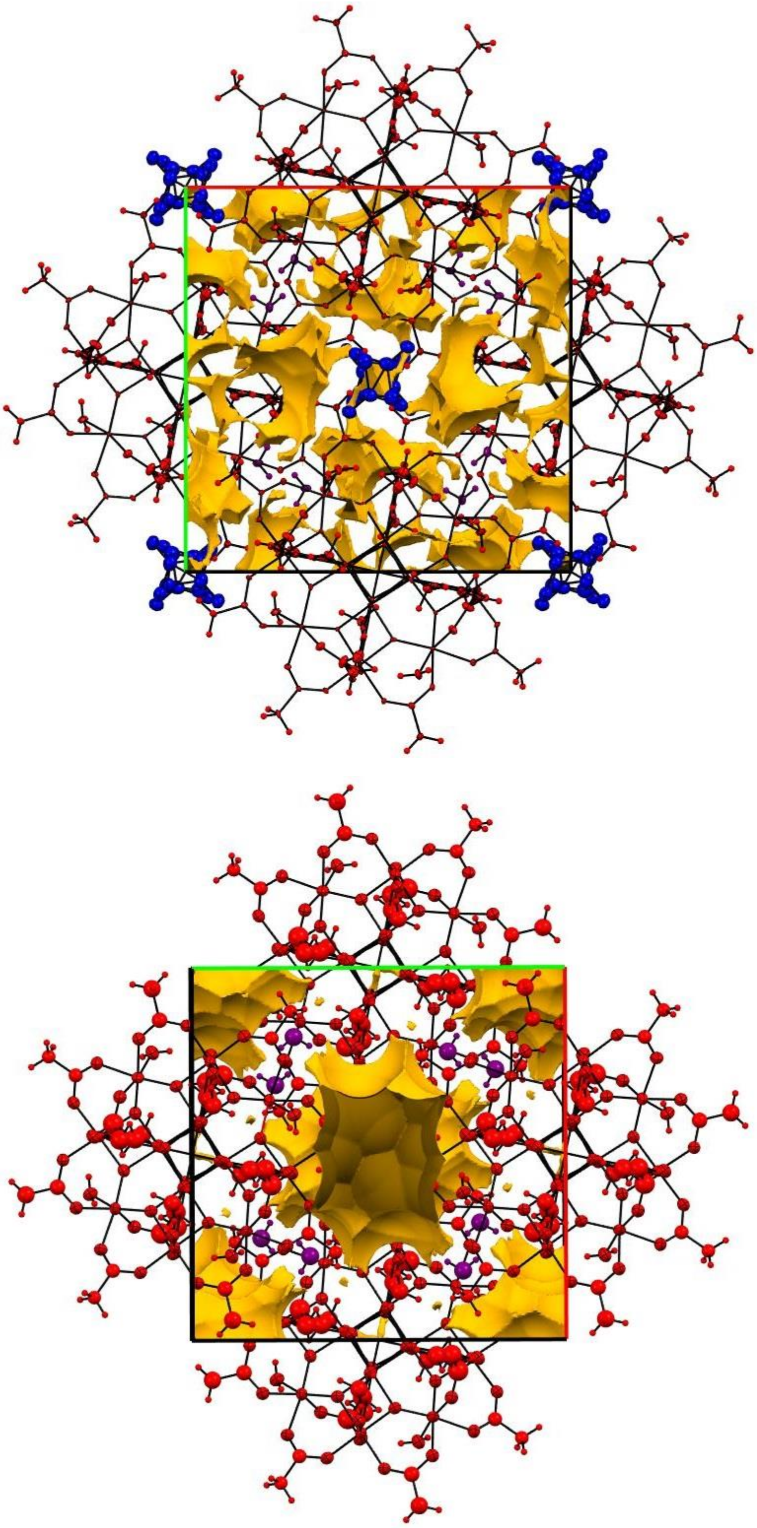

Solvent accessible void volumes exhibit a similar trend, with a void volume of 131.54 Å^3 at 0.15 GPa increasing to 364.03 Å^3 at 0.87 GPa, before undergoing a general reduction to 323.15 Å^3 at 2.02 GPa, accounting respectively for 3.6 %, 10.6 %, and 9.9 % of the unit cell volume. Relaxation of pressure to 0.00 GPa causes the acetic acid to return to its original position with reduced occupancy, with the crystal structure containing an interstitial void volume of 652.25 Å^3 and a solvent accessible void volume of 118.31 Å^3 (18.2 and 3.3 % of unit cell volume respectively).

Table 4.4: Void and cell volumes as a function of pressure

Pressure (GPa)	0.15	0.87	1.40	2.02	0.00
Unit Cell Volume (Å^3)	3619.31	3438.88	3336.1	3252.5	3580
Interstitial Void Volume (Å^3)	683.38	849.86	759.99	687.45	652.25
Interstitial Volume/Cell Volume (%)	18.9	24.7	22.8	21.1	18.2
Solvent Accessible Volume (Å^3)	131.54	364.03	341.38	323.15	118.31
Solvent Volume/Cell Volume (%)	3.6	10.6	10.2	9.9	3.3

4.3.3 Response of the Mn_{12} coordination environment to pressure

The Mn_{12} cluster contains three independent Mn atoms arising from the molecular $\bar{4}$ point symmetry of the complex. The naming scheme and substructure of $Mn_{12}OAc$ is displayed in Figure 4.8. Mn1 resides in the Mn^{IV} cubane core of the molecule whilst Mn2 and Mn3 are situated on the surrounding acetate and oxide-bridged Jahn-Teller distorted Mn^{III} ring. Each of these Mn centres possesses pseudo-octahedral geometry and has six unique coordination bonds, although one of these is disordered over two positions (Mn2-O15/Mn2-O16) with partial occupancies of 40%/60% at 0.15 GPa respectively (discussed below). Mn1 contains three μ_3 oxide bridges to symmetry equivalent Mn1 atoms in the cubane core and two μ_3 oxide bridges to the Jahn-Teller distorted Mn2 and Mn3 centres, whilst both Mn2 and Mn3 similarly possess two μ_3 oxide bridges back to Mn1. The remaining Mn2 and Mn3 coordination sites are occupied by acetate interactions bridging these metal centres, although in the case of Mn3 one of these sites is instead coordinated by a terminal water ligand. Table 4.5 details the response of the Mn_{12} coordination bonds to pressure, and Figure 4.9 displays the trends in bond length of selected Mn-O interactions discussed below.

Figure 4.8: Sub-structure of Mn12 cluster at 0.15 GPa (top) and 0.87 GPa (bottom) showing Mn coordination environment numbering. Hydrogen atoms and crystallized solvents have been removed for clarity. Thermal ellipsoids enclose 50% probability surfaces.

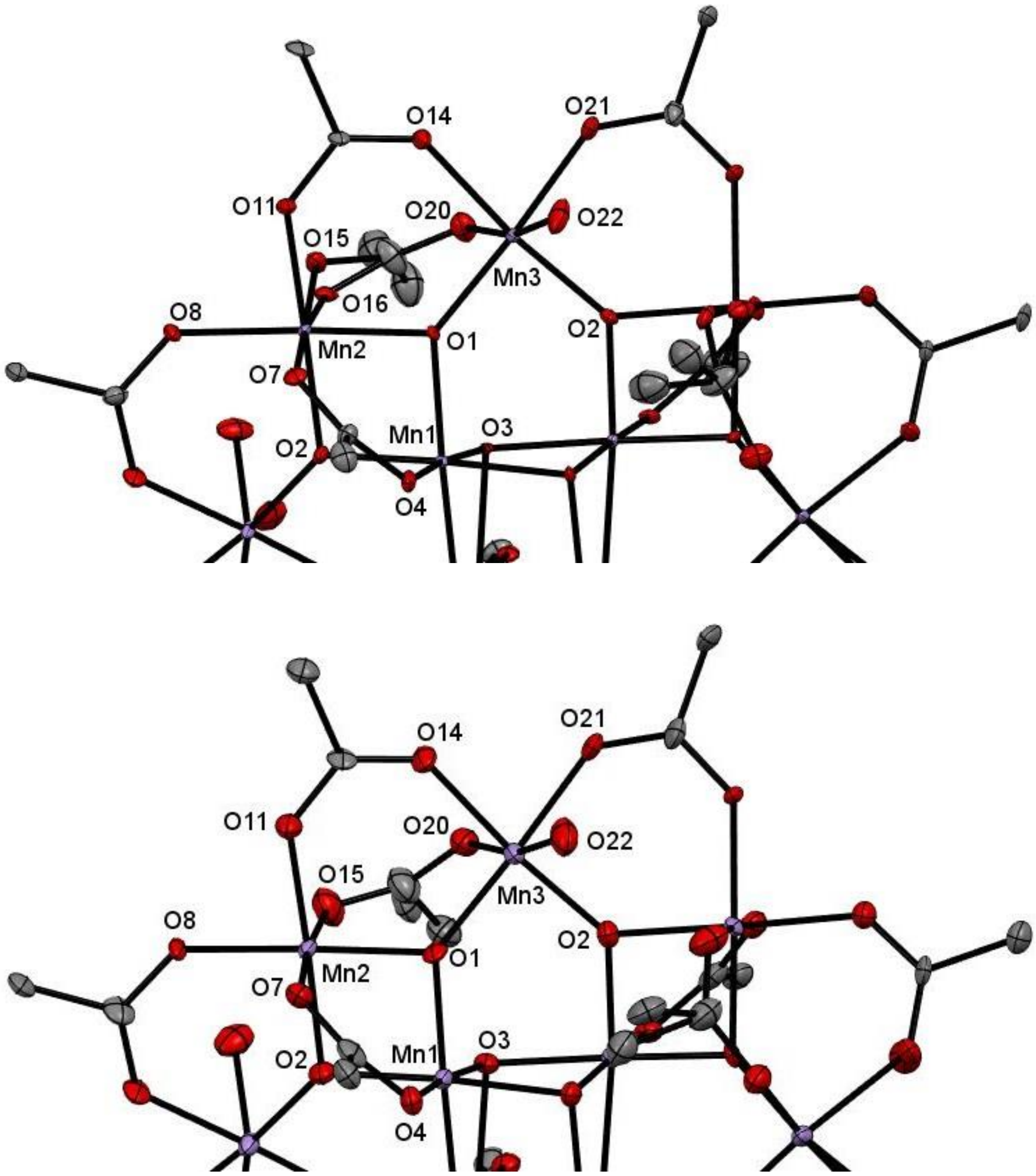

Table 4.5: Intramolecular Mn-O bond lengths (Å) *versus* pressure (AF = ambient pressure 2 K data (Farrell *et al.*, 2013) included for reference)

Pressure (GPa)	0.00 (AF)	0.15	0.87
Mn^{IV} cubane core			
Mn1-Mn2/Mn3 oxide bridges			
Mn1-O1	1.8746(19)	1.874(5)	1.868(7)
Mn1-O2	1.8586(19)	1.865(5)	1.870(7)
Mn1-Mn1 oxide bridges			
Mn1-O3	1.9186(19)	1.916(5)	1.905(5)
Mn1-O3^{i}	1.9153(19)	1.927(5)	1.929(5)
Mn1-O3^{ii}	1.901(3)	1.910(5)	1.911(6)
Mn1-Mn2 acetate bridge			
Mn1-O4	1.916(3)	1.916(5)	1.924(5)
Mn^{III} ring			
Mn2-Mn1 oxide bridges			
Mn2-O1	1.889(2)	1.898(5)	1.898(7)
Mn2-O2	1.8875(19)	1.886(5)	1.889(7)
Mn2-Mn1 acetate bridge			
Mn2-O7	2.224(2)	2.237(5)	2.200(6)
Mn2-Mn3 acetate bridges			
Mn2-O8	1.937(2)	1.947(5)	1.929(5)
Mn2-O11	1.938(2)	1.937(6)	1.924(6)
Mn2-O15	2.126(6)	2.167(11)	2.209(6)
Mn2-O16	2.248(5)	2.227(9)	-
Mn3-Mn1 oxide bridges			
Mn3-O1	1.889(2)	1.902(5)	1.918(7)
Mn3-O2^{ii}	1.894(2)	1.899(5)	1.891(7)
Mn3-Mn2 acetate bridges			
Mn3-O14	1.967(3)	1.989(7)	1.995(7)
Mn3-O20	2.126(6)	2.135(6)	2.119(6)
Mn3-O21^{ii}	1.979(3)	1.976(7)	1.987(7)
Mn3-O22	2.159(3)	2.182(7)	2.175(8)

Symmetry operations: (i) 1-x,-y,z; (ii) 1/2-y,-1/2+x,1/2-z

Table 4.5 continued: Intramolecular Mn-O bond lengths (Å) *versus* pressure (AF = ambient pressure 2 K data (Farrell *et al.*, 2013) included for reference)

Pressure (GPa)	1.40	2.02	% change	0.00
Mn^{IV} cubane core				
Mn1-Mn2/Mn3 oxide bridges				
Mn1-O1	1.887(10)	1.889(15)	0.80	1.878(7)
Mn1-O2	1.876(10)	1.912(14)	2.52	1.865(7)
Mn1-Mn1 oxide bridges				
Mn1-O3	1.933(9)	1.911(14)	-0.21	1.908(6)
Mn1-O3^{i}	1.938(10)	1.944(14)	0.88	1.918(6)
Mn1-O3^{ii}	1.915(10)	1.916(15)	0.31	1.890(8)
Mn1-Mn2 acetate bridge				
Mn1-O4	1.925(9)	1.921(13)	0.26	1.918(6)
Mn^{III} ring				
Mn2-Mn1 oxide bridges				
Mn2-O1	1.926(10)	1.926(14)	1.48	1.895(7)
Mn2-O2	1.889(10)	1.884(14)	-0.11	1.883(7)
Mn2-Mn1 acetate bridge				
Mn2-O7	2.210(9)	2.243(12)	0.27	2.229(7)
Mn2-Mn3 acetate bridges				
Mn2-O8	1.938(9)	1.915(12)	-1.64	1.933(7)
Mn2-O11	1.940(9)	1.904(12)	-1.70	1.938(7)
Mn2-O15	2.211(9)	2.250(12)	3.83	2.187(15)
Mn2-O16	-	-	-	2.210(9)
Mn3-Mn1 oxide bridges				
Mn3-O1	1.887(10)	1.896(15)	-0.32	1.894(7)
Mn3-O2^{ii}	1.874(10)	1.844(14)	-2.90	1.885(7)
Mn3-Mn2 acetate bridges				
Mn3-O14	1.999(9)	2.027(12)	1.91	1.976(7)
Mn3-O20	2.106(10)	2.094(13)	-1.92	2.135(7)
Mn3-O21^{ii}	2.001(9)	2.010(13)	1.72	1.965(7)
Mn3-O22	2.158(11)	2.103(14)	-3.62	2.171(7)

Symmetry operations: (i) 1-x,-y,z; (ii) 1/2-y,-1/2+x,1/2-z

The μ_3-oxide bridges Mn1-O2 and Mn3-O2^{ii} undergo varied responses to compression throughout the pressure study, with Mn1-O2 increasing continually from 1.865(5) Å at 0.15 GPa to 1.912(14) Å at 2.02 GPa, whilst Mn3-O2^{ii} contracts from 1.899(5) – 1.844(14) Å over the same pressure range. Diverging behaviour in response to pressure is similarly observed in several of the Jahn-Teller Mn-acetate bonds. At 0.15 GPa the bond distances for the Mn2-O15 and Mn2-O16 interactions are 2.167(11) Å and 2.227(9) Å respectively, with 40% occupancy for O15 and 60% occupancy for O16. Upon increasing the pressure to 0.87 GPa the Jahn-Teller disorder disappears as the acetic acid solvent is expelled, leaving one oxygen atom O15 with full occupancy and a Mn2-O15 distance of 2.209(6) Å. Continued application of pressure to 2.02 GPa causes this interaction to start expanding to 2.250(12) Å at 2.02 GPa. Similarly unusual behaviour is displayed by Mn2-O7, which initially decreases from 2.237(5) Å to 2.200(6) Å between 0.15 GPa and 0.87 GPa, before subsequently increasing in length to 2.243(12) Å at 2.02 GPa. Mn3-O22 meanwhile exhibits a substantial and continual decrease in length from 2.182(7) Å at 0.15 GPa to 2.103(14) Å at 2.02 GPa. None of the remaining μ_3-oxide bridges and Jahn-Teller bonds experiences any significant change in response to pressure, though data precision is much lower at high-pressure conditions.

Relaxation of pressure to ambient conditions causes all of these interactions to return approximately to their original values. Additionally the Mn-O disorder associated with the Mn2 centre reappears at 0.00 GPa, with O15 and O16 obtaining occupancies of 30% and 70% respectively. This structural behaviour coincides with the previously noted re-inclusion of the acetic acid solvent in the crystal structure at 30% occupancy upon return to ambient pressure.

4.3.4 Response of Mn_{12} Jahn-Teller axis alignment to pressure

The angles between the Jahn-Teller distorted axes of the Mn^{III} centres (Mn2 and Mn3) and the crystallographic **c** axis (tilt angle) have been presented in Table 4.6 and Figure 4.10. At 0.15 GPa the two partially occupied Jahn-Teller axes O15-Mn2-O7 and O16-Mn2-O7 have tilt angles of 15.6(2)° and 10.1(1)° respectively. Increasing the pressure to 0.87 GPa eliminates the Mn2 Jahn-Teller bond disorder and causes these two axes to merge and form a new Jahn-Teller axis with a tilt angle of 10.2(1)°.

Conversely the application of pressure causes the Jahn-Teller axis O20-Mn3-O22 to increase from 35.8(1)° to 36.4(1)° between 0.15 GPa. Relaxation of pressure to 0.00 GPa causes these Jahn-Teller axes to revert approximately to their previous tilt angles at 0.15 GPa, with angles of 35.7(1)°, 15.8(2)°, and 10.3(1)° for O20-Mn3-O22, O15-Mn2-O7, and O16-Mn2-O7 respectively.

Figure 4.9: Statistically significant changes in Mn-O bond lengths *versus* pressure

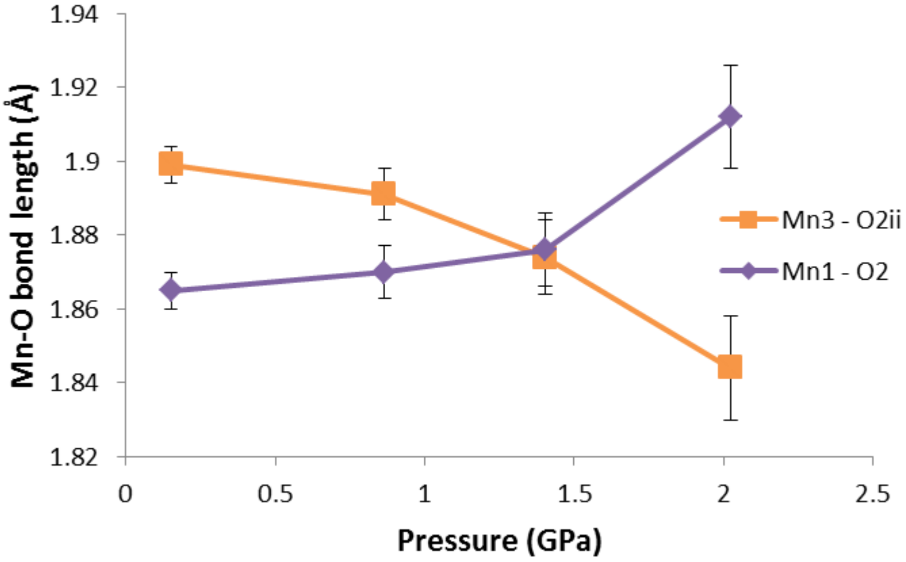

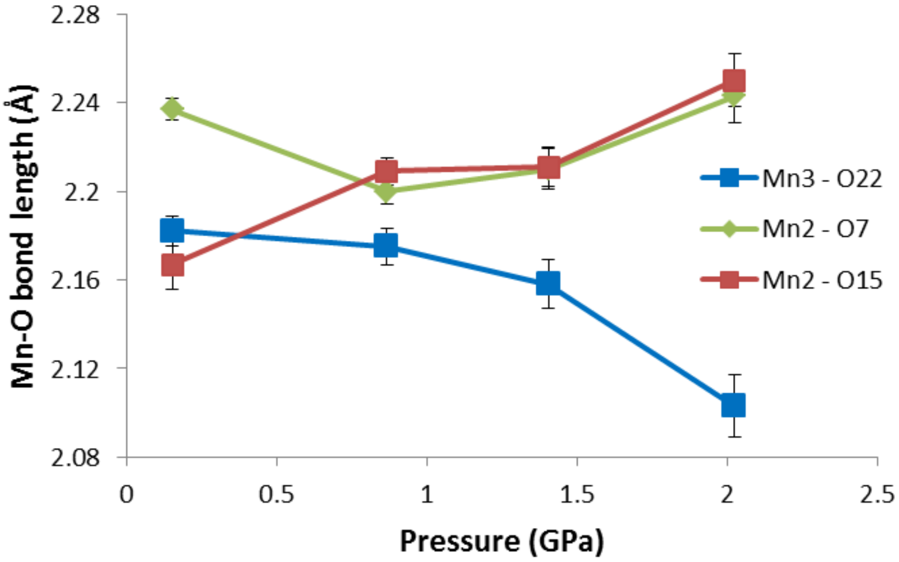

Table 4.6: Jahn-Teller axes alignment (°) with respect to crystallographic **c** axis (AF = ambient pressure 2 K data (Farrell *et al.*, 2013) included for reference)

Pressure (GPa)	1.40	2.02	% change	0.00
<O20-Mn3-O22	36.2(2)	36.0(2)	0.55	35.7(1)
<O15-Mn2-O7	10.3(1)	10.4(2)	-33.33	15.8(2)
<O16-Mn2-O7	-	-	-	10.3(1)

Table 4.6 continued: Jahn-Teller axes alignment (°) with respect to crystallographic **c** axis (AF = ambient pressure 2 K data (Farrell *et al.*, 2013) included for reference)

Pressure (GPa)	0.00 (AF)	0.15	0.87	% change
<O20-Mn3-O22	35.52(8)	35.8(1)	36.4(1)	1.68
<O15-Mn2-O7	15.35(8)	15.6(2)	10.2(1)	-34.62
<O16-Mn2-O7	9.73(7)	10.1(1)	-	-

Figure 6.10: Jahn Teller axis alignment at 0.15 GPa (green) and 0.87 GPa (red)

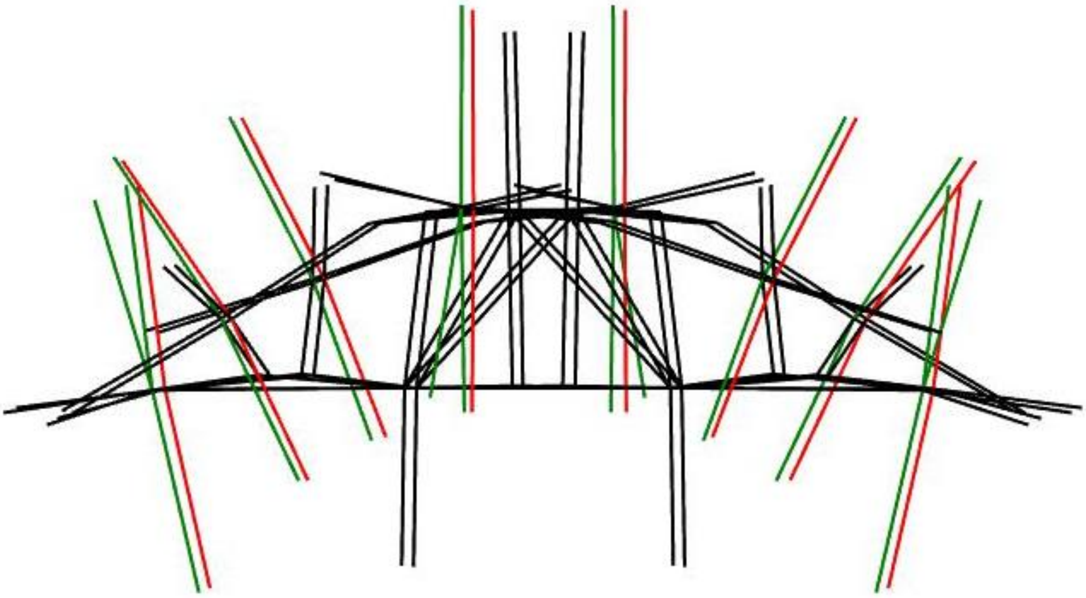

4.4 Discussion

4.4.1 Methodology

This experiment represents the first high-pressure low-temperature single-crystal X-ray study on EH2-I19 using the described setup, and as such attention has to be paid towards potential future improvements and technical difficulties. Overall the experimental time from centring through to removing the cell takes approximately 6 hours with a cryostat temperature of 6.5 K, equilibration period of 20 minutes, and an exposure time of 1.5 s. When combined with auxiliary time sinks such as pressure equilibration and measurement, post collection data analysis, and miscellaneous technical difficulties, it can be approximated that a maximum of two high-pressure low-temperature data sets can be reasonably obtained per experimental day at EH2-I19 using the current setup.

Since beamtime at EH2-I19 is limited one of the principal avenues of improving these experiments is reducing collection time. The largest segment of experimental time is lost to sample cooling and warming (about 1.5 hours each) which cannot be reduced without changing the cryostat, shrouds, or vacuum pump. X-ray diffraction is the second greatest time sink, with a 1.5 s exposure amounting to 2 hours of diffraction time. Elimination from the collection strategy of diffraction positions which consistently produced no reflections (~20% of total) can reduce this time substantially, and with this in mind a revised collection strategy has been developed and tested on EH2-I19 (Table 4.7). Finally the last major source of lost experimental time arises whenever there is a change in goniometer κ axis. Since the crash detection software does not model the presence of the shrouds and cryostat, the user has to enter the experimental hutch to move the goniometer manually to prevent collisions. An updated crash detection model will reduce experimental time by approximately 1 hour. Implementing the above improvements should reduce experimental time significantly.

The measurement of crystal temperature *in-situ* has thus far proven problematic in this experimental setup. A baseline cryostat temperature of 6.5 K was consistently achieved after allowing for approximately 1.5 hours cooling time. By contrast the thermocouple recorded a range of temperatures from 44 – 61 K after the equilibration period, demonstrating potentially significant differences between the applied cryostat temperatures and the environment of the crystal. The thermocouple did not exhibit large variations in measured temperature within each pressure point (0.05 – 0.1 K), suggesting that temperature differential is both systematic and random in nature. Drilling the thermocouple hole deeper into the cell body is one potential method of reducing the temperature differential, in addition to improving the vacuum shroud to prevent ice formation on the cryostat. Variable contact between the thermocouple and the cell body is the most probable source of recorded temperature variation between pressure points, and can potentially be overcome through the insertion of a thermally conducting material to fill the gaps.

Table 4.7: New data collection strategy for experiment

#	Type	Start ω	End ω	2θ	κ	Start φ	End φ
1	ω	-63	-5	20	-135	-32.8	-32.8
2	ω	-63	-35	-10	-135	-32.8	-32.8
3	θ	-33	-33	20	-135	-67.8	3.8
4	θ	-33	-33	-8	-135	-67.8	3.8
5	ω	-96	-40	20	-70	-66	-66
6	ω	-96	-70	-10	-70	-66	-66
7	ω	-138	-90	-20	70	-114	-114
8	ω	-115	-90	10	70	-114	-114
9	ω	-115	-50	20	0	-90	-90
10	ω	-115	-50	-20	0	-90	-90

Detector distance = 110 mm; Width = 0.5°; Attenuators = 3.75 mm Al

Accurate determination of applied pressure is another significant source of error in these high-pressure low-temperature studies. Ideally the pressure should be recorded *in-situ* at the desired cryostat temperature since the low-temperature conditions are anticipated to alter the applied pressure. However the ruby fluorescence frequently used in high-pressure calibrations is both pressure and temperature dependent. This multi-variable problem can be overcome through measurement of $Sm_{1-x}Sr_xB_4O_7$ (Sm:SBO) fluorescence, which possesses similar pressure sensitivity but much reduced temperature sensitivity compared to ruby fluorescence (Datchi *et al.*, 1997). By using both calibrants simultaneously the pressure can be obtained through fluorescence measurement of Sm:SBO, which can then be inserted into the low-temperature fluorescence equation for ruby (calibrated down to 0 K) (Ragan *et al.*, 1992) to obtain the crystal temperature. This dual-calibrant method therefore offers the additional advantage of providing a temperature calculated directly from observed physical properties, and overcomes all the disadvantages and problems associated with using a thermocouple.

A spectrometer has since become available on EH2-I19 for use in-*situ* high-pressure low-temperature experiments, and both ruby and Sm:SBO spectra have been recorded under ambient conditions (Figure 4.11). Powdered Sm:SBO was synthesized following a modified literature method (Kulshreshtha *et al.*, 2007) with 5%-95% H_2-Ar replacing 5%-95% H_2-N_2. Measurements of the fluorescence spectra under low-temperatures have thus far proven difficult, probably resulting from partial scattering of the laser beam by the Mylar windows. The instrument is undergoing a period of optimization to overcome these issues, principally through enhancement of the focussing optics and maximization of laser power. Once this has been completed a low-temperature calibration of the ruby standard under ambient and high-pressure conditions would be highly desirable, in order to fully explore the suitability of the chosen fluorescence equations for these low-temperature experiments.

Figure 4.11: EH2-I19 fluorescence spectra containing characteristic ruby doublet (right) and Sm:SBO singlet (left)

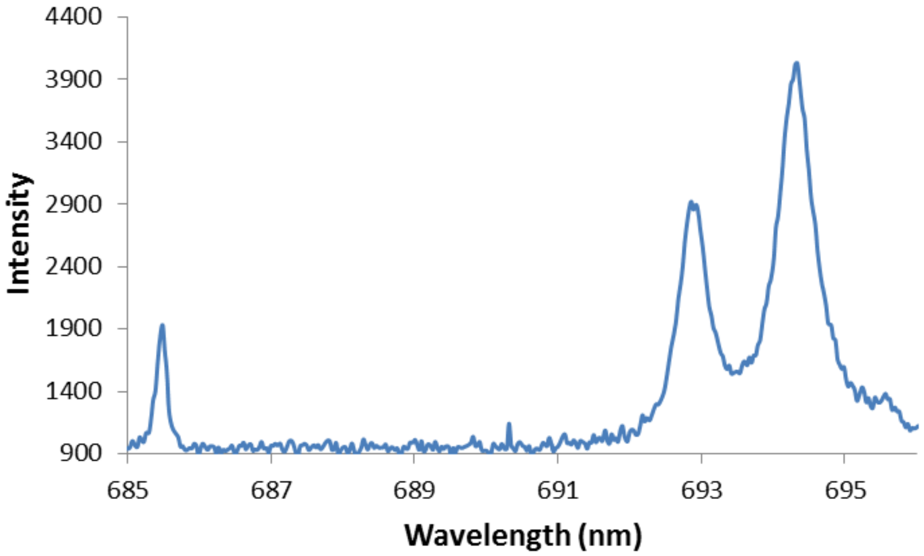

4.4.2 Structural Analysis

The disordered oxygen positions O15/O16 were refined with 40 %/60 % occupancies at 0.15 GPa as this produced better U_{equiv} ratios than a 50:50 ratio (0.015/0.010 versus 0.024/0.002), and with acetic acid occupancies of 40 % resulted in an overall reduction in *R*1 from 0.0500 to 0.0491. One hypothesis for these observations is that the acetic acid has been partially expelled at 0.15 GPa, resulting in more $Mn_{12}OAc$ molecules adopting the Jahn-Teller axis (O7-Mn2-O16) not involved in hydrogen bonding. Another possibility involves crystal desolvation during storage at ambient conditions prior to the experiment, as similar processes have been observed in various SMMs containing other volatile solvent species (Soler *et al.*, 2003, Hill *et al.*, 2005, Redler *et al.*, 2009). Increasing the applied pressure to 0.87 GPa causes the acetic acid to be expelled from the structure, with all attempts at refining their atomic positions and thermal parameters producing significantly higher *R*1 values. A reduction in occupancy to 30 %/70 % upon relaxation of pressure to 0.00 GPa provided improved U_{equiv} ratios (0.028/0.023 versus 0.037/0.015), as well as a decrease in *R*1 from 0.0427 to 0.0415 coupled with a 30 % acetic acid occupancy. Deviations in occupancy values between these data sets may suggest the presence of slow resolvation kinetics, or evaporation of the expelled acetic acid from the cell occurred upon relaxation of applied pressure.

Acetic acid removal thermodynamics are driven by volumetric considerations as solvent accessible voids in the desolvated structure are not large enough to accommodate the acetic acid. Meanwhile the crystallized water molecules are comparatively unaffected by the application of pressure and are observed in the crystal structure at full occupancy at 2.02 GPa, principally resulting from the smaller size of the water molecule. This correlates with previous high-temperature X-ray diffraction data (Farrell *et al.*, 2013) which found that acetic acid molecules could be expelled from the crystal structure before the water molecules, and which was rationalized in the context of relatively strong hydrogen bonding networks provided by the latter. Since high-pressure conditions have the opposite effect to high-temperature conditions of compressing the structure, the relative differences in solvent retention under pressure must also be influenced by the *PV* term of the Gibbs free energy equation and consequently the solvent volume. Compression therefore favours the expulsion of the acetic acid because this provides the crystal structure with a greater ability to reduce volume in response to pressure.

Jahn-Teller distortions for the two Mn^{III} centres display significantly different structural features that substantially affect their contributions to the magnetic properties of $Mn_{12}OAc$. The tilt angle of 35.8(1)° for the O20-Mn3-O22 axis represents a much larger axial misalignment with the magnetic easy axis than the angle of 15.6(2)/10.1(1)° for O15-Mn2-O7/O16-Mn2-O7 respectively. Mn2 also possesses a generally larger magnitude of Jahn-Teller distortion compared with Mn3, with a bond range of 2.167(11) – 2.237(5) Å and 2.135(6) – 2.182(7) Å respectively. Since the magnetic anisotropy is a function of Jahn-Teller distortion magnitude and easy-axis alignment, Mn2 should therefore influence the overall magnetic anisotropy of $Mn_{12}OAc$ substantially more than Mn3.

Expulsion of the acetic acid solvent is responsible for the disappearance of the Mn2 Jahn-Teller axes disorder above 0.15 GPa. The new Jahn-Teller axis possesses a nearly identical tilt angle and similar bond lengths to that exhibited by SR1, suggesting that the magnetic isomer SR2 is entirely converted to SR1 at this pressure. Likewise the same isomeric conversion occurs in the high-temperature desolvated structure (Farrell *et al.*, 2013). Further increasing the pressure to 2.02 GPa increases the length of the Jahn-Teller bonds and decreases the tilt angle, suggesting an increase in magnetic anisotropy for SR1 which was similarly observed in the high-pressure INS study (Sieber *et al.*, 2005). Notably this observation correlates with the previously unpublished AC-susceptibility data by Pascal Parois, which indicated the existence of both SR1 and SR2 isomers and partial conversion from the latter to the former at 1.4 GPa. The discrepancy in pressure required for this behaviour to occur probably originates in the different experimental conditions present during the AC-susceptibility and high-pressure low-temperature diffraction studies. The presence of crystallized acetic acid in the $Mn_{12}OAc$ structure after relaxation of pressure to ambient conditions, combined with the re-emergence of Jahn-Teller disorder on the Mn2 centre, suggests that the conversion is reversible.

By contrast the cubane core and acetate ligands of $Mn_{12}OAc$ are inelastic throughout the pressure series. For the cubane core this likely arises from the strength of the oxide coordination bonds and the more isotropic geometry of Mn1.

Organic bonds meanwhile have been found to be unresponsive to pressure in other high-pressure studies because of their shorter distances and lower polarisabilities.

4.5 Conclusion

The first high-pressure low-temperature single-crystal X-ray diffraction study of $Mn_{12}OAc$ has been conducted at EH2-I19 at a cryostat temperature of 6.5 K and up to 2.02 GPa. Analysis of the crystal structure reveals that solvent-induced Jahn-Teller disorder on one Mn^{III} centre can be directly linked to the observation of two slow-relaxing isomers of $Mn_{12}OAc$. Increasing the applied pressure to 0.87 GPa expels the acetic acid solvent thus resolving the Jahn-Teller disorder and causing complete conversion of one slow-relaxing magnetic species to the other. Resolvation upon relaxation of pressure and analysis of the Jahn-Teller sites indicates that all magnetic species conversion is reversible.

4.6 References

Agilent (2012). *CrysAlis PRO.* Version 171.36.21.

Allan, D. R., Blake, A. J., Huang, D., Prior, T. J. & Schroeder, M. (2006). *Chem. Commun. (Cambridge, U. K.),* 4081-4083.

Aromí, G. & Brechin, E. K. (2006). *Struct. Bonding (Berlin, Ger.)* **122**, 1-67.

Awaga, K., Suzuki, Y., Hachisuka, H. & Takeda, K. (2006). *J. Mater. Chem.* **16**, 2516-2521.

Bagai, R. & Christou, G. (2009). *Chem. Soc. Rev.* **38**, 1011-1026.

Barbour, L. J. (2006). *Chem. Commun. (Cambridge, U. K.),* 1163-1168.

Betteridge, P. W., Carruthers, J. R., Cooper, R. I., Prout, K. & Watkin, D. J. (2003). *J. Appl. Crystallogr.* **36**, 1487.

Boldyreva, E. V. (2008). *Acta Crystallogr., Sect. A: Found. Crystallogr.* **64**, 218-231.

Brandenburg, K. (1999). *DIAMOND.*

Bruker (2001). *Bruker AXS Inc., Madison, Wisconsin, USA.*

Byrne, P. J., Richardson, P. J., Chang, J., Kusmartseva, A. F., Allan, D. R., Jones, A. C., Kamenev, K. V., Tasker, P. A. & Parsons, S. (2012). *Chem. - Eur. J.* **18**, 7738-7748, S7738/7731.

Cavallini, M., Facchini, M., Albonetti, C. & Biscarini, F. (2008). *Phys. Chem. Chem. Phys.* **10**, 784-793.

Christou, G. (2005). *Polyhedron* **24**, 2065-2075.

Christou, G., Gatteschi, D., Hendrickson, D. N. & Sessoli, R. (2000). *MRS Bull.* **25**, 66-71.

Cornia, A., Costantino, A. F., Zobbi, L., Caneschi, A., Gatteschi, D., Mannini, M. & Sessoli, R. (2006). *Struct. Bonding (Berlin, Ger.)* **122**, 133-161.

Cornia, A., Fabretti, A. C., Pacchioni, M., Zobbi, L., Bonacchi, D., Caneschi, A., Gatteschi, D., Biagi, R., Del, P. U., De, R. V., Gurevich, L. & Van, d. Z. H. S. J. (2003). *Angew. Chem., Int. Ed.* **42**, 1645-1648.

Cornia, A., Fabretti, A. C., Sessoli, R., Sorace, L., Gatteschi, D., Barra, A. L., Daiguebonne, C. & Roisnel, T. (2002). *Acta Crystallogr., Sect. C: Cryst. Struct. Commun.* **C58**, m371-m373.

Cornia, A., Sessoli, R., Sorace, L., Gatteschi, D., Barra, A. L. & Daiguebonne, C. (2002). *Phys. Rev. Lett.* **89**, 257201/257201-257201/257204.

Cosier, J. & Glazer, A. M. (1986). *J. Appl. Crystallogr.* **19**, 105-107.

Datchi, F., LeToullec, R. & Loubeyre, P. (1997). *J. Appl. Phys.* **81**, 3333-3339.

Evangelisti, M., Bartolome, J. & Luis, F. (1999). *Solid State Commun.* **112**, 687-691.

Evangelisti, M. & Brechin, E. K. (2010). *Dalton Trans.* **39**, 4672-4676.

Farrell, A. R., Coome, J. A., Probert, M. R., Goeta, A. E., Howard, J. A. K., Lemee-Cailleau, M.-H., Parsons, S. & Murrie, M. (2013). *CrystEngComm* **15**, 3423-3429.

Galloway, K. W., Moggach, S. A., Parois, P., Lennie, A. R., Warren, J. E., Brechin, E. K., Peacock, R. D., Valiente, R., Gonzalez, J., Rodriguez, F., Parsons, S. & Murrie, M. (2010). *CrystEngComm* **12**, 2516-2519.

Gatteschi, D. (2001). *J. Alloys Compd.* **317-318**, 8-12.

Goeta, A. E. & Howard, J. A. K. (2004). *Chem. Soc. Rev.* **33**, 490-500.

Graham, A. J., Allan, D. R., Muszkiewicz, A., Morrison, C. A. & Moggach, S. A. (2011). *Angew. Chem., Int. Ed.* **50**, 11138-11141, S11138/11131-S11138/11137.

Graham, A. J., Tan, J.-C., Allan, D. R. & Moggach, S. A. (2012). *Chem. Commun. (Cambridge, U. K.)* **48**, 1535-1537.

Granier, T., Gallois, B., Gaultier, J., Real, J. A. & Zarembowitch, J. (1993). *Inorg. Chem.* **32**, 5305-5312.

Guetlich, P., Gaspar, A. B., Garcia, Y. & Ksenofontov, V. (2007). *C. R. Chim.* **10**, 21-36.

Hill, S., Anderson, N., Wilson, A., Takahashi, S., Petukhov, K., Chakov, N. E., Murugesu, M., North, J. M., del, B. E., Kent, A. D., Dalal, N. S. & Christou, G. (2005). *Polyhedron* **24**, 2284-2292.

Katrusiak, A. (2008). *Acta Crystallogr., Sect. A: Found. Crystallogr.* **64**, 135-148.

Kim, K., Seo, D. M., Means, J., Meenakshi, V., Teizer, W., Zhao, H. & Dunbar, K. R. (2004). *Appl. Phys. Lett.* **85**, 3872-3874.

Kissel, L. & Pratt, R. H. (1990). *Acta Crystallogr., Sect. A: Found. Crystallogr.* **A46**, 170-175.

Kulshreshtha, C., Cho, S. H., Jung, Y. S. & Sohn, K.-S. (2007). *J. Electrochem. Soc.* **154**, J86-J90.

Langan, P., Robinson, R., Brown, P. J., Argyriou, D., Hendrickson, D. & Christou, G. (2001). *Acta Crystallogr., Sect. C: Cryst. Struct. Commun.* **C57**, 909-910.

Larionova, J., Clerac, R., Boury, B., Le Bideau, J., Lecren, L. & Willemin, S. (2003). *J. Mater. Chem.* **13**, 795-799.

Levchenko, G. G., Zubov, E. E., Varyukhin, V. N., Gaspar, A. B. & Real, J. A. (2004). *J. Phys. Chem. B* **108**, 16664-16669.

Lis, T. (1980). *Acta Crystallogr., Sect. B* **B36**, 2042-2046.

Macrae, C. F., Edgington, P. R., McCabe, P., Pidcock, E., Shields, G. P., Taylor, R., Towler, M. & van, d. S. J. (2006). *J. Appl. Crystallogr.* **39**, 453-457.

Meenakshi, V., Teizer, W., Naugle, D. G., Zhao, H. & Dunbar, K. R. (2004). *Solid State Commun.* **132**, 471-476.

Mertes, K. M., Suzuki, Y., Sarachik, M. P., Paltiel, Y., Shtrikman, H., Zeldov, E., Rumberger, E. M., Hendrickson, D. N. & Christou, G. (2002). *Phys. Rev. B: Condens. Matter Mater. Phys.* **65**, 212401/212401-212401/212404.

Moggach, S. A., Galloway, K. W., Lennie, A. R., Parois, P., Rowantree, N., Brechin, E. K., Warren, J. E., Murrie, M. & Parsons, S. (2009). *CrystEngComm* **11**, 2601-2604.

Moggach, S. A. & Parsons, S. (2009). *Spectrosc. Prop. Inorg. Organomet. Compd.* **40**, 324-354.

Moggach, S. A., Parsons, S. & Wood, P. A. (2008). *Crystallogr. Rev.* **14**, 143-184.

Parois, P., Moggach, S. A., Sanchez-Benitez, J., Kamenev, K. V., Lennie, A. R., Warren, J. E., Brechin, E. K., Parsons, S. & Murrie, M. (2010). *Chem. Commun. (Cambridge, U. K.)* **46**, 1881-1883.

Piermarini, G. J., Block, S., Barnett, J. D. & Forman, R. A. (1975). *J. Appl. Phys.* **46**, 2774-2780.

Prescimone, A., Morien, C., Allan, D., Schlueter, J. A., Tozer, S. W., Manson, J. L., Parsons, S., Brechin, E. K. & Hill, S. (2012). *Angew. Chem., Int. Ed.* **51**, 7490-7494, S7490/7491-S7490/7498.

Ragan, D. D., Gustavsen, R. & Schiferl, D. (1992). *J. Appl. Phys.* **72**, 5539-5544.

Redler, G., Lampropoulos, C., Datta, S., Koo, C., Stamatatos, T. C., Chakov, N. E., Christou, G. & Hill, S. (2009). *Phys. Rev. B: Condens. Matter Mater. Phys.* **80**, 094408/094401-094408/094409.

Seo, D. M., Meenakshi, V., Teizer, W., Zhao, H. & Dunbar, K. R. (2006). *J. Magn. Magn. Mater.* **301**, 31-36.

Sessoli, R., Gatteschi, D., Caneschi, A. & Novak, M. A. (1993). *Nature (London)* **365**, 141-143.

Sheldrick, G. M. (2008). *SADABS.* Version 2008-1.

Sieber, A., Bircher, R., Waldmann, O., Carver, G., Chaboussant, G., Mutka, H. & Guedel, H.-U. (2005). *Angew. Chem., Int. Ed.* **44**, 4239-4242.

Soler, M., Wernsdorfer, W., Sun, Z., Huffman, J. C., Hendrickson, D. N. & Christou, G. (2003). *Chem. Commun. (Cambridge, U. K.)*, 2672-2673.

Spek, A. L. (2003). *J. Appl. Crystallogr.* **36**, 7-13.

Sun, Z., Ruiz, D., Hendrickson, D. N., Dilley, N. R., Maple, M. B., Soler, M., Folting, K., Christou, G. & Ribas, J. (1999). *Chem. Commun. (Cambridge)*, 1973-1974.

Chapter 5

The Effect of Pressure on the Prussian Blue Analogue $Mn_3[Cr(CN)_6]_2.15H_2O$

5.1 Introduction

Prussian blue ($Fe_4[Fe(CN)_6]_3.mH_2O$) is a prototypical cyanide-based polynuclear transition metal compound first discovered in the 18th century, and widely employed in the dye industry due to its characteristic deep blue colour (Samain *et al.*, 2013). The synthesis of Prussian blue is a one-step reaction involving Fe^{III} and $[Fe(CN)6]^{4-}$ salts, and as a result the production of derivative species with substituted metal centres is a facile process (Barsan *et al.*, 2011). An extended family of Prussian blue analogues (PBAs) have subsequently been discovered with the general formula $A_xB_y[M(CN)_6]_z.nH_2O$, where B and M represent transition metal ions and A is a charge-balancing alkali metal cation. In these structures bridging of the octahedral B and M ions by cyanide ligands produces a three-dimensional polymeric network with A or H_2O occupying void spaces in the framework. The high symmetry nature of these structures favours crystallization in cubic space groups with lattice parameters approximately 10 Å (Keggin & Miles, 1936, Ferrari *et al.*, 1962, Ludi *et al.*, 1970, Gudel *et al.*, 1973, Verdaguer *et al.*, 1999, Zentkova *et al.*, 2007).

PBAs have attracted significant interest from researchers because of their extensive properties including photo-induced magnetization (Moritomo *et al.*, 2003, Tokoro *et al.*, 2003, Sato, 2004, Ohkoshi, Tokoro, *et al.*, 2005), negative thermal expansion (Goodwin *et al.*, 2005, Chapman *et al.*, 2006), spin-crossover and electron-transfer phenomenon (Ohkoshi *et al.*, 2002, Kosaka *et al.*, 2005, Ohkoshi, Matsuda, *et al.*, 2005), chromatism (Kettle *et al.*, 2011), and selective porosity (Hoffman, 2003, Kaye & Long, 2005). Curie temperatures (T_c) higher than liquid nitrogen temperatures are characteristic of many PBAs and are critically important in the field of molecular magnetism, since this phenomenon leads to potential applications as room-temperature magnetic storage devices (Verdaguer *et al.*, 2000, Usuki *et al.*, 2001, Lue *et al.*, 2006). These magnetic properties are facilitated through superexchange interactions between the metal centre orbitals mediated by the cyanide bridge π and π^* orbitals. Longer-range magnetic coupling is often assumed to be negligible because of the large distances between next-nearest metal sites (Weihe & Gudel, 2000). Although PBAs possess relatively similar structures they exhibit a wide range ferromagnetic or ferrimagnetic phases depending on the orbital pathways available for magnetic coupling (Verdaguer *et al.*, 2000).

Despite the extensive array of magnetic investigations conducted on PBAs knowledge of the magneto-structural relationship in these compounds is still largely elusive because of the difficulty in obtaining detailed structural information (Usuki *et al.*, 2001, Lue *et al.*, 2006). PBA condensation from the reaction mixture is a fast and frequently irreversible process, leading to the formation of nanocrystalline colloidal suspensions which are unsuitable for single-crystal X-ray diffraction (Ludi *et al.*, 1970). The desire for structural data on PBAs has therefore necessitated the exploration of alternate crystallization methods which are capable of producing larger crystals. Slow-diffusion gel techniques have been one approach to improving PBA crystal formation, which involves the formation of a stable gel nucleation environment followed by slow-diffusion of the reagents (Giriat, 2011). One example of a hexacyanochromate PBA that has been successfully crystallized through this method is $Mn_3[Cr(CN)_6]_2$ (Gudel *et al.*, 1973, Dong *et al.*, 2007).

$Mn_3[Cr(CN)_6]_2.xH_2O$ (x = 12 – 16) (MnCrPBA) consists of octahedral Mn^{II} and Cr^{III} moieties bridged by cyanide ligands where the C terminal coordinates to the Cr centre. The 3:2 stoichiometric ratio of Mn:Cr results in one third of all $Cr(CN)_6$ sites in the crystal structure being vacant, creating statistically random disruptions throughout the framework. Loss of coordination at the Mn octahedra is compensated through bonding with water molecules such that $Mn(NC)_4(H_2O)_2$ represents the average Mn ligand field. Solvent accessible voids are occupied by crystallized water although the number per formula unit varies with humidity and temperature (Gudel *et al.*, 1973). These pore water molecules are distributed across mutually exclusive central zeolitic positions and off-centre positions which facilitate hydrogen bonding to the water ligand (Beall *et al.*, 1977, Herren *et al.*, 1980). Antiferromagnetic alignment of the magnetic spins leads to the formation of a ferrimagnetic state at 74 K followed by another ferrimagnetic state at 61-67 K (Ohkoshi *et al.*, 1997, Usuki *et al.*, 2001, Dong *et al.*, 2007).

Variations in the properties of PBAs have historically been derived through alterations in chemical composition (Verdaguer *et al.*, 1999, Usuki *et al.*, 2001, Ohkoshi, Matsuda, *et al.*, 2005, Chapman *et al.*, 2006, Zentkova *et al.*, 2006, Salmon *et al.*, 2009, Bhatt *et al.*, 2012). Recently however there has been greater interest in the use of non-ambient conditions such as light (Tokoro *et al.*, 2003, Sato, 2004, Lummen *et al.*, 2008), temperature (Ohkoshi, Matsuda, *et al.*, 2005, Ohkoshi, Tokoro, *et al.*, 2005, Lue *et al.*, 2006), X-rays (Margadonna *et al.*, 2004), and pressure (Awaga *et al.*, 1998, Ksenofontov *et al.*, 2003, Moritomo *et al.*, 2003, Coronado *et al.*, 2005, Maeda *et al.*, 2005, Egan *et al.*, 2006, Zentkova *et al.*, 2007, Bleuzen *et al.*, 2008, Catafesta *et al.*, 2008) for probing the structure-property relationship in these materials. High-pressure conditions have been recognized as a very efficient mechanism for inducing structural changes, which have led to the pressure becoming increasingly routine in combination with advances in technology and methodology (Boldyreva, 2008, Katrusiak, 2008, Moggach, Parsons, & Wood 2008). Transition metal coordination bonds are especially susceptible to changes in pressure (Allan *et al.*, 2006, Moggach *et al.*, 2009, Moggach & Parsons, 2009, Prescimone *et al.*, 2012), which has been exploited in studies of other properties such as colour (Galloway *et al.*, 2010, Byrne *et al.*, 2012), porosity (Graham *et al.*, 2011, Graham *et al.*, 2012), and spin state (Granier *et al.*, 1993, Guetlich *et al.*, 2007).

A high-pressure low-temperature magnetic study of MnCrPBA (Figure 5.1) (Giriat *et al.*, 2010) observed an increase in T_c from 63 K to 92 K between ambient pressure and 3.2 GPa, and this was correlated to hypothetical reductions in metal-ligand distances. Reductions in the ferrimagnetic moment over this pressure range were linked to potential tilting of the Mn or Cr octahedra. Further increasing the applied pressure resulted in a gradual decline in T_c and broadening of the spontaneous magnetization transition, with a complete suppression of the ferrimagnetic moment ($T_c = 0$ K) occurring between 8.3 and 10.3 GPa. The relaxation of pressure to ambient conditions did not produce a reversal of the ferrimagnetic suppression, thus indicating the possibility of amorphization as illustrated in the PBA $Fe[Co(CN)_6]$ (Catafesta *et al.*, 2008) between 8 GPa and 10 GPa.

Figure 5.1: High-pressure low-temperature magnetic susceptibility study of MnCrPBA (Giriat *et al.*, 2010)

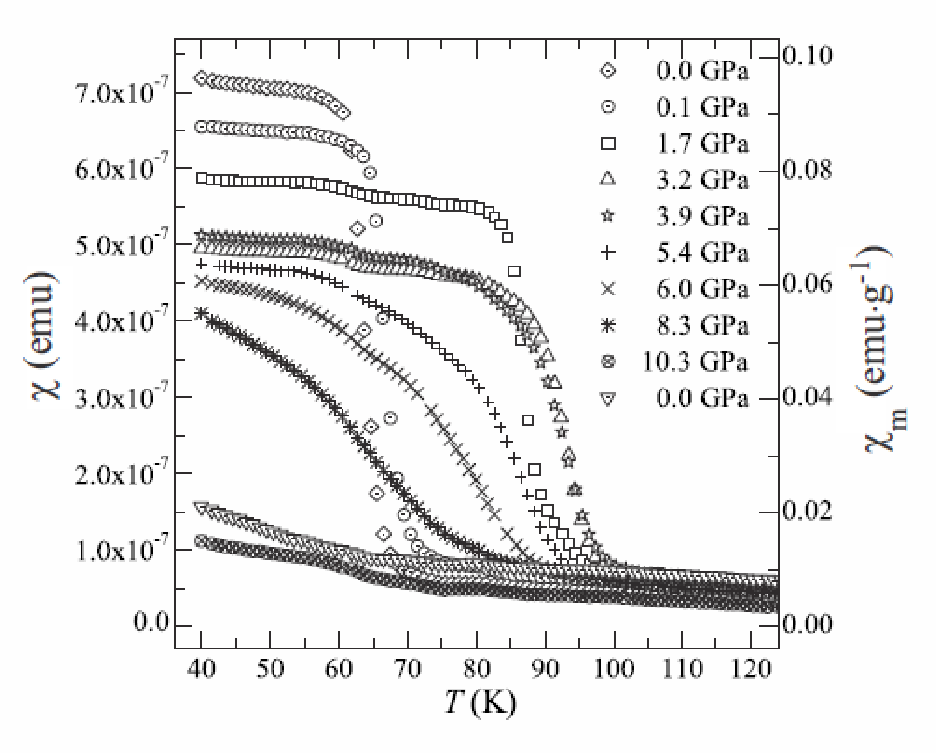

A subsequent high-pressure ambient-temperature single crystal X-ray diffraction study (Giriat, 2011) also correlated the increase in T_c with reductions in metal-metal distances. Notably the response of the metal-ligand interactions to pressure was varied with Cr-C distances decreasing between ambient pressure and 0.9 GPa whilst Mn-N distances increased over the same pressure range (Table 5.1). An explanation for the reversals in these trends upon increasing pressure to 2.1 GPa was not provided given the reduction in data quality available for this refinement. Likewise information regarding the behaviour of the water ligand and solvent was unavailable, although these have been found to have an influential role on magnetic properties in other PBAs. Therefore we report a new structural investigation of the Prussian blue analogue MnCrPBA using high-pressure single-crystal X-ray and neutron powder diffraction, with the aim of furthering our understanding of the magneto-structural data previously reported.

Table 5.1: Previously determined bond lengths (Å) of MnCrPBA (standard deviations not available) (Giriat, 2011)

Pressure (GPa)	0.0	0.4	0.9	2.1
Mn-N	2.115	2.165	2.244	2.100
Cr-C	2.168	2.095	1.986	2.030
C-N	1.123	1.119	1.121	1.115

5.2 Experimental

5.2.1 Sample Preparation

$Mn_3[Cr(CN)_6]_2.15H_2O$ single-crystals were synthesized and crystallized using a slow-diffusion gel technique from $[TBA]_3[Cr(CN)_6]$ (TBA = tetrabutylammonium) and $MnCl_2.4H_2O$ in a tetramethoxysilane gel U-tube setup. After a one month diffusion period the cubic green crystals collected ranged in size from 0.5 mm to a few micrometres. $[TBA]_3[Cr(CN)_6]$ was produced using the literature method (Schlafer *et al.*, 1971) with a yield of approximately 25% and was utilized instead of $K_3[Cr(CN)_6]$ to avoid K^+ contamination of the MnCrPBA crystal structure (Giriat, 2011). $Mn_3[Cr(CN)_6]_2.15D_2O$ powder was obtained following a slightly modified procedure where the water solvent and diffusion matrix were replaced with D_2O. The product was left to crystallize over two weeks in a slow-diffusion reaction vessel that was sealed from the environment to prevent protonation by atmospheric H_2O.

5.2.2 High-Pressure Single Crystal X-ray Diffraction

The high-pressure single-crystal studies utilized a Merrill-Bassett DAC (Merrill & Bassett, 1974) with an opening angle of 40°, 600 µm culet Boehler-Almax cut diamonds, tungsten-carbide backing discs and tungsten gasket (Moggach, Allan, *et al.*, 2008). 4:1 methanol-ethanol was used as the hydrostatic medium. High-pressure single crystal X-ray diffraction measurements were carried-out on a three-circle Bruker APEX diffractometer with Mo-K_α radiation monochromated with a TRIUMPH curved-crystal monochromator. The pressure was measured using the ruby fluorescence method (Piermarini *et al.*, 1975). Data collection strategies were as described by Dawson *et al*. (Dawson *et al.*, 2004).

Cell indexing and integration were carried out using the Bruker APEX II (Bruker, 2001) software with dynamics masks generated by ECLIPSE (Dawson *et al.*, 2004). Absorption corrections were carried out using SADABS (Sheldrick, 2008). The $Fm\overline{3}m$ crystal structure was solved by SHELXS (Sheldrick, 2008) whilst the $R\overline{3}m$ equivalent was solved by SIR92 (Altomare *et al.*, 1994). Distance restraints were applied between the carbon and nitrogen atom in the CN bridging ligand, and thermal similarity restraints were applied between the nitrogen and coordinated oxygen atom. All structures were refined against $|F|$ with reflections $|F| < 4\sigma(|F|)$ omitted. High-pressure single-crystal data are recorded in Table 5.2.

Table 5.2: High-pressure single-crystal X-ray data for MnCrPBA

Pressure (GPa)	0.12	0.55	1.09	1.53	2.06
λ (Å)	0.71073	0.71073	0.71073	0.71073	0.71073
$\sin\theta/\lambda$ (Å)	0.59	0.59	0.59	0.58	0.55
Crystal System	Cubic	Cubic	Cubic	Cubic	Cubic
Space Group	$Fm\overline{3}m$	$Fm\overline{3}m$	$Fm\overline{3}m$	$Fm\overline{3}m$	$Fm\overline{3}m$
a (Å)	10.8092(8)	10.7519(5)	10.6941(7)	10.6525(6)	10.581(10)
V (Å^3)	1262.93(16)	1242.96(10)	1223.02(14)	1208.80(12)	1184.62(19)
Z	1	1	1	1	1
D_{calc} (Mg m^{-3})	1.439	1.463	1.486	1.504	1.535
Reflections	1065	1056	965	825	745
Unique Refl.	67	72	72	67	62
R_{int}	0.019	0.021	0.028	0.032	0.039
R	0.0215	0.0293	0.0330	0.0364	0.0445
R_w	0.0237	0.0332	0.0380	0.0414	0.0301
GooF	1.2050	1.1513	1.2113	1.3502	1.1392
Data:Parameters	62:16	60:16	54:16	49:16	44:16
No. Restraints	4	4	4	4	4
ρ_{max}/ρ_{min} (e.Å^{-3})	0.35/-0.62	0.35/-0.62	0.44/-0.17	0.35/-0.62	0.35/-0.62

Table 5.2 continued: High-pressure single-crystal X-ray data for MnCrPBA

Pressure (GPa)	0.12	0.55	1.09	1.53	2.06
λ (Å)	0.71073	0.71073	0.71073	0.71073	0.71073
Sinθ/λ (Å)	0.59	0.59	0.59	0.58	0.55
Crystal System	Rhombo.	Rhombo.	Rhombo.	Rhombo.	Rhombo.
Space Group	$R\bar{3}m$	$R\bar{3}m$	$R\bar{3}m$	$R\bar{3}m$	$R\bar{3}m$
a (Å)	7.6447(6)	7.6017(4)	7.5671(5)	7.5331(4)	7.4808(11)
c (Å)	18.718(3)	18.6296(16)	18.501(3)	18.4349(15)	18.316(3)
V (Å^3)	947.37(17)	932.3(11)	917.46(15)	905.98(1)	887.7(2)
Z	1	1	1	1	1
D_{calc} (Mg m^{-3})	1.439	1.462	1.486	1.506	1.535
Reflections	1067	1046	1041	898	789
Unique Refl.	147	148	144	139	113
R_{int}	0.018	0.017	0.024	0.025	0.037
R	0.0229	0.0296	0.0288	0.0362	0.0494
R_w	0.0247	0.0342	0.0306	0.0284	0.0539
GooF	1.3007	1.2980	1.2976	1.2000	1.0567
Data:Parameters	125:35	113:35	104:35	95:35	79:35
No. Restraints	8	8	8	8	8
ρ_{max}/ρ_{min} (e.Å^{-3})	0.21/-0.13	0.21/-0.13	0.21/-0.13	0.26/-0.28	0.38/-0.39

Analysis of the bonding interactions was conducted using the program PLATON (Spek, 2003) while MERCURY (Macrae *et al.*, 2006) and DIAMOND (Brandenburg, 1999) were utilized for visualization. Searches of the Cambridge Structural Database v5.34 employed the program CONQUEST v1.15 (Allen, 2002). Calculation of interstitial and solvent accessible voids was carried-out using the contact surface and solvent accessible voids algorithms in MERCURY, using a probe radius of 0.5 Å and a grid spacing of 0.1 Å.

5.2.3 High-Pressure Neutron Powder Diffraction

Neutron data were collected using the time-of-flight technique at the PEARL beamline high-pressure diffractometer at ISIS. Data sets between ambient pressure and 2.93 GPa were collected in the range $0.6 < d < 4.1$ Å using a V3b-type Paris-

Edinburgh press, with deuterated 16:3:1 methanol:ethanol:water as a hydrostatic medium. The TiZr capsule gasket (Marshall & Francis, 2002) containing the sample was also loaded with a small Pb pellet to act as a pressure marker. Pressures were calculated using a Birch-Murnaghan (Birch, 1947) equation of state with V_o = 30.3128 Å^3, K_o = 41.92 GPa, and K' = 5.72, which were derived (Fortes, 2004) as averages of values obtained in three earlier studies (Waldorf & Alers, 1962, Miller & Schuele, 1969, Kuznetsov *et al.*, 2002). High-pressure powder data are shown in Tables 5.3 and 5.4. Analysis of the collected data, consisting of Pawley fitting the patterns with $Fm\overline{3}m$ or $R\overline{3}m$ unit cells, was conducted by Professor Simon Parsons using TOPAS-Academic version 5 (Coehlo, 2012).

Table 5.3: High-pressure neutron powder diffraction data for MnCrPBA

Pressure (GPa)	-0.06	0.11	0.94	1.02
Crystal System	Cubic	Cubic	Cubic	Cubic
Space Group	$Fm\overline{3}m$	$Fm\overline{3}m$	$Fm\overline{3}m$	$Fm\overline{3}m$
a (Å)	10.8356(3)	10.8173(6)	10.7522(6)	10.7467(3)
V (Å^3)	1272.2(1)	1265.8(2)	1243.0(2)	1241.1(2)
Z	1	1	1	1
Pawley R_{wp}	0.0285	0.0460	0.0452	0.0213
Crystal System	Rhombohedral	Rhombohedral	Rhombohedral	Rhombohedral
Space Group	$R\overline{3}m$	$R\overline{3}m$	$R\overline{3}m$	$R\overline{3}m$
a (Å)	7.6770(5)	7.6393(17)	7.5912(10)	7.5893(6)
c (Å)	18.701(2)	18.773(8)	18.662(4)	18.652(2)
V (Å^3)	954.52(16)	948.8(6)	931.3(3)	930.40(18)
Z	1	1	1	1
Pawley R_{wp}	0.0269	0.0455	0.0446	0.0207

5.2.4 High-Pressure Single-Crystal Raman Spectroscopy

The high-pressure Raman studies utilized a Merrill-Bassett DAC (Merrill & Bassett, 1974) with an opening angle of 40°, 600 µm culet Boehler-Almax cut diamonds, tungsten-carbide backing discs and tungsten gasket (Moggach, Allan, *et al.*, 2008). 4:1 methanol-ethanol was used as the hydrostatic medium. Raman spectra were collected using a LabRAM HR spectrometer.

Table 5.4: High-pressure neutron powder diffraction data for MnCrPBA

Pressure (GPa)	1.22	1.98	2.57	2.92
Crystal System	Cubic	Cubic	Cubic	Cubic
Space Group	$Fm\overline{3}m$	$Fm\overline{3}m$	$Fm\overline{3}m$	$Fm\overline{3}m$
a (Å)	10.7326(7)	10.6808(4)	10.6461(7)	10.6230(9)
V (Å^3)	1236.3(2)	1218.44(15)	1206.6(3)	1198.8(3)
Z	1	1	1	1
Pawley R_{wp}	0.0493	0.0252	0.0277	0.0295
Crystal System	Rhombohedral	Rhombohedral	Rhombohedral	Rhombohedral
Space Group	$R\overline{3}m$	$R\overline{3}m$	$R\overline{3}m$	$R\overline{3}m$
a (Å)	7.5985(10)	7.5673(5)	7.5109(15)	7.4885(18)
c (Å)	18.543(5)	18.432(3)	18.522(7)	18.512(11)
V (Å^3)	927.2(4)	914.08(17)	904.9(5)	899.0(7)
Z	1	1	1	1
Pawley R_{wp}	0.0489	0.0207	0.0248	0.0242

5.2.5 Thermogravimetric Analysis

Thermogravimetric analysis was conducted at the University of Glasgow using a TA Instruments SDT Q600 DSC/TGA instrument with a scanning rate 10 °C min^{-1}.

5.3 Results

5.3.1 General comments

The crystal structure of $Mn_3[Cr(CN)_6]_2.15H_2O$ has been determined up to 2.06 GPa in the previously characterized space $Fm\overline{3}m$ group and an alternative $R\overline{3}m$ space group. Further increasing the pressure to 2.47 GPa caused the crystal to disintegrate into many smaller crystallites, precluding any structural analysis at this pressure given the low quantity and quality of data available.

The unit cells for both space groups are displayed in Figure 5.2 and their response to pressure given in Figure 5.3. A linear reduction in unit cell parameters for both space groups is observed throughout the pressure study, with a compression in the $Fm\overline{3}m$ a axis of 10.8103(7) Å to 10.581(10) Å, $R\overline{3}m$ $a = b$ axes of 7.6447(6) Å to 7.4808(11) Å, and $R\overline{3}m$ c axis of 18.718(3) Å to 18.316(3) Å. The change in these parameters under pressure represents a percentage reduction of 2.11 %, 2.14 %, and 2.15 % respectively.

Figure 5.2: Unit cell of (top) $Fm\overline{3}m$ viewed along **b** and (bottom) $R\overline{3}m$ viewed along the (012) Miller plane

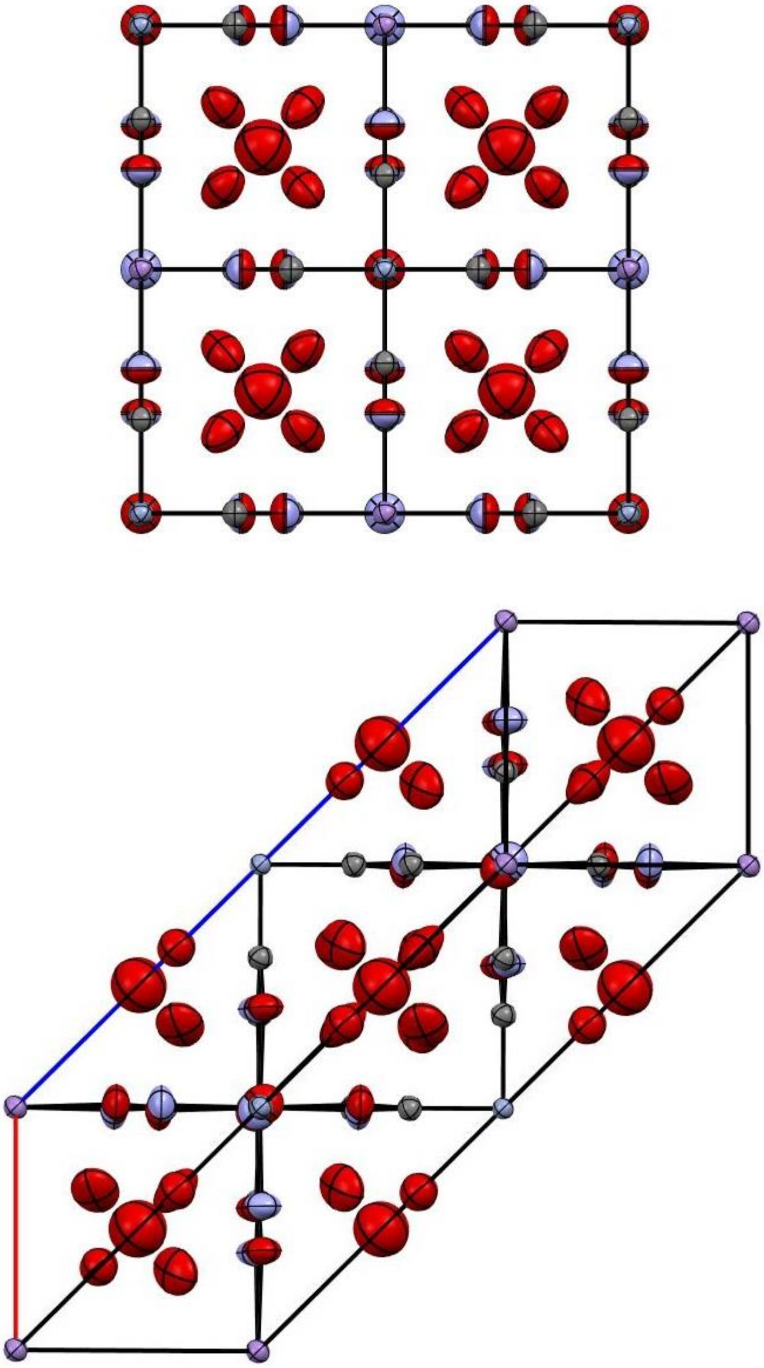

Figure 5.3: Response of $Fm\bar{3}m$ (top) and $R\bar{3}m$ (middle and bottom) unit cell parameters to pressure

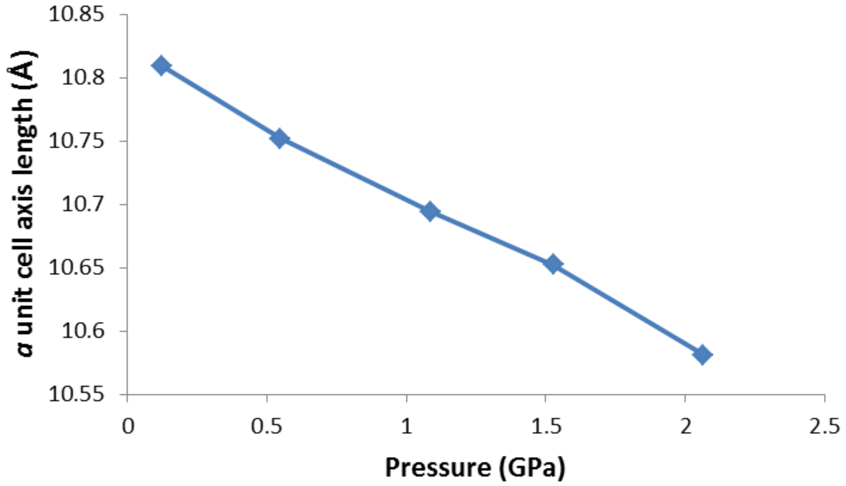

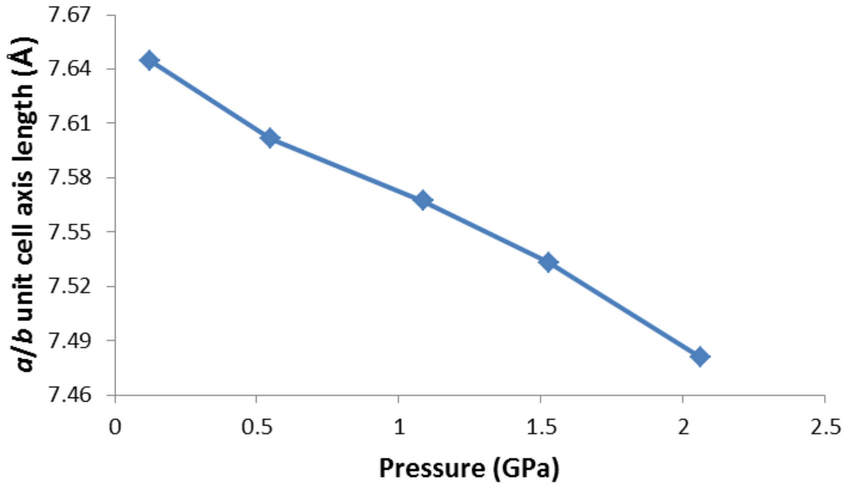

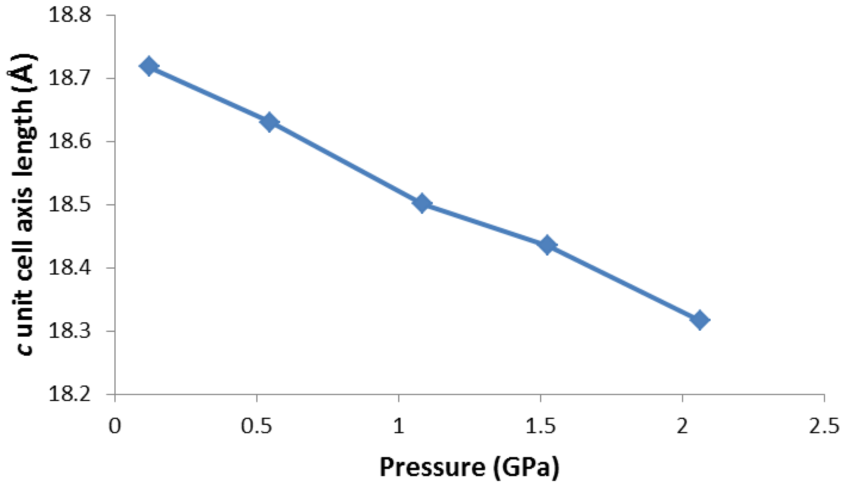

Photographs of the sample chamber at 0.12 GPa and 2.06 GPa are given in Figure 5.4 which reveal the onset of a colour change from colourless to yellow. The disintegration of the crystal at 2.47 GPa made it impossible to test the reversibility of these observations. An unusual structural feature bisecting the crystal (highlighted in lower photograph of Figure 5.4) becomes increasingly apparent over the pressure study that may be indicative of the onset of crystal degradation.

5.3.2 Determination of correct space group

The high-pressure single-crystal $Fm\overline{3}m$ and $R\overline{3}m$ unit cells have visually identical diffraction patterns and were therefore indexed and integrated using the same reflections. Attempts to determine the correct space group using $R1$ values proved impossible in the absence of any decisive trend over the pressure study, with a lower $Fm\overline{3}m$ $R1$ at 0.15 GPa (2.15 % versus 2.29 %) and 2.06 GPa (4.45 % versus 4.94 %) interrupted by a lower $R\overline{3}m$ $R1$ at 1.09 GPa (2.88 % versus 3.30 %). Furthermore the iterative application of three possible $Fm\overline{3}m$ to $R\overline{3}m$ twin laws (Figure 5.5) in the $R\overline{3}m$ refinements made a negligible impact on their $R1$ values and produced twin domain ratios approximating 1:0.

Figure 5.4: MnCrPBA crystal (length = 100 μm) in cell at 0.12 GPa (left) and 2.06 GPa (right – potential structural defect highlighted)

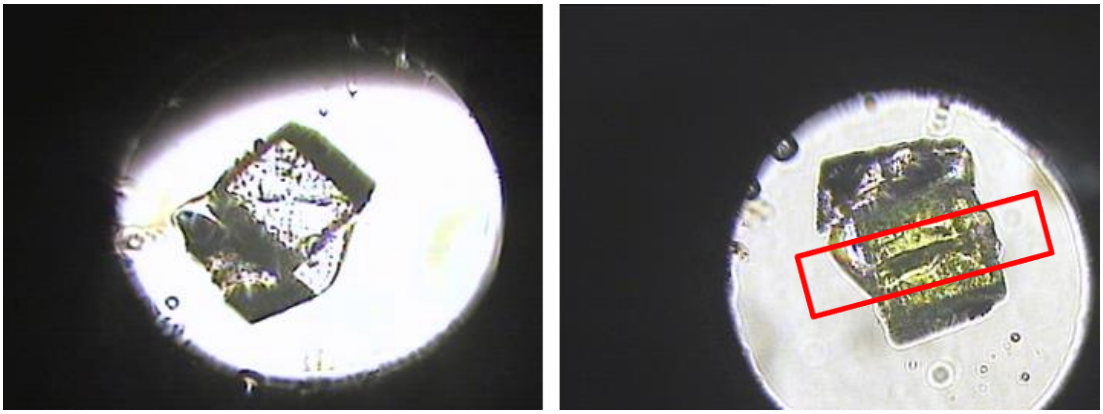

Meanwhile the high-pressure neutron powder Pawley refinements (Figure 5.6) give lower R*wp* factors for the $R\overline{3}m$ unit cell at all pressures, with the largest differences occurring at ambient pressure (2.69 % versus 2.85 %) and 1.98 GPa (2.21 % versus

2.40 %). A reduction in the R*wp* difference at 2.97 GPa (2.42 % and 2.49 % respectively) coincides with a broadening and decline of the diffraction peaks (Figure 5.7), which is indicative of partial amorphization and was also observed at approximately the same pressure in the high-pressure magnetic study by Gaetan Giriat (Giriat *et al.*, 2010).

Figure 5.5: The three possible twin laws representing a transformation from cubic $Fm\overline{3}m$ to rhombohedral $R\overline{3}m$ space groups

$$\begin{pmatrix} 1/3 & 2/3 & -1/3 \\ 0 & -1 & 0 \\ -8/3 & -4/3 & -1/3 \end{pmatrix} \quad \begin{pmatrix} -1/3 & -2/3 & 1/3 \\ -2/3 & -1/3 & -1/3 \\ 4/3 & -4/3 & -1/3 \end{pmatrix} \quad \begin{pmatrix} -1 & 0 & 0 \\ 2/3 & 1/3 & 1/3 \\ 4/3 & 8/3 & -1/3 \end{pmatrix}$$

Figure 5.6: Pawley refinement of neutron powder diffraction patterns for cubic (top) and rhombohedral (bottom) unit cells at ambient pressure (as determined by Professor Simon Parsons)

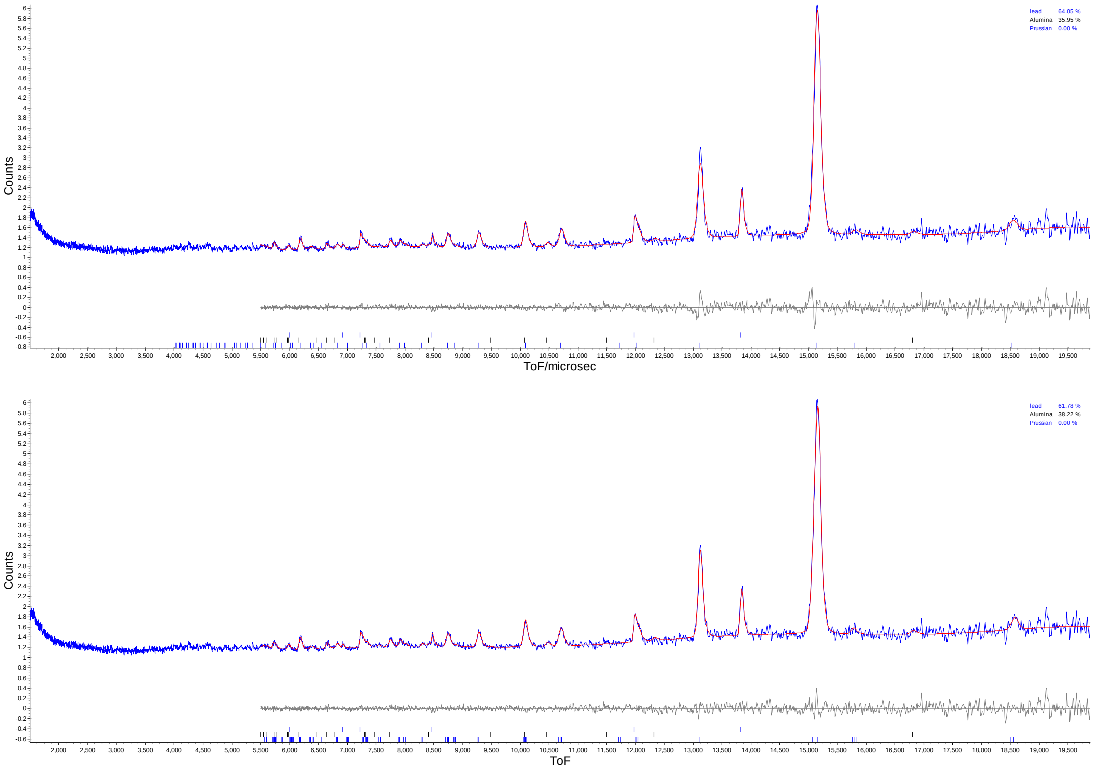

Figure 5.7: Pawley refinement of neutron powder diffraction patterns for cubic (top) and rhombohedral (bottom) unit cells at 2.92 GPa (as determined by Professor Simon Parsons)

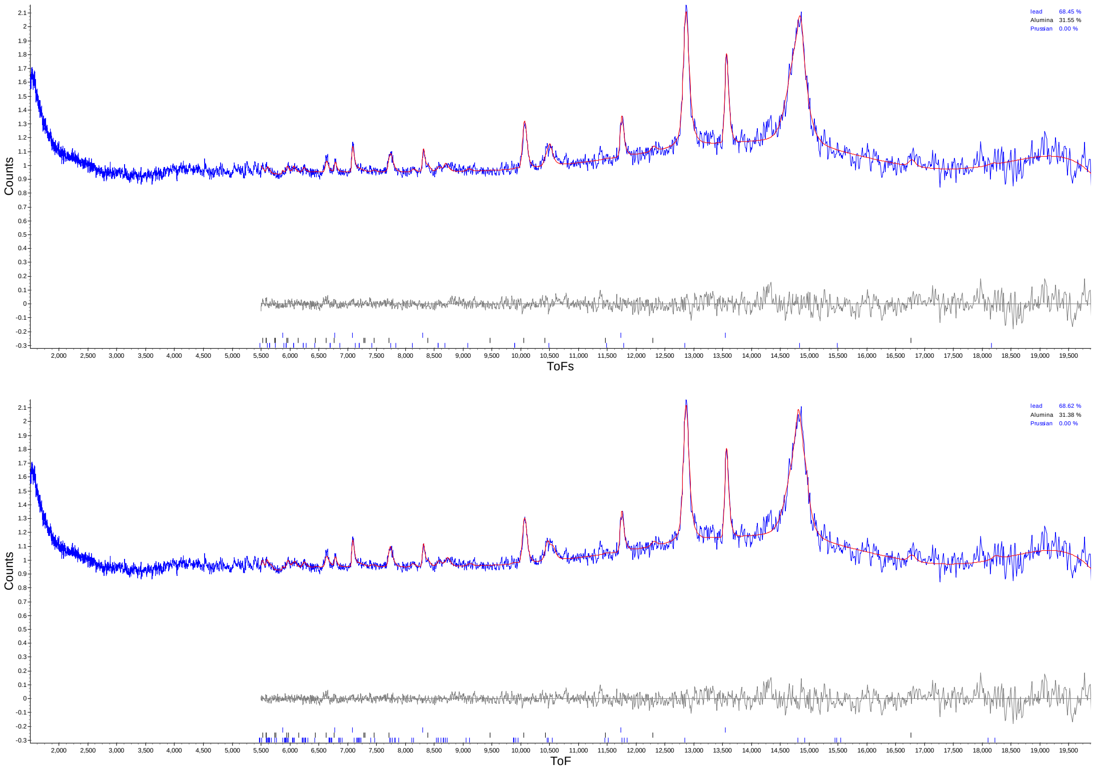

5.3.3 Characterization of the crystallized solvent

A determination of the water content in PBA was performed by thermogravimetric analysis and the resulting TGA spectrum is shown in Figure 5.8. Between 20 °C and 300 °C the percentage weight of the sample continually decreased with the largest decline occurring rapidly between 100 °C and 150 °C. Total weight loss between 20 °C and 200 °C has been calculated as 30.37 % which is equivalent to 15 water molecules per formula unit, resulting in a formal chemical formula for these crystals of $Mn_3[Cr(CN)_6]_2.15H_2O$. The number of water molecules per formula unit was used to calculate the possible occupancy values for the solvent atoms during refinements (see below).

The solvent structure in MnCrPBA consists of three unique oxygen atoms which are arranged in a tetrahedral geometry with O2 at the centre and the vertices pointing towards the Cr1 sites. Through an iterative series of refinements where the occupancy values were altered manually the O2 and O3/O4 sites were determined to have occupancies of 0.82 and 0.17/0.17 respectively, as these gave the lowest *R*1 values whilst satisfying the requirement for 15 water molecules in the crystal structure. Hydrogen positions for the water molecules were not determined because of the highly disordered nature of the oxygen atoms.

Figure 5.8: Thermogravimetric analysis spectrum of MnCrPBA

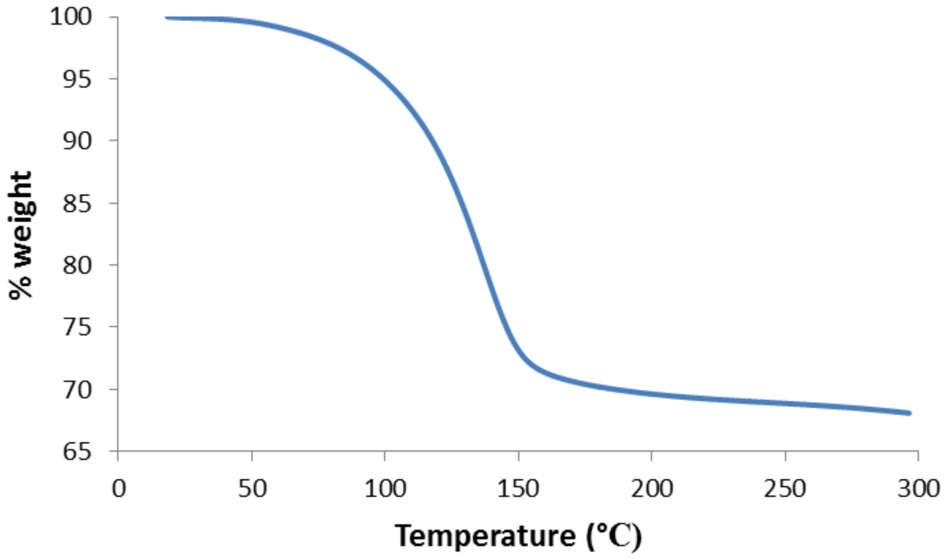

5.3.4 Response of the metal-cyanide framework to pressure

The numbering scheme and asymmetric unit for the MnCrPBA structure is illustrated in Figure 5.9. This structure contains a single unique Mn-N, Mn-O, Cr-C, and C-N distance, in addition to one independent Mn-N-C angle and two N-Mn-N and C-Cr-C angles. All atomic positions except Mn1 possess partial occupancies (Cr1/C1/N1 = 2/3; O1 = 1/3).

Tables 5.5 and 5.6 detail the response of the MnCrPBA metal-cyanide framework to pressure. Between 0.12 GPa and 1.09 GPa the Cr1-C1 bonds remain approximately static with a range of 2.076(5) – 2.079(12) Å, while further increasing the pressure to 2.06 GPa causes a significant decline to 1.98(3) Å. The only other structural feature to undergo any statistically significant change is the N1-Mn1-N1^{i} angle with a gradual linear increase from 93.8(3)° to 96.8(9)° over the pressure study.

Figure 5.9: Asymmetric unit of MnCrPBA with atomic labels displayed. Thermal ellipsoids enclose 50% probability surfaces.

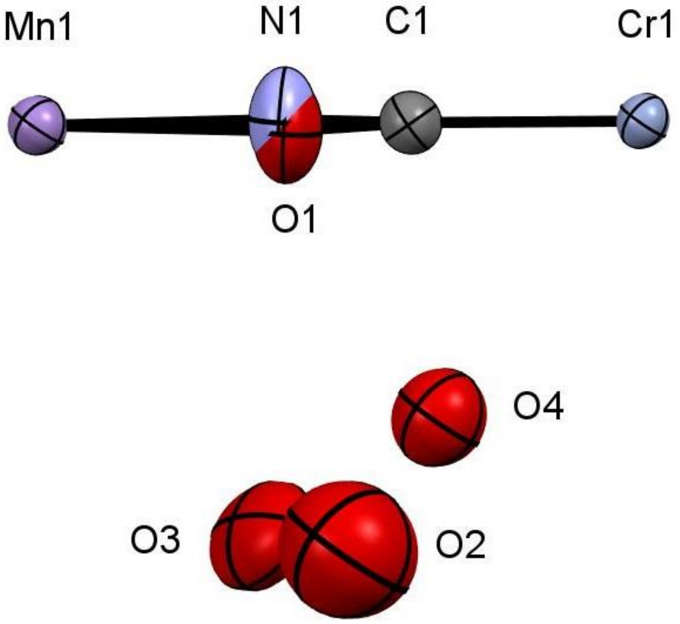

Table 5.5: Intramolecular bond lengths (Å) as a function of pressure

Pressure (GPa)	0.12	0.55	1.09	1.53	2.06
Mn1-N1	2.197(10)	2.173(18)	2.14(2)	2.15(2)	2.19(2)
Mn1-O1	2.23(2)	2.29(3)	2.27(4)	2.23(4)	2.30(5)
Cr1-C1	2.076(5)	2.071(8)	2.079(12)	2.049(12)	1.98(3)
C1-N1	1.140(11)	1.143(18)	1.14(2)	1.14(2)	1.14(4)

Table 5.6: Intramolecular bond angles (°) as a function of pressure

Pressure (GPa)	0.12	0.55	1.09	1.53	2.06
N1-Mn1-N1^{i}	93.8(3)	94.9(6)	95.5(8)	95.9(7)	96.8(9)
N1-Mn1-N1^{ii}	86.2(4)	85.1(6)	84.6(8)	84.0(8)	83.5(9)
C1-Cr1-C1^{iii}	90.1(2)	90.2(3)	90.5(5)	90.1(5)	90.3(11)
C1-Cr1-C1^{vi}	89.9(2)	89.8(3)	89.5(4)	89.9(5)	89.7(11)
Mn1-N1-C1	172.0(8)	170.4(16)	169.6(18)	167.9(15)	167.1(19)

Symmetry operations: (i) 1-y, 1+x-y, z; (ii) -1/3+y, 1/3+x, 4/3-z; (iii) 2-y, 1+x-y, z; (vi) y, x, 1-z

The ambient pressure Raman spectrum of PBA is shown in Figure 5.10, with the main peak at 2161 cm^{-1} assigned to the CN intraligand vibration. Smaller features appear at approximately 2850 cm$^{-1,}$ 2950 cm^{-1}, and below 1000 cm^{-1}. Figure 5.11 demonstrates the response of the CN vibrational wavenumber to pressure. Upon applying pressure the CN peak experiences an initially rapid increase before approximately flattening between 2.04 GPa and 3.03 GPa with a vibrational wavenumber of 2176 cm^{-1}. No splitting of the cyanide CN vibration peak was observed under pressure, and this indicates the absence of pressure-induced cyanide isomerisation as documented in other PBAs (Coronado *et al.*, 2005).

Figure 5.10: Ambient-pressure Raman spectrum of MnCrPBA

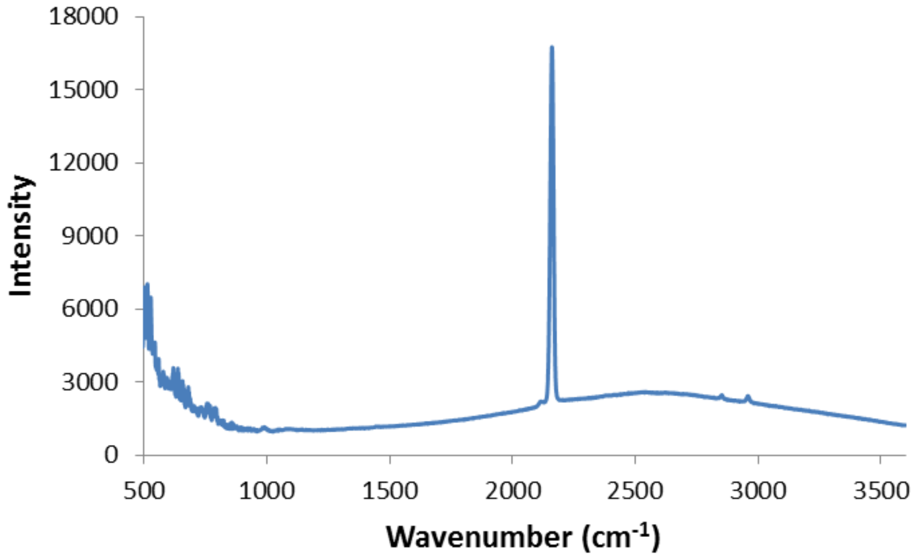

5.3.5 Response of the crystallized solvent to pressure

Interstitial and solvent accessible void volumes in the crystal lattice are displayed in Table 5.7. The interstitial void volume decreases continually from 103.14 Å^3 to 61.10 Å^3 between 0.12 GPa and 2.06 GPa, representing 10.9 % and 6.9 % of the unit cell volume respectively. Likewise the solvent accessible volume contracts from 6.18 Å^3 to 3.94 Å^3 over the pressure study (0.7 % and 0.4 % of unit cell volume respectively).

Figure 5.12 demonstrates the dispersion of the interstitial voids at 0.12 GPa and 2.06 GPa. At 0.12 GPa these voids are principally located on diagonal axes between co-planar Mn centres with smaller voids residing between the Mn centres and O2 solvent atom, and together these voids form an almost continuous network throughout the structure. Increasing the applied pressure to 2.06 GPa causes the voids between the Mn atoms and the solvent atoms to disappear leaving behind a disrupted network of independent voids between the co-planar Mn centres.

Occupancies for the O2 and O3/O4 remain constant at 0.82 and 0.17 respectively up to 1.53 GPa. Further increasing the pressure to 2.06 GPa causes the occupancy of O2 to increases to 0.9 and the occupancy of O3/O4 declines to 0.15.

Figure 5.11: CN vibrational wavenumber as a function of pressure

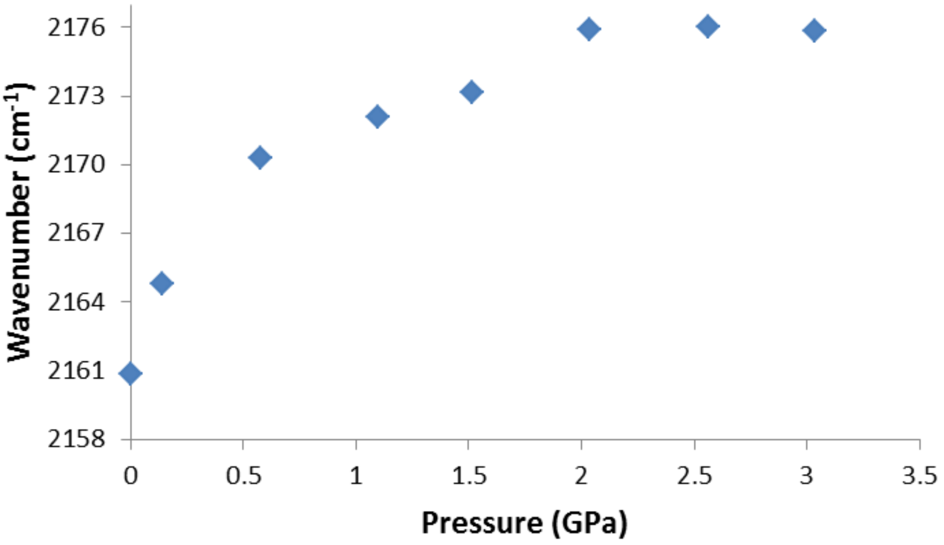

Table 5.7: MnCrPBA void and cell volumes as a function of pressure

Pressure (GPa)	0.12	0.55	1.09	1.53	2.06
Unit Cell Volume ($Å^3$)	947.37	932.3	917.46	905.98	888.4
Interstitial Void Volume ($Å^3$)	122.55	94.39	78.31	71.9	63.16
Interstitial/Cell Volume (%)	12.9	10.1	8.5	7.9	7.1
Solvent Accessible Volume ($Å^3$)	7.9	5.39	4.76	5.6	4.17
Solvent/Cell Volume (%)	0.8	0.6	0.5	0.6	0.5

Figure 5.12: Interstitial voids at 0.12 GPa (top) and 2.06 GPa (bottom) viewed along the (012) Miller plane

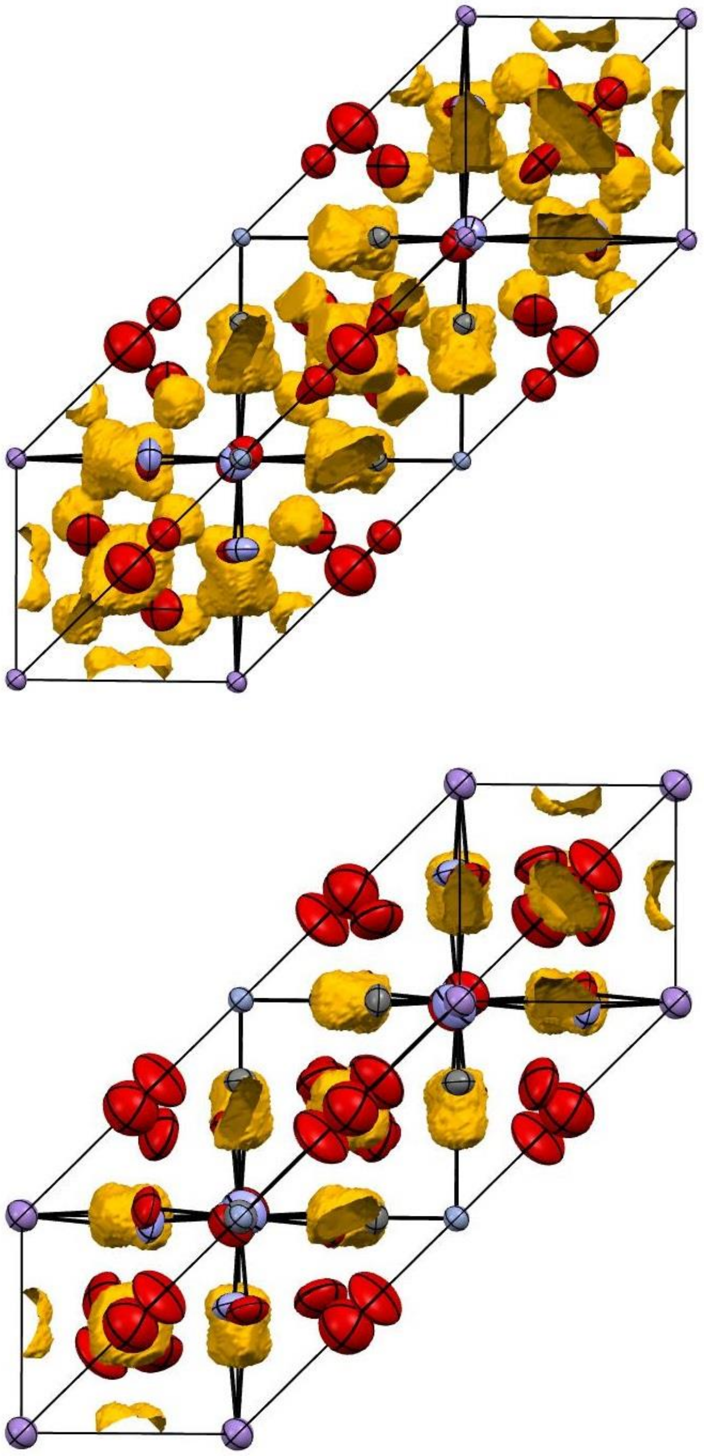

5.4 Discussion

5.4.1 Restraints

The close proximity of the N1 and O1 atomic positions creates substantial problems in refinements due to difficulties in distinguishing between their electron densities. Applying suitable restraints was therefore deemed crucial in obtaining stable refinements and trends in bond distances consistent with the previously collected structural data (Gudel *et al.*, 1973, Dong *et al.*, 2007, Giriat, 2011). Thermal similarity restraints were applied in all data sets between N1 and O1 as the atomic displacement parameters of the latter were frequently unstable in higher pressure refinements. Distance restraints between C1 and N1 were also applied in all refinements since this aided in separating the N1 and O1 atomic positions. This distance restraint was also deemed chemically justifiable because of the negligible compressibility of the CN ligand observed in the high-pressure study by Gaetan Giriat. A comparison of Mn1 coordination bonds with the structural information obtained by Güdel and Dong confirms the validity of these restraints as the Mn-N interaction is the shortest at ambient pressure in these studies.

One problem with implementing a suitable C1-N1 distance restraint arises from the broad variation in this interaction between data sets and refinements. A search of the CSD database for C-N distances in octahedral-coordinated CN ligands revealed a Gaussian distribution centred approximately on 1.14 Å. Subsequently the applied distance restraint was varied iteratively in all the refinements from 1.13 to 1.15 Å and the esd from 0.1 to 0.001 Å to determine their impact on the C1-N1 distances and *R*1 values. Analysis of the collected refinement data suggested that the changes in distance restraint made negligible impact on *R*1 whilst erroneously high C1-N1 distances could be produced when using larger esds. This unusual behaviour is most likely a consequence of the aforementioned difficulty in separating N1 and O1 electron densities, which provides additional freedom to the C1-N1 distance unless restrained more heavily. As a result the cyanide distance restraint chosen for all refinements was 1.140(1) Å.

Additional Mn1-N1-C1 angle restraints of 172(1)° and 167.0(5)° were applied at 0.15 GPa and 2.06 GPa respectively to help stabilize the refinements at these pressures. The values for these restraints were obtained by extrapolating the Mn-N-C angle curve established by the other refinements in the pressure series.

5.4.2 Structural Analysis

The primary structural difference between the literature $Fm\overline{3}m$ space group and the observed $R\overline{3}m$ structure lies in the reduced symmetry of the ligand atoms, thereby allowing the N1, C1, and O1 sites to occupy general positions and produce non-linear Mn1-N1-C1-Cr1 moieties. An important consequence of this structural feature is the ability to adopt different metal-ligand interactions, with Mn-N (2.197(10) Å) and Cr-C (2.076(5) Å) bond lengths at 0.15 GPa contrasting significantly with those reported by Gaetan Giriat at ambient pressure (2.12(2) Å and 2.17(2) Å respectively) (Giriat *et al.*, in preparation).

Variations in the $R\overline{3}m$ metal-ligand coordination environments throughout the pressure study are principally influenced by distortions in the Mn1 octahedral geometry. The adoption of an increasingly pseudo-octahedral geometry between 0.12 GPa and 1.09 GPa by Mn1 accommodates the reduction in inter-metal separation and thereby eliminates the requirement for any significant decreases in metal-ligand bond distances. Beyond this pressure range the capacity of the distorted Mn1 metal centre to relieve the compressive force experienced by the Mn1-N1-C1-Cr1 chains gradually diminishes, leading to preferential reductions in Cr1-C1 driven by reductions in crystal field ($t_{2g}^3e_g^0$) stabilization energy for this metal. Meanwhile the terminal Mn1-O1 bonds remain approximately unchanged by the application of pressure as these are principally influenced by weaker hydrogen bonding interactions with the off-centre O3/O4 atoms. Although similar distortions in the PBAs $K_{0.1}Co^{II}_4[Fe(CN)_6]_{2.7}.18H_2O$ and $Cs_2Co^{II}_{3.3}Co^{III}_{0.7}[Fe(CN)_6]_{3.3}.13H_2O$ were hypothesized to involve interactions between alkali metal cations and the cyanide bridges (Bleuzen *et al.*, 2008), there is currently no evidence that the analogous zeolitic water plays a similar role in MnCrPBA under pressure.

Since the off-centre O3/O4 water positions are created by the statistically random absence of one third of the $Cr(CN)_6$ octahedra absences, it might be expected that these atoms would display complementary occupancy values (i.e. 2/3 Cr1 + 1/3 O3/O4 = 1). Lower than predicted occupancies of the O3/O4 site at ambient pressure

(0.17) suggests that the O2 position is more energetically favourable, possibly due to the minimization of repulsive interactions with the framework. Alternatively the difference in occupancy between O3/O4 and Cr1 may simply be unrepresentative of the correct distribution, and instead be an artefact of the potential errors inherent in modelling closely situated discrete electron density in the pore volume. Water solvent occupancies remain unaffected by pressure between 0.12 and 1.09 GPa most likely because the pore volume has not contracted enough to force some of the O3/O4 water molecules to adopt the O2 position. Beyond this pressure range the interstitial voids between octant diagonal Mn1-Cr sites have almost disappeared which coincides with a gradual decline in O3/O4 occupancy through enhanced repulsive interactions with the cyanide bridges. A new peak in the high-pressure neutron powder patterns at d = 3 Å suggests that solvent expulsion process may occur above 1 GPa, though in the single-crystal the total water content remains unchanged up to 2.06 GPa.

The previously recorded increase in T_c between ambient pressure and 3.02 GPa can be correlated with reductions in metal-metal distances throughout the pressure study. Continual suppression of the ferrimagnetic moment can be explained through the observed distortion of the Mn1 octahedral geometry resulting in partial misalignment of the anti-parallel magnetic moments. Further increasing the pressure above 2.07 GPa may precipitate a non-reversible breakdown of the metal-ligand framework leading to amorphization and a disappearance of long-range magnetic order. This amorphization process was more clearly evidenced at 2.97 GPa by the peak reductions and broadening displayed in the neutron powder data, and could be related to expulsion of water solvent which may play a significant role in stabilizing the framework through hydrogen bonding. Additionally the gradual colour change under pressure can be correlated with the continual distortion of the Mn1 crystal field away from a purely octahedral configuration.

5.4.3 Future Experiments

Refinements and structural analysis of MnCrPBA suffer from significant problems at high-pressures. The high level of disorder in the asymmetric unit combined with the reduction in reciprocal space caused by the cell produce an extremely low data:parameter ratio. As a consequence the crystal structure refinements at higher pressure conditions suffer from occasional instability and imprecision, which is especially evident given the necessity of restraints in these refinements. Since the number of collected reflections will continue declining with pressure it may be technically impossible to refine structures above 2 GPa given the instruments available at the University of Edinburgh.

Another significant issue associated with ambient-temperature high-pressure studies on PBAs is that the magnetic behaviour only occurs under low-temperature conditions. DACs used for high-pressure single-crystal X-ray experiments are not suited for low-temperature conditions due to long cooling times inherent in their design. Currently researchers have to correlate high-pressure ambient-temperature structural data with high-pressure low-temperature magnetic data. This is an undesirable situation since the differences in temperature could induce substantial structural changes and consequently compromise the validity of any magneto-structural relationship (Cornia *et al.*, 2002). Low-temperature conditions would also provide substantial improvements in the accuracy and quality of high-pressure data (Goeta & Howard, 2004), and would prove especially beneficial for characterization of the water solvent and separation of the N1 and O1 electron densities in refinements.

To facilitate these high-pressure low-temperature single-crystal X-ray diffraction experiments a novel DAC has been designed here at the University of Edinburgh. The cell is substantially smaller than a typical DAC and constructed from a beryllium-copper alloy (BERYLCO25) which allows for more rapid cooling times and greater thermal stability. Experimental techniques and apparatus have been implemented and utilized at Diamond Light Source I19 EH2 for conducting high-pressure low-temperature studies down to approximately 50 K. Future single-crystal X-ray diffraction experiments should exploit these facilities with the aim of collecting higher quality high-pressure low-temperature structural data on MnCrPBA. A separate high-pressure UV-Vis absorption study would also provide important information regarding the nature of the colour change.

5.5 Conclusion

The correct space group of $Mn_3[Cr(CN)_6]_2.15H_2O$ between ambient pressure and 2.9 GPa has been determined as $R\bar{3}m$ through analysis of high-pressure single-crystal X-ray and high-pressure neutron powder diffraction data. A gradual distortion of the framework between 0.12 GPa and 2.06 GPa can be correlated with increases in T_c, reductions in ferrimagnetic moment, and colour changes that occur in this pressure region. Higher quality data collected at low-temperature conditions using the micro-cell at I19 EH2 are essential for improving upon the obtained structural information.

5.6 References

Allan, D. R., Blake, A. J., Huang, D., Prior, T. J. & Schroeder, M. (2006). *Chem. Commun. (Cambridge, U. K.),* 4081-4083.

Allen, F. H. (2002). *Acta Crystallogr., Sect. B: Struct. Sci.* **B58**, 380-388.

Altomare, A., Cascarano, G., Giacovazzo, C., Guagliardi, A., Burla, M. C., Polidori, G. & Camalli, M. (1994). *J. Appl. Cryst.* **27**, 435.

Awaga, K., Sekine, T., Okawa, M., Fujita, W., Holmes, S. M. & Girolami, G. S. (1998). *Chem. Phys. Lett.* **293**, 352-356.

Barsan, M. M., Butler, I. S., Fitzpatrick, J. & Gilson, D. F. R. (2011). *J. Raman Spectrosc.* **42**, 1820-1824.

Beall, G. W., Milligan, W. O., Korp, J. & Bernal, I. (1977). *Inorg. Chem.* **16**, 2715-2718.

Bhatt, P., Yusuf, S. M., Bhatt, R. & Schuetz, G. (2012). *Appl. Phys. A: Mater. Sci. Process.* **109**, 459-469.

Birch, F. (1947). *Phys. Rev.* **71**, 809-824.

Bleuzen, A., Cafun, J.-D., Bachschmidt, A., Verdaguer, M., Munsch, P., Baudelet, F. & Itie, J.-P. (2008). *J. Phys. Chem. C* **112**, 17709-17715.

Boldyreva, E. V. (2008). *Acta Crystallogr., Sect. A: Found. Crystallogr.* **64**, 218-231.

Brandenburg, K. (1999). *DIAMOND.*

Bruker (2001). *Bruker AXS Inc., Madison, Wisconsin, USA.*

Byrne, P. J., Richardson, P. J., Chang, J., Kusmartseva, A. F., Allan, D. R., Jones, A. C., Kamenev, K. V., Tasker, P. A. & Parsons, S. (2012). *Chem. - Eur. J.* **18**, 7738-7748, S7738/7731.

Catafesta, J., Haines, J., Zorzi, J. E., Pereira, A. S. & Perottoni, C. A. (2008). *Phys. Rev. B: Condens. Matter Mater. Phys.* **77**, 064104/064101-064104/064105.

Chapman, K. W., Chupas, P. J. & Kepert, C. J. (2006). *J. Am. Chem. Soc.* **128**, 7009-7014.

Coehlo, A. (2012). *TOPAS-Academic.* Version 5.

Cornia, A., Fabretti, A. C., Sessoli, R., Sorace, L., Gatteschi, D., Barra, A. L., Daiguebonne, C. & Roisnel, T. (2002). *Acta Crystallogr., Sect. C: Cryst. Struct. Commun.* **C58**, m371-m373.

Coronado, E., Gimenez-Lopez, M. C., Levchenko, G., Romero, F. M., Garcia-Baonza, V., Milner, A. & Paz-Pasternak, M. (2005). *J. Am. Chem. Soc.* **127**, 4580-4581.

Dawson, A., Allan, D. R., Parsons, S. & Ruf, M. (2004). *J. Appl. Crystallogr.* **37**, 410-416.

Dong, W., Zhang, W., Yan, O.-Y., Zhu, L.-N., Liao, D.-Z., Yoshimura, K., Jiang, Z.-H., Yan, S.-P. & Cheng, P. (2007). *J. Magn. Magn. Mater.* **309**, 7-10.

Egan, L., Kamenev, K., Papanikolaou, D., Takabayashi, Y. & Margadonna, S. (2006). *J. Am. Chem. Soc.* **128**, 6034-6035.

Ferrari, A., Tani, M. E. & Morisi, E. (1962). *Acta Crystallogr.* **15**, 90.

Fortes, A. D. (2004). University of London.

Galloway, K. W., Moggach, S. A., Parois, P., Lennie, A. R., Warren, J. E., Brechin, E. K., Peacock, R. D., Valiente, R., Gonzalez, J., Rodriguez, F., Parsons, S. & Murrie, M. (2010). *CrystEngComm* **12**, 2516-2519.

Giriat, G. (2011). PhD thesis, University of Edinburgh, Edinburgh.

Giriat, G., Kamenev, K., Moggach, S. A. & Parsons, S. (in preparation). Edinburgh: University of Edinburgh.

Giriat, G., Wang, W., Attfield, J. P., Huxley, A. D. & Kamenev, K. V. (2010). *Rev. Sci. Instrum.* **81**, 073905/073901-073905/073905.

Goeta, A. E. & Howard, J. A. K. (2004). *Chem. Soc. Rev.* **33**, 490-500.

Goodwin, A. L., Chapman, K. W. & Kepert, C. J. (2005). *J. Am. Chem. Soc.* **127**, 17980-17981.

Graham, A. J., Allan, D. R., Muszkiewicz, A., Morrison, C. A. & Moggach, S. A. (2011). *Angew. Chem., Int. Ed.* **50**, 11138-11141, S11138/11131-S11138/11137.

Graham, A. J., Tan, J.-C., Allan, D. R. & Moggach, S. A. (2012). *Chem. Commun. (Cambridge, U. K.)* **48**, 1535-1537.

Granier, T., Gallois, B., Gaultier, J., Real, J. A. & Zarembowitch, J. (1993). *Inorg. Chem.* **32**, 5305-5312.

Gudel, H. U., Stucki, H. & Ludi, A. (1973). *Inorg. Chim. Acta* **7**, 121-124.

Guetlich, P., Gaspar, A. B., Garcia, Y. & Ksenofontov, V. (2007). *C. R. Chim.* **10**, 21-36.

Herren, F., Fischer, P., Ludi, A. & Haelg, W. (1980). *Inorg. Chem.* **19**, 956-959.

Hoffman, R. S. (2003). *Toxicol. Rev.* **22**, 29-40.

Katrusiak, A. (2008). *Acta Crystallogr., Sect. A: Found. Crystallogr.* **64**, 135-148.

Kaye, S. S. & Long, J. R. (2005). *J. Am. Chem. Soc.* **127**, 6506-6507.

Keggin, J. F. & Miles, F. D. (1936). *Nature (London, U. K.)* **137**, 577-578.

Kettle, S. F. A., Diana, E., Marchese, E. M. C., Boccaleri, E. & Stanghellini, P. L. (2011). *J. Raman Spectrosc.* **42**, 2006-2014.

Kosaka, W., Nomura, K., Hashimoto, K. & Ohkoshi, S. (2005). *J. Am. Chem. Soc.* **127**, 8590-8591.

Ksenofontov, V., Levchenko, G., Reiman, S., Gutlich, P., Bleuzen, A., Escax, V. & Verdaguer, M. (2003). *Phys. Rev. B: Condens. Matter Mater. Phys.* **68**, 024415/024411-024415/024416.

Kuznetsov, A., Dmitriev, V., Dubrovinsky, L., Prakapenka, V. & Weber, H. P. (2002). *Solid State Commun.* **122**, 125-127.

Ludi, A., Guedel, H. U. & Ruegg, M. (1970). *Inorg. Chem.* **9**, 2224-2227.

Lue, Z., Wang, X., Liu, Z., Liao, F., Gao, S., Xiong, R., Ma, H., Zhang, D. & Zhu, D. (2006). *Inorg. Chem.* **45**, 999-1004.

Lummen, T. T. A., Gengler, R. Y. N., Rudolf, P., Lusitani, F., Vertelman, E. J. M., van Koningsbruggen, P. J., Knupfer, M., Molodtsova, O., Pireaux, J. J. & van Loosdrecht, P. H. M. (2008). *J. Phys. Chem. C* **112**, 14158-14167.

Macrae, C. F., Edgington, P. R., McCabe, P., Pidcock, E., Shields, G. P., Taylor, R., Towler, M. & van, d. S. J. (2006). *J. Appl. Crystallogr.* **39**, 453-457.

Maeda, T., Mito, M., Deguchi, H., Takagi, S., Kaneko, W., Ohba, M. & Okawa, H. (2005). *Polyhedron* **24**, 2497-2500.

Margadonna, S., Prassides, K. & Fitch, A. N. (2004). *Angew Chem Int Ed Engl* **43**, 6316-6319.

Marshall, W. G. & Francis, D. J. (2002). *J. Appl. Crystallogr.* **35**, 122-125.

Merrill, L. & Bassett, W. A. (1974). *Rev. Sci. Instrum.* **45**, 290-294.

Miller, R. A. & Schuele, D. E. (1969). *J. Phys. Chem. Solids* **30**, 589-600.

Moggach, S. A., Allan, D. R., Parsons, S. & Warren, J. E. (2008). *J. Appl. Crystallogr.* **41**, 249-251.

Moggach, S. A., Galloway, K. W., Lennie, A. R., Parois, P., Rowantree, N., Brechin, E. K., Warren, J. E., Murrie, M. & Parsons, S. (2009). *CrystEngComm* **11**, 2601-2604.

Moggach, S. A. & Parsons, S. (2009). *Spectrosc. Prop. Inorg. Organomet. Compd.* **40**, 324-354.

Moggach, S. A., Parsons, S. & Wood, P. A. (2008). *Crystallogr. Rev.* **14**, 143-184.

Moritomo, Y., Hanawa, M., Ohishi, Y., Kato, K., Takata, M., Kuriki, A., Nishibori, E., Sakata, M., Ohkoshi, S., Tokoro, H. & Hashimoto, K. (2003). *Phys. Rev. B: Condens. Matter Mater. Phys.* **68**, 144106/144101-144106/144107.

Ohkoshi, S.-i., Iyoda, T., Fujishima, A. & Hashimoto, K. (1997). *Phys. Rev. B: Condens. Matter* **56**, 11642-11652.

Ohkoshi, S.-i., Tokoro, H. & Hashimoto, K. (2005). *Coord. Chem. Rev.* **249**, 1830-1840.

Ohkoshi, S., Matsuda, T., Tokoro, H. & Hashimoto, K. (2005). *Chem. Mater.* **17**, 81-84.

Ohkoshi, S., Tokoro, H., Utsunomiya, M., Mizuno, M., Abe, M. & Hashimoto, K. (2002). *J. Phys. Chem. B* **106**, 2423-2425.

Piermarini, G. J., Block, S., Barnett, J. D. & Forman, R. A. (1975). *J. Appl. Phys.* **46**, 2774-2780.

Prescimone, A., Morien, C., Allan, D., Schlueter, J. A., Tozer, S. W., Manson, J. L., Parsons, S., Brechin, E. K. & Hill, S. (2012). *Angew. Chem., Int. Ed.* **51**, 7490-7494, S7490/7491-S7490/7498.

Salmon, L., Vertelman, E. J. M., Murgui, C. B., Cobo, S., Molnar, G., van, K. P. J. & Bousseksou, A. (2009). *Eur. J. Inorg. Chem.*, 760-768.

Samain, L., Grandjean, F., Long, G. J., Martinetto, P., Bordet, P. & Strivay, D. (2013). *J. Phys. Chem. C* **117**, 9693-9712.

Sato, O. (2004). *J. Photochem. Photobiol., C* **5**, 203-223.

Schlafer, V. H. L., Wasgestian, H. W. F. & Herzog, G. (1971). *Berichte der Bunsen-Gesellschaft fur physikalische Chemie* **75**, 878.

Sheldrick, G. M. (2008). *SADABS.* Version 2008-1.

Spek, A. L. (2003). *J. Appl. Crystallogr.* **36**, 7-13.

Tokoro, H., Ohkoshi, S.-i. & Hashimoto, K. (2003). *Appl. Phys. Lett.* **82**, 1245-1247.

Usuki, N., Yamada, M., Ohba, M. & Okawa, H. (2001). *J. Solid State Chem.* **159**, 328-335.

Verdaguer, M., Bleuzen, A., Marvaud, V., Vaissermann, J., Seuleiman, M., Desplanches, C., Scuiller, A., Train, C., Garde, R., Gelly, G., Lomenech, C., Rosenman, I., Veillet, P., Cartier, C. & Villain, F. (1999). *Coord. Chem. Rev.* **190-192**, 1023-1047.

Verdaguer, M., Bleuzen, A., Train, C., Garde, R., De, B. F. F. & Desplanches, C. (2000). *Spec. Publl. - R. Soc. Chem.* **252**, 105-122.

Waldorf, D. L. & Alers, G. A. (1962). *J. Appl. Phys.* **33**, 3266-3269.

Weihe, H. & Gudel, H. U. (2000). *Comments Inorg. Chem.* **22**, 75-103.

Zentkova, M., Arnold, Z., Kamarad, J., Kavecansky, V., Lukacova, M., Mat'as, S., Mihalik, M., Mitroova, Z. & Zentko, A. (2007). *J. Phys.: Condens. Matter* **19**, 266217/266211-266217/266210.

Zentkova, M., Mihalik, M., Kovac, J., Zentko, A., Mitroova, Z., Lukacova, M., Kavecansky, V. & Kiss, L. F. (2006). *Phys. Status Solidi B* **243**, 272-276.

Chapter 6

A High-Pressure Low-Temperature Single-Crystal X-ray Study of KCP(Br)

6.1 Introduction

Partially-oxidized tetracyanoplatinates (POTPs) constitute a subgroup of mixed-valence square-planar compounds that have been the subject of extensive theoretical and practical investigations. Columnar stacking of the tetracyanoplatinate moieties (Figure 6.1) is a characteristic structural feature of these materials in the crystalline state, leading to the formation of linear isolated platinum chains along one crystallographic axis (Underhill & Wood, 1978). The close proximity of adjacent platinum atoms within these chains allows for significant overlap of their $5d_z^2$ orbitals, causing delocalization of electron density and giving rise to a one-dimensional band structure (Kuse & Zeller, 1971).

Figure 6.1: Schematic of (a) POTP precursor with fully occupied $5d_z^2$ orbital and (b) one-dimensional chains formed through overlap of orbitals (Minot & Perlstein, 1971)

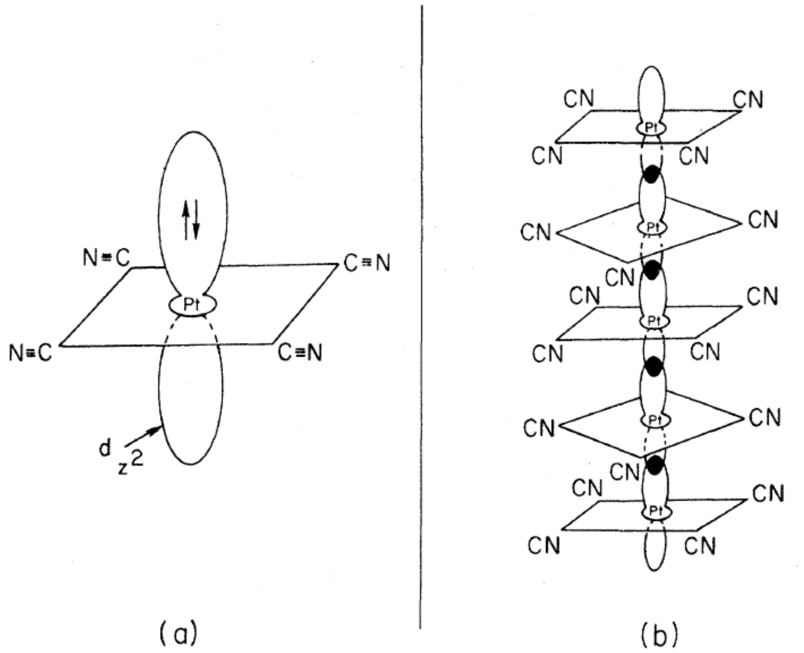

Unlike the purely Pt(II) tetracyanoplatinates which are insulators with a fully occupied $5d_z^2$ valence band, POTPs possess a non-integer platinum oxidation state and partially depopulated valence band (Figure 6.2) arising from comproportionation of Pt(IV) with Pt(II). Removal of electron density from the most anti-bonding portion of the valence band results in a contraction of the platinum chain, with ensuing Pt-Pt distances only slightly longer than those found in the bulk metal (Minot & Perlstein, 1971, Lecrone *et al.*, 1972, Zeller, 1972). These structural features and their associated properties have been of significant interest to solid-state researchers, particularly with regard to improving understanding of phenomena such as one-dimensional conductivity (Peters & Eagen, 1975), room-temperature superconduction (Gomm & Underhill, 1972), and Peierls transitions (Comes *et al.*, 1973).

Figure 6.2: Metallic band structure of KCP(Br) generated through overlap of partially depopulated $5d_z^2$ orbitals (Krogmann, 1969)

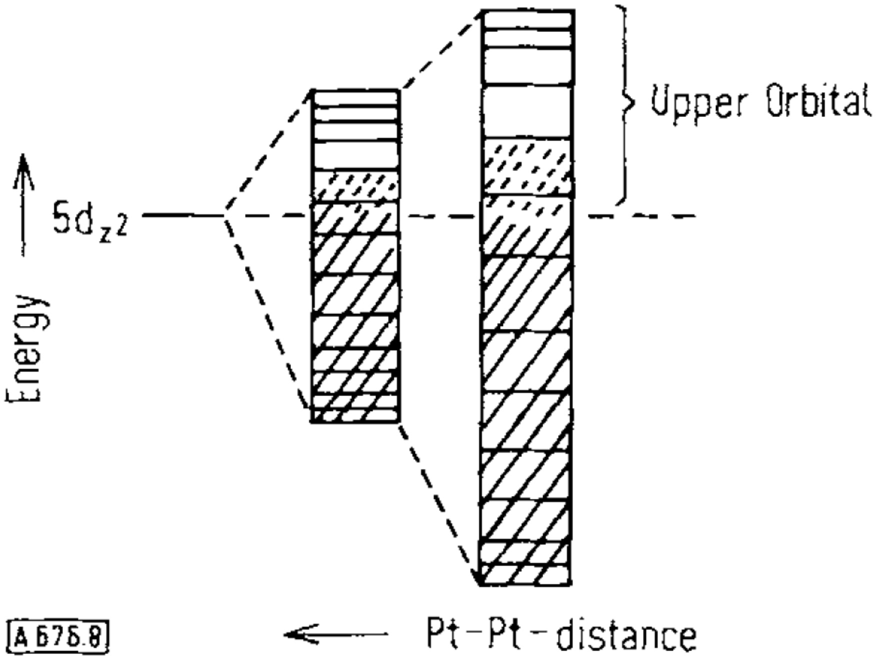

$K_2[Pt(CN)_4]Br_{0.3}.3.2H_2O$ (KCP(Br)) (Figure 6.3) is one of the prototypical POTPs having been synthesized in 1969 alongside its chloride analogue (KCP(Cl)) (Krogmann & Hausen, 1968). The platinum chains in KCP(Br) are formed of adjacent square-planar tetracyanoplatinate centres stacked antiprismatically along the crystallographic *c* axis of a *P*4*mm* unit cell (Minot & Perlstein, 1971, Williams *et al.*, 1974, Peters & Eagen, 1976). Alternating layers of potassium ions and water molecules lying perpendicular to these platinum chains interact with the cyanide ligands through electrostatic and hydrogen bonding interactions respectively (Deiseroth & Schulz, 1974).

Figure 6.3: KCP(Br) unit cell viewed along the **c** (top) and **b** (bottom) axes. Colour scheme: Pt white, C grey, N blue, O red, K purple, and Br orange. Hydrogen atoms removed for clarity.

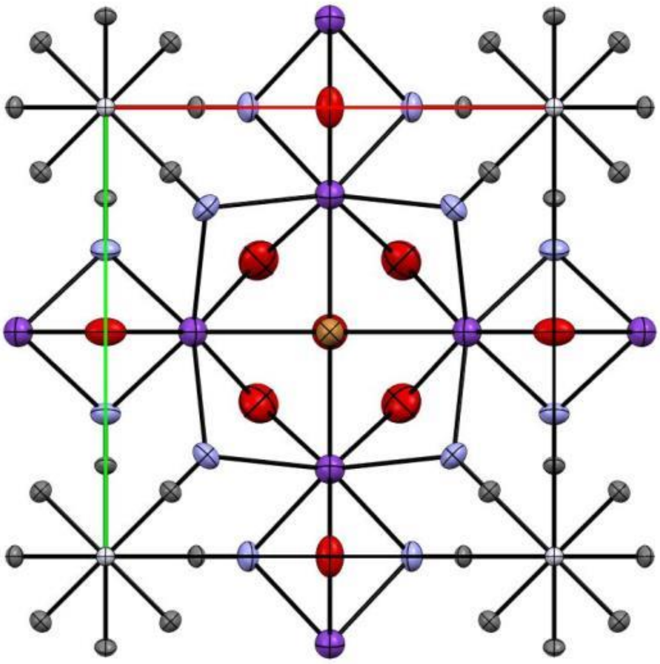

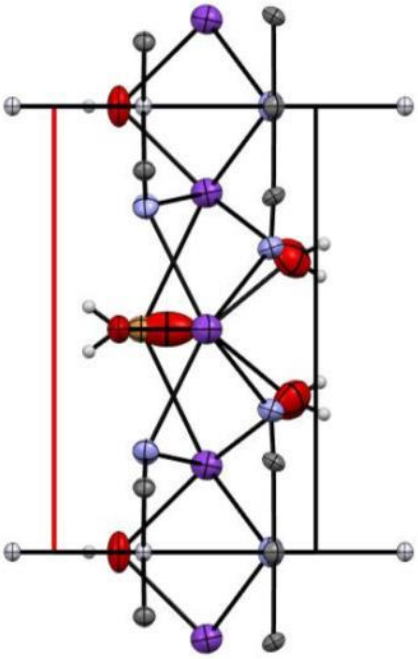

Distortions of the platinum centre geometry allow the cyanide ligands to bend further towards the potassium layers leading to an overall enhancement of the electrostatic interactions (Heger *et al.*, 1978). At the centre of the *ab* plane between the potassium and water layers are the residual solvent voids, containing statistically disordered charge-balancing bromide anions and water molecules in non-overlapping atomic positions (Peters & Eagen, 1975). Bromine fulfils the role of oxidizing agent during synthesis and possesses an occupancy of 60% in the crystal structure, indicating a shared formal platinum oxidation state of +2.3 (Kuse & Zeller, 1971, Gomm & Underhill, 1972, Thomas, Hsu, *et al.*, 1972) and an approximately 5/6 full valence band (Comes *et al.*, 1973).

The highly one-dimensional structure of KCP(Br) gives rise to similarly anisotropic electrical properties, with room-temperature conductivity along the *c* axis several orders of magnitude greater compared with the *ab* plane. Electrical conductivity measurements along *c* have been shown to vary significantly between crystals, and furthermore their values are more characteristic of a semiconductor despite possessing a theoretically metallic band structure (Bernasconi *et al.*, 1972, Gomm & Underhill, 1972, Peters & Eagen, 1976). These unusual observations have been rationalized using an interrupted strands model which hypothesizes that long-range order in the platinum chains is disrupted by crystal lattice defects, thus creating an energy barrier to electron movement which can only be overcome through hopping to an adjacent chain. Lowering the temperature decreases the probability of electron hopping leading to a decline in conductivity and the onset of an insulating three-dimensional electronic structure (Kuse & Zeller, 1971, Thomas, Labes, *et al.*, 1972, Zeller, 1972, Renker *et al.*, 1973, Rice & Bernasconi, 1973, Ruegg *et al.*, 1973, Peters & Eagen, 1976). This model is further complicated by the presence of an energetically favourable Peierls distortion at extremely low temperatures, and is structurally manifested through the formation of alternating long and short bonds in the Pt chains (Comes *et al.*, 1973, Renker *et al.*, 1973, Ruegg *et al.*, 1973, Heger *et al.*, 1978).

Investigations of the structure-property relationship in POTPs have historically involved the creation of synthetic analogues containing a range of cations and anions. (Krogmann, 1969, Keefer *et al.*, 1976, Williams *et al.*, 1976, Williams *et* *al.*, 1977, Brown & Williams, 1978, Brown *et al.*, 1978, Johnson *et al.*, 1978, Schultz *et al.*, 1978, Underhill & Wood, 1978, Williams, Schultz, *et al.*, 1978, Williams, Johnson, *et al.*, 1978, Brown *et al.*, 1979). There has however been growing interest in the application of non-ambient conditions such as pressure for altering the electronic properties of these systems. High-pressure conditions are a particularly efficient mechanism for producing structural changes, and have become increasingly facile through improvements in technology and methodology (Boldyreva, 2008, Katrusiak, 2008, Moggach *et al.*, 2008). Metal-ligand coordination bonds have proven particularly responsive to changes in pressure (Allan *et al.*, 2006, Moggach *et al.*, 2009, Moggach & Parsons, 2009, Prescimone *et al.*, 2012), and this has been exploited in studies of other coordination compound properties such as porosity (Graham *et al.*, 2011, Graham *et al.*, 2012), colour (Galloway *et al.*, 2010, Byrne *et al.*, 2012), and spin state (Granier *et al.*, 1993, Guetlich *et al.*, 2007).

The effect of pressure on the structure and electrical properties of KCP(Br) has been explored in several studies reported in the literature. A logarithmic increase in parallel conductivity between ambient pressure and 2.5 GPa in one high-pressure study was correlated with simultaneous reductions in the unit cell parameters, and this was believed to indicate an enhancement of $5d_z^2$ orbital overlap and inter-chain electron hopping (Interrante & Bundy, 1972). Reductions in conductivity above this pressure could not be explained using the data obtained in this experiment since the unit cell parameters continued to decline beyond this pressure region. Further high-pressure experiments identified a major structural distortion of the cyanide ligands above 2.1 GPa which were thought to produce a significant impact on the conductivity perpendicular to the platinum chains (Kobayashi *et al.*, 1980). More recently collected and unpublished high-pressure conductivity measurements by Nicholas Funnell, Anna Kusmertseva, and Konstantin Kamenev (Funnell *et al.*, 2011) suggested a conductivity maximum at approximately 4.5 GPa and 3.4 GPa respectively (Figures 6.4 and 6.5), revealing the potential for significant variation in the pressure-induced conductivity of this compound.

Figure 6.4: Resistivity measurements of KCP(Br) at high-pressures conducted by Nicholas Funnell (Funnell *et al.*, 2011)

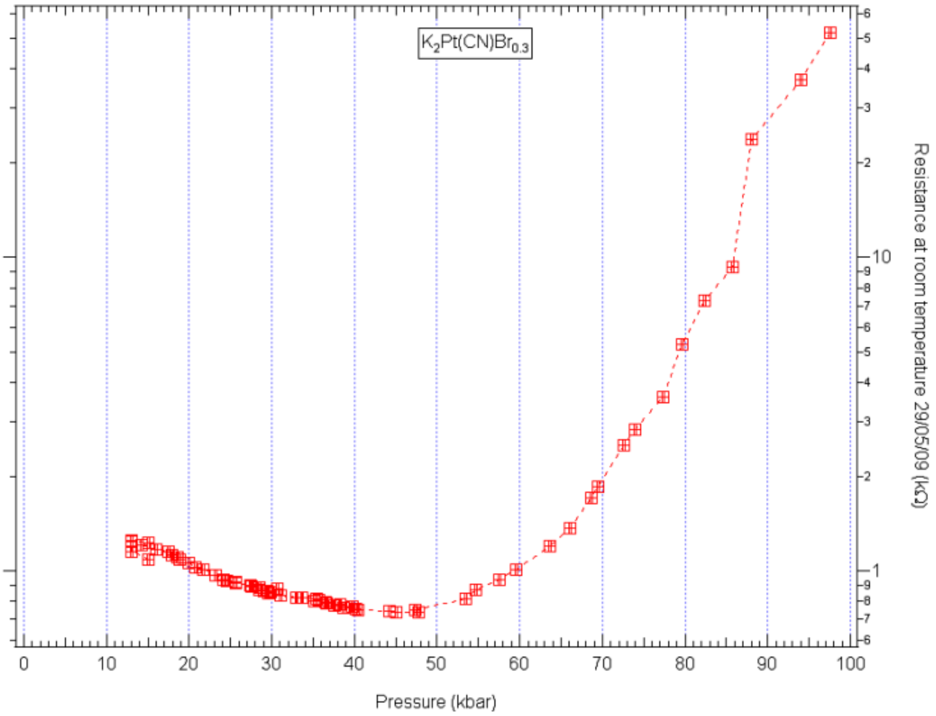

Figure 6.5: Resistivity measurements *versus* inverse thermal energy of KCP(Br) at high-pressures conducted by Anna Kusmertseva (Funnell *et al.*, 2011)

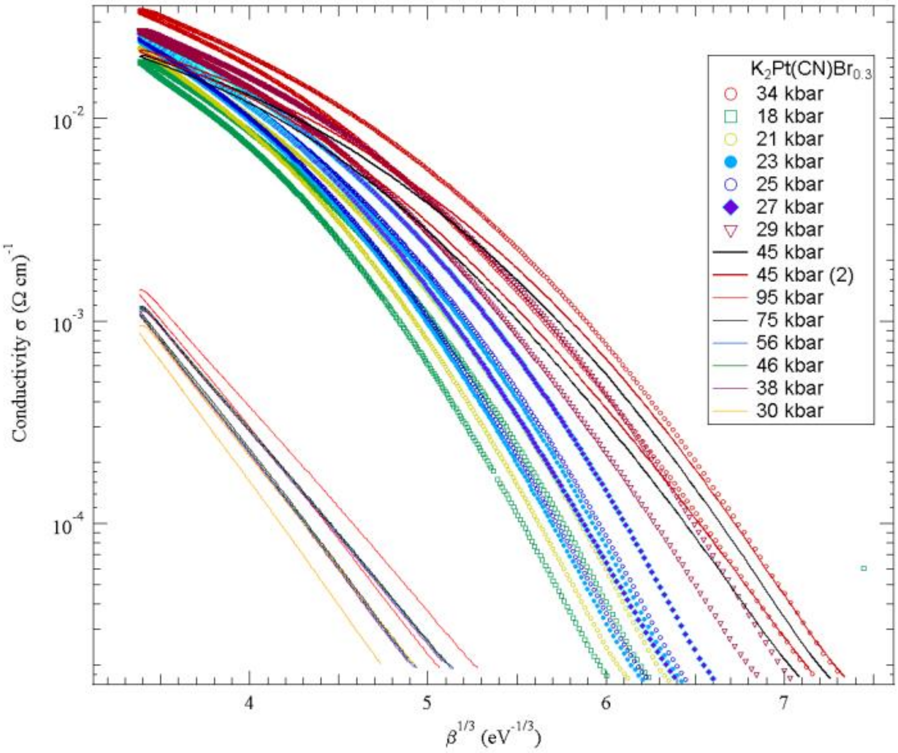

The impact of high-pressure conditions on the previously determined temperature-dependence of KCP(Br) electrical conductivity has also been investigated by solid-state researchers. A high-pressure high-temperature study discovered a logarithmic increase in conductivity upon heating from 30°C to 80°C throughout a pressure range between 0.15 GPa and 6.0 GPa, and furthermore identified a minimum in the thermal activation of conductivity at approximately 3.7 GPa (Interrante & Bundy, 1972). Likewise unpublished high-pressure low-temperature resistivity data collected by Nicholas Funnell, Anna Kusmertseva, and Konstantin Kamenev (Funnell *et al.*, 2011) (Figure 6.6) displayed an increasingly rapid decline in conductivity at both 1.8 GPa and 3.2 GPa until 50 K and 30 K respectively which indicates the appearance of an insulating electronic structure. However this behaviour changes drastically below approximately 40 K at 1.8 GPa and 20 K at 3.2 GPa as the conductivity is enhanced by several orders of magnitude before flattening at 20 K and 5 K respectively. The lack of single-crystal diffraction data collected under these conditions means that the structural features responsible for this electronic transition are currently unknown.

Figure 6.6: Resistivity measurements of KCP(Br) at high-pressures and low-temperatures collected by Anna Kusmertseva (Funnell *et al.*, 2011)

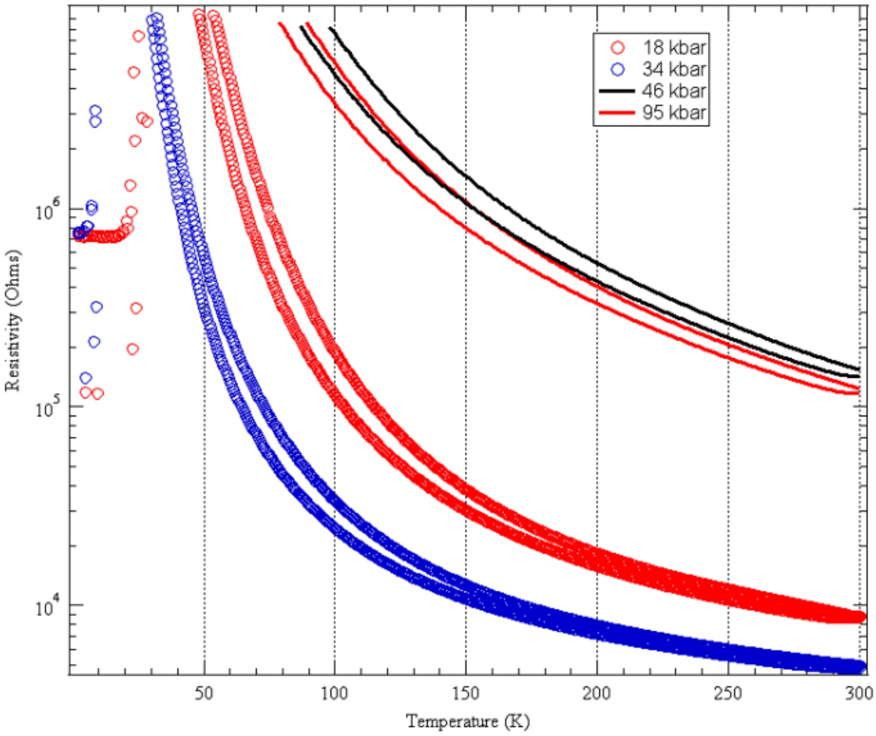

A significant technical challenge associated with investigating structure-property relationships under high-pressure low-temperature conditions is the extremely long cooling times inherent in typical Diamond Anvil Cells (DACs). Therefore we have designed a novel DAC here at the University of Edinburgh (Figure 6.7) with the purpose of conducting such high-pressure low-temperature X-ray diffraction experiments. This cell is significantly smaller than a normal DAC and constructed from a beryllium-copper alloy (BERYLCO25), allowing it to cool much more quickly in a closed-cycle cryostat. Pressure is generated through the turning of screws which force opposing diamond culets closer together. Holes have been drilled in each side of the cell allowing it to be mounted in multiple orientations on an accompanying BERYLCO25 table. Another slot on one side of the cell allows a thermocouple to be inserted for *in-situ* temperature measurements. Here we report the first high-pressure low-temperature single-crystal X-ray diffraction study on the prototypical one-dimensional conductor KCP(Br), with the aim of improving our understanding of the previously observed high-pressure low-temperature conductivity measurements.

Figure 6.7: Micro-cell (left) sitting next to a typical Merrill-Bassett cell (right)

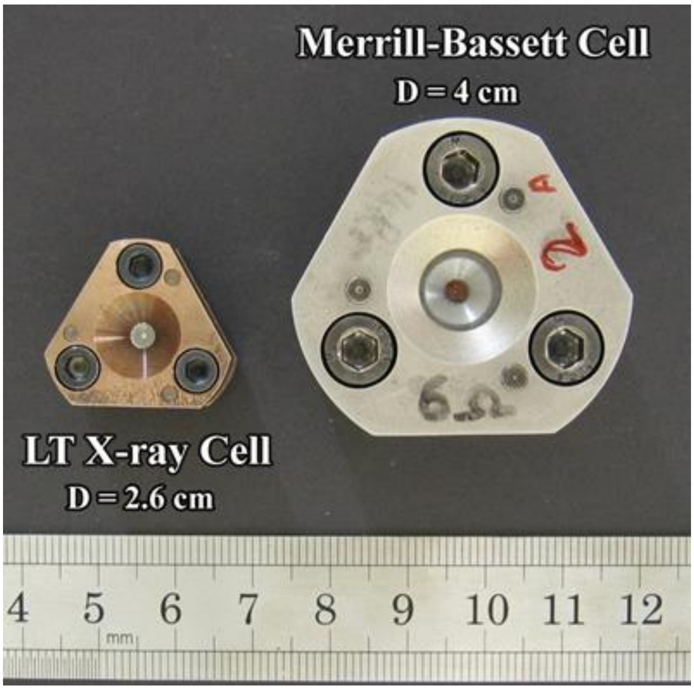

6.2 Experimental

6.2.1 Sample Preparation

KCP(Br) was synthesized in accordance with the literature method and recrystallized from water (Krogmann & Hausen, 1968).

6.2.2 Apparatus

The high pressure experiments utilized a miniature Boehler-Almax Merrill-Bassett DAC, constructed from a beryllium-copper alloy (BERYLCO25) with an opening angle of 40°, 1000 μm culet brilliant-cut diamonds (a backing disc supporting one diamond whilst the platen supports the other), and a tungsten gasket. A table for mounting the cell on the goniometer head has also been constructed from the same beryllium-copper alloy as the cell body. Paraffin was used as the hydrostatic medium. High-pressure single-crystal X-ray diffraction studies were performed at the University of Durham using the XIPHOS instrument (Figure 6.8), consisting principally of a χ-geometry four-circle Huber goniometer, Bruker APEXII CCD area detector, and Helios-focussed monochromatic Mo-K_α radiation. Low-temperature conditions were provided by a modified APD 2023 Displex cryogenic refrigerator and fully enclosed beryllium shroud (Probert *et al.*, 2010). Separate data collection strategies were employed for the XIPHOS ambient-temperature and low-temperature experiments (Tables 6.1 and 6.2), due to a combination of instrument time constraints and greater uncertainty in the low-temperature structure. The pressure inside the gasket hole was measured using the ruby fluorescence method (Piermarini *et al.*, 1975) between data sets at ambient temperature. Ambient-pressure ambient-temperature measurements were carried out at the University of Edinburgh using a three-circle Bruker APEX diffractometer (Bruker, 2001) with TRIUMPH curved-crystal monochromatic Mo-K_α radiation. Data collection strategies were as described by Dawson *et al*. (Dawson *et al.*, 2004).

Figure 6.8: XIPHOS instrument (top) and with shroud attached (bottom)

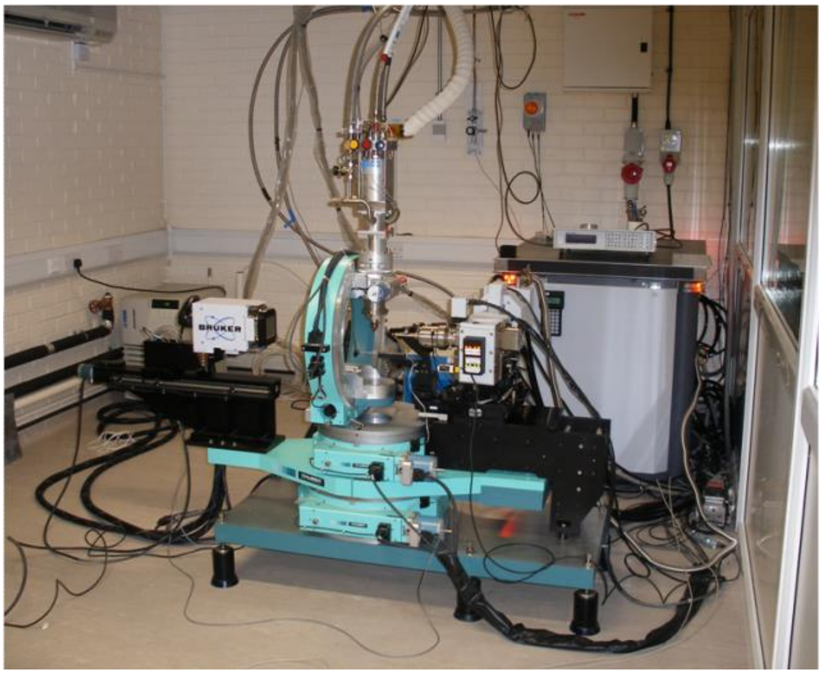

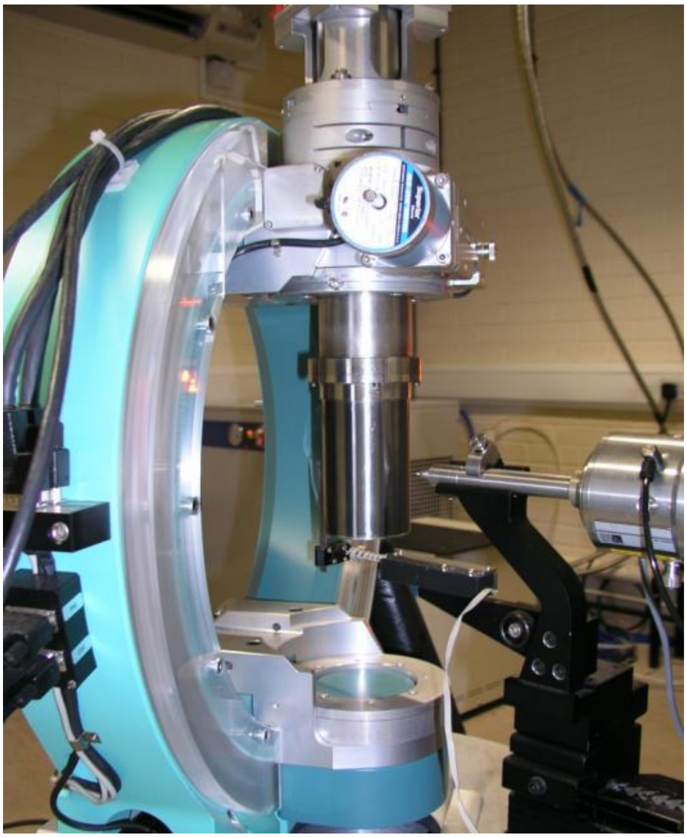

Table 6.1: XIPHOS data collection strategy for high-pressure ambient-temperature

#	Type	Start	End	2θ	ω	χ	dd
1	φ	356.5	41	27	15	180	60
2	φ	6.50	322	27	15	180	60
3	φ	176.5	218.5	27	15	180	60
4	φ	186.5	142	27	15	180	60
5	φ	359.5	36	-27	345	180	60
6	φ	9.5	333	-27	345	180	60
7	φ	179.5	216	-27	345	180	60
8	φ	189.5	153	-27	345	180	60

Table 6.2: Additional diffraction runs utilized for the XIPHOS high-pressure low-temperature data collection

#	Type	Start	End	2θ	ω	χ	dd
9	φ	356.5	41	27	15	180	110
10	φ	6.50	322	27	15	180	110
11	φ	176.5	218.5	27	15	180	110
12	φ	186.5	142	27	15	180	110
13	φ	359.5	36	-27	345	180	110
14	φ	9.5	333	-27	345	180	110
15	φ	179.5	216	-27	345	180	110
16	φ	189.5	153	-27	345	180	110
17	φ	355	37	0	0	180	60
18	φ	5	323	0	0	180	60
19	φ	175	217	0	0	180	60
20	φ	185	143	0	0	180	60
21	φ	341	21	27	15	-160	60
22	φ	351	311	27	15	-160	60
23	φ	161	201	27	15	-160	60
24	φ	171	131	27	15	-160	60

6.2.3 Data Processing

Cell indexing and integration were carried out using the Bruker APEX II (Bruker, 2001) software with dynamic masks generated by ECLIPSE (Dawson *et al.*, 2004). Absorption corrections were carried out using SADABS (Sheldrick, 2008). The crystal structure was solved by SIR92 (Altomare *et al.*, 1994). Merging and refinement of the data was performed using CRYSTALS (Betteridge *et al.*, 2003). Distance and thermal similarity restraints were derived from the ambient-pressure 150 K structure determination and applied to the positions of non-metal atoms. All structures were refined against $|F|$ with reflections $|F| < 4\sigma(|F|)$ omitted. Crystal data and refinement statistics are recorded in Table 6.3.

Table 6.3: Crystal data for KCP

Pressure (GPa)	0.00	1.80	1.80
T_{cryo} (K)	300	300	4
λ (Å)	0.7107	0.7107	0.7107
Sinθ/λ (Å)	0.80	0.80	0.80
Crystal System	Tetragonal	Tetragonal	Tetragonal
Space Group	*P*4*mm*	*P*4*mm*	*P*4*mm*
a (Å)	9.893(8)	9.6286(4)	9.6310(4)
c (Å)	5.800(4)	5.7031(7)	5.6933(5)
V (Å^3)	567.7(8)	528.73(7)	528.09(6)
Z	2	2	2
D_{calc} (Mg m^{-3})	2.658	2.854	2.858
Reflections	1655	1233	2898
Unique Reflections	488	338	392
R_{int}	0.018	0.041	0.049
R	0.0148	0.0451	0.0485
R_w	0.0369	0.0520	0.0569
GooF	1.0438	1.0456	1.1433
Data:Parameters	486:54	228:54	275:54
No. Restraints	47	47	47
ρ_{max}/ρ_{min} (e.Å^{-3})	1.24/-1.13	1.29/-1.44	2.23/-2.40

6.2.4 Structural Analysis

Analysis of the bonding interactions was conducted using the program PLATON (Spek, 2003), while MERCURY (Macrae *et al.*, 2006) was utilized for visualization and calculation of the void volumes using a probe radius of 0.5 Å and a grid spacing of 0.1 Å. Searches of the Cambridge Structural Database v5.35 (Allen, 2002) employed the program CONQUEST v1.16.

6.3 Results

6.3.1 General comments

The crystal structure of KCP(Br) has been determined at ambient-conditions, 1.8 GPa at ambient-temperature, and 1.8 GPa at 4 K. KCP(Br) is a rare example of a compound crystallizing in the *P*4*mm* space group, and a search of the CSD reveals that by 2014 no other crystal structures using this space group had been reported (Allen, 2002). No change in crystal system or space group was observed throughout these experiments. The application of pressure followed by cooling produces different responses in the unit cell parameters. A substantial reduction in the unit cell *a* = *b* axes of 9.897(8) Å to 9.6286(4) Å between 0.0 and 1.8 GPa (2.71 % reduction) is followed by a comparatively small increase to 9.6310(4) Å upon cooling to 4 K (0.02 % increase). By contrast the significant *c* axis contraction of 5.802(4) Å to 5.7031(7) Å over the same pressure range at ambient-temperature is continued with a further small decline to 5.6933(5) Å at 1.8 GPa and 4 K (1.70 % and 0.17 % decline respectively).

6.3.2 Response of the Pt chains to pressure and cooling

Platinum chains in KCP(Br) consist of two independent and adjacent square-planar tetracyanoplatinate centres arranged in a square antiprismatic conformation. The naming scheme and sub-structure of KCP(Br) are displayed in Figure 6.9, and the response of the Pt coordination environments to high-pressure and low-temperature conditions is given in Tables 6.4 and 6.5. Compression and cooling of the KCP(Br) structure produces divergent responses in the Pt coordination environments. An initial Pt1-Pt2 reduction of 2.897(5) Å to 2.846(16) Å between 0.00 GPa and 1.80 GPa remains unchanged at 4 K, whilst Pt1-Pt2^{i} (see Table 6.4 footnote) is unaffected by pressure but does decline significantly between 0.0 GPa and 1.80 GPa at 4 K from 2.905(5) Å to 2.847(12) Å. Meanwhile the decrease in C1-Pt1-C1^{ii} (see Table 6.5 footnote) angles between 0.00 GPa and 1.80 GPa from 179.3(5)° to 171.9(17)° contrasts with the comparatively insensitive C2-Pt2-C2^{ii} angles exhibiting a range of 179.3(5)° – 177.1(17)° under pressure. None of the remaining Pt chain interactions are significantly affected by variations in pressure and temperature throughout the experiment. The inter-chain Pt···Pt distances are determined by the length of the *a* = *b* axes and decline from 9.897(8) Å to 9.6286(4) Å between 0.0 GPa and 1.8 GPa before expanding to 9.6310(4) Å upon cooling to 4 K.

Figure 6.9: KCP(Br) sub-structure showing labelling scheme of Pt coordination environment with hydrogen atoms removed for clarity. Thermal ellipsoids represent 50% probability surfaces.

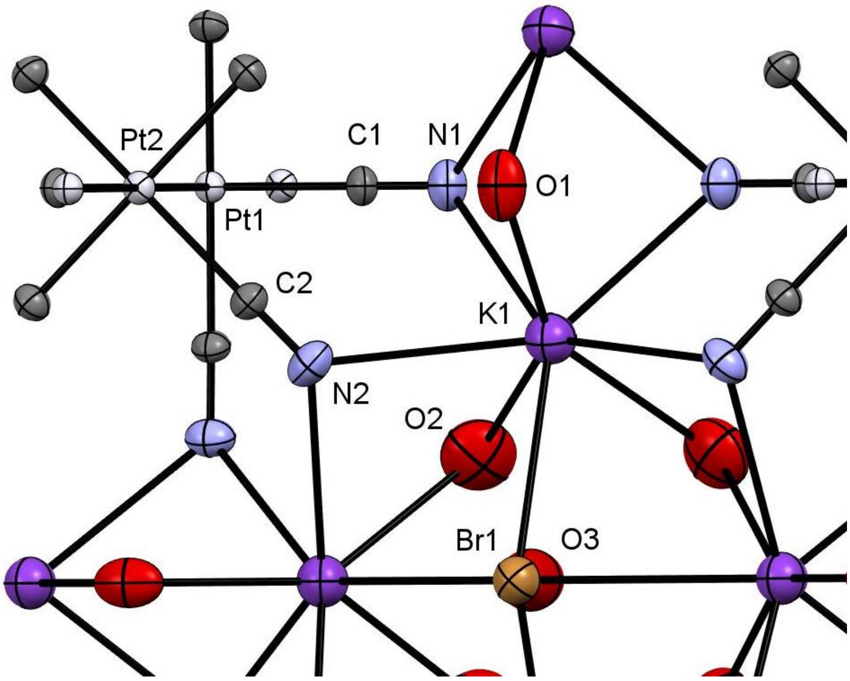

6.3.3 Response of the intermolecular interactions to pressure

The crystal structure of KCP(Br) contains three independent water molecules, one independent potassium cation, and one independent bromine anion. Intermolecular interactions between these components in addition to other notable interactions are listed in Table 6.6. Between 0.00 GPa and 1.80 GPa the K1···N1 and K1···N2 interactions decrease significantly from 3.000(8) Å to 2.92(2) Å and 3.058(8) Å to

2.92(2) Å respectively. Similar contractions in the N1···N1, N2···Br1, and O2···H22-N2 distances of 3.608(9) Å to 3.47(3) Å, 3.863(5) Å to 3.648(15) Å, and 3.055(13) Å to 2.84(5) Å respectively occur over the same pressure. All the remaining intermolecular interactions remain effectively unchanged in response to changes in pressure and temperature.

Table 6.4: Intramolecular bond lengths (Å) as a function of pressure and temperature

Pressure (GPa) T_{cryo} (K)	0.00 300	1.80 300	1.80 4
Pt1-Pt2	2.897(5)	2.846(16)	2.846(12)
Pt1-Pt2^{i}	2.905(5)	2.857(16)	2.847(12)
Pt1-C1	2.003(6)	2.03(3)	2.02(3)
Pt2-C2	2.021(5)	1.994(17)	1.998(15)
C1-N1	1.143(8)	1.06(3)	1.07(3)
C2-N2	1.116(7)	1.17(2)	1.18(2)

Symmetry operations: (i) x, y, 1+z

Table 6.5: Intramolecular bond angles (°) as a function of pressure and temperature

Pressure (GPa) T_{cryo} (K)	0.00 300	1.80 300	1.80 4
Pt2-Pt1-C1	89.6(3)	86.0(12)	88.8(12)
C1-Pt1-C1^{i}	90.00(1)	89.72(12)	89.98(4)
C1-Pt1-C1^{ii}	179.3(5)	171.9(17)	177.6(17)
Pt1-Pt2-C2	89.6(3)	91.5(12)	90.9(1)
C2-Pt2-C2^{i}	90.0(2)	90.0(7)	90.0(6)
C2-Pt2-C2^{ii}	179.1(5)	177.1(17)	178.2(15)
Pt1-C1-N1	177.5(10)	176(4)	177(4)
Pt2-C2-N2	178.5(11)	177(4)	175(3)

Symmetry operations: (i) 2-y, x, z; (ii) 2-x, 2-y, z

Table 6.6: Intermolecular distances (Å) as a function of pressure and temperature

Pressure (GPa)	0.00	1.80	1.80
T_{cryo} (K)	300	300	4
K1···N1	3.000(7)	2.92(2)	2.91(2)
K1···N2	3.058(7)	2.92(2)	2.90(2)
N1···N1	3.608(9)	3.47(3)	3.45(3)
N2···Br1	3.863(5)	3.648(15)	3.637(14)
O1-H11···N1	3.033(12)	2.95(5)	2.94(4)
O2-H22···N2	3.055(13)	2.84(5)	2.93(5)

6.3.4 Response of the crystallized solvent to pressure

Interstitial and solvent accessible voids in the crystal structure are exhibited in Table 6.7 and Figures 6.10 and 6.11. The interstitial void volume decreases from 6.90 Å^3 at 0.00 GPa to 1.09 Å^3 at 1.80 GPa and remains approximately constant upon cooling to 4 K, amounting to 1.2 %, 0.2 %, and 0.2 % of the unit cell volume respectively. No significant solvent accessible voids can be detected in the structure under any conditions. At ambient pressure the interstitial voids reside mainly in the *ab* plane between crystallized water and cyanide ligands on adjacent KCP(Br) layers, with an additional site between the disordered bromine atoms and water molecules. Compression of the crystal structure causes the disappearance of the *ab* planar sites leaving behind the bromine co-axial interstitial and residual solvent voids. The occupancies of the disordered bromine or oxygen site did not change throughout the high-pressure low-temperature study.

Table 6.7: Void and cell volumes as a function of pressure

Pressure (GPa)	0.00	1.80	1.80
T_{cryo} (K)	300	300	4
Unit Cell Volume (Å^3)	568.3	528.73	528.09
Interstitial Void Volume (Å^3)	6.90	1.09	0.95
Interstitial Volume/Cell Volume (%)	1.2	0.2	0.2
Solvent Accessible Volume (Å^3)	0.07	0.01	0.01
Solvent Volume/Cell Volume (%)	0.0	0.0	0.0

Figure 6.10: Interstitial voids at 0.00 GPa (top) and 1.80 GPa (bottom) viewed along **c**

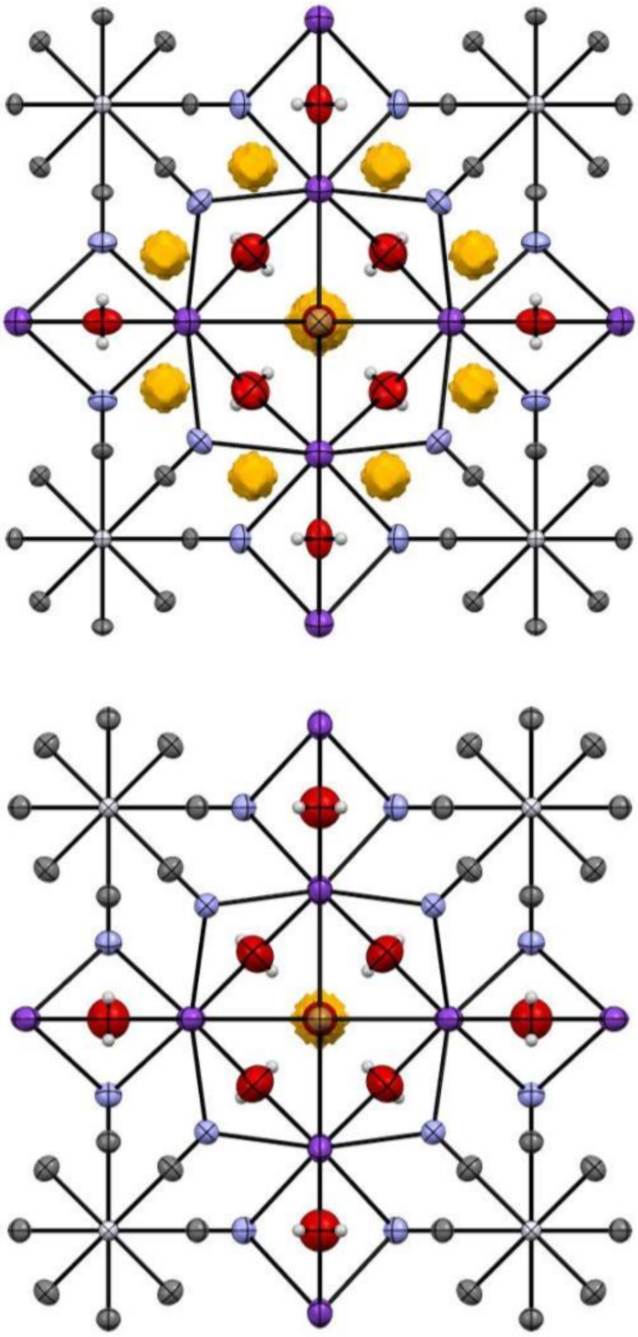

Figure 6.11: Interstitial voids at 0.00 GPa (left) and 1.80 GPa (right) viewed along **b**

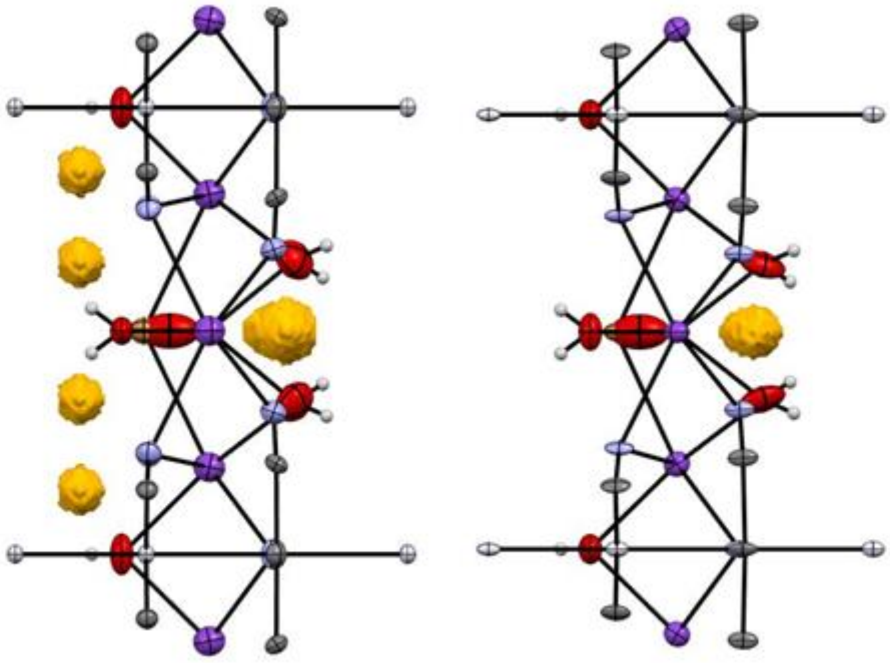

6.4 Discussion

6.4.1 Methodology

This high-pressure low-temperature KCP(Br) study is amongst the first experiments under these conditions to be performed using the XIPHOS facility, and therefore the current methodology must be reviewed to identify advantages of this approach and possible future improvements. Data collection times for these experiments were highly variable given the much larger collection strategy employed at high-pressure low-temperatures, and currently range from 6 to 26 hours when using a 20 s exposure time. Vacuum pumping and cooling constitute additional major contributions to experimental time, with the cryostat requiring at least 24 hours before reaching a stable temperature of 4 K. As a result obtaining a single high-pressure low-temperature data set on the XIPHOS currently requires approximately two days of diffractometer time.

Considering the very limited instrument time available at the XIPHOS facility a shorter well-defined collection strategy would be highly advantageous for future high-pressure low-temperature experiments. A significant amount of time can be saved by eliminating many of the low and medium resolution phi scans from the run list, as these were solely intended to provide additional redundancy. The removal of diffracting positions located at the peripheries of runs which contain no sample reflections (~10% of total) would also provide a significant reduction in collection time. By implementing the suggested changes in collection strategy it is possible to decrease the time required for each data set by approximately 50% and therefore increase the number of data points obtainable in high-pressure low-temperature studies using the XIPHOS facility. The warming and cooling cycles would still require large amounts of experimental time but this cannot be changed using the current setup.

The utilization of a fully enclosed beryllium shroud to facilitate these high-pressure low-temperature studies creates several difficulties for probing structure-property relationships under these conditions. X-ray transmission through the polycrystalline beryllium leads to the presence of beryllium powder rings in the diffraction images (Figure 6.12) which cannot be masked using ECLIPSE (Dawson *et al.*, 2004). Overlap between the beryllium intensities and sample reflections compromises the overall quality of data collected in these experiments, as exemplified by the necessary exclusion of numerous outliers from the refinement and higher *R*1 factor compared to the equivalent high-pressure ambient-temperature data collection. This problem can be overcome by using a suitable algorithm for masking the beryllium powder line contributions during integration, and a program designed for this purpose has been recently developed by Dr Mike Probert at the University of Newcastle.

Apparatus and techniques for conducting high-pressure low-temperature X-ray diffraction experiments have similarly been developed at Diamond Light Source I19 EH2. There are several advantages to utilizing the XIPHOS facility for conducting these experiments, most prominently among them the ability to reach temperatures down to 2 K, as well as the more convenient access and longer allocated diffractometer times of the latter compared with the former. However the facilities available at Diamond Light Source possess other features that are desirable for conducting high-pressure low-temperature studies, such as the availability of high-intensity short-wavelength X-ray radiation, absence of beryllium powder rings in the diffraction images, and ability to measure pressure and temperature in-*situ* (experimental work still in progress). Determining the best facility to utilize for these experiments will depend mainly on the system being investigated, coupled with the ability to obtain diffractometer time.

Figure 6.12: Detector images of KCP(Br) at 1.8 GPa (left) and 1.8 GPa and 4 K (right) illustrating the contribution of beryllium powder rings to diffraction pattern

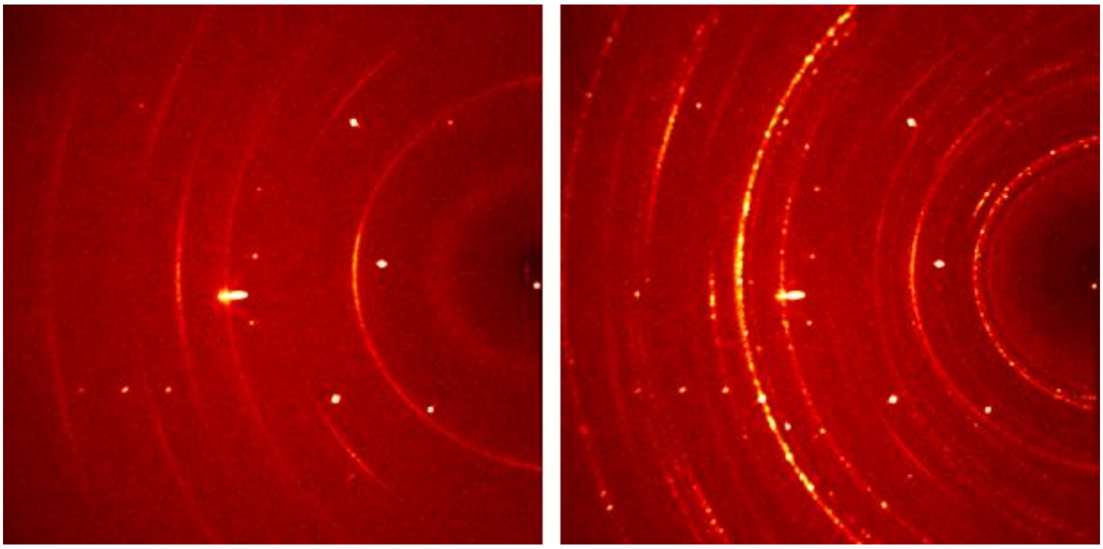

6.4.2 Structural Analysis

The statistically equivalent Pt-Pt distances (2.897(5) Å and 2.904(5) Å) observed in KCP(Br) under ambient conditions are consistent with the previously identified delocalization of electron density along the Pt chains. Approximately equivalent decreases in these distances upon the application of pressure are consistent with the high-pressure studies reported in the literature (Kobayashi *et al.*, 1980), and would be expected to produce a more effective overlap in the $d_z{}^2$ orbitals and therefore lead to a minor improvement in conductivity along the Pt chains (Interrante & Bundy, 1972). However given that the overall conductivity is limited by the probability of electron hopping between Pt chains, the substantially greater reductions in the inter-chain Pt···Pt distances will be more influential in the pressure-induced conductivity behaviour of KCP(Br). Relatively higher reductions in the *a* = *b* axes are achieved through compression of the relatively weak inter-chain interactions (hydrogen bonding and electrostatic) and distortion of the Pt1 square-planar geometry. The relatively short N1····N1 contacts (3.47(3) Å at 1.8 GPa) favour a non-linear herringbone type arrangement in the Pt1-C1-N1 moiety under pressure with the cyanide ligand pointing away from the potassium layer. Further increases in pressure may produce large enough distortions in the Pt1 coordination geometry to effectively disrupt the perpendicular conductivity pathway, and thereby cause the continual decline in overall conductivity observed in the literature at higher pressures (Interrante & Bundy, 1972).

A mechanism for the change in electrical properties under high-pressure low-temperatures is difficult to discern because of the limited data available and lack of many significant structural changes under these conditions. Nearly all of the crystal structure interactions are unaffected by cooling at high-pressure with the notable exception of the Pt1-Pt2^{i}, although it is impossible to ascertain whether this occurs only in the ultra-low temperature regime without additional data sets collected at different temperatures. Expansions along the a = b axis upon cooling would be expected to lead to a reduction in the probability of electron hopping between Pt chains and consequently an overall reduction in perpendicular conductivity. Since the conductivity of KCP(Br) has been found to increase under high-pressures at 4 K the origin of this unusual phenomenon must be dominated by the contraction of the Pt1-Pt2^{i} distance along the *c*-axis.

The structural feature responsible for the differing behaviour of the Pt-Pt distances upon cooling at high-pressures is currently unclear due to the absence of any statistically significant alteration to the crystal structure. A preferential contraction of the Pt1-Pt2^{i} interaction leads to a convergence of the Pt-Pt distances, and consequently suppresses the Peierls distortion responsible for the insulating electrical properties of KCP(Br) under ambient-pressure low-temperature conditions. The reductions in resistivity at high-pressure low-temperature conditions previously observed (Funnell *et al.*, 2011) can therefore be ascribed to a concurrent equalization of the Pt intrachain distances under these regimes.

6.5 Conclusion

The first high-pressure low-temperature single-crystal X-ray diffraction of KCP(Br) has been conducted using the XIPHOS diffraction facility with an applied pressure 1.8 GPa down to a cryostat temperature of 4 K. Improvements in conductivity at 1.8 GPa arise from enhanced $5d_z^2$ orbital overlap and reduced inter-chain distances. The high-pressure low-temperature electrical properties of KCP(Br) previously observed are derived principally from the disappearance of the Pt chain Peierls distortion. More high-quality data is required before the analysis of the high-pressure low-temperature behaviour of KCP(Br) can be validated.

6.6 References

Allan, D. R., Blake, A. J., Huang, D., Prior, T. J. & Schroeder, M. (2006). *Chem. Commun. (Cambridge, U. K.),* 4081-4083.

Allen, F. H. (2002). *Acta Crystallogr., Sect. B: Struct. Sci.* **B58**, 380-388.

Altomare, A., Cascarano, G., Giacovazzo, C., Guagliardi, A., Burla, M. C., Polidori, G. & Camalli, M. (1994). *J. Appl. Cryst.* **27**, 435.

Bernasconi, J., Kuse, D., Rice, M. J. & Zeller, H. R. (1972). *J. Phys. C* **5**, L127-L130.

Betteridge, P. W., Carruthers, J. R., Cooper, R. I., Prout, K. & Watkin, D. J. (2003). *J. Appl. Crystallogr.* **36**, 1487.

Boldyreva, E. V. (2008). *Acta Crystallogr., Sect. A: Found. Crystallogr.* **64**, 218-231.

Brown, R. K., Johnson, P. L., Lynch, T. J. & Williams, J. M. (1978). *Acta Crystallogr., Sect. B* **B34**, 1965-1968.

Brown, R. K., Vidusek, D. A. & Williams, J. M. (1979). *Inorg. Chem.* **18**, 801-804.

Brown, R. K. & Williams, J. M. (1978). *Inorg. Chem.* **17**, 2607-2609.

Bruker (2001). *Bruker AXS Inc., Madison, Wisconsin, USA.*

Byrne, P. J., Richardson, P. J., Chang, J., Kusmartseva, A. F., Allan, D. R., Jones, A. C., Kamenev, K. V., Tasker, P. A. & Parsons, S. (2012). *Chem. - Eur. J.* **18**, 7738-7748, S7738/7731.

Comes, R., Lambert, M., Launois, H. & Zeller, H. R. (1973). *Phys. Rev. B* **8**, 571-575.

Dawson, A., Allan, D. R., Parsons, S. & Ruf, M. (2004). *J. Appl. Crystallogr.* **37**, 410-416.

Deiseroth, H. J. & Schulz, H. (1974). *Phys. Rev. Lett.* **33**, 963-965.

Funnell, N., Kusmertseva, A. & Kamenev, K. (2011). unpublished data: University of Edinburgh.

Galloway, K. W., Moggach, S. A., Parois, P., Lennie, A. R., Warren, J. E., Brechin, E. K., Peacock, R. D., Valiente, R., Gonzalez, J., Rodriguez, F., Parsons, S. & Murrie, M. (2010). *CrystEngComm* **12**, 2516-2519.

Gomm, P. S. & Underhill, A. E. (1972). *J. Chem. Soc., Dalton Trans.*, 334-337.

Graham, A. J., Allan, D. R., Muszkiewicz, A., Morrison, C. A. & Moggach, S. A. (2011). *Angew. Chem., Int. Ed.* **50**, 11138-11141, S11138/11131-S11138/11137.

Graham, A. J., Tan, J.-C., Allan, D. R. & Moggach, S. A. (2012). *Chem. Commun. (Cambridge, U. K.)* **48**, 1535-1537.

Granier, T., Gallois, B., Gaultier, J., Real, J. A. & Zarembowitch, J. (1993). *Inorg. Chem.* **32**, 5305-5312.

Guetlich, P., Gaspar, A. B., Garcia, Y. & Ksenofontov, V. (2007). *C. R. Chim.* **10**, 21-36.

Heger, G., Deiseroth, H. J. & Schulz, H. (1978). *Acta Crystallogr., Sect. B* **B34**, 725-731.

Interrante, L. V. & Bundy, F. P. (1972). *Solid State Commun.* **11**, 1641-1645.

Johnson, P. L., Schultz, A. J., Underhill, A. E., Watkins, D. M., Wood, D. J. & Williams, J. M. (1978). *Inorg. Chem.* **17**, 839-844.

Katrusiak, A. (2008). *Acta Crystallogr., Sect. A: Found. Crystallogr.* **64**, 135-148.

Keefer, K. D., Washecheck, D. M., Enright, N. P. & Williams, J. M. (1976). *J. Am. Chem. Soc.* **98**, 233-234.

Kobayashi, H., Kobayashi, A., Asaumi, K. & Minomura, S. (1980). *Solid State Commun.* **35**, 293-296.

Krogmann, K. (1969). *Angew. Chem., Int. Ed. Engl.* **8**, 35-42.

Krogmann, K. & Hausen, H. D. (1968). *Z. Anorg. Allg. Chem.* **358**, 67-81.

Kuse, D. & Zeller, H. R. (1971). *Phys. Rev. Lett.* **27**, 1060-1063.

Lecrone, F. N., Minot, M. J. & Perlstein, J. H. (1972). *Inorg. Nucl. Chem. Lett.* **8**, 173-179.

Macrae, C. F., Edgington, P. R., McCabe, P., Pidcock, E., Shields, G. P., Taylor, R., Towler, M. & van, d. S. J. (2006). *J. Appl. Crystallogr.* **39**, 453-457.

Minot, M. J. & Perlstein, J. H. (1971). *Phys. Rev. Lett.* **26**, 371-373.

Moggach, S. A., Galloway, K. W., Lennie, A. R., Parois, P., Rowantree, N., Brechin, E. K., Warren, J. E., Murrie, M. & Parsons, S. (2009). *CrystEngComm* **11**, 2601-2604.

Moggach, S. A. & Parsons, S. (2009). *Spectrosc. Prop. Inorg. Organomet. Compd.* **40**, 324-354.

Moggach, S. A., Parsons, S. & Wood, P. A. (2008). *Crystallogr. Rev.* **14**, 143-184.

Peters, C. & Eagen, C. F. (1975). *Phys. Rev. Lett.* **34**, 1132-1134.

Peters, C. & Eagen, C. F. (1976). *Inorg. Chem.* **15**, 782-788.

Piermarini, G. J., Block, S., Barnett, J. D. & Forman, R. A. (1975). *J. Appl. Phys.* **46**, 2774-2780.

Prescimone, A., Morien, C., Allan, D., Schlueter, J. A., Tozer, S. W., Manson, J. L., Parsons, S., Brechin, E. K. & Hill, S. (2012). *Angew. Chem., Int. Ed.* **51**, 7490-7494, S7490/7491-S7490/7498.

Probert, M. R., Robertson, C. M., Coome, J. A., Howard, J. A. K., Michell, B. C. & Goeta, A. E. (2010). *J. Appl. Crystallogr.* **43**, 1415-1418.

Renker, B., Rietschel, H., Pintschovius, L., Glaeser, W., Bruesch, P., Kuse, D. & Rice, M. J. (1973). *Phys. Rev. Lett.* **30**, 1144-1147.

Rice, M. J. & Bernasconi, J. (1973). *J. Phys. F* **3**, 55-66.

Ruegg, W., Kuse, D. & Zeller, H. R. (1973). *Phys. Rev. B* **8**, 952-955.

Schultz, A. J., Gerrity, D. P. & Williams, J. M. (1978). *Acta Crystallogr., Sect. B* **B34**, 1673-1674.

Sheldrick, G. M. (2008). *SADABS.* Version 2008-1.

Spek, A. L. (2003). *J. Appl. Crystallogr.* **36**, 7-13.

Thomas, T. W., Hsu, C.-H., Labes, M. M., Gomm, P. S., Underhill, A. E. & Watkins, D. M. (1972). *J. Chem. Soc., Dalton Trans.*, 2050-2053.

Thomas, T. W., Labes, M. M., Gomm, P. S. & Underhill, A. E. (1972). *J. Chem. Soc., Chem. Commun.*, 322-323.

Underhill, A. E. & Wood, D. J. (1978). *Ann. N. Y. Acad. Sci.* **313**, 516-524.

Williams, J. M., Gerrity, D. P. & Schultz, A. J. (1977). *J. Am. Chem. Soc.* **99**, 1668-1669.

Williams, J. M., Johnson, P. L., Schultz, A. J. & Coffey, C. C. (1978). *Inorg. Chem.* **17**, 834-839.

Williams, J. M., Keefer, K. D., Washecheck, D. M. & Enright, N. P. (1976). *Inorg. Chem.* **15**, 2446-2455.

Williams, J. M., Petersen, J. L., Gerdes, H. M. & Peterson, S. W. (1974). *Phys. Rev. Lett.* **33**, 1079-1081.

Williams, J. M., Schultz, A. J., Cornett, K. B. & Besinger, R. E. (1978). *J. Am. Chem. Soc.* **100**, 5572-5573.

Zeller, H. R. (1972). *Phys. Rev. Lett.* **28**, 1452-1455.

Chapter 7

Conclusions

7.1 Conclusions

The aim of this research project was to develop high-pressure low-temperature single-crystal X-ray diffraction techniques and methodology, and subsequently to perform structural studies on compounds known to exhibit unusual properties under these conditions.

A calibration curve for a novel turnbuckle diamond anvil cell has been developed for high-pressure experiment on an open-flow cryostat down to 148 K. Thermocouples were found to be an unreliable method of measuring the temperature in these experiments and additionally acted as a thermal conduit between the room temperature laboratory and the sample.

High-pressure low-temperature apparatus at Diamond Light Source I19 EH2 has been developed to allow access to temperature regions down to 4 K. Major advantages of performing experiments on this beamline include high-intensity short-wavelength X-ray radiation, in-*situ* pressure and temperature measurements (still in development), and lack of beryllium powder rings in the diffraction pattern. Systematic errors in the cryostat thermocouple measurements suggest that this setup is only suitable for high-pressure experiments down to approximately 60 K.

The XIPHOS diffraction facility at the University of Durham has similarly been designed for high-pressure low-temperature single-crystal X-ray experiments down to 2 K. The principal advantage offered by the XIPHOS compared to I19 EH2 lies in the ability to reliably reach the base temperature of the cryostat, although the beryllium powder rings contaminating the diffraction pattern negatively impacts the quality of data obtainable during experiments.

High-pressure single-crystal X-ray studies under low-temperature environments have been successfully performed on the single-molecule magnet $Mn_{12}OAc$ (Chapter 4) and one-dimensional conductor KCP(Br) (Chapter 6). Compression of the $Mn_{12}OAc$ crystal structure results in the expulsion of crystallized acetic acid and ordering of the Jahn-Teller axes between 0.12 GPa and 0.87 GPa, and this has been correlated with the previously reported magnetic isomerism over the same pressure range. Meanwhile the convergence of the Pt intrachain distances and associated suppression of the predicted Peierls distortion in KCP(Br) at 1.80 GPa and 4 K has been linked to reductions in resistivity recorded under the same conditions.